TECHNISCHE UNIVERSITÄT MÜNCHEN

Lehrstuhl für Biotechnologie

Electro-switchable DNA layers for the analysis of antibody-antigen and p53-DNA interactions

Valentina Villa

Vollständiger Abdruck der von der Fakultät für Chemie der Technischen Universität München zur Erlangung des akademischen Grades eines

Doktors der Naturwissenschaften (Dr. rer. nat.)

genehmigten Dissertation.

Vorsitzender: Univ.-Prof. Dr. Aymelt Itzen

Prüfer der Dissertation: 1. Univ.-Prof. Dr. Johannes Buchner

2. Priv.-Doz. Dr. José Antonio Garrido Ariza

Die Dissertation wurde am 11.10.2012 bei der Technischen Universität München eingereicht und durch die Fakultät für Chemie am 03.12.2012 angenommen.

Ad Ester, Diana, Alessandro e Samuele

Table of contents

1. Abstract 1

2. Zusammenfassung 3

3. Objectives 5

4. Materials & methods 7

4.1 Materials 7

4.2 Methods 11

4.2.1 Buffer solutions 11

4.2.2 General methods in molecular biology and microbiology 12

4.2.3 Expression and purification of full-length wild type human p53 13

4.2.4 Methods in electrophoresis 15

4.2.5 Methods for "hCA1-DNA mono conjugate" project 19

4.2.6 Methods in SPR (Biacore™ X-100) 24

5. Introduction to *switch*SENSE 27

5.1 Physical basics 28

5.1.1 DNA structure 28

5.1.2 The electrical double layer 29

5.1.3 Energy transfer of fluorescence to metal surface 30

5.2 Experimental setup 31

5.2.1 Chip design and flow channel in Prototype1 and Prototype2 31

5.2.2 Chip design and flow channel setup in SWA1 33

5.2.3 Optical setup 34

5.3 Electrical manipulation of surface-tethered DNA strands 35

5.3.1 Methods 35

5.3.2 Factors affecting the switching behavior of DNA strands 41

6. Switchable hCA1-DNA layers 43

6.1 Introduction 43

6.1.1 Solulink™ conjugation chemistry 43

6.1.2 Human Carbonic Anhydrase 1 46
6.1.3 Binding kinetics 47
6.2 Results, part 1: hCA1-DNA conjugate preparation 50
6.2.1 Aldehydic functionalization of aminated oligonucleotide 50
6.2.2 Hydrazide functionalization of hCA1 51
6.2.3 Optimization of conjugation and purification steps 54
6.3 Discussion, part 1: optimized protocol of hCA1-DNA mono conjugate 64
6.4 Results and discussion, part 2: hCA1-DNA conjugates on *switch*SENSE 67
6.4.1 Hybridization kinetics of hCA1-DNA conjugates on surface 67
6.4.2 Voltage Response of hybridized hCA1-DNA 70
6.4.3 Time Resolved Measurement of hybridized hCA1-DNA 74
6.4.4 Sizing of hCA1 79
6.4.5 Acetazolamide influence on hCA1 functionalized layers 82
6.5 Conclusion 83
7. Antibody kinetics analysed in *switch*SENSE 85
7.1 Introduction 85
7.1.1 Surface-based sensor 85
7.1.2 SPR-based sensor 86
7.2 Results 88
7.2.1 Employed monoclonal antibodies and experimental design 88
7.2.2 Kinetic analysis on the SPR system Biacore™ X100 90
7.2.3 Kinetic analysis on *switch*SENSE 95
7.2.4 Tested cross-binding of monoclonal antibodies on *switch*SENSE 103
7.2.5 Discussion 106
7.3 Conclusion 119
8. Human p53 analysed in *switch*SENSE 121
8.1 Introduction: p53 tumour suppressor 121
8.1.1 Structure and function of individual p53 domains 122
8.2 Motivation 129

8.3 Experimental design 130
8.3.1 The protein characterization 131
8.3.2 Oligonucleotide design 133
8.4 Results 134
8.4.1 EMSA results 134
8.4.2 Detection of p53-DNA binding activity on *switch*SENSE 135
8.5 Discussion 146
8.5.1 The nonspecific binding of p53 to DNA 146
8.5.2 The p53 dimer-tetramer transition detected on surface 148
8.5.3 The DNA bending upon p53 binding 150
8.5.4 The role of the half site response elements 152
8.6 Conclusion 153
9. Conclusion 155
10. References 157
11. Publications 165
12. Acknowledgements 167
13. Declaration 169
14. Appendix 171
14.1 C-48-mer folding 171
14.2 Hybridization kinetics 171
14.3 Antibody kinetic analysis in Biacore 173
14.4 Antibody kinetic analysis in *switch*SENSE 177
14.5 Cross-binding experiments of antibodies on prototype2 185
14.6 LFM data of initial ds-DNA layers on SWA1 and on Prototype2 187
14.7 p53 project 188

1. Abstract

The *switch*SENSE technique is a new bioanalytical method for the characterization of interactions between biomolecules on a chip in a real-time and label-free manner. Short double stranded oligonucleotides are electrically switched on microelectrodes by alternating electric fields and their switching dynamics are measured in real-time by fluorescence energy transfer. The binding of proteins to modified DNA probes is detected by time-resolved measurements of dynamic motion, whereby the increase in hydrodynamic drag slows down the electrically induced switching movement.

This thesis investigates two types of molecular interactions: (i) high-affinity protein-protein interactions between human Carbonic Anhydrase 1 and monoclonal antibodies, and (ii) protein-DNA interactions between the tumor suppressor protein p53 and DNA response elements. The development of *switch*SENSE assays is described and compared to complementary techniques.

In order to assess the potential of the *switch*SENSE method to quantify strong protein-protein interactions, the affinity of various monoclonal antibodies against human Carbonic Anhydrase 1 (hCA1) was studied. To this end, coupling methods were developed to obtain stoichiometrically defined hCA1-DNA mono-conjugates, which were used as switchable surface probes. Antibody association and dissociation to surface-tethered hCA1 were monitored based on the dynamic switching response of the electrically modulated layers. The kinetic rate constants (k_{on}, k_{off}) and the dissociation constants (K_D) were quantified and compared to complementary measurements with a Biacore™ surface plasmon resonance (SPR) sensor. SPR data yielded dissociation constants in the nanomolar concentration range, which strongly depended on the employed chip surface, while picomolar dissociation constants were obtained from *switch*SENSE data. The discrepancies are attributed to two factors: (i) the higher detection sensitivity of the *switch*SENSE method, and (ii) avidity effects observed on the switchable hCA1-DNA surface, which stabilized the antibody-hCA1 complex.

The tumour suppressor protein p53 was characterized regarding its DNA-binding activity employing steady-state fluorescence quenching as well as dynamic DNA-switching experiments. Hereby, the kinetic binding of human full-length wild-type p53 was detected on DNA layers comprising *p21* and *half-p21* response elements. For the first time, human wild-type p53 could be characterized in the absence of any purification tags or stabilizing mutations. In DNA switching dynamics measurements,

the oligomerization of p53-dimers to p53-tetramers could be directly observed with the surface-based sensor and a transition was identified at 60 nM of p53 monomer concentration. In the dimerization concentration regime, the kinetic analysis evidenced the *specific* binding of p53 to *p21* and *half-p21* sequences, with an association rate k_{on} of 1.7×10^{4} $M^{-1}s^{-1}$, which was independent of the length of the response elements. In the tetramerization concentration regime, p53 exhibited similar binding kinetics to specific and to nonspecific DNA sequences, characterized by an association rate which is app. 10 times higher than for the dimeric form and an apparent equilibrium constant K_D of approximately 1 nM. Moreover, p53-induced conformational changes of the DNA structure, that is a pronounced bending, were detected by fluorescence quenching.

The presented results demonstrate the relevance of electro-switchable DNA layers for the analysis of proteins, and show the merit of obtaining multiple parameters – k_{on}, k_{off}, K_D, size and oligomerization state, occurrence of structural changes – in a single assay.

2. Zusammenfassung

Die *switch*SENSE Technologie stellt eine neue alternative Methode für die Bioanalytik dar, mit der eine Charakterisierung von Proteinen ohne Fluoreszenzmarkierung und in Echtzeit möglich ist.

Für die markierungsfreie Analyse von Protein-Interaktionen in Echtzeit werden elektrisch schaltbare DNA-Schichten eingesetzt. Dazu werden kurze DNA-Doppelstränge auf einer Goldelektrode gebunden und ihre Orientierung auf der Oberfläche durch elektrische Felder beeinflußt (geschaltet). Die Dynamik der DNA wird mit Hilfe des Fluoreszenz-Resonanzenergietransfers beobachtet.

Die Bindung der Proteine an modifizierte DNA-Stränge wird durch zeitaufgelöste Messmethoden der Molekulardynamik untersucht wobei der erhöhte hydrodynamische Widerstand die elektrisch induzierte Schaltbewegung verlangsamt.

Im Rahmen dieser Doktorarbeit wurden zwei verschiedene Arten von molekularen Interaktionen untersucht: (i) hochaffine Protein-Protein-Interaktionen zwischen humaner Carboanhydrase 1 (hCA1) und monoklonalen Antikörpern und (ii) Protein-DNA-Interaktionen zwischen dem Tumorsuppressorprotein p53 und seiner DNA-Konsensussequenz. In dieser Dissertation wird die Entwicklung der *switch*SENSE Methode beschrieben und mit komplementären Techniken verglichen.

Um zu überprüfen, ob die *switch*SENSE-Technik starke Protein-Protein-Interaktionen quantifizieren kann, wurden verschiedene monoklonale Antikörper gegen hCA1 untersucht. Dazu wurde die Chip-Oberfläche mit Protein-DNA-Konjugaten, bestehend aus hCA1 und kurzer einzelsträngiger DNA, funktionalisiert. Dieser Aufbau ermöglichte eine kinetische Charakterisierung der Antikörperbindung. Die Antikörper wurden mit nanomolarer Konzentration auf die Oberfläche injiziert und deren Assoziation und Dissoziation mit Hilfe der Dynamik der DNA-Schichten verfolgt. So konnten die Ratenkonstanten (k_{on}, k_{off}) sowie die Dissozationskostante (K_D) von vier verschiedenen Antikörpern bestimmt werden. Die Affinität der Antikörper lag im picomolaren Bereich und wurde mit den Werten, die mittels *surface plasmon resonance* SPR-Biacore™-Technologie bestimmt wurden, verglichen. Die Affinitäten, die sich aus den SPR-Messungen ergaben und sehr stark abhängig von der Oberflächenstruktur sind, lagen im nanomolaren Bereich. Diese Diskrepanz könnte zum einen auf die höhere Sensitivität der Detektion mit der *switch*SENSE Technologie zurückzuführen sein. Zum anderen könnte die Avidität des Antikörpers und der damit verbundenen Stabilität des Antigen-Antikörper-Komplexes Grund dafür sein.

Des weiteren wurde mittels der *switch*SENSE-Technologie die DNA-Bindung des Tumorsuppressorproteins p53 charakterisiert, wobei steady-state Fluoreszenz-quenching und dynamische DNA-switching Experimente benutzt wurden. Es wurde die Kinetik der p53-Bindung an die DNA-Schicht, die aus den *p21* und *half-p21* Konsensussequenzen bestand, untersucht. In dieser Studie konnte zum ersten Mal humanes wildtyp p53 ohne jegliche Reinigungs-*tags* oder stabilisierende Mutationen charakterisiert werden. In den DNA-Dynamik-Messungen wurde mit dem Oberflächen-Biosensor direkt die Oligomerisierung von p53-Dimeren und Tetrameren beobachtet. Über 60 nM Monomerkonzentration liegt p53 als Tetramer vor und keine Dimere werden beobachtet. Bei Konzentrationen niedriger als 60 nM bindet p53 spezifisch an die p21- und half-p21-Sequenzen mit einer Assoziationskonstante k_{on} von 1.7×10^{4} $M^{-1}s^{-1.}$ Bei einer Konzentration über 60 nM weist p53 ähnliche Bindungseigenschaften zu spezifischer und unspezifischer DNA-Sequenz auf, mit einer etwa 10 mal höheren Assoziationskonstante als das p53 Dimer und einer apparenten Dissozationskostante von 1 nM. Außerdem wurde mittels Fluoreszenzquenching ein Krümmen der DNA durch die Bindung von p53 beobachtet.

Diese Ergebnisse demonstrieren, dass mit nur einer Technologie, die der elektrisch schaltbaren DNA-Schichten, verschiedene Parameter der Proteinanalyse, wie k_{on}, k_{off}, K_D, Größe, Oligomerisierungszustand und Strukturänderungen, erhalten werden können.

3. Objectives

The development in biotechnological research and in the area of life sciences requires efficient analytical methods to characterize *in vitro* interactions between biomolecules. Traditional methods, such as gel electrophoresis, immunoassays, fluorescence anisotropy, analytical ultracentrifugation and calorimetry, are currently employed. However, those techniques have some drawbacks; their use can be complicated or time-consuming. Furthermore, these methods might necessitate the labelling of proteins, which may alter their conformation and interfere with their function and in general they are techniques that require large amounts of sample.

Surface based biosensors allow an effective functionalization of the surface by immobilization of the ligand and a consequent detection of loaded target, using amounts below the microgram range. Hereby, the employment of these technologies enables researchers to perform an extensive parallel detection in real-time on a single platform in a label-free manner. Currently, several label-free biosensors are being employed for affinity interactions. These biosensors can be optical platforms, based on either surface plasmon resonance (SPR) (Liedberg et al, 1983), or on interferometry, like biolayer interferometry (Yang et al, 2003). Other platforms belong either to surface acoustic wave sensor or to quartz crystal microbalance sensors (Janshoff et al, 2000).

The *switch*SENSE technology is a new powerful choice for bioanalytics, detecting on a chip biomolecular interactions in a real-time label-free manner. Currently, this biosensor is intended to be commercialized by Dynamic Biosensors GmbH, a spin-off company from the Technische Universität München (TUM). In *switch*SENSE the electrically actuated DNA layers combine electrical modulation of surface-tethered ds-DNA probes with an optical method to observe the dynamics of DNA conformational changes and enable the detection of biomolecules, such as DNA probes, antibodies and DNA-binding protein (Arinaga et al, 2007; Kaiser & Rant, 2010; Knezevic et al., 2012; Rant et al, 2006a; Rant et al, 2007; Rant et al, 2006b; Rant et al, 2009; Spuhler et al, 2010). The aim of this work is to demonstrate the versatile employment of electro-switchable DNA surface in characterizing protein/protein and protein/DNA interactions.

This thesis investigates two types of molecular interactions: (i) high-affinity protein-protein interactions between human Carbonic Anhydrase 1 and monoclonal antibodies, and (ii) protein-DNA interactions between the tumour suppressor protein p53 and DNA

response elements. The development of switchSENSE assays is described and compared to complementary techniques.

In the first project the chip surface was functionalized with protein-DNA mono conjugates made out of human Carbonic Anhydrase 1 (hCA1). The ligand present on the surface enabled the kinetic characterization of monoclonal antibodies, monitoring the switching dynamic response of the electrically modulated layers. The dynamics identified the binding state of antibodies on hCA1, due to the increase in hydrodynamic drag which slowed the switching movement.

In the second project in collaboration with Makiko Maruyama (Walter Schottky Institute, TU München), the tumour suppressor p53 was characterized on surface based on its DNA-binding activity. Hereby, the kinetic binding of human full-length wild-type p53 was detected on DNA layers integrating *p21* and *half-p21* response elements. This project presented for the first time p53 characterization in the absence of any purification tags or stabilizing mutations.

4. Materials & methods

4.1 Materials

CHEMICALS

Acrylamide solution (38% with 2% bisacrylamide)	Serva, Heidelberg, DE
Agarose, ultra-pure	Serva, Heidelberg, DE
Albumin from bovine serum	Sigma-Aldrich, Taufkirchen, DE
Ammoniumperoxodisulfate (APS)	Roth, Karlsruhe, DE
Ampicillin	Roth, Karlsruhe, DE
Anhydrous DMF	Solulink, San Diego, USA
Bromphenol blue S	Serva, Heidelberg, DE
Coomassie Brilliant Blue G-250	Serva, Heidelberg, DE
Dithiothreitol	Roth, Karlsruhe, DE
ECL+plus Western Blotting Detection System	GE Healthcare, München, DE
Ethanol, p.a.	Roth, Karlsruhe, DE
Ethidiumbromide	Sigma-Aldrich, Taufkirchen, DE
Glycerol, 99%	Roth, Karlsruhe, DE
Glycine	Roth, Karlsruhe, DE
2-hydrazinopyridyl HCl, 2-HP	Solulink, San Diego, USA
Kanamycin	Roth, Karlsruhe, DE
2-Mercaptoethanol, pure	Sigma-Aldrich, Taufkirchen, DE
Ethansulfonic acid (Hepes)	Roth, Karlsruhe, DE
N,N,N',N'-Tetramethylethylendiamin (TEMED)	Roth, Karlsruhe, DE
Protease inhibitor mix G	Serva, Heidelberg, DE
Sodiumdodecylsulfate (SDS)	Roth, Karlsruhe, DE
Succinimidyl 4-formylbenzoate, S-4FB	Solulink, San diego, USA
Succinimidyl 6-hydrazinonicotinamide S-HyNic	Solulink, San diego, USA
Tris(2-carboxyethyl)phosphine hydrochloride solution, pH 7	Sigma-Aldrich, Taufkirchen, DE
Tris-(hydroxymethyl)-aminomethan (Tris)	Roth, Karlsruhe, DE
Titriplex (EDTA)	Roth, Karlsruhe, DE
Triton X-100	Sigma-Aldrich, Taufkirchen, DE
Isopropyl ß-D-1-thiogalactopyranoside (IPTG)	Roth, Karlsruhe, DE

Other chemicals were supplied by Sigma-Aldrich or Roth in p.a. biochemical or molecular biology quality. For the preparation of buffers double distillated water was used.

SIZE MARKERS AND KITS

Amine Coupling Kit	GE Healthcare, München, DE
BenchMark™ Fluorescent Protein Standard	Life Technologies, Darmstadt, DE

Full-Range Rainbow Molecular Weigh Markers	GE Healthcare, München, DE
High Pure PCR Product Purification Kit	Promega, Mannheim, DE
LMW-SDS Marker Kit	GE Healthcare, München, DE
S-HyNic Conjugation Kit (S-9002-1)	Solulink, Inc., San Diego, USA
SilverXpress® Silver Staining Kit	Life Technologies, Darmstadt, DE
Wizard® Plus SV Mini-Preps DNA purification kit	Promega, Mannheim, DE

OLIGONUCLEOTIDES

NAME	5' – SEQUENCE - 3'
SS-SH-48-MER-CY3	$HS-(CH_2)_6$ - TAG TCG TAA GCT GAT ATG GCT GAT TAG TCG GAA GCA TCG AAC GCT GAT - Cy3
SS-48-MER-CY3	TAG TCG TAA GCT GAT ATG GCT GAT TAG TCG GAA GCA TCG AAC GCT GAT - Cy3
SS-48-MER	TAG TCG TAA GCT GAT ATG GCT GAT TAG TCG GAA GCA TCG AAC GCT GAT
C-SS-48-MER	ATC AGC GTT CGA TGC TTC CGA CTA ATC AGC CAT ATC AGC TTA CGA CTA
C-SS-AMINO-48-MER	$NH_2-(CH_2)_6$ - ATC AGC GTT CGA TGC TTC CGA CTA ATC AGC CAT ATC AGC TTA CGA CTA
P21 **(SS-SH-74-MER-CY3)**	$HS-(CH_2)_6$ - CTT TCT GGC CAT CAT AGC TCT GGC ATA GAA TAG TCG TGA GAT GAG GAA CAT GTC CCA ACA TGT TGA GCT CTG AT - Cy3
C-P21 **(C-SS-74-MER)**	ATC AGA GCT CAA CAT GTT GGG ACA TGT TCC TCA TCT CAC GAC TAT TCT ATG CCA GAG CTA TGA TGG CCA GAA AG
HALF-P21 **(SS-SH-74-MER-CY3)**	$HS-(CH_2)_6$ - CTT TCT GGC CAT CAT AGC TCT GGC ATA GAA TAG TCG TGA GCA CAT TCG TAA TGA GGA ACA TGT CCA ACG CTG AT - Cy3
C-HALF-P21 **(C-SS-74-MER)**	ATC AGC GTT GGA CAT GTT CCT CAT TAC GAA TGT GCT CAC GAC TAT TCT ATG CCA GAG CTA TGA TGG CCA GAA AG
NEGCTR **(SS-SH-74-MER-CY3)**	$HS-(CH_2)_6$ - CTT TCT GGC CAT CAT AGC TCT GGC ATA GAA TAG TCG TGA GCA CAT GAA AGG TGG ATT TAG GTG GAA ACG CTG AT - Cy3
C- NEGCTR **(C-SS-74-MER)**	ATC AGC GTT TCC ACC TAA ATC CAC CTT TCA TGT GCT CAC GAC TAT TCT ATG CCA GAG CTA TGA TGG CCA GAA AG
C-BIOTIN **(C-SS-74-MER)**	ATC AGC GTT TCC ACC TAA A**T**(biotin)C CAC CTT TCA TGT GCT CAC GAC TAT TCT ATG CCA GAG CTA TGA TGG CCA GAA AG

Oligonucleotides used in this work were purchased from IBA GmbH,

PROTEINS AND ANTIBODIES

DNAseI	Roche, Mannheim, DE,
Human Carbonic Anhydrase I	Sigma-Aldrich, Taufkirchen, DE
mAb anti-Biotin, mouse clone BN-34	Sigma-Aldrich, Taufkirchen, DE
mAb anti hCA1, mouse IgG2a, clone 7G12	Abnova, Taiwan
mAb anti hCA1, mouse IgG1, clone G-6	Santa Cruz Biotechnology
mAb anti hCA1, mouse IgG1, clone M2	AbDSerotec, Düsseldorf, DE
mAb anti hCA1, mouse IgG2a, clone 10E4	AbNova, Taiwan
mAb anti hCA1, mouse IgG2b, clone 1F1	AbNova, Taiwan
mAb anti hp53, mouse clone DO-1	AbDSerotec, Düsseldorf, DE
Polyclonal anti-mouse κ (kappa chain), rabbit HRP conjugated	Rockland Immunochemicals Inc., USA

MATERIAL FOR CHROMATOGRAPHY

BioPro QA	YMC Europe Dinslaken, DE
HiTrap Q FF 5 ml	GE Healthcare, München, DE
HiTrap SP FF 5ml	GE Healthcare, München, DE
HiTrap ™ Con A 4B 1 ml	GE Healthcare, München, DE
HiTrap Heparin HP 5 ml	GE Healthcare, München, DE
Superdex 75 10/300 GL	GE Healthcare, München, DE
Superdex 200 HiLoad 26/60	GE Healthcare, München, DE
Superdex 200 HiLoad 10/300	GE Healthcare, München, DE

MISCELLANEOUS MATERIAL

96-well-Plate	Greiner & Söhne, Nürtingen, DE
Amicon® Ultra-0.5 ml Centrifugal Filters (3, 10, 30 kDa CO)	Merk Millipore, Darmstadt, DE
Amicon® Ultra-4 ml Centrifugal Filters (3, 10, 30 kDa CO)	Merk Millipore, Darmstadt, DE
Amicon® Ultra-15 ml Centrifugal Filterr (3, 10, 30 kDa CO)	Merk Millipore, Darmstadt, DE
Deoxyribonucleic acid, low molecular weight from salmon sperm	Sigma-Aldrich, Taufkirchen, DE
Disposable cuvettes	Brand, Wertheim, DE
Drystrip gel pH 4-7, 7CM IMMOBILINE	GE Healthcare, München, DE
D-Tube™ Dialyzers Midi	Merk Millipore, Darmstadt, DE
Filter paper	Whatman, Maidstone, UK
Immobilon-NC(Nitrocellulose) membrane	Merk Millipore, Darmstadt, DE
Immobilon-P (PVDF) membrane	Merk Millipore, Darmstadt, DE
Membrane filter (0.2 µm)	Sartorius, Göttingen, DE
Micro BCA-Proteinassay	Thermo Fisher Scientific, USA
Microcentrifugation tube (0.2 ml)	Biorad, München, DE
Microcentrifugation tube (0.5, 1.5, 2 ml)	Eppendorf, Hamburg, DE
pH-indicator strip	Roth, Karlsruhe, DE

Sensor Chip C1	GE Healthcare, München, DE
Sensor Chip CM5	GE Healthcare, München, DE
Serva Gel™ TG Vertical Tris-Glycine Gel 2D 14 %	Serva, Heidelberg, DE
Sterile syringe filters 0.2 µm	Merk Millipore, Darmstadt, DE
Whatman 3MM	GE Healthcare, München, DE
X-ray films X-OMAT AR	Kodak, Rochester, USA
Zeba Spin Desalting Columns	Thermo Fisher Scientific, USA

EQUIPMENT

Balances

Analysis balance BP 121 S	Sartorius, Göttingen, DE
Halfmicro balance BL 310	Sartorius, Göttingen, DE

Centrifuges

Avanti J 25 with JA-10 and JA-25.50 rotors	Beckman, Krefeld, DE
Beckman XL-I analytical ultracentrifuge	Beckman, Krefeld, DE
Eppendorf table-top centrifuge 5415 C	Eppendorf, Hamburg, DE
Rotina 46 R coolable centrifuge	Hettich, Tuttlingen, DE
Universal 32 R coolable centrifuge	Hettich, Tuttlingen, DE

Chromatographic machines and their accessories

Agilent 1200 Infinity Series LC	Agilent, Waldbronn, DE
Äkta Explorer	GE Healthcare, München, DE
Super loop 150 ml	GE Healthcare, München, DE

Gelelectrophoresis and blotting devices

Blue Vertical 102	Serva, Heidelberg, DE
Fast Blot B44 apparatus	Biometra, Göttingen, DE
Hoefer Mighty Small II gelelectrophoresis unit	GE Healthcare, München, DE
Hoefer SE600 Ruby	GE Healthcare, München, DE
Mini-PROTEAN Tetra Electrophoresis System	Biorad, München, DE

Spectrophotometers

Cary 50 Bio UV-VIS-spectrophotometer	Varian, Palo Alto, USA
Nanodrop	Peqlab, Erlangen, DE

Voltage sources

LKB-GPS 200/400	Amersham, Uppsala, Sweden
EPS 3500, 301 und 1001	Amersham, Uppsala, Sweden

Further equipment

Air circulation incubator	New Brunswick Scientific, DE
Biacore™ X100	GE Healthcare, München, DE
Cell disruption machine Basic Z	Constant Systems, England
Culture shaker Certomat S	Braun Biotech, DE
Eppendorf thermomixer	Eppendorf, DE

ImageQuant LAS 4000	GE Healthcare, München, DE
Laboratory ice machine	Ziegra, Isernhagen, DE
Magnetic stirrer Heidolph MR 2000	Heidolph, Kelheim, DE
Optimax, X-ray film developer	TRMS Laborgeräte, DE
pH-meter	WTW, Weilheim, DE
Thermocycler Primus	MWG, Ebersberg, DE
Typhoon 9400	GE Healthcare, München, DE
Varioklav steam autoclave EP-Z	H+P, Oberschleißheim, DE
Vortex MS2	IKA. Wilmington, USA

COMPUTER SOFTWARE

Biacore X100 Evaluation Version 2.01	GE Healthcare, München, DE
ChemDraw Ultra 12.0	PerkinElmer Informatics, Cambridge, USA
DeepView / Swiss-PDBViewer v4.0.3	SIB, Basel, Switzerland
ImageQuant TL	GE Healthcare, München, DE
OligoCalculator 3.26	Northwestern University, Chicago, USA
Origin 8.5	OriginLab Corporation, Northampton, USA
ProtParamTool	ExPasy http://expasy.hcuge.ch/

4.2 Methods

4.2.1 Buffer solutions

Here the recipes of buffer solutions used in the following chapters were described. All the other buffer solutions for methods were indicated in each section of this chapter.

Chapter 5:

Hybridization Buffer: Tris 10 mM pH 7.3, NaCl 200 mM;

Standard Buffer: Tris 10 mM pH 7.3, NaCl 50 mM.

Chapter 6:

Con A Binding Buffer: Tris 20 mM pH 7.4, NaCl 0.5 M, $MnCl_2$ 1 mM, $CaCl_2$ 1 mM;

Con A Elution Buffer: Tris 20mM pH 8.5, NaCl 0.5 M, Glucose 1 M;

Conjugation buffer: Na_2HPO_4 100 mM pH 6.0, NaCl 150 mM;

Inhibition Buffer Tris 10mM pH 8.1, NaCl 50mM;

Modification buffer: Na_2HPO_4 100 mM pH 7.4, NaCl 150 mM;

PBS Buffer0.1 M pH 7.4: Na_2HPO_4 75 mM, NaH_2PO_4 25 mM;

Standard Buffer: Tris 10 mM pH 7.3, NaCl 50 mM.

Chapter 7:

Acetate Buffer:	Sodium Acetate 10 mM pH 5.5;
HBS-P:	HEPES 10 mm pH 7.4, NaCl 150 mm, Surfactant P-20 0.05% (v/v);
StdB-T:	Standard Buffer containing 0.05 % (v/v) Tween20;
Binding Buffer:	Hepes 40 mM pH 8.0, $MgCl_2$ 10 mM, KCl 50 mM, glycerol 5 % (v/v), TCEP-HCl 10 mM.

4.2.2 General methods in molecular biology and microbiology

E. COLI STRAINS

STRAINS	GENO- / PHENOTYPE	SOURCE / REFERENCE
E. coli XL1 Blue	*rec*A1 *end*A1 *gyr*A96 *thi*-1 *hsd*R17 *sup*E44 *rel*A1 *lac* [F'proAB *lac*IqZDM15 Tn10 (*Tet*R)]	Stratagene, Waldbronn, DE
E. coli BL21 (DE3)	F– *omp*T hsdS(rB– mB–) *dcm*+ *Tet*r *gal* l (DE3) *end*A *Hte* [*arg*U *ile*Y *leu*W *Cam*R]	Stratagene, Waldbronn, DE

BACTERIAL VECTOR

NAME	VECTOR	SOURCE
hp53 wt FL	pET28a	Rohrberg Julia, TU München
p53 R280E	pET28a	Rohrberg Julia, TU München
p53 ΔN93ΔC37	pET28a	Rohrberg Julia, TU München

MEDIA AND ANTIBIOTIC SOLUTION FOR E. COLI CULTIVATION

LB:	LB-Medium 20 g/l for plate Agar Agar 20g/l;
Antibiotics:	Ampicillin 200 µg/ml in ddH_2O;
Kanamycin:	50 µg/ml in ddH_2O.

LB media was sterilized in autoclave (20 min at 121°C). Antibiotic solutions were filtered and kept at -20°C.

CULTIVATION AND STORAGE OF E. COLI

E. coli was cultivated at 30°C or 37°C either on LB plates or in LB liquid media. By addition of appropriate antibiotics to the media the transformed strains by the plasmid were selected. Liquid cultures were inoculated from fresh overnight cultures or by transferring single colonies from plates. Bacterial division was monitored at 600 nm

(OD600nm = 1 corresponding to approx. $8x10^8$ cells/ml). For long-term storage, 5 mL of a freshly inoculated culture were centrifuged at 5,000 x g and the sediment was resuspended in 1 ml medium. 300 µl 50% glycerol were added to 700 µl of bacterial suspension resulting in a 15% glycerol culture stock. The culture was frozen using liquid nitrogen and stored at -80°C.

TRANSFORMATION OF COMPETENT E. COLI CELLS AND CULTIVATION

200 µL of chemical competent *E. coli* cells were mixed with 50 ng of plasmid DNA, and incubated on ice for at least 30 min, then transferred for 60 s to 42°C for a heat step, and cooled down on ice for another 5 min. After the addition of 1ml LB liquid media, cells were gently shaken at 37°C for at least 45 min, which enabled transcription of resistance genes and synthesis of the antibiotics processing enzymes. Subsequently, cells were centrifuged at 4000 x g for 5 min and either plated or inoculated in to the liquid media, with the respective antibiotics. *E.coli* cultures were grown at 37°C.

AMPLIFICATION OF PLASMID DNA AND STORAGE

Single colonies were transferred into 4 ml of selecting LB media for amplification of plasmid DNA, and grown in a rotary shaker at 37°C. Next, Wizard Plus SV Minipreps DNA Purification System was employed to isolate the plasmid. DNA was stored in sterile H2O at -20°C.

4.2.3 Expression and purification of full-length wild type human p53

The following protocols for human full-length wild-type p53 expression and purification were gently received from Dr. Julia Rohrberg.

BUFFER RECIPE FOR CELL LYSIS AND COLUMNS

Lysis Buffer:	40 mM KH_2PO_4/K_2HPO_4 pH 7.5, 50 mM KCl, 1 mM DTT, 1 mM EDTA;
Heparin A:	40 mM KH_2PO_4/K_2HPO_4 pH 7.5, 5 % glycerol, 50 mM KCl, 1 mM DTT;
Heparin B:	40 mM KH_2PO_4/K_2HPO_4 pH 7.5, 5 % glycerol, 1 M KCl, 1 mM DTT;
Dilution buffer:	20 mM KH_2PO_4/K_2HPO_4 pH 7.5;
Sepharose A:	50 mM KH_2PO_4/K_2HPO_4 pH 7.5, 50 mM KCl, 5 mM ETDA, 1 mM DTT;
Sepharose B:	50 mM KH_2PO_4/K_2HPO_4 pH 7.5, 1 M KCl, 5 mM ETDA, 1 mM DTT;
GF-Buffer:	50 mM KH_2PO_4/K_2HPO_4 pH 7.5, 100 mM KCl, 1 mM TCEP.

The buffers were previously 0.2 μm filtered, degassed, and kept at 4°C, ready to be used for the cold purification step. Furthermore DTT and TCEP were freshly added.

EXPRESSION

E. coli BL21 (DE3) competent cells were transformed with pET28a plasmid containing hp53 wt-FL as described in Section 4.2.3. After transformation, the cells were plated selecting for Kanamycin and let them grown at 37°C overnight. For the expression four 100-ml LB_{Kan} pre-cultures were inoculated with one single colony of transformed *E. coli* and kept at 37°C overnight. Next day four 2-l flasks were poured with a single pre-culture, and kept at 37°C. At OD_{600} 0.5-0.8, the flasks were cooled down to 25 °C and the protein expression was induced adding 1 mM IPTG and 100 μM $ZnSO_4$ and the incubation was done overnight at 20 °C. The cells were harvested centrifuging at 7000 rpm at 4 °C for 15 min.

CELL LYSIS

The pellet was resuspended in cold Lysis Buffer containing freshly added a bit of DNAseI and one aliquot of protease inhibitor mix G (1:50 dilution), then the cells were disrupted in French press and the lysate was collected centrifuging at 20,000 rpm at 4°C for 30 min. Finally the supernatant was immediately processed in purification step.

PURIFICATION

The purification was done in Äkta Fast Protein Liquid Chromatography (FPLC) in the cold room at 4°C. After each column, the interesting fractions were checked in SDS-PAGE to select the one to be joined together for the next purification step. Finally the purity of hp53 wt FL was checked in SDS-PAGE and the identity was confirmed in western blot. The plasmid and all protocols were received from Dr. Julia Rohrberg, and after checking the plasmid in restriction enzyme digestion, the western blot was the only control step.

A. AFFINITY CHROMATOGRAPHY IN HEPARIN COLUMN

Heparin is a highly sulfated glycosaminoglycan and used for affinity purification of DNA binding proteins.

The lysate was loaded on HiTrap Heparin HP column, followed by a wash step with 5 column-volumes (CV) of buffer Heparin A 95%+ Heparin B 5%. The elution was performed by linear gradient of buffer Heparin B. Usually p53 is eluted at 350-400 mM KCl. After checking in SDS-PAGE the relevant fractions were collected and diluted 1:3 in dilution buffer to adjust the salinity before ion exchange columns, in presence of protease inhibitor mix G.

B. ION EXCHANGE COLUMNS

Since the pI value of p53 is almost at neutral pH, the eluate was loaded on anion and cation exchange columns in succession. Then for both columns was performed a wash step with 5 CV in buffer Sepharose A 95% + Sepharose B 5%, and an elution step in linear gradient with buffer Sepharose B.

The important fractions were joined and concentrated with 5-ml Amicon® 10 kDa MWCO at 4°C centrifuging at 4,000 rpm.

C. SIZE EXCLUSION COLUMN

The concentrate was injected in Superdex 200 HiLoad 26/60 and the isocratic elution was performed in GF-buffer. After SDS-PAGE, the fractions containing the protein were concentrated in Amicon® 10 kDa MWCO till 20 µM concentration and frozen quickly in liquid nitrogen at -80°C in 20 µl aliquots.

4.2.4 Methods in electrophoresis

4.2.4.1 EMSA for hp53 DNA binding activity

BINDING REACTION

The reaction was performed in a 0.2 ml microcentrifugation tube. The Cy3 labelled ds-74-mer DNA (*p21*, *half-p21* and random sequences) were previously hybridized with a final concentration of strand and c-strand, equal to 20 µM, in Hybridization Buffer; the solution was heated up to 95°C for 15 min and slowly cooled down to RT. In order to decrease the unspecific binding of p53 in the reaction oligonucleotides from salmon sperm were added, as competitor.

The final concentration of DNA-binding buffer (BB 1x) was:

Hepes 40 mM pH 8.0, KCl 50 mM, $MgCl_2$ 10 mM, glycerol 5% (v/v),

Triton X-100 0.1% (v/v), BSA 1 mg/ml, TCEP 10 mM.

The protein was added just before starting the incubation for 30 min in ice.

	Reagents	**Volume (µl) (tot 25 µl)**	**Final concentration**
	BB 5x	4	1x
	ds-DNA 74 mer 0.5 µM	0.36	0.34 µg/ml (7 nM)
	competitor 200 µg/ml	0.25	2 µg/ml
	nuclease-free water	15.39	
Last step	p53 40 ng/µl in 1x BB	5	200 ng monomer (8 ng/µl; 186 nM)

ELECTROPHORETIC MOBILITY SHIFT ASSAY, EMSA

The buffer for following preparation was TBE 1x:

Tris 30 mM pH 8.0, Boric acid 30 mM, EDTA 5 mM.

Gel recipe:	acrylamide 4% (v/v) in TBE 1x, glycerol 2.5% (v/v)
	big gel (18x16 cm);
Laemmli Buffer (5x):	glycerol 33% (v/v) in TBE 5x, Bromophenol blue 0.05% (m/v)
	N.B. Bromophenol runs like 100 bp shift ds-DNA;
Running buffer:	TBE 1x, Triton X-100 0.1% (v/v).

Each sample was loaded in one big well; the run was always compared to the negative control reaction (no protein). The run was in cold room at 4°C, applying constant current 25 mA/gel, for 3-4 h (until Bromophenol blue reached three quarter of gel length). The fluorescence picture was taken by Typhoon 9400 scanner, using filters for Cy3 λ_{ex} 532nm/λ_{em} 580 BP30.

4.2.4.2 Isoelectric focusing (IEF)

IEF is a technique to separate different proteins by their different isoelectric point (pI). It requires the addition of ampholyte solution into immobilized pH gradient (IPG) gels. IPGs are the acrylamide gel matrix co-polymerized with a stable pH gradient. This is obtained by the continuous change in the ratio of immobilines (weak acids or bases, from GE Healthcare).

A protein is positively charged when it is in a pH region below its isoelectric point (pI), therefore it migrates towards the cathode (negative charge). The protein's overall charge decreases till the protein reaches the pH region that corresponds to its pI (no migration). The technique is capable of extremely high resolution with proteins differing by a single charge being fractionated into separate bands.

To allow this migration is important the presence of ampholytes in medium.

Thanks to Bettina Richter (Buchner's laboratory, Chemistry dept., TU München) for the assistance.

BUFFER FOR IPG STRIP

Sample buffer:	Urea 3.5 M, Thiourea 1 M, SERDOLIT® MB-1 1% m/v,
	DTT 32 mM, CHAPS 1% m/v,
	Pharmalyte broad range pH 3–10 2% v/v;
Equilibration solution A:	Tris/HCl 50 mM pH 8.8, urea 6M, glycerol 30% (v/v),
	SDS 2%, DTT 1% (w/v);

Equilibration solution B:	Tris/HCl 50 mM pH 8.8, urea 6M, glycerol 30%, SDS 2% SDS, Iodoacetamide 260 mM;
Running buffer:	Tris 25 mM, Glycine 192 mM pH 8.8, SDS 1% m/v SDS.

The protein of interest was dissolved in Sample buffer, 15 µg in total volume 125 µl, and the strip was immersed in this solution (Drystrip gel pH 4-7, 7cm IMMOBILINE), silicone oil was used to seal the system to perform IEF in flat bed chamber IEF program was so set: 6 h 30 V, 6 h 60 V, 30 min 300 V, gradient in 30 min 300-1000 V, gradient in 1.5 h 1000-5000 V, 2.5 h 5000 V.

Once finished the IEF run, first the strip was incubated in Equilibration solution A then in B for 15 min each step at RT. After a brief wash in Running buffer, the strip was inserted and correctly aligned in the upper part of precast gel (Serva Gel™ TG Vertical Tris-Glycine Gel 2D 14%). To fix the strip was used 0.5% m/v Agarose in Running buffer, containing Bromophenol Blue.

The electrophoresis run was so set: 10 min 10 mA per gel, 1.5 h 20 mA per gel.

4.2.4.3 Native gel for p53

The buffer for the following preparation were:

TBE 1x:	Tris 30 mM pH 8.0, Boric Acid 30 mM, EDTA 5 mM;
Laemmli Buffer (5x):	glycerol 30% (v/v), TBE 5x, Bromophenol blue 0.05% (v/v);
Resolving Buffer:	acrylamide 12.5% (v/v) in TBE 1x, glycerol 2.5% (v/v) N.B.: for p53 it was 8% acrylamide;
Stacking Buffer:	acrylamide 5% (v/v) in TBE 1x, glycerol 2.5% (v/v);
Running Buffer:	TBE 1x.

The samples were loaded in 1x Laemmli buffer and the run was done at constant current 20 mA per gel at 4°C, till disappearing of Bromophenol blue.

4.2.4.4 SDS-Polyacrylamide Gel Electrophoresis, SDS-PAGE

Gels were freshly prepared.

Laemmli Buffer (5x):	Tris/HCl 300 mM pH 6.8, SDS 10% (w/v), glycerol 50% (v/v), Bromophenol blue 0.05% (w/v), ß-Mercaptoethanol 5% (v/v);
Resolving Buffer:	SDS 0.2%, Tris/HCl 375 mM pH 8.8, acrylamide 12.5% (v/v) But it depends on the studied proteins;
Stacking Buffer:	SDS 0.2%, Tris/HCl 125 mM pH 6.8, acrylamide 5% (v/v);
SDS-Running Buffer:	SDS 0.1% (w/v), Tris/HCl 25 mM pH 8.8, Glycin 200 mM.

Polymerization of acrylamide solutions was induced by adding TEMED and APS.
The samples were loaded in 1x Laemmli buffer after a denaturation step at 95°C for 15 min. Electrophoresis was carried out at constant current 30 mA per gel in SDS-Running Buffer till disappearing of Bromophenol blue.
For semi-native condition, ß-Mercaptoethanol and high temperature treatment were avoided.
LMW-SDS Marker Kit (GE Healthcare) was usually employed as protein ladder.

COOMASSIE BLUE STAINING

This staining method has a detection limit of 0.1 µg of protein.

Staining solution:	25% (v/v) Isopropanol, 10% (v/v) Acetic acid,
	0.05% (w/v) Coomassie Blue R250;
destaining solution:	10% (v/v) Acetic acid.

After the electrophoresis, the gel was dipped in Staining solution and incubated there for 10 min, then the colour was removed in destaining solution till the visualization of protein bands.

SILVER STAINING

The silver staining is more sensitive (a few ng of protein). SilverXpress® Silver Staining Kit was employed, varying the suggested protocol for Tris-Glycine gels (in term of percentages).

Fixing solution:	40% (v/v) Methanol, 20% (v/v) Acetic acid;
Sensitizing solution:	3% (v/v) Sensitizer, 50% (v/v) Methanol;
Staining solution:	3% (v/v) Stainer A, 3% (v/v) Stainer B;
Developing solution:	3% (v/v) Developer;
Stopping solution:	like it is.

First the gel was immersed in fixing solution for 10 min, and then passed in sensitizing solution twice, each time for 15 min exchanging the solution. After 5 min wash in water, it was dipped in staining solution for 10 min, and then again washed in water 5 min. The development in developing solution lasted till needed time to correctly display the bands and it was stopped with stopping solution.

4.2.4.5 Western blot

This method follows usually SDS-PAGE separation, that the reason why was inserted after it. Full-Range Rainbow Molecular Weigh Markers (GE Healthcare) was used as protein ladder in SDS-PAGE, being visible on the membrane after electroblotting.

Transfer buffer:	25 mM Tris, 200 mM Glycin pH 7.5, 20% (v/v) methanol, 0.01% (m/v) SDS;
TBS-T:	50 mM Tris, 150 mM NaCl pH 7.5, 0.1% (v/v) Tween 20.

The proteins were transferred by electroblotting onto a nitrocellulose membrane. The membrane and 6 pieces of Whatman paper were rinsed in transfer buffer for 10 min, keeping the gel in water. The sandwich was assembled from bottom to top with 3 paper sheets, membrane, gel and 3 paper sheets removing all air bubbles and the excess of buffer, since it was a semi-dry transfer. The transfer occurred at 72 mA for 80 min. To avoid unspecific binding of Ab, the membrane was incubated for 1 h at RT in 10 ml TBS-T containing 5% (w/v) milk powder. After washing 3 times in TBS-T for 5 min each step, the membrane was rinsed in 10 ml of primary antibody 1:2,000, diluted in in 5% (w/v) milk powder TBS-T for 1 h at RT. After repeating the wash step, the membrane was incubated for 1 h at RT in 10 ml 1:2,000 secondary antibody in 5% (w/v) milk powder TBS-T. Finally the membrane was washed and the detection was performed using ECL Western substrate (0.125 ml reagent/cm^2), keeping 1 min at RT and exposing the membrane on X-ray Film in a cassette.
These dilutions were optimized for Ab1 anti-hp53 and Ab2 anti-mouse *k* chain.

4.2.5 Methods for "hCA1-DNA mono conjugate" project

4.2.5.1 HiTrap Con A 4B for characterization of glycosylated forms in hCA1

The protein hCA1 was loaded in affinity column HiTrap Con A 4B in FPLC to isolate and estimate the concentration of glycosylated forms in the purchased hCA1. The column contains Concanavalin A (Con A), a tetrameric metalloprotein, 104 kDa, which can interact specifically and reversibly with α-d-mannopyranosyl, α-d-glucopyranosyl, and sterically related residues (Agrawal & Goldstei.Ij, 1968; Bahar & Tuncel, 2004; Bereli et al, 2005; Schaumann et al, 1993; Selvaraju & El Rassi, 2012).
The used buffer had the following recipes:

Con A Binding Buffer:	Tris 20 mM pH 7.4, NaCl 0.5 M, $MnCl_2$ 1 mM, $CaCl_2$ 1 mM;
Con A Elution Buffer:	Tris 20mM pH 8.5, NaCl 0.5 M, Glucose 1 M.

hCA1 was injected at 0.1 ml/min in Con A Binding Buffer. After 2.5 CV wash, the elution step was started at 0.4 ml/min in 100% Con A Elution. The chromatogram was taken at 280 nm, wash and elution fractions were collected and concentrated using 10 kDa MWCO Amicon® Ultra spin column, and finally their content was analysed in SDS-PAGE (denaturing condition, 12.5% AA, silver staining). The concentration of glycosylated form was estimated from band intensity and correlated to the dilution factors of wash and elution fractions.

4.2.5.2 Solulink™ methods adapted to hCA1-DNA conjugation

The methods based on Solulink™ chemistry were optimized on hCA1-DNA conjugate preparation (Solulink, S-9002-1).

A. MODIFICATION OF AMINO TERMINAL SS-DNA

The c-ss-Amino-48-mer, 5' amino modified, was employed to be modified. Its molecular weight was 14823.57 Da and extinction factor E_{260} 458.01 $mM^{-1}*cm^{-1}$, the aliquot contained 1 ml of 0.1 mM final concentration.

The aliquot was first concentrated to 1mM solution by 3 kDa MWCO Amicon® 0.5 ml, exchanging twice the buffer into 1x Modification Buffer. The centrifugation speed was set at 15,000 x g. After recovering a final volume of 100 µl, the concentration was checked in Nanodrop at 260 nm, diluting 600x the DNA solution in water.

The reaction was assembled in a 0.5 ml microcentrifugation tube, by adding 20 eq of S-4FB (succinimidyl 4-formylbenzoate, previously dissolved in DMF) to 1 eq of oligo DNA, in 45% (v/v) DMF, 1x Modification buffer, final volume of 200 µl. The solution was mixed for 3 h at RT.

Next, the buffer was exchanged into Conjugation buffer by 3 kDa MWCO Amicon® 0.5 ml, recovering a final volume of 100 µl. The concentration was detected in Nanodrop, as mentioned before.

B. DETERMINATION OF MSR FOR MODIFIED SS-DNA

The aldehyde amount present on DNA was detected adding 5µl of modified oligo to 245 µl of 0.5mM 2-HP (2-hydrazinopyridyl HCl), 100 mM MES pH 5, and incubating this solution 30 min at 37°C. Finally the absorbance at 350 nm was measured blanking the spectrophotometer with Conjugation buffer, since at 350 nm the bare DNA did not display a background signal. Based on E_{350} 18,000 $M^{-1}cm^{-1}$ for formed hydrazone bonds from the secondary reaction with 2-HP, the MSR was calculated dividing the concentration of hydrazone by concentration of ss-DNA.

C. MODIFICATION OF HCA1

The reaction was performed in a 1.5 ml microcentrifugation tube. The reactive S-HyNic (succinimidyl 6-hydrazinonicotinamide) was first dissolved in DMF, final concentration of 140 mM. Protein hCA1 was prepared in Modification Buffer, the final concentration ranged between 1-1.2 mg/ml. Next, S-HyNic was added to 400 µl of hCA1, in ratio 10 eq S-HyNic to 1 eq hCA1. The reaction solution was mixed for 3 h at RT.

Next, the buffer was exchanged into Conjugation Buffer by Zeba spin desalting column 2-ml and protein concentration was determined performing MicroBCA assay (Section 4.2.5.3).

D. DETERMINATION OF MOLAR SUBSTITUTION RATIO (MSR) FOR MODIFIED HCA1

The hydrazide present on hCA1 was detected adding 5µl of modified protein to 245 µl of 0.5mM 4-NB (4-Nitrobenzaldehyde), 100 mM MES pH 5.0, and incubating this solution 30 min at 37°C. Finally the absorbance at 390 nm for hydrazone bonds was measured blanking the spectrophotometer with sample containing just Conjugation buffer (E_{390} 24,000 $M^{-1}cm^{-1}$). The MSR was calculated dividing the concentration of hydrazone bonds by concentration of modified hCA1.

The absorbance signals were corrected subtracting the signal of unmodified hCA1 control (a protein sample, treated in the same manner, with no S-HyNic addition). N.B.: the absorbance control wasn't zero, meaning 4-NB and hCA1 somehow caused a background signal.

E. CONJUGATION REACTION

Modified protein and ss-DNA, both dissolved in Conjugation buffer, were joined in a 0.5-ml microcentrifugation tube at ratio 2 eq of hCA1 to 1 eq of ss-DNA. The reaction was mixed overnight at RT. The bis-aryl hydrazone bonds, formed in the conjugate, absorbed at 354 nm (E_{354} 29,000 $M^{-1}cm^{-1}$). Upon mono conjugate purification this absorbance signal could not be significantly used, probably due to the low detection limit of the method.

4.2.5.3 Micro BCA

Micro BCA Protein Assay Kit (Pierce) was used to estimate the concentration of hydrazide activated hCA1 and the concentration of hCA1 in purified hCA1-DNA mono conjugate fractions. The two protocols were slightly different.

A. *MODIFIED hCA1 CONCENTRATION*

A 1:1 serial dilution of BSA standard (2-128 µg/ml) was assembled in a 96-well plate using PBS (Na_2HPO_4 16 mM, KH_2PO_4 40 mM, NaCl 115 mM pH 7.4), final volume of protein solution 150 µl. The 30x diluted solution of modified hCA1 was serial diluted 1:1 in the microplate in PBS, final volume of protein solution 150 µl. The PBS buffer was used as blank in absorbance. All points were prepared in duplicates.

A fresh solution of working reagent was made following the volumetric ratio among all three reagents, MA:MB:MC=25:24:1, and 150 µl was pipetted into each well. After a short incubation, the plate was incubated at 37°C for 2 h, and then the absorbance was read out at 562 nm. Finally the concentration of modified hCA1 was calculated with BSA standard curve

B. *hCA1 CONCENTRATION IN MONO CONJUGATE FRACTIONS*

In presence of chelating agents, such as DNA, the protocol of Micro BCA kit suggests the addiction of higher amount of copper, present in reagent MC.

The used protocol was therefore modified, having as working reagent ratio (MA:MB:MC=23:24:3), and starting from 15x dilution of mono conjugate solution to prepare 1:1 serial dilution in the plate.

4.2.5.4 hCA1-DNA conjugates on gel

The quality of conjugation reaction and purification step was carried out in SDS-PAGE Tris-Gly buffer, 12.5% polyacrylamide (Section 4.2.4.4), loading the crude of reaction and the collected eluted fractions together with controls like aldehydic modified 48-mer and hCA1 (respectively defined as DNA and CA in gel pictures).

The addition of an equal amount of ss-48-mer-Cy3 to each loaded sample enabled the visualization of protein-DNA conjugates by fluorescence (1 µl 0.05 mM of ss-48-mer-Cy3 in 5 µl of each sample). The 3'-Cy3 labelled strand was complement to c-ss-Amino-48-mer, and upon hybridization protein-DNA conjugates emitted fluorescence and were detected in the gel. For the run BenchMark™ Fluorescent Protein Standard was used, which is a labelled protein ladder by Alexa® Fluor 488. The fluorescence pictures were taken by Typhoon 9400 scanner, using filters for Cy3 λ_{ex} 532nm/λ_{em} 580 BP30 and for Alexa® Fluor 488 λ_{ex} 532nm/λ_{em} 526.

Afterwards all the protein and DNA contents were displayed in silver staining, locating all species present in the reaction and purified fraction.

4.2.5.5 Native gel for hCA1-DNA before electroelution

The buffer for the following preparation were:

TBE 1x:	30 mM Tris pH 8.0, 30 mM Boric acid, 5 mM EDTA.
Laemmli Buffer (5x):	30% (v/v) glycerol, TBE 5x, 0.05% (v/v) Bromophenol blue;
Resolving Buffer:	12.5% (v/v) acrylamide in TBE 1x, 2.5% (v/v) glycerol N.B.: for p53 it was 8% acrylamide;
Stacking Buffer:	5% (v/v) acrylamide in TBE 1x, 2.5% (v/v) glycerol;
Running Buffer:	TBE 1x.

The sample from conjugation reaction was loaded on 10-well gel, 1.5 mm thick. The sample was divided in 20 µl aliquots, and 3 µl of 5x Laemmli buffer was added to each aliquot. The first two lines of the gel were filled each with 5 µl of reaction sample, one in particular contained ss-48-mer-Cy3. The run was carried out at constant current 20 mA per gel at 4°C, till disappearing of Bromophenol blue.
To locate the mono conjugate band, the left side of the gel (first two lines) was cut out. The fluorescence picture for Cy3 for mono conjugates was taken in Typhoon 9400 scanner, using filter 532nm/λ_{em} 580 BP30. Next step Coomassie Blue staining was performed to visualize all protein content (unreacted hCA1) integrating and completing the information. Finally, the left side of stained gel was readjusted to the unstained portion of the gel and used as a ruler to excise the mono conjugate band.

4.2.5.6 Electroelution

The buffer used in this method was:

Running Buffer:	TBE 1x.

The electroelution is a common method used to extract a nucleic acid, a protein or a protein/DNA complex sample from an electrophoresis gel by applying a negative current in the plane of the gel slide for extraction and subsequent analysis (Lin et al, 2010; Mollenbeck et al, 2003; Zarzosa-Alvarez et al, 2010). The electroelution was carried out in D-Tube™ Dialyzers Midi. These tubes possess a dual membrane system in parallel position. The membranes are made of regenerated cellulose, characterized by a negligible nonspecific protein binding. Once introduced the gel slide into the tube, this one is fixed on the supporting tray compatible to horizontal electrophoresis unit.
The excised slice of gel containing the mono conjugate (Section 4.2.5.5) was inserted into D-Tube™ Dialyzers Midi, filling the tube to the top with TBE 1x running buffer (⌣600 µl). Afterwards, the tube was placed in the supplied supporting tray and the whole assembly was set in the horizontal electrophoresis chamber, containing TBE 1x

Running Buffer, being careful to keep the two membranes perpendicular to the electric field.

The risk of protein denaturation in reduced carrying the run out in the cold room (4°C), in absence of SDS and reductive agents in buffers. The run lasted 2 h at 100 v constant voltage, at 4°C. The conjugates were then collected by pipetting up the eluate and concentrated in Amicon® 10 kDa MWCO, exchanging the buffer into Standard Buffer. The protein content of the mono conjugate fraction was determined in Micro BCA (Section 4.2.5.3 B).

4.2.6 Methods in SPR (Biacore™ X-100)

For the following protocols, consumables and buffers from Biacore GE Healthcare were employed.

Acetate Buffer:	Sodium Acetate 10 mM pH 5.5;
HBS-P:	HEPES 10 mm pH 7.4, NaCl 150 mm,
	Surfactant P-20 0.05% (v/v).

Prior to immobilisation, the C1 sensor chips were cleaned by consecutive injections of 10 µl and 5 µl of 0.1 M glycine-NaOH 0.3% Triton-X100, followed by 5 µl of HBS-P buffer at 5 µl/min.

Protein immobilization on the chip was performed via amine-coupling, first activating the carboxyl groups on surface by 50 mM N-hydroxy-succinimide (NHS) and 200 mM 1-Ethyl-3-(3-dimethylaminopropyl)-carbodiimide (EDC), contact time 420 s, followed by protein loading. For all experiments, the protein was diluted to 20 µg/ml in Acetate Buffer and injected until the required surface coverage was reached. The surface was subsequently inactivated by 1.0 M ethanolamine-HCl pH 8.5 (ETA), contact time 420 s. The flow rate for immobilization step was 10 µl/min.

The amount of ligand, required to be immobilized on the surface, was calculated using Biacore's equation (Eq. 4.1):

Eq. 4.1
$$\boldsymbol{binding\ capacity\ (RU) = \frac{MW_{analyte}}{MW_{ligand}} \cdot immobilized\ ligand\ (RU)}$$

It is expressed in Response Unit (RU), whereby 1 RU corresponds approximately to 1 pg of protein per mm^2, and it considers the stoichiometric ratio the interaction, 100 RU as maximum binding capacity for optimal kinetic analyses and molecular weights of 150 kDa for mAb and 29 kDa for hCA1 (GE Healthcare, 2009).

In multi-cycle assay, analytes were diluted by HBS-P buffer at concentrations ranging from 1 to 125 nM for Ab3, from 6.2 to 500 nM for hCA1, and injected at highest flow rate

of 30 µl/min in order to maximize analyte mass transport. The association was observed for 180 s, at 25°C, followed by 600 s of dissociation. To achieve complete removal of bound analyte, an adequate regeneration step was required after each injection cycle. As for bound Ab3 removal from hCA1 immobilized on surface, this step was found to be problematic; solutions with a pH higher than 2.5 were ineffective, below pH 2.0 harmful, and neither high salinity nor addition of detergents were effective. Only 30 s injection at 10 µl/min of 10 mM NaOH was found to be suitable to bring the response to a level below the initial value. This indicated a loss of active binding sites after each regeneration step, due to unavoidable hCA1 denaturation on surface. On the other hand, bound hCA1 to mAb could be easily removed by injecting 10 mM glycine-HCl pH 2.0 for 30 s at 10 µl/min. The dilution series was loaded twice, and a buffer-only tube was run between each single series.

In single-cycle assay, dilutions of mAb analytes were prepared as previously in HBS-P buffer (concentration range from 7.8 to 125 nM) and one after each other flowed over the surface at 30 µl/min, temperature set 25°C. The association was observed for 130 s and dissociation shortly for 170 s. After the last analyte concentration, the observed dissociation lasted 600 s, followed by a single regeneration step, 10 mM NaOH 30 s.

For each strategy, only one independent experiment was performed, meaning one single chip was used for each mAb measurement. The reference flow cell Fc1 was equally treated like measurement flow cell Fc2, activation and passivation steps of surface were performed without adding the ligand.

The output data corresponded to observe RU already subtracted with the reference signal (Fc2-Fc1).

As suggested in the instruction sheet, C1 hydrophobic surface was blocked, after ligand immobilization, by an injection of bovine serum albumin (0.2 mg/ml in running buffer, 120 s contact time). This step allowed the reduction of non-specific protein binding on surface.

The methods of the surface preparation of switchable DNA layers and of the biomolecule detection are entirely described in Chapter 5, together with the introduction to *switch*SENSE technology.

5. Introduction to *switch*SENSE

The *switch*SENSE is a novel biosensor technology, which is based on an electrically actuated bio-interface, schematically represented in Figure 5.1. The probe DNA is tethered to the surface of a gold electrode and subjected to AC fields, with respect to a platinum counter electrode. As consequence its conformation is electrically modulated. Particularly, when negative potentials are applied the repelled strands adopt an upright position, while at positive potentials the attracted strands occupy a lying position. This is due to the intrinsic negative charge of nucleic acids.

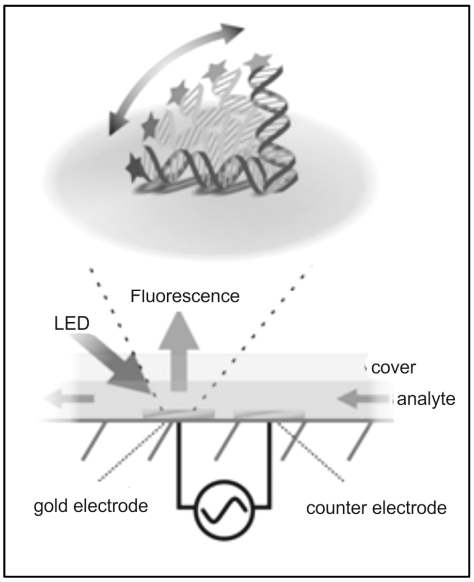

Figure 5.1 The *switch*SENSE schematically represented. Lower part: a fluidic channel with analyte solution is formed on gold electrodes, which have a low density layer of DNA probes. AC potentials are applied to the Au work electrode with respect to a Pt counter/reference electrode. Upper part: the conformation of surface-tethered DNA probes is modulated by AC fields, which cause the molecules to extend away from or fold onto the biased surface, due to the intrinsic negative charge of nucleic acids. The nonradiative energy transfer to metal surface suppresses the fluorescence as the dyes get close to the surface and simultaneously, the orientation of the nucleic acids is indirectly detected by fluorescence intensity, emitted from dyes attached to the DNA's upper ends upon LED light excitation. Reproduced from (Rant et al, 2007).

Simultaneously, by illumination with a light-emitting diode (LED) the orientation of the nucleic acids is optically detected by fluorescence intensity, being a Cy3 moiety covalently attached to the DNA's distal ends. In effect as the dyes approach the surface of the gold electrodes, energy transfer to metal surface occurs, quenching the fluorescence. Hence through the application of AC fields, the fluorescence intensity is modulated and characterized by an amplitude, with a maximum value for DNA standing position, and

minimum for DNA lying position (Arinaga et al, 2007; Rant et al, 2006a; Rant et al, 2007; Rant et al, 2006b).

In order to fully comprehend the technology, a brief description of the physical fundamentals of *switch*SENSE will be given, followed by the experimental setup description with chip and fluidic channel formats, which must enable highly sensitive serial detections. Finally the electrical manipulation of DNA conformation on surface is presented, by a method section for layer preparation and measurement mode descriptions, clarifying furthermore which factors mostly affect the switching behaviour of oligonucleotides.

5.1 Physical basics

5.1.1 DNA structure

Deoxyribonucleic Acid (DNA) is a linear polymer of four different nucleotides. Each nucleotide is composed of a nitrogenous base (adenine (A), cytosine (C), guanine (G) and thymine (T)), a five-carbon sugar (2-deoxyribose) and one phosphate group. The polynucleotide chain is linked by phosphodiester bonds and the sequences are written by convention from monophosphate 5' end to hydroxyl 3' end (Figure 5.2_A-B).

Since each phosphate group carries one negative charge, the backbone is a highly charged structure, an essential characteristic for electrically induced manipulation on gold surface.

Two anti-parallel oriented DNA strands (sense and antisense strands) can hybridize, due to the interaction between A-T (two hydrogen bonds) and G-C (three hydrogen bonds) base pairs. Three different conformations are known to be biologically active double helical structures, defined as A-, B- and Z-form; however B-DNA is the most common one with its right-handed helical conformation. It has a diameter of 2 nm and 10 base pairs (bp) display a complete turn of a 3.4 nm length, whereby every single bp contributes 0.34 nm to the total DNA-length (Alberts et al, 2008; Watson & Crick, 1953) (Figure 5.2_A). The hydrophobic bases are located between the two hydrophilic sugar-phosphate backbones; therefore the double helix is not just stabilized by base-pairing, but by the additional interactions in base stacking (pi-stacking) which position all bases perpendicularly to the DNA direction. An addtional dominant feature of B-DNA is the presence of two distinct grooves, a major and a minor groove. These grooves play an important role in protein-DNA recognition, as described in Chapter 7, which enable the detection by *switch*SENSE of human p53 binding to DNA response elements.

Furthermore external factors, such as temperature, pH and salinity, influence the double strand stability in solution. In fact high temperature or extreme pH values or low salt concentration cause the dehybridization of double stranded (ds) helix. Remarkably double and single stranded (ss) DNA differ from each other on mechanical properties; while ss-DNA is quite flexible and tends to form a random coil with a persistence length of 1 nm (Smith et al, 1992), ds-DNA is highly rigid, with a persistence length of 50 nm (Brinkers et al, 2009; Bustamante et al, 2003; Smith et al, 1996).

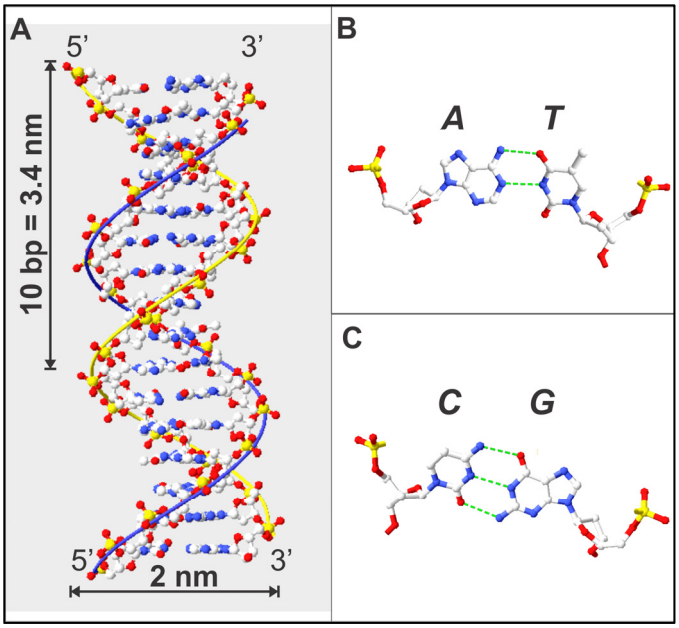

Figure 5.2 B-DNA helix. A: the nucleotides are linked via a phospodiester bond, between 5' phosphate and 3' hydroxyl group, conferring a 5' to 3' direction topology of polynucleotide. Each turn of DNA is made up of 10.4 bp covering a distance of 3.4 nm. The right handed coiling of these two strands around each other creates two grooves in the double helix, as indicated the major and the minor groove. B-C: the DNA sequence is made of four bases: adenine (A), cytosine (C), guanine (G) and thymine (T); here the hydrogen bonds are shown for AT and CG pairs. The pictures were made by Web 3DNA software (http://w3dna.rutgers.edu/)(Lu & Olson, 2008) for the structure prediction of 16-mer DNA sequence 5'-TAGTCGTAAGCTGATA-3', then displayed by DeepView.

5.1.2 The electrical double layer

Due to an electrically induced redistribution of ions in solution, near the metal surface the electric field is screened by an increased concentration of counter ions, which forms a diffuse layer. The formation of this double layer is described by the Gouy-Chapman theory (Bard, 2001). A characteristic parameter is the Debye screening length, which is defined as the length scale, over which the electric field is screened by the counter ions.

Note that the variation of the salt concentration changes the Debye screening length, upon reduction of salt concentration the outreach of the electric field increases (Figure 5.3).

In this particular case, the nucleic acids tethered on charged metal surfaces are in contact with electrolyte solution and the electric field decays quasi-exponentially into solution on a scale of a few nm (Figure 5.3), which corresponds to the length of oligonucleotides (the DNA strands used in this study are 16 nm (48-mer) and 25 nm (74-mer) long, respectively).

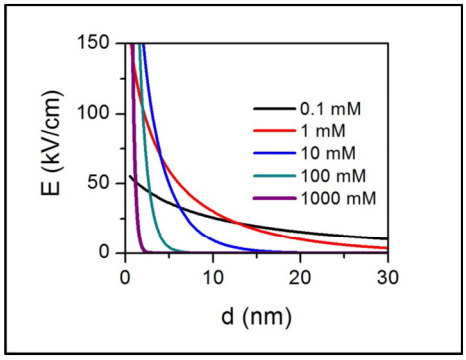

Figure 5.3 The electric field E in electrolyte solution, calculated by Gouy-Chapman potential, is plotted as a function of the distance d to a surface, which is biased at 100 mV. The curves were calculated for solutions having varying concentrations of monovalent salt (Kaiser & Rant, 2010). It is remarkable that already at 100 mM monovalent salinity, the electric field propagates just for 4-5 nm from the surface.

5.1.3 Energy transfer of fluorescence to metal surface

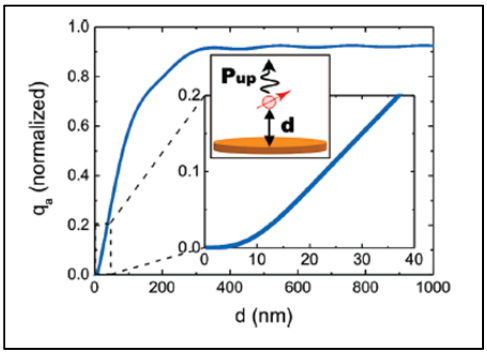

Figure 5.4 Fluorescence energy transfer to metal surface, as function of dye-surface distance. Kaiser and Rant calculated the apparent quantum yield q_a of an isotropically oriented dipole (red), located at distance d above a gold surface (Kaiser & Rant, 2010). P_{up} denotes the power radiated into the upper half space. The coupling of the dye`s dipole to the surface reduces the apparent quantum yield. This coupling is most effective below 10 nm, where the quenching of the fluorescence results nearly complete, as shown in the enlargement of the curve. A bigger distance between surface and dye reduces the coupling efficiency, which leads to a larger q_a, beyond 300 nm distance the dye cannot couple anymore and q_a remains unaffected.

The Cy3 dyes are excited and relaxed by absorption and emission of photons, respectively. The fluorescence corresponds to the relaxation phase. However, the presence of a metal surface gives rise to a new relaxation pathway, where the dye can transfer its energy radiationless to the metal (Chance, 2007). When the dipole approaches the metal surface, the energy from the dipole can be absorbed by the gold film or transformed into plasmon excitations propagating at the film surface.

Kaiser and Rant analysed the fluorescence energy transfer of the dye to the surface as function of their distance(Kaiser & Rant, 2010). The apparent quantum yield q_a of an isotropically oriented dipole was calculated, located at distance d above a gold surface. The isotropic dipole orientation was assumed since the dye is normally attached to the DNA's distal terminal by a flexible linker, which allows for an almost free rotation of the dye. As shown in Figure 5.4 the coupling of the dye`s dipole to the metal surface is most effective below 10 nm, where the quenching of the fluorescence results nearly complete (the apparent quantum yield is strongly reduced). Then a bigger distance between surface and dye reduces the coupling efficiency, which leads to a larger q_a, and finally beyond 300 nm distance the dye cannot couple anymore and q_a remains unaffected.

5.2 Experimental setup

5.2.1 Chip design and flow channel in Prototype1 and Prototype2

The majority of measurements performed on surface in this thesis were achieved employing Prototype2 (Chococino setup) and Prototype1 (Olympus setup) on a polished ⦰2-inch glass (SiO_2) wafer (Fujitsu Laboratories Ltd., Japan), within are arranged twelve disc shaped gold (Au) work electrodes (Figure 5.5). The electrodes are distributed into four different areas, each area surrounded by a platinum (Pt) counter electrode which acts as a reference electrode. These separated areas allow simultaneous experiment runs without risk of cross contamination.

The work electrode possesses a diameter of 120 µm (active area 0.01 mm^2) and the distance between this and the counter electrode is 100 µm. This geometry has proven to be most effective, providing a charging time of roughly 1.8 µs (Hampel, 2009). From the Au electrodes thin connecting lines lead to connector pads which can separately be addressed. The lead lines are designed ensuring that the charging behaviour of the electrodes is not affected by their resistance.

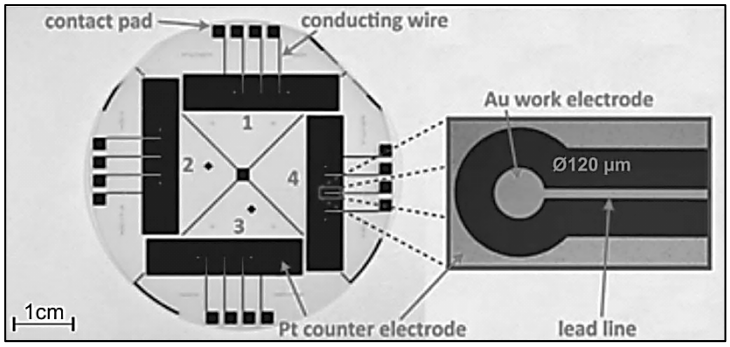

Figure 5.5 Chip design with electrodes, conducting wires and contact pads. The ⌀2-inch glass chip is divided into four channels (1-4), each with three Au work electrodes and one Pt counter electrode. A circular Au work electrode of ⌀120 µm is zoomed in, and it is surrounded by the large Pt counter electrode (picture reproduced from (Hampel, 2009)).

In order to provide an adequate method for buffer exchange and analyte solutions on the chip, a flow channel must be built on top of each area with a top mounted coverplate and a rubber o-ring to seal each flow channel. Hereby the coverplate is made out of Topas®, which shows high optical quality requirements, like a low auto-fluorescence and absorption of the excitation light. Tygon® tubings of ⌀1.6 mm can be connected to the flow channels via in- and outlets in the coverplate. The height of this flow channel is 0.8 mm and width 4 mm. The sample is maintained by a metal plate on top with apertures on flow channels to provide optical access to the electrodes.

Electrical contacts to the connector pads are made by spring contact pins. The temperature of the system can be set and controlled by a thermoelectric cooler which is fixed underneath the chip (Figure 5.6). Additionally, a gear pump, set in remote control and connected to tubings, is used to flow buffer solutions and to inject samples over each flow channel.

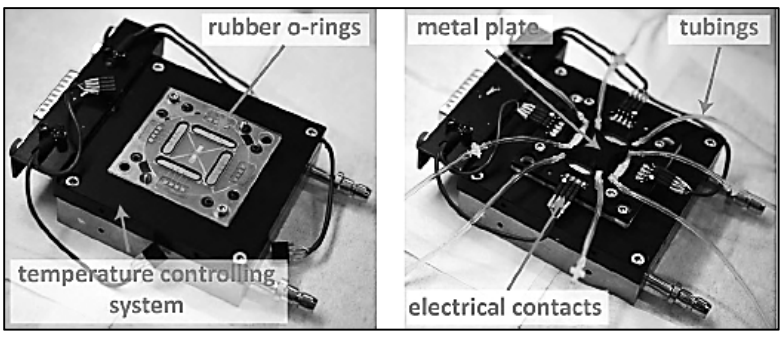

Figure 5.6 Flow channel setup. Left: the wafer is set on top of the temperature controlling system; the flow channel geometry is defined and sealed by four o-rings. Right: a Topas® coverplate is mounted on top of the chip, and a metal plate, which maintains whole system, is electrically contacted via spring contact pins. Apertures provide optical access to the electrodes in the channel and tubings are connected to in- and outlets in the coverplate (picture reproduced from (Hampel, 2009)).

5.2.2 Chip design and flow channel setup in SWA1

The kinetic measurements for monoclonal antibodies anti-hCA1 were performed on a new prototype, *switch*SENSE Analyzer 1 (SWA1) by Dynamic Biosensors GmbH (Chapter 6). This prototype contains a new chip format of dimensions (40 × 27) mm (Figure 5.7), consisting of six Au work electrodes in each channel. This high number of work electrodes allows reference measurements to be performed in the same channel, realized by DNA-encoded addressing. The selective surface functionalization could be carried out by using different DNA sequences.

But the most important difference is the microfluidic geometry of channels, created by a defined glass cover slide. The entire flow channel volume is considerably reduced, ~1.5 µl (depth 1 mm, the whole length ~25 mm), as well as the channel height, which is narrowed to 60 µm. This microfluidic geometry enables high linear velocity for kinetic measurements, reducing the mass transfer limitation (Squires et al, 2008).

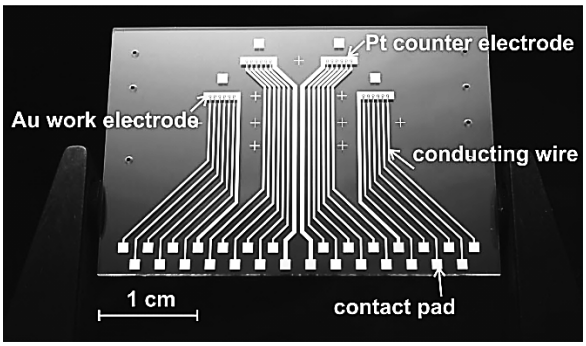

Figure 5.7 New chip design, with electrodes, conducting wires and contact pads. Similarly to the previous one, the chip of dimensions (40×27) mm is divided into four channels, each with six Au work electrodes surrounded by one Pt counter electrode. The Pt counter electrodes are the lighter blue lines. The picture was taken from Dynamic Biosensors GmbH.

The mass transfer limitation of kinetics is reduced by a narrower channel and higher linear velocity. The equation (Eq. 5.1) describes the profile of velocity *u* for a Newtonian fluid at volumetric flow rate *Q* in a channel with width *w* and height *h:*

Eq. 5.1 $$\boldsymbol{u = \frac{6Q}{h^3 \cdot w} \cdot z(h - z)}$$

As can be observed in Figure 5.8, the maximum velocity occurs at the center of height section; reducing the height, the velocity next to the surface (z=0) gets higher therefore decreasing the mass transfer limitation.

However, a disadvantage of a reduced channel height is the resulting increase of electrical charging time, due to decreased amount of solution over the surface, and its consequent rise of electrical resistance. Consequently Pt counter electrode was

exchanged with a glass cover slide coated with *Indium-Tin-Oxide ITO* (~150 nm), to reduce the resistance and decrease the charging time.

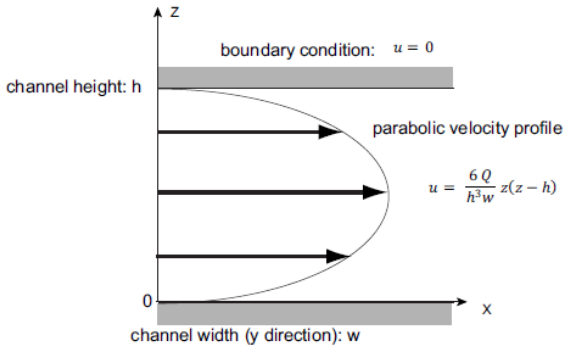

Figure 5.8 The cross section of the parabolic velocity profile in the channel of width *w* and height *h*, describe by Navier-Stokes equation (Eq. 5.1). The maximum velocity lies in the middle of height section. Consequently a reduced *h* decreases the mass transfer limitation, bringing the maximum velocity next to the surface (z = 0) (Maruyama, 2008).

5.2.3 Optical setup

The optical system of the setup provides a combined optical excitation and detection pathway (Figure 5.9). A LED lamp is used as the excitation light source of Cy3 dyes (nominal wavelength 530 nm). Initially the light is filtered through 517(±20) nm band pass filters. In this system the power of LED can be regulated, from 0.1 to 5 V, and the aperture *iris* diaphragm aids to reduce the background level through the control amount of light that illuminates the electrode. Hereby, a dichroic beam splitter reflects the excitation light onto the electrode, letting the emission light passing through to reach the PMT, the temperature controlled photomultiplier detector. To get rid of stray light in front of the photosensor, the collected light is filtered by optical band pass. Furthermore, the single photon counting unit (SPCU) is used to convert single electron pulses of fluorescence decay from the PMT into digital signal. From SPCU, the digital signal is then sent to a multichannel photon counting system (MCPC) with a minimum time resolution of 32 ns.

The alignment of the electrodes under the optical setup is ensured by the presence of a linear stage. A camera is used for the electrode automatic alignment. The bias potential is applied by a function generator, while a switch matrix allows the possibility of addressing the potential to the different electrodes on the chip. LabVIEW© software provides the option to control the electrical parts and to record the fluorescence and the optical system allows the detection in real-time of one single electrode.

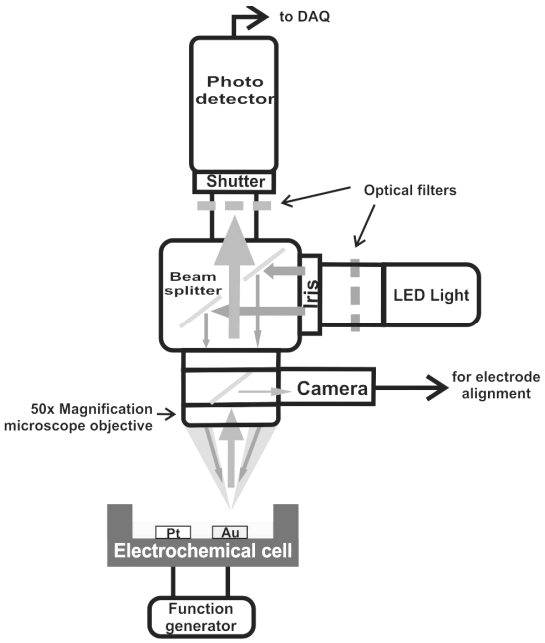

Figure 5.9 Schematic picture of optical setup. A LED is used as light source and optical band pass filters 517/20 nm select the excitation wavelength for Cy3. The *iris* diaphragm ensures that only the electrode is illuminated. Then a beam splitter directs excitation light to the microscope objective, the latter focuses the light (shown in green) onto the electrode and similarly collects the fluorescence light (in yellow). A camera assists the electrode automatic alignment. The remained fluorescence goes to the photosensor module. Optical bandpass filters are used to block stray light in front of the photosensor. All data are then collected by a data acquisition system. The bias potential is applied to the electrochemical cell by function generator. A shutter makes sure that the photosensor is safely locked when the machine is opened.

5.3 Electrical manipulation of surface-tethered DNA strands

This method section describes the layer preparation on gold electrodes and measurement modes, once the chip is installed on the experimental setup. All measurement modes are controlled by LabVIEW©.

Lastly the factors which affect the switching movement are briefly described to allow a complete comprehension.

5.3.1 Methods

5.3.1.1 DNA layer preparation

The electrode chip was initially cleaned in piranha-solution (H_2SO_4: H_2O_2 (30%) = 2: 1) treatment for 15 min, followed by 15 min exposure to HNO_3 (60%). The chip was finally rinsed in DI-water and dried under nitrogen stream.

Self-assembled monolayers (SAM) of double stranded oligonucleotides were prepared on gold electrodes by adsorption from aqueous solution. All used oligonucleotides are

listed in Section 4.1. The sense strands were thiolated modified at 5' end by $(CH_2)_6$-SH for Au-S SAM, and labelled by Cy3 at 3'end for optical detection; the antisense strands, called complement strands (c-strand), were instead modified at 5'end or along the backbone, depending on the addressed application.

The ds-DNA was hybridized with a final concentration of strand and c-strand, equal to 20 µM, in Hybridization Buffer; the solution was heated up to 60/95 °C for 15 min (for ds-48-mer and ds-74-mer, respectively) and slowly cooled down to room temperature (RT). Subsequently, 1 µM of prepared ds-DNA was spotted on each gold electrode covering the electrode completely, using an Autodrop Pipette AD-K-501. This picoliter pipette is set in a glovebox in order to maintain a constant humidity level around 60% ensuring the stability of spotted drops. The immobilization drops were let for 30 min at RT.

To prevent unspecific interactions between DNA and the gold surface, surface passivation was carried out flowing mercaptohexanol (MCH) 1 mM in Standard Buffer at a flow rate of 0.1 ml/min in each channel for 1 h.

For the new chip format with ITO counter electrode, the DNA solution was spotted with a micropipette, followed by a short incubation of 10 min for SAM and a wash of surface by MCH 1 mM in Standard Buffer. Microfluidic channel was created, gluing ITO cover slide on glass chip.

5.3.1.2 Low Frequency Measurement (LFM) mode

The Low Frequency Measurement (LFM) applies two electric potentials to the gold electrode while recording the fluorescence signal. Through switching at a low frequency (0.4 Hz) between -0.4/+0.3 V, the fluorescent signal changes from a minimal value (lying-state F_{ly}) to a maximal value (standing-state F_{st}) and back (Figure 5.10). The switching amplitude, or fluorescence modulation amplitude, ΔF, can be measured and is defined as the difference of fluorescence intensity between standing- and lying-state (Eq. 5.2):

Eq. 5.2 $$\boldsymbol{\Delta F = F_{st} - F_{ly}}$$

An additional characteristic value for the measurement is the relative switching amplitude, ΔF_{rel} expressed in percentage (Eq. 5.3). This value displays the efficiency of the switching.

Eq. 5.3 $$\boldsymbol{\Delta F_{rel} = \Delta F / F_{st} \cdot 100}$$

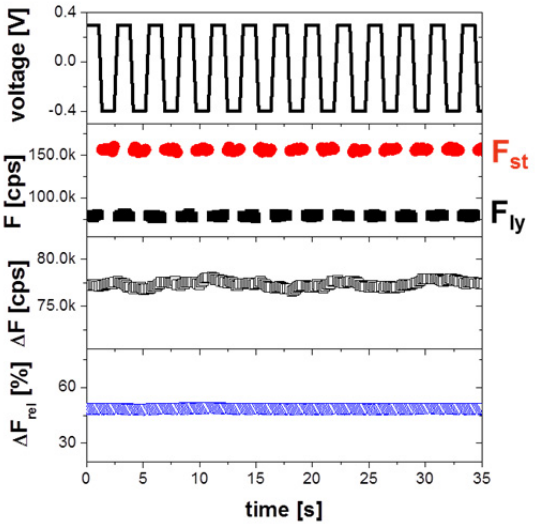

Figure 5.10 Typical switching data from low frequency measurement, LFM, of ds-48-mer layer. From top to bottom: applied switching bias square wave potential (frequency: 0.4 Hz) between -0.4/0.3 V vs. Pt; resultant fluorescent signals applying LED power 1 V, the high level F (F_{st}, standing state) and the low level F (F_{ly}, lying state); switching amplitude ΔF resulting from the difference between F_{st} and F_{ly}; relative switching amplitude, ΔF_{rel}, expressed in percentage, is the ratio of ΔF over F_{st} and displays the efficiency of switching (ID: C53FGW33_06_07).

5.3.1.3 Electrical desorption to control density DNA layer

"Ultra-low density" layers were obtained by repetitive electrical desorption (Arinaga et al, 2007) to exclude any steric interactions of the strands, which limit the electrical manipulation efficiency.

Sulfur–gold bonds possess a dissociation energy of 120 kJ/mol (1.2 eV/bond)(Nuzzo et al, 1990), roughly a third of a typical C-C bond, and can be broken by electrochemical reduction through the application of negative potentials (Wang et al, 1999).

Applying to the electrodes potentials around -0.8 V to -1.2 V vs. Pt, the DNA layer is thinned-out. This occurs since DNA is electrostatically repelled from the surface when negative potentials are applied and at the same time, the sulphur–gold bonds break by electrochemical reduction through the application of negative potentials (Yang et al, 1997; Zhong & Porter, 1997). The void sites, originating from repelled DNA, were refilled by MCH present in buffer solution, followed by the rinsing of the flow channels with Standard Buffer.

ΔF_{rel} is used to estimate the obtainment of "ultra-low density" layer during the electrical desorption. At high densities the manipulation of the DNA strands is limited through steric hindrances between neighbouring strands, resulting in small switching amplitudes. Furthermore, the crowding effect is reduced thinning out the layer by

desorption. Upon critical density, the average distance between two neighbouring strands exceeds the minimum distance for interactions, DNA can completely lie down at attractive potential, and the fluorescence reaches its minimum. For ds-48-mer, Rant assumed a hexagonal-close packing (hcp) 2D model of ds-DNA population, having a critical density layer of 10^{11} molecules/cm^2 (Rant, 2005). This upper limit was confirmed by measurement from Arinaga *et al.* (Arinaga et al, 2007). Further desorption results in an additional reduction of F_{st} value due to a higher release of DNA, while F_{ly} value does not change significantly. Consequently, ΔF_{rel} value undergoes a further decrease, obtaining "ultra-low density" layers.

5.3.1.4 Voltage Response (VR) mode

The Voltage Response (VR) measurement applies a sequence of bias potentials to the gold electrode while recording the fluorescence signal. Figure 5.11 illustrates a typical VR measurement for ds-48-mer, where fluorescence signal is detected increasing the potential from -0.4 to 0.4 V at 0.02 V/s sweep rate.

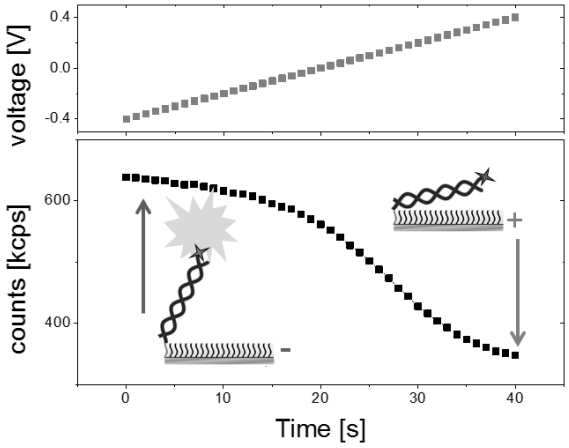

Figure 5.11 Voltage Response (VR) of DNA layer (ds-48-mer). Top: bias potential applied to the Au electrode vs. Pt, -0.4/+0.4 sweep rate 0.02 V/s. bottom: fluorescence counts, recorded at LED power 5 V, decrease by increased positive potential; at negative potentials the strands are repelled from the surface and occupy a vertical orientation, while at positive potentials the strands move towards the surface. The quenching mechanism is quite effective in that case, resulting in a low fluorescence signal (ID: C86FGW50_SCM_08_01).

This type of measurement clearly shows the plateau voltage points of standing and lying positions of the DNA, and how the oligonucleotides react towards the electric applied potential. This reference measurement has been used to correct the switching potential window in Time Resolved Measurement (TRM), based on the plateau points, making possible a cross comparison among all measurements made at different time, buffer or sample loading condition. The correction of switching potential window for TRM was

done based on the inflection point (Ip) of VR curve, resulting from the second derivative of curve data. The window was then adjust setting as attractive potential (Ip+0.2) V, and as repulsive potential (Ip-0.8) V. The Ip corresponds to the potential conformation transition (pct), which denotes the potential value whereby the DNA conformation on surface flips from an extended to a compact state.

5.3.1.5 Time Resolved Measurement (TRM) mode

An in depth understanding of the dynamics of DNA layers can be achieved through the TRM method. Applying at very high frequency (10 kHz) a square wave potential with amplitude of 0.8 V, the fluorescence response is recorded. The current pulses generated by detected photons are collected on the nanosecond scale.

In order to obtain all information, required curves of typically one million sweeps are recorded and summed up, resulting in an averaged fluorescence single curve (Figure 5.12). Applying this method, the change of the fluorescence intensity as a function of applied electrode potential can be analysed in a time-resolved manner. The big feature of this method is that the "rise" and "fall" motions of DNA probes are recorded and can be further analysed.

A typical TRM measurement is described in Figure 5.12. A single sweep of square wave potential lasts 100 µs, from +0.3V to -0.5V at 10 kHz. At 0µs, the voltage is switched from +0.3V to -0.5V (exponential electrode charging) and at 50µs it is switched back to +0.3V. The resulting curves of summed recorded sweeps are given in output already split in falling (at positive potentials) and in rising (at negative potentials) data set. The normalization of raw data counts is usually done on the levels of the upper and lower signal plateau, set respectively as 1 and zero values. The smoothing of normalized fluorescence is commonly obtained by Fast Fourier Transform (FFT) filter, and the derivative is calculated on smoothed normalized data. The derivative of falling and rising movements expresses the velocity of DNA during these motions, revealing Rising Maximum Velocity and Falling Maximum Velocity (V_{max}).

Remarkably, the rising movement from the surface is faster than the falling movement toward the surface (Figure 5.12). By a stochastic effect, the lying strands can be pushed away from the surface efficiently, as all their charges are within the electric field, leading to a fast transition. On the other hand, as long as DNA is in an upright orientation, only a few bases are within the screened field, meaning the electric force is quite small and cannot easily overcome the thermal motion. Due to the thermal motion, some strands are tilted more than other and can be pulled toward the electrode, while other strands

take longer to reach the critical angle for being attracted to the surface (Rant et al, 2006b).

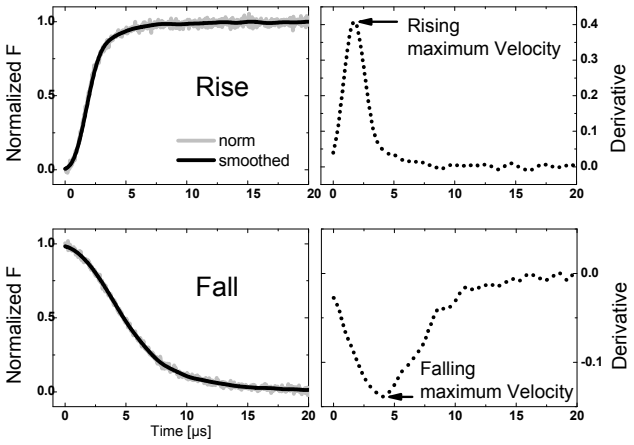

Figure 5.12 Typical Time Resolved Measurement (TRM) data of ds-48-mer. The fluorescence (F) is recorded over time, switching the potential at high frequency 10 kHz between -0.5 V/+0.3 V vs. Pt. The LED power was 5 V. From TRM data the dynamics of switching ds-DNA is observed and determined. The rising and falling motions are separatily analysed. On left side are shown normalized fluorescence signals (gray lines) and smoothed data (black lines), on right side the corresponding derivative (short dotted lines) of the smoothed data which gives the maximum velocity of the corresponding motion. The normalization is done on the levels of the upper and lower signal plateau, the smoothing by FFT filter and the derivative on smoothed normalized data (ID: C87FGW50_TR_03_01).

5.3.1.6 Kinetic Measurement (KM) mode

Kinetic measurements (KM) can be performed based on TRM mode. Following the dynamic variation of DNA probes presenting a ligand, the real time association and dissociation between a protein and ligand-DNA can be recorded, such as antibody/antigen affinity binding, proteins binding to DNA, His-tagged proteins bound to ds-DNA modified by tris-NTA (Knezevic et al, 2012; Langer et al, Paper in progress B; Spuhler et al, 2010).

The dynamics of DNA is related to the Dynamic Response. Considering the rising fluorescence curve, the Dynamic Response corresponds to the integrated counts in a time interval under this curve. Figure 5.13 schematically represents the integration of the curves at, e.g., 0-10 µs boundary, recorded for bare ds-DNA and ds-DNA upon protein binding. Initially the ds-DNA moves fast and is characterized by a high number of integrated counts, or better, by an elevated Dynamic Response value. After protein association, the dynamics gets slower, therefore the Dynamic Response decreases. Hence the observation in real time of Dynamic Response displays the variation of the dynamics consequent to binding and unbinding of a protein.

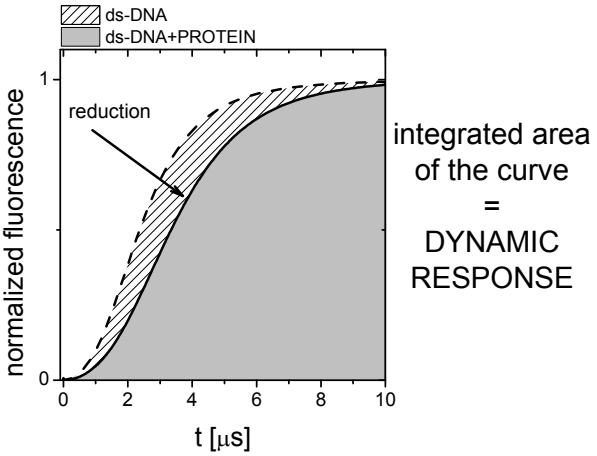

Figure 5.13 Schematic representation of the Dynamic Response data. The Dynamic Response corresponds to the integrated area of the rising fluorescence curve. E.g. considering ds-DNA and ds-DNA upon protein binding (sparse pattern and grey areas, respectively), the integration of the curves at 0-10 μs boundary reveals a reduction of integrated counts, because initially the ds-DNA moves fast and is characterized by an elevated Dynamic Response value. However, after protein association, the dynamics gets slower, therefore the Dynamic Response decreases.

5.3.2 Factors affecting the switching behavior of DNA strands

Several factors affect the molecular dynamics of DNA switching.

Considering DNA strand length, the longer DNA possesses higher hydrodynamic drag, resulting in a slower motion (Hampel, 2009); similarly behaviour can be observed increasing the solution viscosity, which primarily affects the hydrodynamic friction of ds-DNA switching (Hampel, 2009).

Other facts like the charging of the supporting electrode are of crucial importance, hereby a slow electrode charging results in slow DNA movement. The electrodes must be "super-fast" to let molecular dynamics overcome the electrode charging, and this depends strongly on the geometrical properties of the electrode (Hampel, 2009). A fast charging time value, $\tau_{el.}$, evaluated from oscilloscope data, must be around 1.8/1.9 μs.

Due to the different mechanical properties, ss- and ds-probes can be recognized in the switching amplitude. The ss-DNA layers show always smaller signal than hybridized layers (Figure 5.14) (Rant et al, 2006a). Ds-DNA acts like stiff rods on a short length keeping a persistence length till 50 nm (the length of the DNA strands used in this thesis differs between 16 and 25 nm, respectively 48-mer and 74-mer; 50 nm length corresponds to 150 bp), whereas ss-DNA has a very flexible form (persistence length of a few nanometer) and tends to form a random coil. Only the lower part of the flexible ss-DNA can be affected by the electric field, while the upper part of single-strand stays uncontrolled in a random orientation. Instead, rod-like ds DNA can be well oriented by

electric potential on its lower part, as consequence at negative potentials it can stretch further away from the gold surface, giving a higher fluorescence signal.

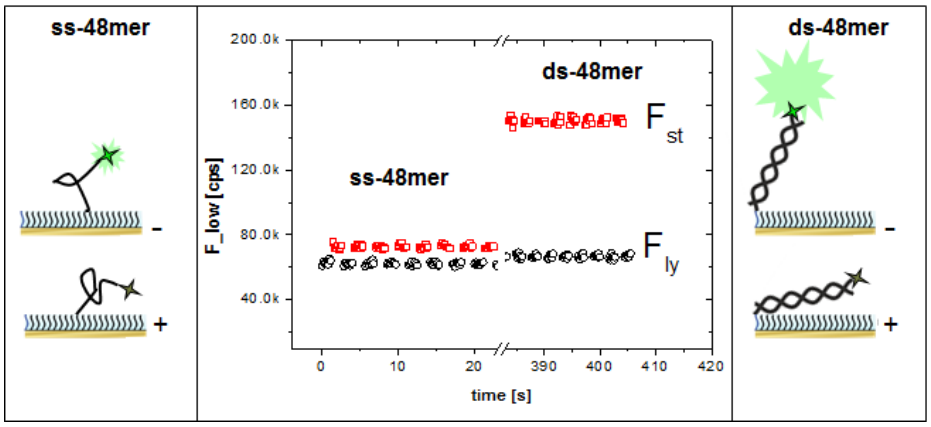

Figure 5.14 Switching fluorescent signal of a single-stranded and a double-stranded layer 48-mer applying -0.4/+0.3 V vs. Pt. Center panel graph: the high level F (F_{st}, standing state) and the low level F (F_{ly}, lying state) for ss-48-mer and ds-48-mer. Left panel cartoon: only the lower part of the ss-DNA is stabilized by the screened electric field, while the upper part occupies a random orientation. Right panel cartoon: ds-DNA, being more rigid, can be oriented better by the electric field than ss-DNA, the higher F_{st}. signal results from the less quenching of dyes, as ds-DNA stretches more far away from Au surface (ID: C86FGW45_LFM_11_03, LED power 1).

Another parameter that has to be taken in account is the temperature. Kaiser and Rant observed that the temperature affects mostly ss-DNA conformations and not ds-DNA (Kaiser & Rant, 2010). Moreover at intermediate range of ionic strength ([NaCl] 10-100 mM) it is possible to efficiently manipulate ds-DNA conformation applying AC potentials as the electric field can interact with the surface-proximal parts of oligonucleotides. At high ionic strength ([NaCl] 1 M), the electric interactions are almost completely suppressed and ds-DNA rigid conformations aren't affected by variations of potential (Kaiser & Rant, 2010).

Moreover, the layer density is an essential factor for TRM and KM, whereby only "ultra-low density" layers have ds-DNA switching at the maximum velocity (Hampel, 2009). The density is controlled by electrical desorption, as already mentioned. The measured surface density of ds-DNA was quantified using electrochemical methods, based on hexaammineruthenium(III) chloride (RuHex) (Steel et al, 1998), and as upper limit was measured 10^{11} molecules/cm^2(Arinaga et al, 2007), which corresponds to an average inter-strand distance of more than 30 nm.

6. Switchable hCA1-DNA layers

6.1 Introduction

The conjugation of a protein to an oligonucleotide is a common strategy to direct the localization of the protein on surface. The oligonucleotide acts as a robust tag which enables a highly specific assembly by spatial-encoding, generating the desired functionalized surface. Therefore, protein-DNA conjugates are used in a variety of applications, ranging from biomedical diagnostics assays (such as "high-throughput immunophenotyping using transcription" (HIT) (Kattah et al, 2008), "fluorescent amplification catalysed by T7 polymerase technique" (Zhang et al, 2006), "immuno-PCR" (Niemeyer et al, 2003)) to DNA-based nanofabrication (e.g DNA-encoded antibody libraries for microarray (Bailey et al, 2007; Kattah et al, 2008; Kuzuya et al, 2009; Malou & Raoult, 2011)).

A large assortment of covalent and non-covalent conjugation methods are available to be employed based primarily on protein stability and desired outcome. However, currently a precise stoichiometric control and a site-selectivity during the conjugation reaction remain elusive for non-engineered protein (Hermanson, 2008).

In this project protein-DNA mono conjugates were employed for *switch*SENSE surface functionalization by human Carbonic Anhydrase 1 protein, hCA1. The Solulink™ conjugation chemistry was applied on hCA1 and 48-mer oligonucleotide to link these two biomolecules together (Solulink, S-9002-1).

The preparation of *switch*SENSE surface was carried out hybridizing hCA1-DNA mono conjugates, whereby the hybridization kinetics was analysed from LFM data. Upon hybridization of mono conjugates, the correct surface functionalization was demonstrated in VR and TRM measurement modes.

6.1.1 Solulink™ conjugation chemistry

Solulink™ conjugation chemistry is based on two reagents: succinimidyl 4-formylbenzoate (S-4FB) and succinimidyl 6-hydrazinonicotinamide (S-HyNic) (Kozlov et al, 2004). The chosen biomolecules that have to be coupled are mutually modified and activated by either S-HyNic or S-4FB. Then joining the biomolecules, the reaction between S-HyNic and S-4FB forms a bis-aryl hydrazone bond. The bond created is a Schiff base that is UV-traceable and stable and requires no additional steps to stabilize the bond. Each step is performed at mild conditions which limited the possible protein

denaturation, such as in phosphate buffer, at pH 7.4 and 6.0 for modification and conjugation reactions, respectively, and at room temperature.

In details, the ss-48-mer DNA, 5'-NH_2-C_6 terminus modified (c-ss-Amino-48-mer) was functionalized by nucleophilic substitution of S-4FB, an aromatic aldehyde, via an activated N-hydroxysuccinimide ester, to obtain a 48-mer 5'-aldehydic terminus (Figure 6.1).

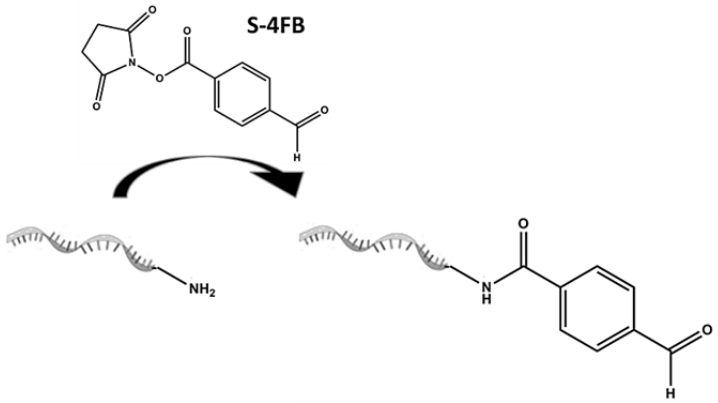

Figure 6.1 Aldehydic functionalization reaction by S-4FB of 5'-amino modified 48-mer oligo DNA.

With regards to the protein, the superficial lysine residues of hCA1 were modified by nucleophilic incorporation of S-HyNic, an aromatic hydrazide, obtaining hCA1 hydrazide activated (Figure 6.2). The protein had 18 lysine moieties, meaning the reaction was not site-specific, but stochastic, therefore after functionalization a distributed population of modified hCA1 was obtained.

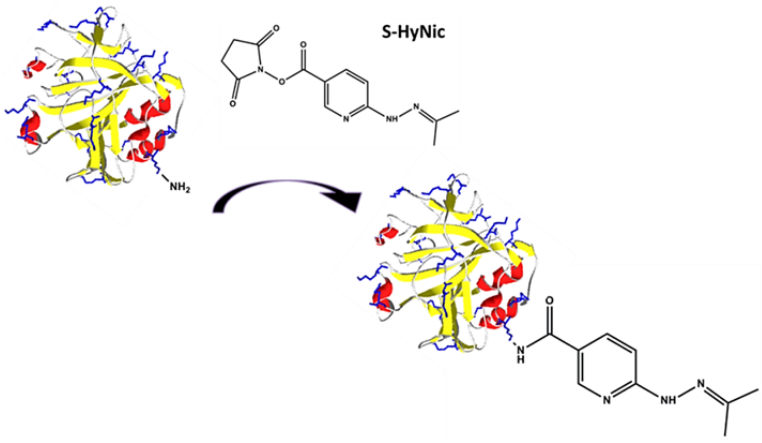

Figure 6.2 Hydrazide functionalization reaction by S-HyNic of hCA1. PBD 1CRM of hCA1 crystallographic structure (Kannan et al, 1972) displayed in DeepView, β-sheets in yellow, α-helix in red and the 18 target lysine residues in blue color.

Next, the conjugation reaction between these modified biomolecules was straightforward. The driven factor was simply the pH reduction, from 7.4 to 6.0 in

phosphate buffer, which resulted in the deprotection of hydrazide groups from acetone moieties. Successively hydrazide reacted with aldehydic groups of 48-mer DNA and the condensation reaction formed bis-aryl hydrazone bonds (Figure 6.3).

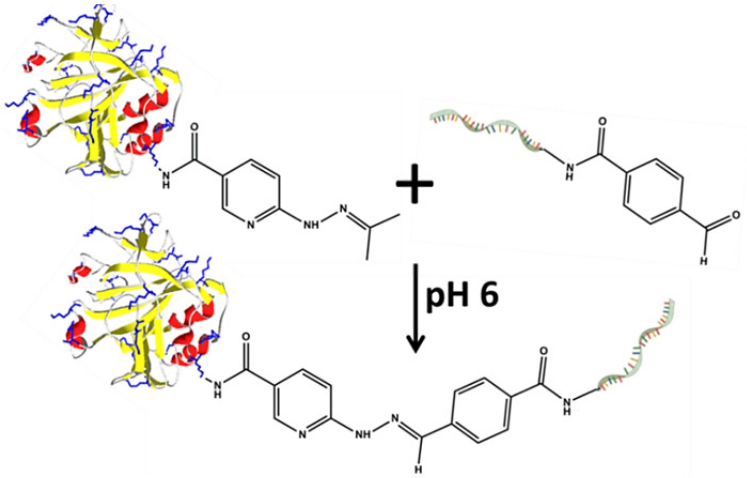

Figure 6.3 Conjugation Reaction of hydrazide functionalized hCA1 and aldehydic 48-mer oligo DNA. The reaction is driven by the variation of pH, from 7.4 to 6.0.

The formation of multi conjugates presenting multiple 48-mer DNA covalently bound to one protein was avoided, consequent to a severe optimization of each reaction step and purification method. However, the aldehydic functionalization of amino 48-mer DNA was straightforward and it did not require any particular adjustment of given Solulink's protocol.

It is important to emphasize that whole optimization was done in an iterative way. At first Solulink's protocol was used with no variations, trying instead to find a good chromatographic purification method. The initial belief was to keep high the conjugation yield production and afterwards to separate mono conjugates in chromatography.

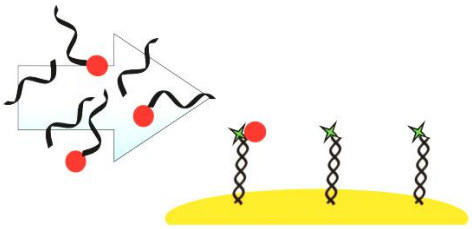

Figure 6.4 Schematic view of reduced surface functionalization by protein mono conjugates, if free 48-mer remains in hybridization solution.

Finally the collected fractions in chromatography, containing the supposed mono conjugates, always presented a rest of free unreacted 48-mer, reducing significantly the final surface functionalization with the protein (Figure 6.4).

Finally, the best strategy resulted to be the production of hCA1-DNA mono conjugates purified in electroelution, to effectively clean up the eluted fraction from unreacted DNA.

6.1.2 Human Carbonic Anhydrase 1

The protein hCA1 was chosen as a model for the production of protein-DNA mono conjugates since it possesses suitable biochemical characteristics: stability, slightly acidic pI, monomeric state, globular tertiary structure and a molecular weight below 50 kDa. The small size of protein-DNA assembly on *switch*SENSE allows further investigations, such as the affinity analysis of antibodies anti-hCA1, since the variation of switching dynamics upon antibody binding can be still detected and differentiated.

Purified in 1933 from human erythrocytes in the cytosol fraction (Meldrum & Roughton, 1933), hCA1 belongs to α-family, one of the five isoform families which have been characterized in mammals, plants and bacteria.

The protein is a zinc metalloenzym (EC 4.2.1.1) that catalyses the reversible hydration of carbon dioxide to maintain acid-base balance in blood and other tissues. The hydration/dehydration equilibrium of carbon dioxide is described by the following reaction (Eq. 6.1):

Eq. 6.1 $$\mathbf{CO_2 + H_2O \leftrightarrow H^+ + HCO_3^- \leftrightarrow H_2CO_3}$$

Generally, most of carbonic acid in solution is deprotonated into bicarbonate anions HCO_3^-. At 25°C the rate constant of CO_2 hydration reaction is 0.0375 s^{-1}, while for CO_2 dehydration is 13.7 s^{-1} (Chien & Sturtevant, 1963; Gibbons & Edsall, 1963), therefore, the majority of the carbon dioxide is not converted into carbonic acid, but remains as gassed CO_2 molecules. But in presence of hCA1 enzyme the equilibrium is strongly moved to hydration of CO_2, the carbonic anhydrase has in fact a high catalytic power with k_{cat} equal to 10^5 reactions per second (Lehtonen et al, 2004). This reaction rate of carbonic anhydrase is one of the fastest of all enzymes.

Due to its feature, it is not surprising that hCA1 and its large family have high relevance in medical and pharmaceutical research, being involved in various physiological reactions, including cellular respiration (Vitale et al, 2007), pH regulation (De Simone & Supuran, 2010), calcification (Bosley et al, 2011), sodium retention (Schliebe et al, 2008) and tumourigenesis (Said et al, 2010). Consequently carbonic anhydrase inhibitors, CAI, are used in the medical treatment of a number of conditions and researchers are continuing looking for high-affinity compounds that bind to specific CA isozymes, to reduce side effects (Aggarwal & McKenna, 2012; Lopez et al, 2010).

In this project Acetazolamide inhibitor (AAZ) was selected to be tested on *switch*SENSE, upon reaction with hCA1 present on functionalized DNA layer. The molecule AAZ (trade name Diamox) binds by the reactive sulfonamide group the zinc ion present in catalytic pocket, inhibiting the enzymatic activity (Chakravarty & Kannan, 1994) (Figure 6.5). The inhibition constant on hCA1 is K_I 200 nM (Lehtonen et al, 2004).

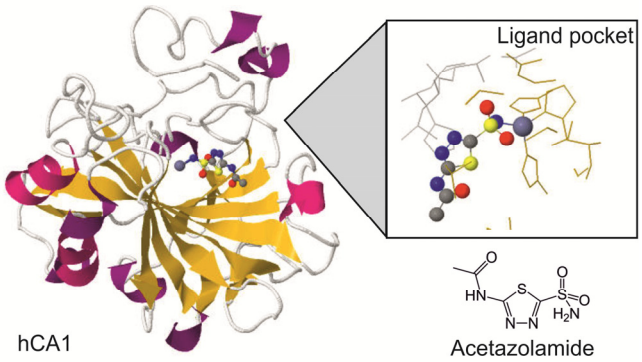

Figure 6.5 Complex of hCA1/acetazolamide. Acetazolamide binds the catalytic zinc in hCA1 by its sulfonamide group, inhibiting the enzymatic activity. PDB file 1AZM (Chakravarty & Kannan, 1994). The picture was displayed by DeepView.

Another relevant possible analysis on hCA1/DNA layer it was monoclonal antibody (mAb) detection, as model of protein/protein interaction study. On market many diverse mAb anti-hCA1 are available, but in most of the case they are not kinetically characterized. Therefore a comparative study in kinetics was done, selecting five different mAb, and testing them on *switch*SENSE surface and on Biacore™, a SPR based sensor.

6.1.3 Binding kinetics

In this work kinetic analyses were performed on *switch*SENSE technology for different experiments (e.g. hybridization of hCA1-DNA mono conjugates on surface-tethered ss-DNA, antibody binding on ds-DNA layers presenting hCA1, human p53 binding to DNA response elements) and on Biacore™ (antibody binding on hCA1 immobilized on surface and vice-versa). Hereby the Langmuir adsorption isotherm was used in all analyses to estimate rate constants of association and dissociation events, and subsequent determination of equilibrium binding constant.

LANGMUIR ADSORPTION ISOTHERM

The Langmuir adsorption isotherm describes the equilibrium state resulting in a system characterized by the presence on surface of a defined number of free binding sites, *B*, defined as probes, and a species in solution of concentration *A* which recognizes the

ligand, defined as target. The equilibrium is reached between free and occupied sites, follows:

Eq. 6.2 $$\boldsymbol{A + B \leftrightarrow AB}$$

Eq. 6.3 $$\boldsymbol{\frac{d[A]}{dt} = [A] \cdot [B] \cdot k_{on} - [AB] \cdot k_{off}}$$

At the equilibrium Eq. 6.3 is equal to zero and

Eq. 6.4 $$\boldsymbol{[A] \cdot [B] \cdot k_{on} = [AB] \cdot k_{off}}$$

Eq. 6.5 $$\boldsymbol{K_D = \frac{k_{off}}{k_{on}} = \frac{[A] \cdot [B]}{[AB]}}$$

Eq. 6.6 $$\boldsymbol{[B_{tot}] = [B] + [AB]}$$

where $[B]$ is the number of free probes and $[AB]$ the number of bound probes, and K_D the equilibrium binding constant of the system, defined as *steady state* K_D. Joining Eq. 6.5 and Eq. 6.6 results:

Eq. 6.7 $$\boldsymbol{K_D = [A] \cdot \left(\frac{[B_{tot}]}{[AB]} - 1\right)}$$

Eq. 6.8 $$\boldsymbol{\frac{[AB]}{[B_{tot}]} = \frac{[A]}{[A]+K_D}}$$

Therefore, in the system at equilibrium the surface occupancy of probes, Γ_{eq}, which depend on target concentration $[A]$, as described below:

Eq. 6.9 $$\boldsymbol{\Gamma_{eq}(A) = \frac{[A]}{[A]+K_D} \cdot \Gamma_{max}}$$

where Γ_{max} is the maximum response, when all probes are bound by target molecules. Deriving the surface occupancy as function of time results:

Eq. 6.10 $$\boldsymbol{\frac{\partial \Gamma}{\partial t} = [A] \cdot k_{on} \cdot (\Gamma_{max} - \Gamma) - k_{off} \cdot \Gamma}$$

Solving Eq. 6.10, the bound fraction is:

Eq. 6.11

$$\boldsymbol{bound\ fraction\ (t) = \frac{\Gamma(t)}{\Gamma_{max}} = \frac{[A]}{[A]+K_D} \cdot \{1 - exp[-([A] \cdot k_{on} + k_{off})t]\}}$$

Finally the dissociation rate of the target from the bound probe is described as single exponential function dependent on k_{off}:

Eq. 6.12 $$\boldsymbol{dissociation}\ (\boldsymbol{t}) \propto \boldsymbol{exp}\{-\boldsymbol{t}/\boldsymbol{\tau_{off}}\} \rightarrow \boldsymbol{1}/\boldsymbol{\tau_{off}} = \boldsymbol{k_{off}}$$

As well as the association rate of target to probe depends on k_{on} and concentration of target:

Eq. 6.13 $$\boldsymbol{association}\ (\boldsymbol{t}) \propto \boldsymbol{exp}\{-\boldsymbol{t}/\boldsymbol{\tau_{on}}\} \rightarrow \boldsymbol{1}/\boldsymbol{\tau_{on}} = [\boldsymbol{A}] \cdot \boldsymbol{k_{on}} + \boldsymbol{k_{off}}$$

The first-order rate equation of Langmuir adsorption isotherm is valid under the assumption that all binding sites are identical.

To estimate a correct association rate constant, there must be no diffusion limited regime and whenever possible the target molecule should be supplied in abundance ensuring a constant concentration near the surface. These conditions provide the reaction kinetic with a characteristic reaction rate, called reaction limited regime.

In surface biosensor, the diffusion limited regime is mainly affected by the geometry of microfluidic flow cell and volumetric flow rate. This is accentuated working with strong binder biomolecules, for example monoclonal antibodies (normally association rate is $>10^5$ $M^{-1}s^{-1}$). Hereby the flow velocity becomes an important parameter to assure meaningful rate constants (Squires et al, 2008).

6.2 Results, part 1: hCA1-DNA conjugate preparation

6.2.1 Aldehydic functionalization of aminated oligonucleotide

The chosen oligonucleotide, c-ss-Amino-48-mer, had the following sequence:
5' -NH_2-$(CH_2)_6$-ATC AGC GTT CGA TGC TTC CGA CTA ATC AGC CAT ATC AGC TTA CGA CTA-3'.

The functionalization reaction and the determination of molar substitution ratio, MSR, were performed as described in Section 4.2.5.2. Typically the estimated yield of reaction was very high, around 95% with a molar substitution ratio (MSR) of 1.

The effective functionalization was further checked on Matrix-Assisted Laser Desorption/Ionization Time-of-Flight (MALDI-TOF) mass spectrometry, following the method described by Haff *et al.* (Haff et al, 1998). The mass analysis showed a successful modification of c-ss-Amino-48-mer (Figure 6.6), having a single mass peak for aldehydic functionalized 48-mer of 14964 Da (theoretical molecular weight, MW, 14955.7 Da) and a measured mass for original c-ss-Amino-48-mer of 14837 Da (theoretical MW 14823.6 Da). The $\Delta_{measured}$ equal to 127 Da is in agreement with $\Delta_{theoretical}$ of 132.1 Da.

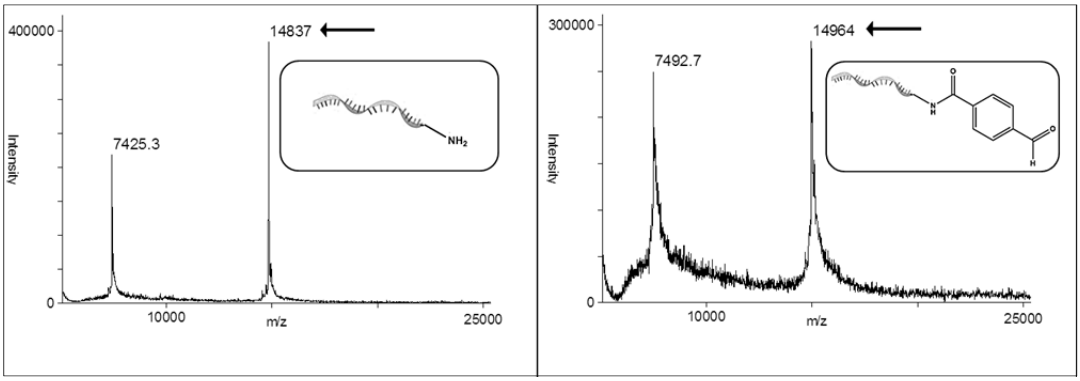

Figure 6.6 MALDI-TOF MS results for aldehydic modified 48-mer. Left side, original c-ss-Amino-48-mer had a measured mass peak of 14837 Da; right side, aldehydic modified 48-mer showed a mass peak of 14964. The spectra showed a typical m/z peaks (z= +2, +1).

The specific functionalization of the primary amine was verified measuring the melting temperature, Tm, of aldehydic functionalized 48-mer and compared to the original oligonucleotide, previously let hybridize with the complement strand, ss-48-mer (Figure 6.7). In case of a functionalization occurred on aromatic amines of nucleotide bases, the melting temperature should be decreased.

The melting curve obtained for aldehydic 48-mer was a bit noisy, but still obtained Tm was comparable to the original oligonucleotide one (68 ˚C and 72 ˚C, respectively), meaning the modification reaction occurred specifically on 5'-amino-terminus which is

characterized by a higher nucleophilicity, without compromising the following hybridization even to ss-48-mer, a critical issue for switching DNA layers.

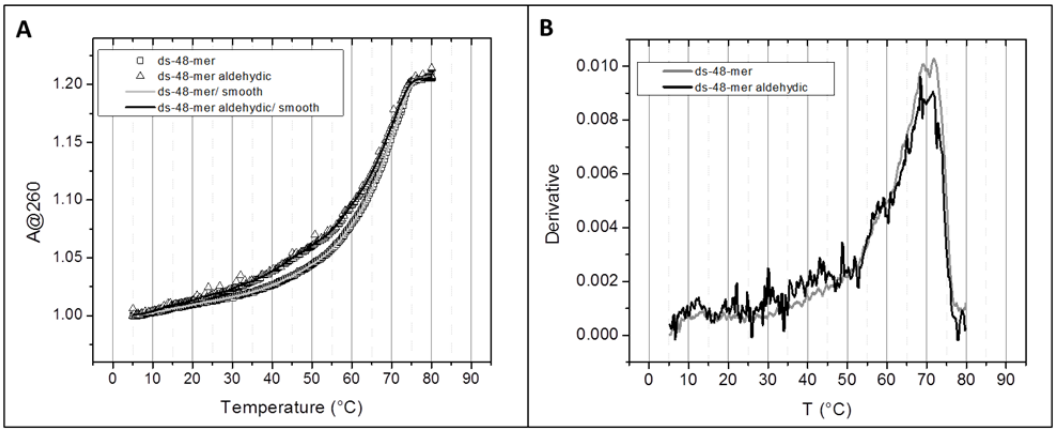

Figure 6.7 Melting curve results of aldehydic modified 48-mer, compared to original c-ss-Amino-48-mer. A: the melting curves were measured in Standard Buffer, having 0.5 µM hybridized ds-48-mer, here raw data and smoothed ones (15 point filter). B: Tm was calculated by first derivative of melting curve functions.

6.2.2 Hydrazide functionalization of hCA1

Initially Solulink's functionalization protocol was carried out with no variations. This protocol considers a molar reaction ratio of hCA1/S-HyNic equal to 1/20. As it is elucidated afterwards, this ratio led to the formation of undesired multi conjugates.

That's the reason why the variation of MSR by increased hCA1/S-HyNic reaction ratio was observed, to find out at which condition MSR gets close to 1.

It is true though that using a protein solution which has an extremely low distributed amount of reactive group, as 1 per protein molecule, reduces a lot the yield of conjugation reaction. But the advantage was subsequently in electroelution step, where was easy to identify the mono conjugate band in native gel to then cut it out (Section 6.2.3.2).

6.2.2.1 Characterization of hCA1

The protein hCA1 from human erythrocytes was supplied by Sigma-Aldrich. It was chromatographically purified, but nevertheless checked on SDS-PAGE Tris-Gly buffer, 12.5% polyacrylamide denaturing conditions (SDS, reductive and high temperature treatments). Figure 6.8 A shows the high purity grade of hCA1, by the presence of a single band at approximately 30 kDa.

Furthermore, in TBE native gel performed for hCA1-DNA mono conjugate purification in electroelution (Section 6.2.3.2.1), hCA1 was loaded as sample reference and revealed the

presence of a broad smeared band, suggesting the presence of isoforms in the supplied hCA1 preparation (Figure 6.8 B).

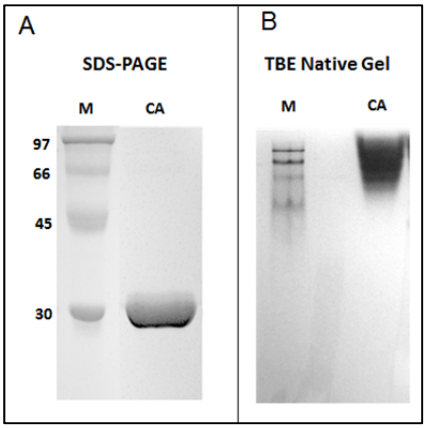

Figure 6.8 A: The purity of hCA1 was verified in SDS-PAGE at denaturing conditions, displaying the gel in Coomassie Blue staining. B: The TBE native gel, carried out for mono conjugate purification in electroelution (Section 6.2.3.2.1), revealed the presence of isoforms in the sample, resulting in a large smeared band at the top of the gel.

In literature Kondo *et al.* observed the presence of 3.4% glycosylated form in hCA1 extracted from human erythrocyte of healthy patients (Kondo et al, 1987). Consequently the presence of glycosylated forms in hCA1 Sigma-Aldrich preparation was investigated.

6.2.2.1.1 Glycosylated forms in purchased hCA1

The protein was loaded in affinity column HiTrap Con A 4B in FPLC to isolate and estimate the concentration of glycosylated forms present in purchased hCA1 (Method Section 4.2.5.1).

Figure 6.9 A presents the corresponding chromatogram and relative collected wash and elution fractions. Their content was analysed in SDS-PAGE (Figure 6.9 B), revealing the presence of a band, below 20 kDa, in the elution fraction. The impurity could be the monomeric Con A, released from the column, even though its expected molecular weigth is 25 kDa. This explains the constant high absorbance observed in the chromatogram during the elution. Despite this column instability, the experiment could show the presence of slight heavier form of hCA1 in the elution fraction, compared to the form present in the wash fraction, thus confirming the presence of glycosylated population of hCA1, which was found to be 7% of the total hCA1.

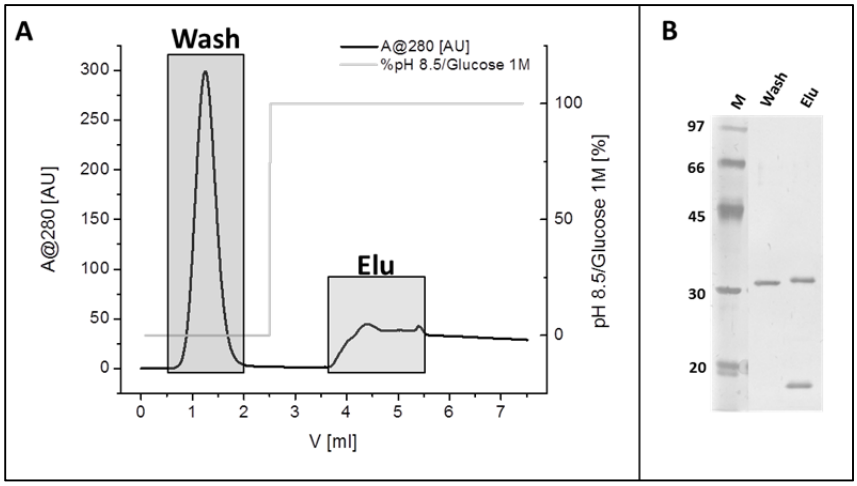

Figure 6.9 A: HiTrap Con A 4B chromatogram in FPLC for hCA1. In grey squares, the wash and elution fractions are highlighted. B: The collected fractions were analysed in SDS-PAGE 12.5% acrylamide, and visualized in silver staining.

6.2.2.2 Setting MSR of functionalized hCA1

To reduce multi conjugate formation, the amount of linker required to functionalize hCA1 was determined, having possibly one hydrazide moiety per protein.

The chosen parameter for this evaluation was MSR; the MSR namely indicates how many modified lysine residues are present on the protein after functionalization. The titration experiment was performed preparing different reaction batches for hCA1/S-HyNic ratio equal to 1:0 as negative control, then 1:1, 1:5, 1:10 and 1:20 (Methods Section 4.2.5.2 and 4.2.5.3).

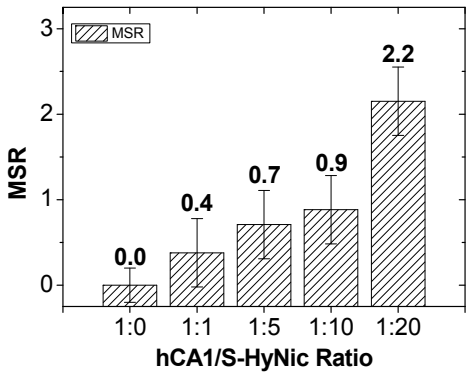

Figure 6.10 Obtained MSR values for S-HyNic on hCA1 by increased hCA1/S-HyNic ratio in the functionalization reaction. In column chart MSR values are plotted together with the SD for two experimental replicates.

As shown in Figure 6.10, at 1:5 hCA1/S-HyNic reaction ratio, 3 mol of hCA1 had just 2 modified hydrazide molecules, while 1:10 ratio resulted in the desired distribution of approximately one active hydrazide per protein.

6.2.3 Optimization of conjugation and purification steps

The production of hCA1-DNA mono conjugates required a cross-optimization of conjugation and purification steps and the quality of this optimization was followed by loading the crude of reaction and the collected eluted fractions in SDS-PAGE Tris-Gly buffer (Section 4.2.4.4 and 4.2.5.4), together with controls like aldehydic modified 48-mer and hCA1 (defined as DNA and CA in gel pictures, respectively).

The protein-DNA conjugates and the unreacted 48-mer were displayed by fluorescence method, adding ss-48-mer-Cy3 to each loaded sample. The unreacted hCA1 protein was located after gel silver staining.

Figure 6.11 presents a necessary guide to read the gel pictures, shown in the following sections; the expected molecular weight for each species is indicated as well as where this band is detected, either in Cy3 fluorescence or in silver staining picture, allowing a complete understanding. On the left side the pictures always show Cy3 fluorescence detection, while on the right side the silver staining visualization.

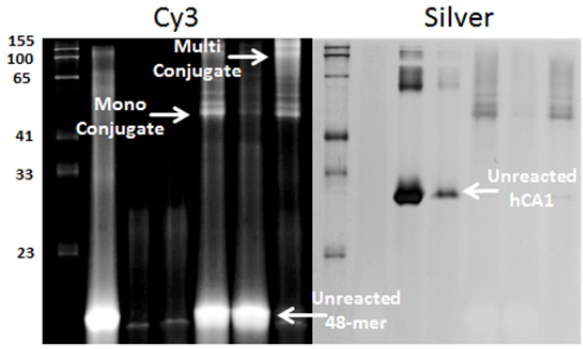

Conjugate gel legend

Molecule	In which picture side	MW ladder
Multi conjugate	**Cy3**	**ca. 100 kDa**
Mono conjugate	**Cy3**	**41-65 kDa**
Unreacted 48-mer	**Cy3**	**< 23kDa**
Unreacted hCA1	**silver**	**23-33 kDa**

Figure 6.11 Legend to read out the gel pictures, shown in the following sections. Left, the locations of the interesting molecules were pointed out in the gel pictures; multi and mono conjugates together with unreacted 48-mer detected in Cy3 fluorescence, unreacted hCA1 displayed in silver staining. Right, a table listed the expected MW for each species as well as where this band was detected, in Cy3 fluorescence or in silver staining picture.

The protein-DNA conjugate bands, in Cy3 emission filter, around 100 kDa protein ladder, are related to multi conjugates (1 hCA1 molecule plus 2/3/4 48-mer molecules, correspond numerically to 59/74/89 kDa. N.B.: the expected MW could not be directly translated in the gel and compared to the protein ladder, especially at high MW. This is due to the unique biochemical nature of conjugates in gel electrophoresis, which is a combination of protein and DNA characteristics).

The protein-DNA conjugate bands, in Cy3 emission filter, between 41-65 kDa protein ladder, are referred to mono conjugates (1 CA/1 48-mer numerically equal to 44 kDa).

The brilliant DNA bands, in Cy3 emission filter, below 23 kDa protein ladder are associated to unreacted 48-mer DNA (ds 48-mer around 30 kDa, but, since is strongly negatively charged, it runs through the gel much way faster than a protein with the same MW).

The dark protein bands, in Silver staining, between 23-33 kDa protein ladder, are correlated to unreacted hCA1 (29 kDa).

The tried combinations between reaction conditions and purification methods are listed in Table 6.1.

Table 6.1 Tried combinations between reaction conditions and purification methods. * SEC, size exclusion chromatography; + AEX, anion exchange chromatography.

	hCA1/S-HyNic	hCA1/48-mer	Purification	Figure
1	*1:20 (MSR 2.2)*	*1:1*	*SEC* →AEX+*	Figure 6.12, Figure 6.13, Figure 6.14
2	*1:1 (MSR 0.4)*	*1:2*	*AEX*	Figure 6.17, Figure 6.18
3	*1:5 (MSR 0.7)*	*1:2*	*AEX*	Figure 6.17, Figure 6.18
4	*1:5 (MSR 0.7)*	*2:1*	*Electroelution*	Figure 6.19
5	*1:10 (MSR 0.9)*	*2:1*	*Electroelution*	Figure 6.19

6.2.3.1 Purification step: chromatographic methods

The preferable method to purify protein-DNA conjugates is in chromatography, using either SEC column or AEX column (Kozlov et al, 2004). The estimated pI of hCA1 is 6.6[1], therefore above pH 7.6 the protein is negatively charged, hence AEX is a suitable separation method.

Several tries were performed in chromatography, exploring the purification in different columns. Finally the chromatography was not chosen since the mono conjugate fractions presented a rest of unreacted 48-mer.

6.2.3.1.1 SEC and AEX columns in FPLC

For SEC separation Superdex 75 10/300 GL was used, performing an isocratic elution by PBS Buffer 0.1M pH 7.4, NaCl 0.3 M, at 0.4 ml/min flow rate and reading out absorbance at 280 nm.

Figure 6.12 shows the chromatogram of a conjugation reaction (hCA1/S-HyNic 1:20 functionalization ratio, MRS 2.2 + hCA1/48-mer 1:1 conjugation ratio).

[1] pI was calculated by ProtParam, UniProt #P00915. http://web.expasy.org/protparam/.
This value is also indicated in the product datasheet.

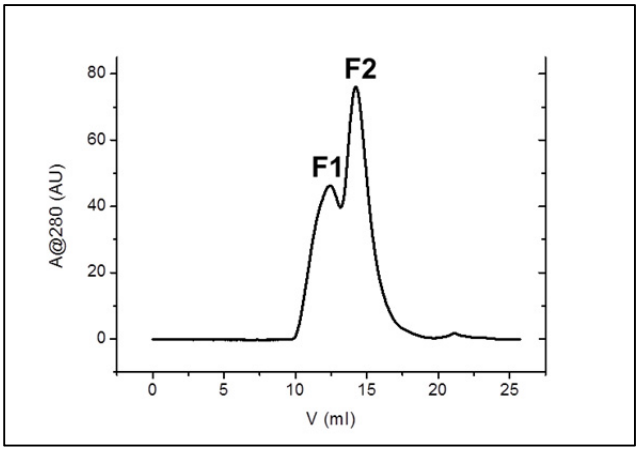

Figure 6.12 SEC in FPLC for reaction (hCA1/S-HyNic 1:20 functionalization ratio, MRS 2.2 + hCA1/48-mer 1:1 conjugation ratio). Two peaks were separated and further analyzed in AEX column.

SEC column resolved two peaks, which were collected as F1 and F2 fractions. After concentration in Amicon® 3 kDa, the two fractions were injected in AEX column, HiTrap Q FF, having Tris 20mM pH 8.0 and linear salt gradient for elution, from 50 mM NaCl to 1.05M, at 1 ml/min flow rate.

Figure 6.13 A displays the AEX chromatograms of F1 and F2. In the salt gradient, F1 gave one peak, F1.1, while F2 was resolved collecting three fractions, F2.1, F2.2 and F2.3. As displayed in the gel (Figure 6.13 B) F1.1 contained a distributed profile of conjugates (mono and multi) and no hCA1 and 48-mer unreacted species. While F2.1 presented unreacted hCA1, F2.2 had mostly mono conjugates and a rest of unreacted DNA, F2.3 contained just unreacted DNA. Once more this column was not able to separate mono conjugates from unreacted DNA. Therefore HiTrap Q FF column was useless, since it did not resolve better the fractions.

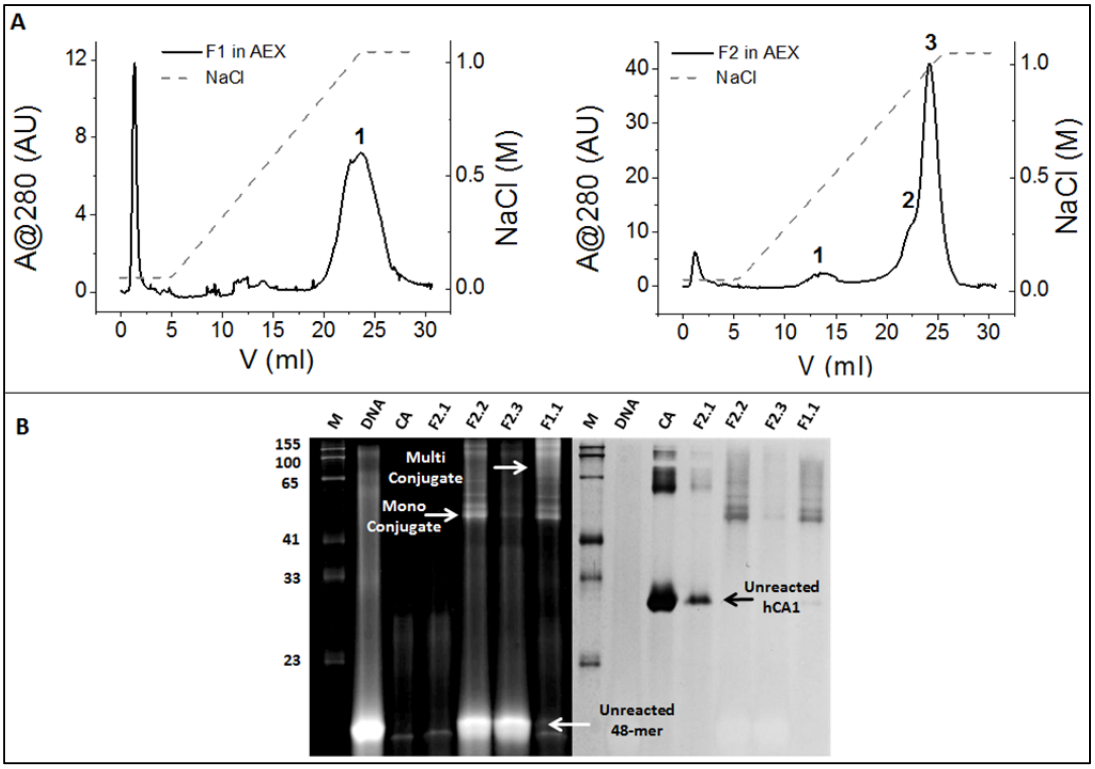

Figure 6.13 Purification results of F1 and F2 in AEX. F1 and F2 were collected first in SEC from sample reaction (hCA1/S-HyNic 1:20 functionalization ratio, MRS 2.2 + hCA1/48-mer 1:1 conjugation ratio) and then re-injected in AEX. A: left, chromatogram of F1, just one fraction was collected, F1.1; right, chromatogram of F2, with 3 different collected fractions, F2.1, F2.2 and F2.3.
B: SDS-PAGE results of AEX collected fractions, F2.1, F2.2, F2.3 and F1.1, they were compared to protein marker, aldehydic modified 48-mer and hCA1; Cy3 fluorescence and silver staining pictures were taken, left and right side respectively.

In order to obtain better resolved fractions for multi and mono conjugates and unreacted DNA, a second try was carried out in Superdex 75 10/300 GL column, performing the same isocratic elution for the same reaction sample (hCA1/S-HyNic 1:20 functionalization ratio, MRS 2.2 + hCA1/48-mer 1:1 conjugation ratio), but this time collecting smaller fraction from the two peaks (Figure 6.14 A), 5 fractions in total, F1,F2, F3, F4 and F5.

Figure 6.14 B-C display the collected fractions in SDS-PAGE, showing that F1 presented just multi conjugates, while F2 multi and mono conjugates, and unreacted hCA1. As for F3, it contained mainly mono conjugates, unreacted DNA and unreacted hCA1. The fractions F4 and F5 had unreacted DNA and unreacted protein. Concluding that neither Superdex 75 10/300 GL column was able to separate mono conjugates from unreacted DNA.

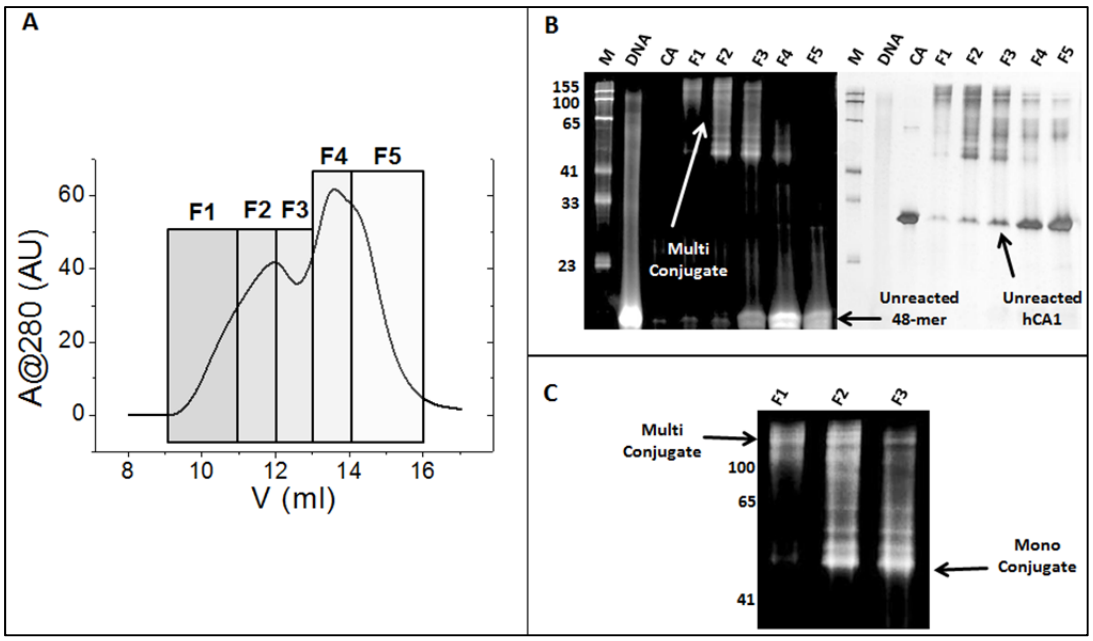

Figure 6.14 A: SEC in FPLC for reaction (hCA1/S-HyNic 1:20 functionalization ratio, MRS 2.2 + hCA1/48-mer 1:1 conjugation ratio). The two peaks were collected separately in five smaller fractions. B: SDS-PAGE results for collected fractions, F1, F2, F3, F4 and F5, they were compared to protein marker, aldehydic modified 48-mer and hCA1; Cy3 fluorescence and silver staining pictures were taken, respectively left and right side. C: The enlargement of Cy3 fluorescence picture remarks the presence of multi conjugates mostly in fractions F1 and F2.

The removal of unreacted DNA present in fractions F2.2 (Figure 6.13 B) and F3 (Figure 6.14 B) was attempted in Amicon® 30 kDa, washing the aliquots with Standard Buffer. However, the unreacted DNA remained in both fractions (Figure 6.15).

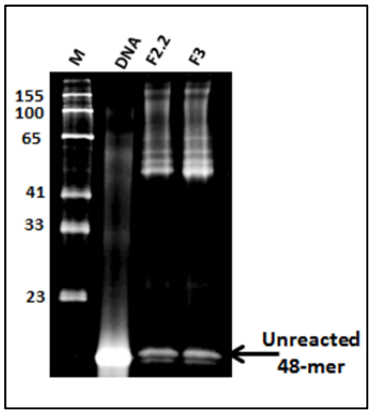

Figure 6.15 Results of Amicon® 30 kDa cleaning. The removal of unreacted DNA was attempted in Amicon® 30 kDa on fractions F2.2 (Figure 6.13) and F3 (Figure 6.14). However, the DNA remained in the fractions, visible at the bottom part of the gel.

In FPLC a cation exchange (CEX) column, HiTrap SP FF, was used in Sodium Acetate 50mM pH 4.5 with linear salt gradient for elution, from 0 to 1 M NaCl at 1 ml/min with no success.

6.2.3.1.2 AEX column in HPLC

In principle, AEX method is the best strategy to separate the conjugates from the solated protein based on their negative charge. Though, the issue was to clean up the conjugates from unreacted DNA.

A second AEX column was tested in HPLC, the analytical column BioPro QA, having Tris 20mM pH 8.0 and linear salt gradient for elution, from 50 mM NaCl to 1.05M, at 0.5 ml/min flow rate.

The HPLC machine here employed possesses a diode-array detector, which enables simultaneous multi-wavelength detection; therefore the characteristic absorbance for bis-aryl hydrazone bond at 354 nm was monitored.

Initially the references, hydrazide modified hCA1 and aldehydic modified 48-mer, were injected, obtaining in the void column volume the protein and at 0.7 M NaCl 48-mer (Figure 6.16).

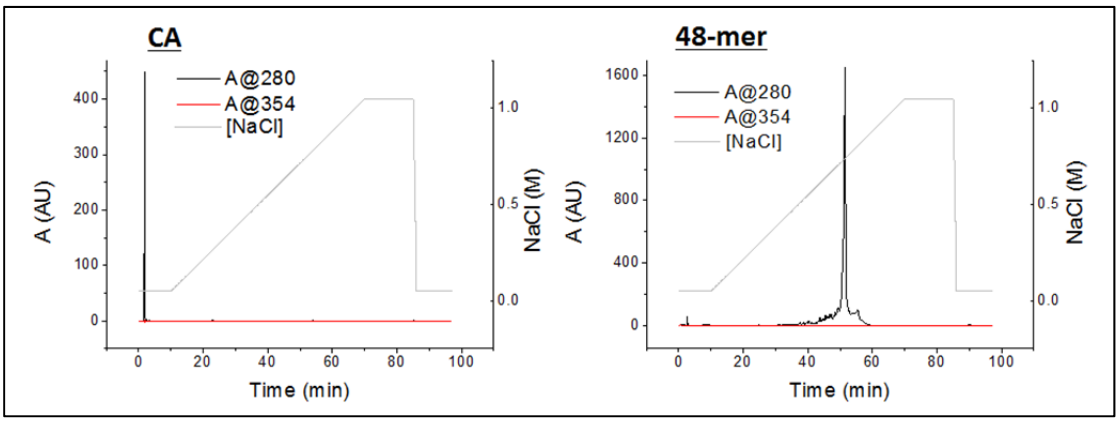

Figure 6.16 Reference chromatograms for modified hCA1 and 48-mer in AEX column, BioPro QA, HPCL.

Further, two different conjugation reactions were prepared:

- Reaction 1 (hCA1/S-HyNic 1:1 functionalization ratio (MRS 0.4) + hCA1/48-mer 1:2 conjugation ratio);
- Reaction 5 (hCA1/S-HyNic 1:5 functionalization ratio (MRS 0.7) + hCA1/48-mer 1:2 conjugation ratio).

Each reaction was injected, collecting eight fractions from each reaction sample at 0.47-0.83 M NaCl (Figure 6.17_A; Figure 6.18_A).

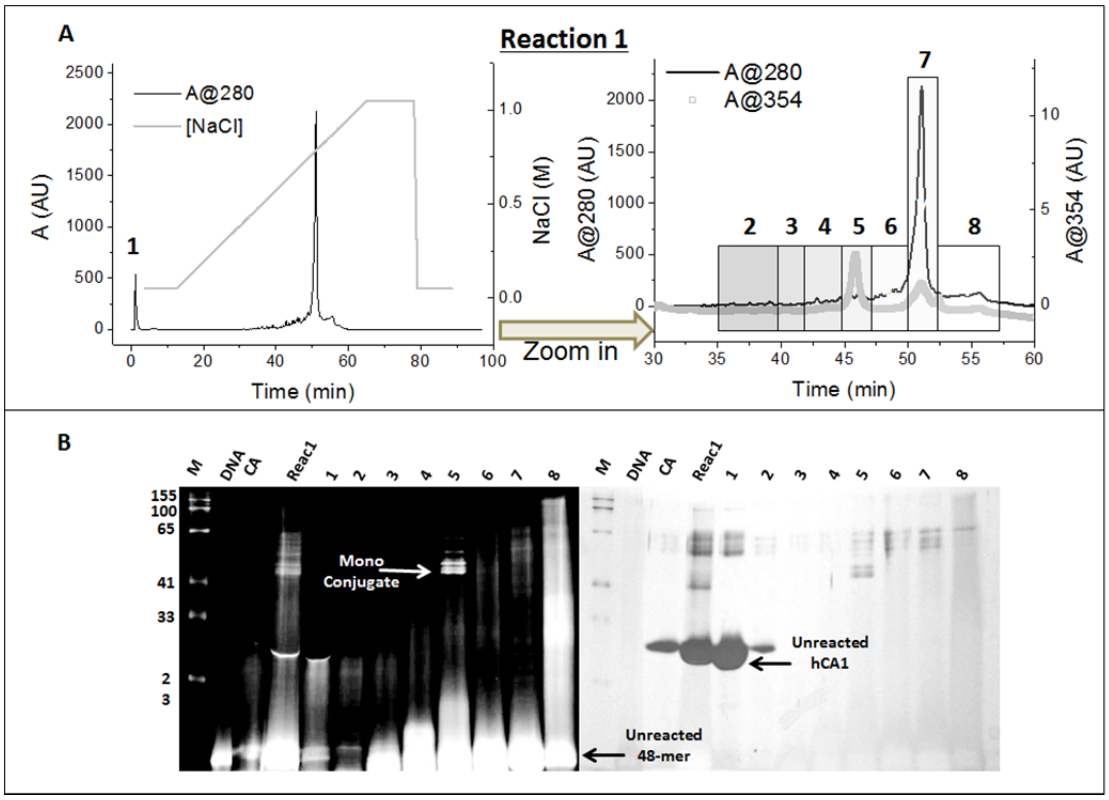

Figure 6.17 A: AEX chromatogram in HPLC for Reaction 1 (hCA1/S-HyNic 1:1 functionalization ratio (MRS 0.4) + hCA1/48-mer 1:2 conjugation ratio). On the right, the chromatogram was enlarged to show the collected fractions from 2 to 8 at 0.47-0.83 M NaCl; the fraction 1 came out with the void column volume. B: SDS-PAGE results for collected fractions, compared to protein marker, aldehydic modified 48-mer DNA and hCA1; Cy3 fluorescence and silver staining pictures were taken, left and right side respectively.

Reaction 1 gave mostly mono conjugates; the bands were distributed between 41-65 kDa (Figure 6.17 B); while Reaction 5 contained also multi conjugates, indicated by the presence of band 100 kDa (Figure 6.18 B).

With regards to Reaction 1 (Figure 6.17 A-B), hCA1was eluted in the void column volume, fraction n. 1. The mono conjugates were present only in fraction n. 5, in agreement with the absorbance signal at 354 nm.

However, again the unreacted DNA remained in most eluted fractions, from 3 to 8 (bright bands visible as at the bottom of the gel).

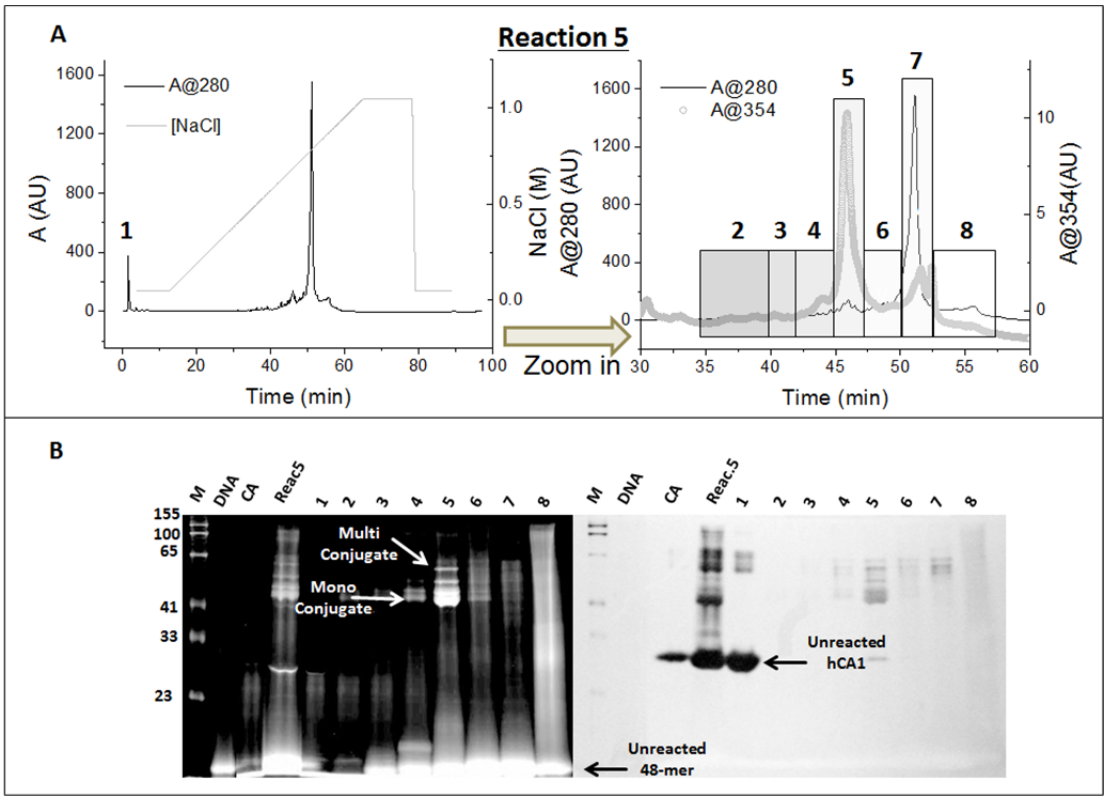

Figure 6.18 A: AEX chromatogram in HPLC for Reaction 5 (hCA1/S-HyNic 1:5 functionalization ratio (MRS 0.7) + hCA1/48-mer 1:2 conjugation ratio). The enlargement of the chromatogram on the right to point out the 7 collected fractions between NaCl 0.47-0.83 M, while fraction number 1 came out with the void column volume. B: SDS-PAGE results for collected fractions, compared to protein marker, aldehydic modified 48-mer DNA and hCA1; Cy3 fluorescence and silver staining pictures were taken, left and right side respectively.

The Reaction 5 showed similar outcomes as Reaction 1 (Figure 6.18_A-B), with the same disadvantage of unreacted DNA, present in most eluted fractions.

Concluding, the tried chromatographic methods were not successful in purifying mono conjugates from unreacted 48-mer.

About the conjugation reaction, Reaction 5 (hCA1/S-HyNic 1:5 functionalization ratio (MRS 0.7) + hCA1/48-mer 1:2 conjugation ratio) showed a significant formation mono conjugates but also a small presence of multi conjugates.

Taking inspiration from obtained gel picture, the best obtained resolution was in electrophoresis. Indeed in gel the unreacted 48-mer runs much faster than the conjugates, due to the combination of dimension and charge. Hence the electroelution of mono conjugate was performed to recover highly pure mono conjugate fractions.

6.2.3.2 Purification in electroelution

6.2.3.2.1 Native gel electrophoresis

The mono conjugates were initially separated in native gel electrophoresis, carried out at 4°C and in an optimized buffer solution avoiding the heating up of the electrophoretic chamber and resulting in sharp bands (Method Section 4.2.5.5).

Two different reactions were assembled to be loaded in TBE gel for mono conjugate separation:

- Reaction 5 1/2 (Reac 5 1/2 in gel pictures) = hCA1/S-HyNic 1:5 functionalization ratio (MRS 0.7) + hCA1/48-mer 2:1 conjugation ratio;
- Reaction 10 1/2 (Reac 10 1/2 in gel pictures) = hCA1/S-HyNic 1:10 functionalization ratio (MRS 0.9) + hCA1/48-mer 2:1 conjugation ratio.

The conjugation ratio reaction from hCA1/48-mer 1:2 was reduced to 2:1 to produce only mono conjugates and to facilitate the electroelution, whereby the achievement of just a single mono conjugate band in native gel ensured a successful purification.

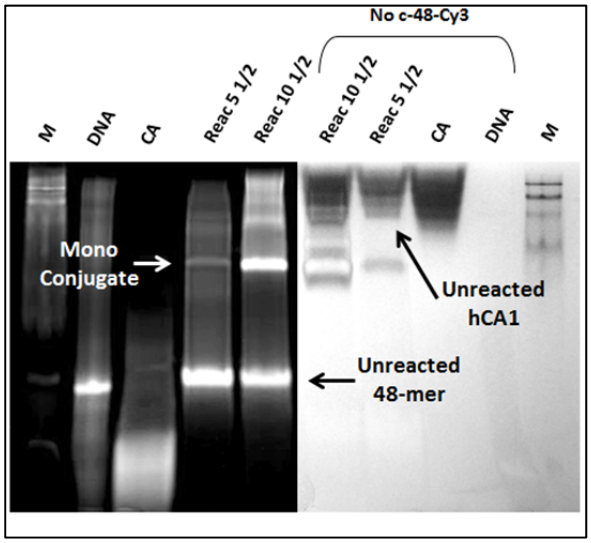

Figure 6.19 Native electrophoresis in TBE buffer. The samples, Reac 5 1/2 (hCA1/S-HyNic 1:5 functionalization ratio, MRS 0.7 + hCA1/48-mer 2:1 conjugation ratio) and Reac 10 1/2 (hCA1/S-HyNic 1:10 functionalization ratio, MRS 0.9 + hCA1/48-mer 2:1 conjugation ratio) were loaded in presence and absence of ss-48-mer-Cy3 and compared to protein marker, aldehydic modified 48-mer and hCA1. The fluorescence and silver staining pictures were taken, left and right side respectively.

Figure 6.19 shows a typical native TBE gel made for mono conjugate separation: DNA sample had a single bright band, visible in fluorescence picture; hCA1 loaded with ss-48-

mer-Cy3 did not show any unspecific band in fluorescence, while, in silver staining part, the protein did not evidently run through the gel, giving a smeared band at the top of the gel. The broad smeared band was related to the presence of glycosylated forms in the supplied hCA1 preparation.

Having a look at the fluorescence picture (Figure 6.19), the both two reaction samples displayed a band in line with ds-48-mer reference one, indicating that this was unreacted 48-mer hybridized to ss-48-mer-Cy3. Looking from top to bottom, in Reaction 10 1/2 was present another single bright band, which was much less bright in Reaction 5 1/2. These bands were mono conjugates, visible in silver staining too, below hCA1 bands.

Concluding, the native electrophoresis resolved mono conjugates from unreacted protein and unreacted 48-mer. Furthermore, Reaction 10 1/2, characterized by hCA1/S-HyNic 1:10 functionalization ratio (MRS 0.9) and hCA1/48-mer 2:1 conjugation ratio, gave mono conjugates, and with a higher yield than Reaction 5.

6.2.3.2.2 Electroelution

The elctroelution step followed the native electrophoresis, and was performed inserting the excised mono conjugate band into D-Tube™ Dialyzers Midi (Section 4.2.5.6).

The concentration of hCA1 in mono conjugate fraction was measured in Micro BCA assay (Section 4.2.5.3) and the content of bis-aryl hydrazone bond was detected at 354 nm in UV region. The eluate was checked in Tris-Gly 1x 12.5 % AA gel electrophoresis, in presence of SDS.

Table 6.2 presents the entire set of data, measuring also the absorbance at 260 nm for DNA quantification in NanoDrop ND-2000. This spectrophotometer has an absorbance detection limit of 0.002 at 1mm path, while for DNA the minimum concentration which can be read is equal to 2 ng/µl. The oligonucleotide c-ss-Amino-48-mer used for conjugation reaction has ε_{260} 458,010 $M^{-1}cm^{-1}$, equivalent to an OD260 of 32.4 ng/µl for 1 cm path, or 324 ng/µl for 1 mm path. Therefore the limit detection of the absorbance value at 1 mm path corresponds to 0.006. Eventually, all absorption measurements were valid; however the ratios calculated for DNA/hCA1 and hydrazone/hCA1 displayed an underestimation of DNA concentration in UV absorbance and a consistent 1 to 1 hCA1 to hydrazone proportion, indicating the presence of mono conjugates in the collected fractions.

Table 6.2 The fractions obtained in electroelution were characterized in Micro BCA for hCA1 concentration and in UV spectrophotometry for DNA and hydrozone bonds, at 260 and 354 nm, respectively. The ratios calculated for DNA/hCA1 and hydrazone/hCA1 showed an underestimation of DNA concentration and a consistent 1 to 1 hCA1 to hydrazone proportion, indicating the presence of mono conjugates in the collected fractions.

Fraction electroelution	[hCA1] (μM)⧫	A_{260} ✧	A_{354} ✧	[DNA] (μM)○	[hydrazone] (μM)♠	DNA/hCA1	hydrazone/hCA1
25.05.12	5.4	0.133	0.016	2.90	5.5	0.5	1.0
30.04.12	1.0	0.030	0.005	0.66	1.7	0.7	1.7
1_15.02.12	2.1	0.038	0.008	0.83	2.8	0.4	1.3
2_15.02.12	2.1	0.041	0.007	0.90	2.4	0.4	1.1
12.12.11	1.4	0.026	0.006	0.57	2.1	0.4	1.5
12.12.11	1.4	0.028	0.006	0.61	2.1	0.4	1.5
1_13.10.11	1.3	0.029	0.003	0.63	1.0	0.5	0.8
2_13.10.11	2.3	0.041	0.007	0.90	2.4	0.4	1.0

⧫ The value was determined in Micro BCA (Section 4.2.5.3);

✧ The absorbance values were measured in NanoDrop ND-2000 spectrophotometer, with 1 mm path;

○ ε_{260} 45,801 $M^{-1}mm^{-1}$; ♠ ε_{354} 2,900 $M^{-1}mm^{-1}$.

6.3 Discussion, part 1: optimized protocol of hCA1-DNA mono conjugate

The optimized steps for hCA1-DNA mono conjugate preparation are summarized in Figure 6.20, while in Chapter 4 the methods are fully listed.

In brief, the aldehydic functionalization of c-ss-Amino-48-mer by S-4FB was performed at 1:20 molar reaction ratio, followed by MSR detection. The protein hCA1 was functionalized by S-HyNic at 1:10 molar ratio, afterwards the protein concentration was determined in Micro BCA assay and the MSR was estimated. Next the two modified molecules were joined in hCA1/48-mer 2:1 ratio and the successful reaction was verified in SDS-PAGE Tris-Gly. Afterwards, the mono conjugates were resolved in native gel and purified from the excised gel band in electroelution. Finally, the eluate was displayed in SDS-PAGE Tris-Gly and the protein concentration in the mono conjugate fraction was determined in Micro BCA assay.

Figure 6.21 displays the typical checking steps in gel electrophoresis, during mono conjugate production, adding to loaded samples ss-48-mer-Cy3. Those were significant to follow each applied step. At first, the conjugation reaction was loaded on SDS-PAGE Tris-Gly; next there was the location of mono conjugate band in TBE native gel; finally the eluate was visualized on SDS-PAGE Tris-Gly, again in presence of SDS.

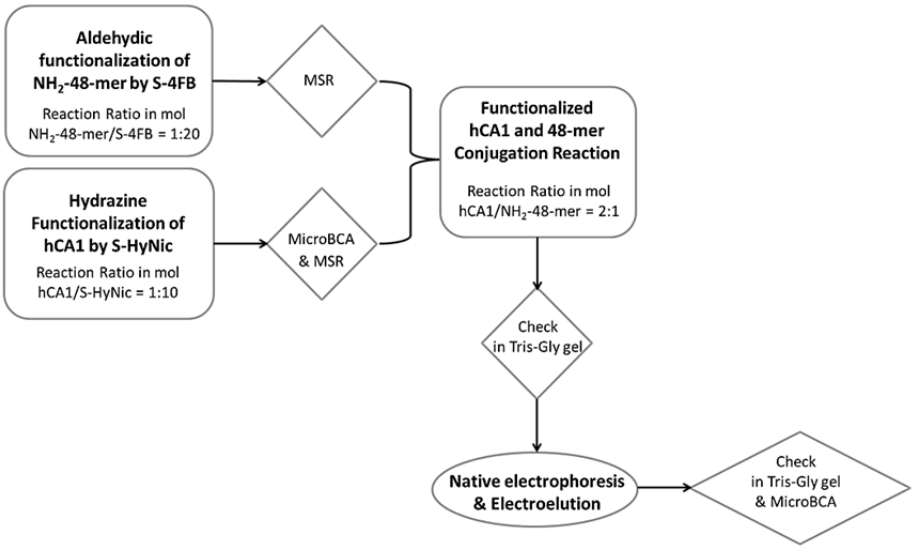

Figure 6.20 Flow chart of optimized procedure for hCA1-DNA mono conjugate production. In rounded rectangle frame the reaction steps, in oval the purification step and in diamond the checking points.

Remarkably, the behaviour of mono conjugates in native TBE gel differs from their behaviour in SDS-PAGE Tris-Gly. The mono conjugates purified in electroelution, from a single excised band displayed in SDS-PAGE multiple small bands, indicating that, upon the protein denaturation treatment, SDS conferred a significant negative charge to the protein affecting the run of protein-DNA conjugates. Oppositely, in native gel the oligo DNA drove the run through the gel being the protein slightly negatively charged.

Regarding the conjugation reaction, the left amount of unreacted DNA visible in the gel is significantly high even in presence of hCA1 excess. This reduced coupling yield is explained by the salinity of the Conjugation Buffer, NaCl 150 mM, and the applied room temperature, which stabilized secondary structures of ss-DNA. The computer simulations performed with the DINAMelt web server (Markham & Zuker, 2005) predict thermodynamically stable secondary structures, within ss-48-mer and as homodimer (Appendix, Section 14.1). These folding conformations limited the aldehydic modified 5' terminus of ss-DNA to encounter hCA1 by steric hindrance. One strategy to raise the coupling would be the simultaneous salt concentration decrease and temperature increase; however the protein folding would consequently be affected resulting in a possible denaturation.

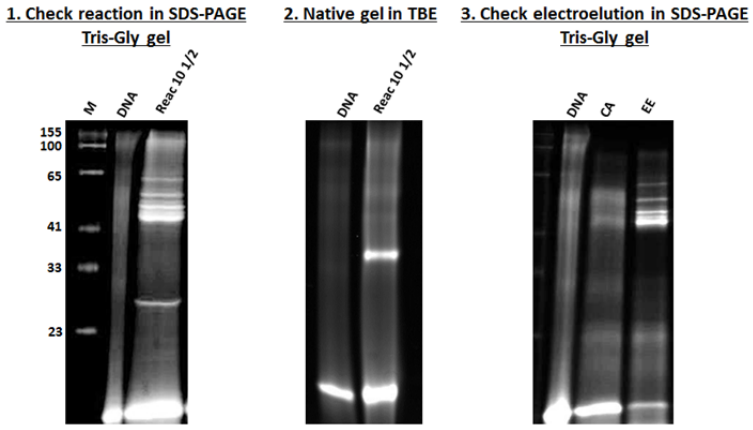

Figure 6.21 The checking points in gel electrophoresis for hCA1-DNA mono conjugate preparation. 1: control the outcome of conjugation reaction in SDS-PAGE Tris-Gly 1x. 2: verify the resolution of mono conjugates in native gel TBE 1x 12.5 %, before band excision. 3: confirm the electroelution (EE) in SDS-PAGE Tris-Gly 1x. In each gel, the detection of mono conjugates was performed by addition and hybridization of ss-48-mer-Cy3.

6.4 Results and discussion, part 2: hCA1-DNA conjugates on *switch*SENSE

The hCA1-DNA mono conjugate enabled a correct surface functionalization, demonstrated in LFM, VR and TRM measurement modes. In switching dynamics the hydrodynamic diameter of hCA1 was determined and finally small molecule detection was carried out loading Acetazolamide inhibitor on hCA1-DNA layers, to observe a variation in switching performance, upon the interaction of the inhibitor with the protein (Figure 6.22).

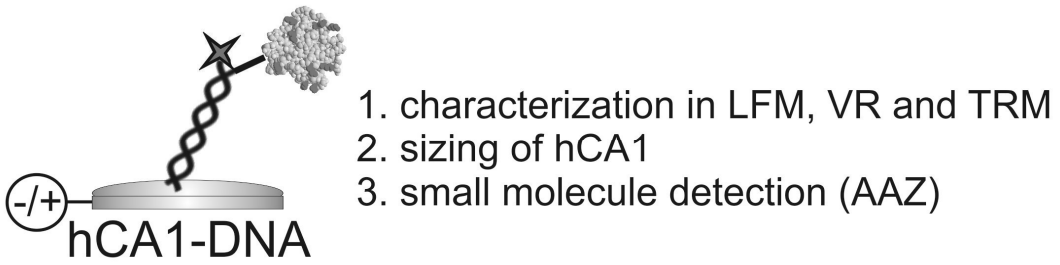

Figure 6.22 hCA1-DNA mono conjugates on *switch*SENSE. Upon hybridization, the conjugates were characterized in LFM, VR and TRM. Next the hydrodynamic diameter was evaluated in switching dynamics. Finally the small detection of Acetazolamide ihnibitor (AAZ) was tested on surface. PBD 1CRM of hCA1 crystallographic structure (Kannan et al, 1972) displayed in DeepView, VDW spacing, 18 target lysine residues in dark grey.

6.4.1 Hybridization kinetics of hCA1-DNA conjugates on surface

Due to different mechanical properties, ds-DNA layers switch more efficiently than ss-DNA layers. Thus, the switching amplitude, ΔF, is the response parameter to monitor hybridization events, since ΔF increases while the target molecule, c-ss-DNA, hybridizes to the probe, ss-DNA, tethered on gold surface. The hybridization event is considered complete once ΔF reaches plateau.

Maruyama characterized the hybridization kinetics of c-ss-DNA on switchable layers (Maruyama, 2008), observing that the target molecule c-ss-DNA supplied in abundance hybridized in reaction limited regime (Pascault & Zhou, 2008). The flow rate does not affect the hybridization kinetics, allowing the hybridization in stop-flow. Therefore the Langmuir adsorption isotherm was used to describe the characteristic reaction rate between DNA probes on surface and targets in solution c**.** The off-rate term of dehybridization was neglected, since this reaction is nonspontaneous and requires drastic changes (e.g. increased temperature, reduced salinity, the presence of enzymes). Hence the equation of surface occupancy velocity (Eq. 6.10) becomes:

Eq. 6.14 $$\frac{\partial \Gamma}{\partial t} = c \cdot k(\Gamma_{max} - \Gamma)$$

Solving Eq. 6.14, the bound fraction is

Eq. 6.15 $$\Gamma(t) = \Gamma_{max} \left\{1 - exp\left[-\left(t/\tau_{hybr}\right)\right]\right\} \rightarrow 1/\tau = c \cdot k$$

The initial ds-48-mer DNA layers (ss-SH-48-mer-Cy3 + c-ss-48-mer) were dehybridized with NaOH, then to detect the hybridization of either ss-hCA1-DNA multi conjugate fractions, or ss-hCA1-DNA mono conjugate fractions, or c-ss-48-mer.

The target solutions were diluted in Standard Buffer at a final DNA concentration of 200 nM. For hCA1-DNA multi conjugate, the DNA amount present in purified fractions was estimated by UV at 260 nm. While the DNA content in mono conjugate sample corresponded to hCA1 concentration determined by Micro BCA (Section 6.2.3.2.2). The channel was quickly covered with 100 µl target solution and the hybridization of target to ss-SH-48-mer-Cy3 probes occurred in stop flow at 25°C. The hybridization was monitored in real-time in LFM mode (-0.4/+0.3 V vs. Pt, LED 1 V). All electrodes in the same channel were electrically connected to electric power, even if not directly observed in real-time.

The ΔF was normalized considering 0 % the surface coverage before target injection at t = 0 s, and 100 % as the saturation level. The data were fitted in Origin 8.5 by Exponential Decay 1 ($y = y_0 + A \cdot e^{-x/\tau}$) getting τ (s), the time constant. The fits of hybridization curves of mono conjugate, multi conjugate and c-ss-48-mer are presented in Appendix, Section 14.2. The obtained averaged time constant τ and rate constant k were listed in Table 6.3 .

Table 6.3 Hybridization rate constant k of c-ss-48-mer, ss-hCA1-DNA multi conjugate, and ss-hCA1-DNA mono conjugate on surface. The time constant τ was averaged over fitted experiments and the rate constant k was calculated considering the target concentration equal to 200 nM. The SD is indicated in round brackets.

	Averaged τ [s]	Averaged Rate constant, k [10^5 $M^{-1}s^{-1}$]
c-ss-48-mer	26 (5)	2.0 (0.4)
multi hCA1-DNA	23 (5)	2.2 (0.5)
mono hCA1-DNA	250 (50)	0.21 (0.04)

On surface hCA1-DNA multi conjugates hybridized as fast as c-ss-48-mer (10^5 $M^{-1}s^{-1}$), the mono conjugates took 10 times longer (10^4 $M^{-1}s^{-1}$); this was evident from the comparison of the hybridization curve (Figure 6.23), where mono conjugate finished to hybridized after 25 min, while multi conjugate and c-ss-48-mer required a few minutes.

The off rate was not recorded as a dehybridization event was considered improbable; after exchanging to Standard Buffer the hybridized layers were all found to be stable during switching measurements.

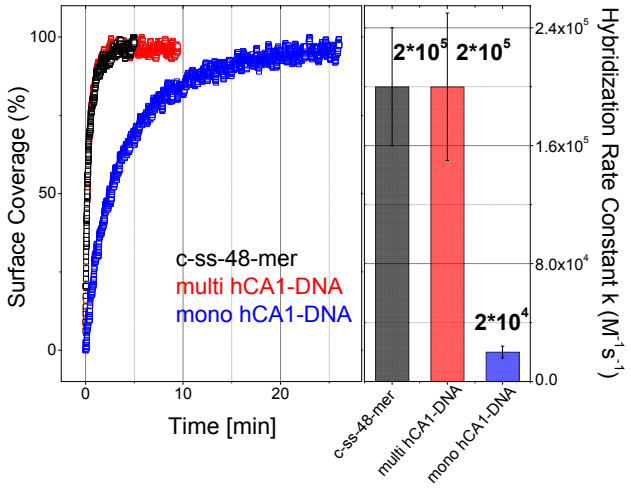

Figure 6.23 Observed hybridization kinetics of hCA1-DNA, mono and multi conjugates, and c-ss-48-mer loading 200 nM of DNA concentration. Left, comparison of hybridization curves of c-ss-48-mer (black), hCA1-DNA multi conjugates (red) and hCA1-DNA mono conjugate (blue) (ID: C90FGW50_c48_09_01; C53FGW33_10_07; C65FGW33_10_04). Right, measured hybridization rate constant *k* for c-ss-48-mer, multi and mono conjugates (black, red and blue, respectively), plotted with the corresponding standard deviation (SD). While hCA1-DNA multi conjugates hybridized on surface as fast as c-ss-48-mer (10^5 $M^{-1}s^{-1}$), the mono conjugates took 10 times longer (10^4 $M^{-1}s^{-1}$).

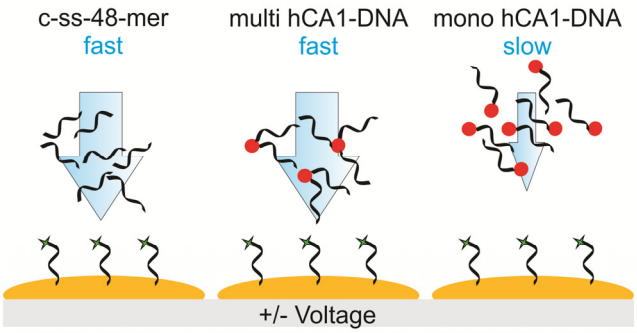

Figure 6.24 A schematic depicting of the hybridization for hCA1-DNA, mono and multi conjugates, and c-ss-48-mer on surface. Loading on surface the same concentration of DNA molecules, multi conjugates hybridized 10 times faster than mono conjugates, probably due to different orientations, which made then higher the probability to contact a complement DNA strand on surface. On the other hand, mono conjugates had a single oligonucleotide bound on hCA1, having less chance to encounter the probes on surface.

As for multi conjugate experiments and all subsequent comparisons, the fraction F1.1 was loaded onto the surface, which was purified in SEC and AEX columns in FPLC (Figure 6.13); this fraction was evidently enriched with high molecular weight

conjugates, meaning that around 2-3 DNA oligo could be covalently bound to one hCA1 protein. This could explain why loading on surface the same concentration of DNA molecules, multi conjugates hybridized faster than mono conjugates. Multi conjugates had indeed a reduced amount of hCA1 for the same number of oligonucleotides; in that way even if the hydrodynamic friction was increased, one single "multi conjugate" could bind quicker to the probes present on surface, based on different orientations. These orientations made then higher the probability to contact a complement DNA strand on surface. As resulted, the hybridization of multi conjugate was reaction limited like for c-ss-48-mer (Figure 6.24).

However the mono conjugates presented one single oligonucleotide per hCA1, having less chance to encounter the probes on surface (Figure 6.24).

6.4.2 Voltage Response of hybridized hCA1-DNA

The VR was measured for newly hybridized ds-DNA layers, with hCA1-DNA multi and mono conjugate and c-ss-48-mer. The applied bias potential was -0.5/+0.5 V vs. Pt, sweep rate of 0.02 V/s, the fluorescence was recorded at LED power of 5 V. These VR curves were then compared to reference measurements (VR of initial ds-DNA layers).

As previously mentioned in Section 5.3.1.4, VR is an important reference measurement, since based on the inflection point (Ip) of the curve, the switching potential window is corrected to be next used in TRM. Furthermore VR curves were used to observe variation in standing (F_{st}) and lying (F_{ly}) fluorescence level plateaus (Figure 6.25) and shifts of switching potential window (Figure 6.26).

After hybridization F_{ly} and F_{st} were compared to fluorescence of initial ds-DNA layer. For both Fly and Fst the fluorescence reduction was calculated (Table 6.4) as:

Eq. 6.16 $$\boldsymbol{F\ reduction = F_{final}/F_{initial} \cdot 100}$$

F_{ly} did not significantly change with respect to the initial ds-DNA layer for all re-hybridized layer, in fact F_{ly} reduction was between 2-7%, explained by a typical variation of focus point of the camera on the measured electrode.

Considering F_{st}, this level was significantly reduced in presence of hybridized hCA1-DNA conjugates (approximately 20 % of signal reduction); on the contrary re-hybridized c-ss-48-mer layers resulted in the initial florescence intensity (Figure 6.25).

This evaluation confirmed the quenching of Cy3 dye adjacent to hCA1, observed on surface. In fact energy transfer from excited dye to the aromatic amino acids of the protein can occur, when the two species are in close proximity (Steinber.Iz, 1971), e.g. in (Gruber et al, 2000) the authors showed an anomalous enhancement of Cy3

fluorescence and anomalous quenching of Cy5 fluorescence during antibody labeling, and they assumed that for Cy3, it could couple with lysine residues of the protein.

Table 6.4 Observed variations in Voltage Response for newly hybridized ds-DNA layers, with c-ss-48-mer, hCA1-DNA multi and mono conjugates, compared to initial ds-DNA layers. The percentage reduction of F_{ly} and F_{st} levels was calculated based on Eq. 6.16. The initial and final potentials at normalized fluorescence 0.5 were considered and the potential shift was calculated subtracting the initial potential to the final (average over 18 electrodes). The SD values are indicated in round brackets.

	F_{st} reduction %	F_{ly} reduction %	Potential shift [V]
c-ss-48-mer	0 (6)	2 (4)	+0.03 (0.03)
multi hCA1-DNA	21 (2)	3 (2)	-0.08 (0.02)
mono hCA1-DNA	22 (4)	7 (9)	-0.08 (0.02)

Measurements in liquid phase were not performed as a control, nevertheless on *switch*SENSE a quenching effect of Cy3 was already detected by binding of IgG anti-biotin and IgG anti-digoxigenin on ds-DNA layers presenting the corresponding antigen (Hampel, 2009), and an enhancement effect of Cy 3 fluorescence was observed in presence of bound Fab fragment anti-digoxigenin (Hampel, 2009) and with DHFR enzyme bound on ds-DNA layers functionalized with methotrexate inhibitor (Langer Andreas, PhD data). Overall this effect on fluorescence intensity by an adjacent protein remains complex to predict, since many factors are involved, such as the distance between them, or the surface charge of the protein adjacent to the dye which might affect the dye orientation, or the presence of coenzymes in the protein like NADH (Steinber.Iz, 1971).

Moreover, another interesting effect was seen in VR curves in presence of hybridized hCA1-DNA. At 0.5 normalized fluorescence the corresponding potential was considerably shifted to more negative value, approximately -0.08 V, in comparison to the initial ds-48-mer response, however in re-hybridized c-ss-48-mer layers no significant shift was detected (Table 6.4, Figure 6.26). This indicates that the potential conformation transition (pct), which corresponds to the potential value where the DNA conformation on surface flips from an extended to a compact state, shifted in presence of hCA1. This observation is explained by an additive negative charge to the ds-DNA system coming from hCA1. In VR mode, at the beginning a voltage of -0.5 V was applied, here ds-DNA and hCA1-DNA layers were equally repelled from the surface. Then at -0.16 V hCA1-DNA started to come closer to the surface, attracted by voltage (Figure 6.27).

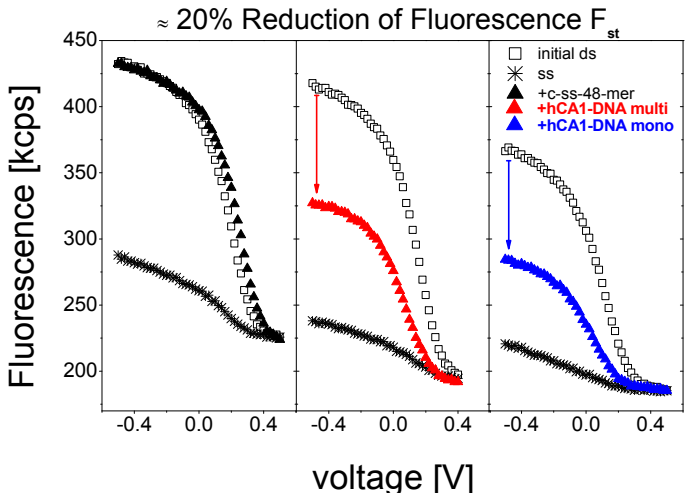

Figure 6.25 Voltage Response results of hybridized hCA1-DNA, mono and multi conjugates, and c-48-mer. Bias potential was applied to the Au electrode vs. Pt, -0.5/+0.5 sweep rate of 0.02V/s and fluorescence counts were recorded, at LED power of 5 V. The obtained voltage response was compared to initial ds-48-mer (white symbol) and dehybridized ss-48-mer (star symbol). After hybridization of mono (blue symbol) and multi conjugate (red symbol) fractions, the fluorescence F_{st} was significantly reduced, around 20%. To notice, hybridization of c-48-mer (black symbol) gave back the same initial florescence intensity. The presence on surface of hCA1 gave a quenching effect on Cy3 dyes (+c-48-mer ID:C65FGW33_06_01/ C65FGW33_06_03/ C65FGW33_06_05; +CA-oligo multi ID: C54FGW33_06_01/ C54FGW33_06_03/ C54FGW33_06_05; +CA-oligo mono ID: C64FGW33_12_01/ C64FGW33_12_03/ C64FGW33_12_05).

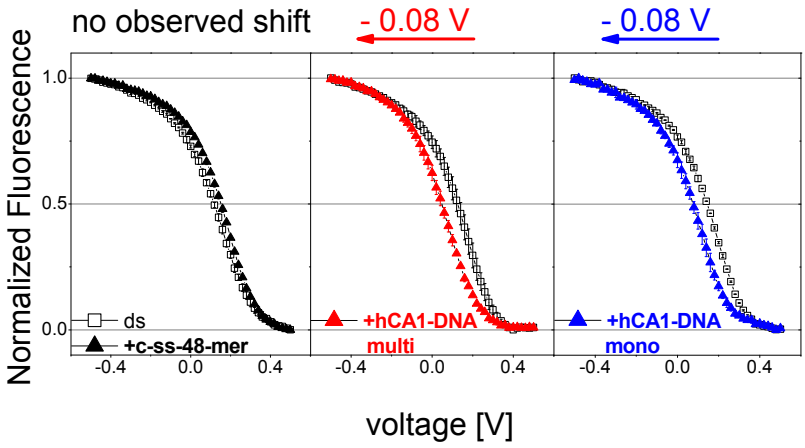

Figure 6.26 Potential shift observed in Voltage Response measurements, after hybridizing hCA1-DNA mono and multi conjugates. The fluorescence was recorded in VR mode for initial ds-DNA layer (open square) and for newly hybridized layers with c-ss-48-mer, or hCA1-DNA multi conjugate, or mono conjugate (black, blue and red triangle, respectively); the normalized F was averaged over 3 electrode data set, from the same channel, and plotted with error bars. Hybridized hCA1-DNA layers, with multi and mono conjugates, gave a significant shift in voltage response, to more negative potentials, -0.08 V, compared to the initial ds-48-mer response. Whereas hybridized c-ss-48-mer layers gave a little positive shift, +0.03 V. The initial and final potentials at 0.5 normalized fluorescence were considered and the potential shift was calculated subtracting the initial potential

to the final (+c-48-mer ID: C65FGW33_area04; +CA-oligo multi ID: C54FGW33_area02; +CA-oligo mono ID: C64FGW33_area04).

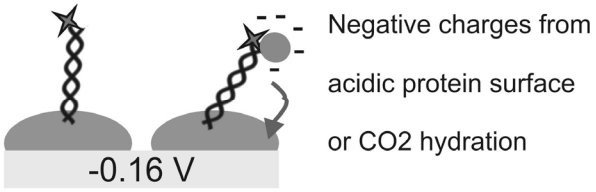

Figure 6.27 The potential shift observed in Voltage Response measurements on hCA1-DNA layers was explained by an additive negative charge to the ds-DNA system in presence of hCA1. In VR mode, the initial applied voltage was -0.5 V, here ds-DNA and hCA1-DNA layers were equally repelled from the surface. Then at about-0.16 V hCA1-DNA started to come closer to the surface. This shift of the attractive potential could be due to an enrichment of negative charges around hCA1, coming from the acidic character of the protein or from CO_2 hydration.

This shift of the attractive potential was due to an enrichment of negative charges around hCA1; those charges may rise from CO_2 hydration or from the acidic character of the protein.

The hydration of carbon dioxide is highly catalysed by hCA1, which presents a k_{cat} equal to 10^5 reactions per second (Lehtonen et al, 2004). The high amount of HCO_3^- resulting from the catalysis could affect the surrounding of hCA1-DNA layer and shift the potential in VR measurements; even in presence of Standard Buffer. This hypothesis was hard to prove, since the impossibility of the complete removal of CO_2 present in buffers and in the air surrounding the sample. However the presence of Acetazolamide inhibitor on hCA1-DNA kept the shift to negative potential in VR measurements (the experiment is described in Section 6.4.5), so either the inhibition of hCA1 was not observed on surface or either the CO_2 hydration was not correlated with the observed shift.

Considering the negative charges originating from the acidic character of the protein, unfolded hCA1 has a predicted net charge of -0.7 V at pH 7.3[2]. Furthermore, the supplied hCA1 extracted from erythrocytes presented approximately 7% of glycosylated form population (Figure 6.9) and the glycosylation decreases the pI value, due to addition of sugar moieties on protein surface as a post-translational modification (Furukawa & Kobata, 1992; Kondo et al, 1987). The observed shift of the pct eventually resulted from the acidic character of the protein hCA1.

[2] http://www.scripps.edu/~cdputnam/protcalc.html
UniProt #P00915.

6.4.3 Time Resolved Measurement of hybridized hCA1-DNA

The TRM was taken for newly hybridized ds-DNA layers, with hCA1-DNA multi and mono conjugates and c-ss-48-mer. The applied bias potential was chosen based on the inflection point (Ip) of VR curve, calculated by the second derivative. The attractive potential was set as Ip voltage plus 0.2 V, whereas the repulsive potential was defined as the attractive potential menus 0.8 V. The change of fluorescence (F) coming from applied switching amplitude, at high frequency 10 kHz, was recorded over time, with LED power of 5 V. The normalization of raw data counts was done on the levels of the upper and lower signal plateau, set respectively as 1 and zero values. The smoothing of normalized fluorescence was obtained by Fast Fourier Transform (FFT) filter, and the first derivative was calculated on smoothed normalized data. These TRM normalized curves were then compared to reference measurements (TRM of initial ds-DNA layers). Each plotted curve was averaged over 3 electrode signals belonging to the same flow channel.

As stated in Section 5.3.1.5, from TRM the dynamics of switching ds-DNA could be analysed, by the first derivatives of rising and falling curves. The derivatives gave the maximum velocities of rising and falling motions.

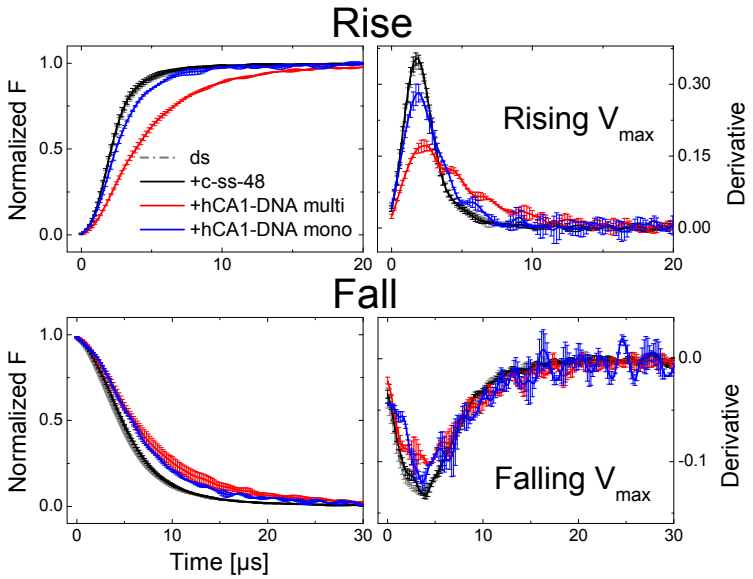

Figure 6.28 Time Resolved Measurements of hybridized hCA1-DNA mono and multi conjugates, and c-ss--48-mer. A switching potential amplitude of 0.6 V was applied at high frequency 10 kHz with LED power 5 V. The recorded fluorescence by time was normalized and smoothed; the first derivatives were calculated on smoothed data. Here TRM curves of c-ss-48-mer (black line), hCA1-DNA multi (red line) and mono conjugate (blue line) were compared to initial ds-DNA signal (black dashed line). The normalized smoothed curves and derivatives were averaged on electrode signal belonging to the same flow channel, and the corresponding SD was plotted (ds ID:

C54FGW33_area04; +c-48-mer ID: C54FGW33_area01; +CA-oligo multi ID: C54FGW33_area04; +CA-oligo mono ID: C63FGW33_area03).

Figure 6.28 shows the TRM comparison among ds-DNA layers hybridized with hCA1-DNA multi and mono conjugates and c-ss-48-mer. Those measurements were taken at switching amplitude of applied voltage of 0.6 V, instead of 0.8 V, simply because initially this was the chosen amplitude for TRM. Looking at the rising motion, the normalized fluorescence signal of hybridized hCA1-DNA multi conjugates took till 20 µs to reach the plateau, much longer compare to mono conjugate (7.5 µs). The fall profiles were instead similar for mono and multi conjugates, completed around 30 µs. The re-hybridized c-ss-48-mer gave back the signals of initial ds-DNA layers, reaching a standing position at already 5 µs and a lying position at 15 µs. The derivatives reflected the same observations, and they were further analysed calculating maximum velocity percentages (V_{max} %), the percentage ratio of re-hybridized layer and initial ds-DNA layer maximum velocities, for rising and falling movements. Those V_{max} percentages were plotted in Figure 6.29. The ratios show that multi conjugates slowed down the dynamics, resulting in 58 % of the initial rising velocity and 74 % of falling velocity. In comparison, the mono conjugate displayed faster dynamics, characterized by 75 % and 84 % of rising and falling speed compared to initial ds-DNA layers.

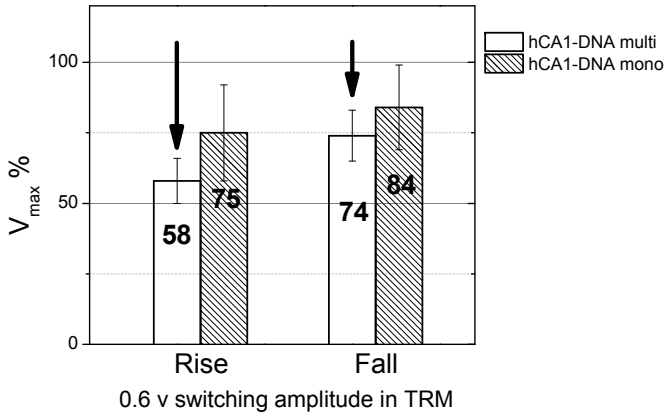

Figure 6.29 Maximum velocity percentage for rising and falling motions of hybridized layers with hCA1-DNA multi and mono conjugates. V_{max} % corresponded to the percentage ratio of re-hybridized layer and initial ds-DNA layer maximum velocities and it was calculated for rising and falling movements, here plotted with corresponding SD.

On the *switch*SENSE the multi conjugate state of hCA1-DNA present in fraction F1.1 was confirmed. They possess slower switching dynamics compared to mono conjugates, purified in electroelution. One possible explanation is that these observations are due to

increased hydrodynamic friction caused by the presence of not hybridized oligonucleotides. Those were covalently attached to hCA1 and they could assume random conformations around hCA1 (Figure 6.30 A). A second hypothesis is a limited dynamics due to inter-linking on surface, e.g. a multi conjugate hybridized on multiple ss-48-mer (Figure 6.30 B). However, according to data analysis of antibody binding in Chapter 7 (Section 7.2.5.4), the first theory looks being the most probable, since no enhancement of fluorescence intensity in lying state F_{ly} was observed upon multi conjugate hybridization, but only a reduction of F_{st}.

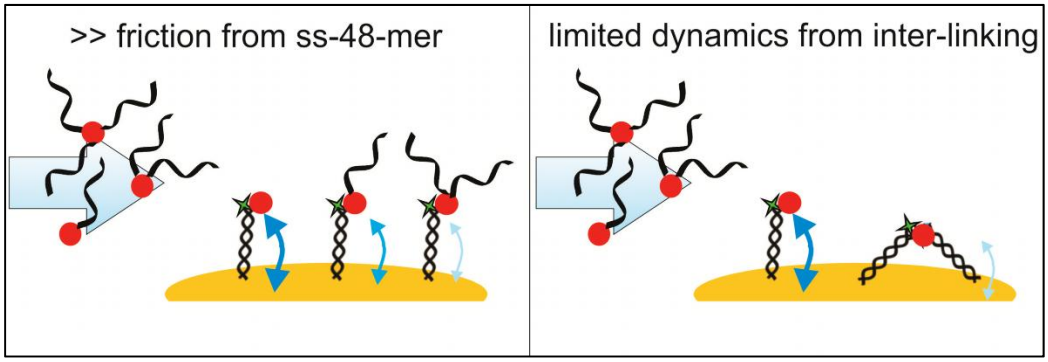

Figure 6.30 The slowest dynamics observed for hCA1-DNA multi conjugate layers could be explained by two effects: the first (left panel) an increased hydrodynamic friction caused by the presence of not hybridized oligonucleotides, which being covalently attached to hCA1 can assume random conformations around hCA1; second (right panel) a limited dynamics resulted upon inter-linking, e.g. one hCA1-DNA hybridized on two ss-DNA.

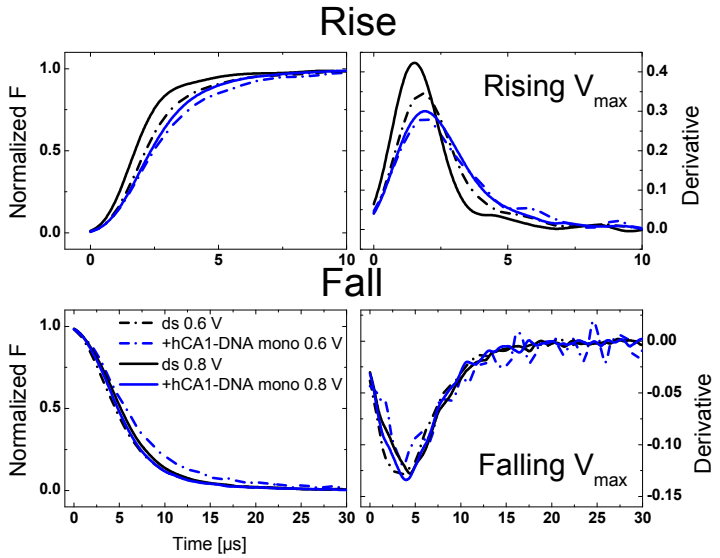

Figure 6.31 Comparison of Time Resolved Measurements for hCA1-DNA mono conjugate layer at 0.6 V and 0.8 V switching amplitude of applied potential. The normalized fluorescence was recorded in TRM applying a switching amplitude of 0.6 V (dash lines) and of 0.8 V (solid lines) on initial ds-DNA layer (black lines) and on re-hybridized layer with hCA1-DNA mono conjugate (blue lines).

In the following section the "Lollipop model" is presented and it will be used to estimate the hydrodynamic diameter of hCA1 based on dynamic data of hCA1-DNA mono conjugate layers. In order to get good fits with this model, in TRM the switching voltage amplitude had to be 0.8 V. In fact broader amplitude allowed a complete repulsion and attraction of ds-DNA, even in presence of bound proteins, improving the resolution of used model. Figure 6.31 presents the comparison of TRM curves taken at switching amplitude of 0.6 V, and at 0.8 V, for initial ds-DNA and hCA1-DNA conjugate layers. At 0.8 V amplitude, both initial ds-DNA and mono conjugates displayed faster dynamics, due to the applied potential, which were more attractive and repulsive. Figure 6.32 illustrates the maximum velocity % of hCA1-DNA mono conjugates related to initial ds-DNA, at 0.6 and 0.8 V applied amplitude. While the ratio remained similar in rising motion (75 % and 78% at respectively 0.6 and 0.8 V), the most evident effect was that at 0.8 V amplitude the mono conjugate could fall almost quickly as ds-DNA layer (V_{max} % = 94).

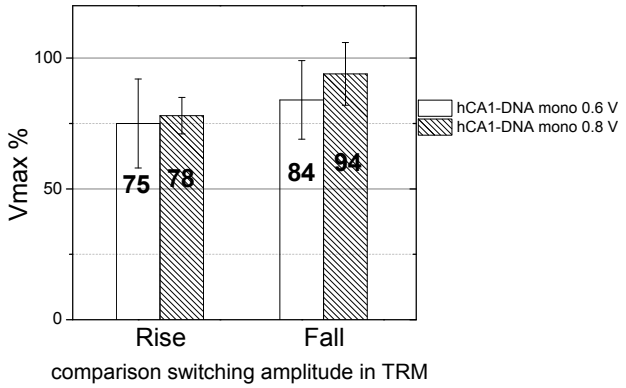

Figure 6.32 V_{max} % for hCA1-DNA layers at switching amplitude of 0.6 V and 0.8 V, for rising and falling motions (n=18 for mono conjugate at 0.6 V amplitude; n=27 for mono conjugate at 0.8 V amplitude).

As supporting information, Table 6.5 displays the absolute fluorescence, F_{ly} and F_{st}, and ΔF_{rel} of initial ds-DNA layers used in the previous analysis. The values were taken in LFM (-0.4/+0.3 V vs. Pt, LED 1 V) in Standard Buffer after electrical desorption, and they were averaged over 18 (for multi and mono conjugates at 0.6 V amplitude) and 27 (for mono conjugate at 0.8 V amplitude) independent electrode signals. Throughout all experiments, the initial ds-DNA density could be considered constant and comparable. Furthermore in Table 6.6, Rising V_{max} data were listed for of initial ds-DNA and hybridized hCA1-DNA layer. Finally, Figure 6.33 shows two consecutive injections of hCA1-DNA mono conjugate with no Standard Buffer flowed in between in LFM and TRM, proving the reached saturation level of hCA1-DNA hybridized on surface.

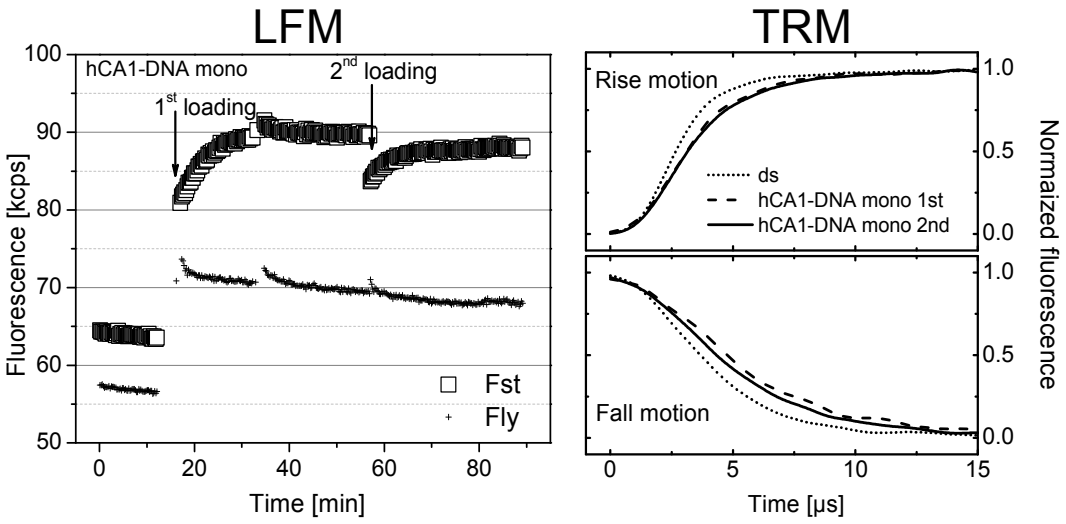

Figure 6.33 Two consecutive injections of hCA1-DNA mono conjugate, no Standard Buffer was flowed in between. The fluorescence levels Fly and Fst in Low Frequency Measurements and Time Resolved Measurements, in rise and fall motions, confirmed a saturation of the layer already after the first injection (Time Resolved Measurement: hCA1-DNA 1st injection (dashed lines), hCA1-DNA 2nd injection (solid lines), compared to ds-DNA (dotted lines)). (ID: C63FGW33_area04).

Table 6.5 The absolute fluorescence, F_{ly} and F_{st}, and ΔF_{rel} of initial ds-DNA layers, measured in Low Frequency Measurements. The Time Resolved Measurements were supported by these data, which indicates that through all experiments, the initial ds-DNA density could be considered constant and comparable. The values were averaged over ∝ 18 and ⊗ 27 independent experiments; the SD values are indicated in round brackets.

Initial ds-DNA layer			
	F_{ly} [kcps]	F_{st} [kcps]	ΔF_{rel} %
"Multi conjugate 0.6 V" meas∝	66 (7)	137 (31)	50 (10)
"Mono conjugate 0.6 V" meas∝	63 (6)	108 (11)	42 (4)
"Mono conjugate 0.8 V" meas⊗	71 (9)	144 (30)	49 (7)

Table 6.6 Rising V_{max} data of initial ds-DNA and hybridized hCA1-DNA layers, measured in Time Resolved Measurements. The value was averaged over ∝ 18 and ⊗ 27 independent experiments. The SD values are indicated in round brackets.

Rising V_{max} [AU]		
	Initial ds-DNA	hybridized hCA1-DNA
"Multi conjugate 0.6 V" meas∝	0.35 (0.03)	0.21 (0.02)
"Mono conjugate 0.6 V" meas∝	0.33 (0.05)	0.25 (0.04)
"Mono conjugate 0.8 V" meas⊗	0.38 (0.03)	0.30 (0.02)

6.4.4 Sizing of hCA1

The functionalized *switch*SENSE surface with hCA1-DNA mono conjugate could be used for further investigations. One big feature of this technology is that through dynamic analysis of DNA switching, the increased hydrodynamic friction due to the presence of a bound protein can be detected. Andreas Langer and Wolfgang Kaiser developed a model, so called the "Lollipop Model" (Langer et al, Paper in progress A) in order to evaluate the hydrodynamic diameter D_h from switching dynamics data.

Some traditional methods are usually employed in protein size analysis, such as sedimentation velocity analysis in analytical ultracentrifugation (SV-AUC)(Brown & Schuck, 2006; Gokarn et al, 2012), gel filtration chromatography (Kunji et al, 2008; Le Maire et al, 2008) and Dynamic Light Scattering, DLS (Faggiano et al, 2010; Gast & Fiedler, 2012; Xia et al, 1994). In order to cross-check the evaluation of D_h of hCA1 by the Lollipop model based on *switch*SENSE dynamics, hCA1 D_h was measured first in DLS.

6.4.4.1 Hydrodynamic diameter of hCA1 in Dynamic Light Scattering

The D_h of hCA1 was measured in DLS, by Nano ZS (ZEN3600, Malvern Instruments Ltd.). DLS (also known as PCS - Photon Correlation Spectroscopy) measures Brownian motion and relates it to the size of the particles. The particles are illuminated by a laser and the intensity fluctuations in the scattered light are measured. The particles suspended in a liquid are continually moving due to Brownian motion, and small particles move more quickly than large particles. The relation between particle size and its diffusion due to Brownian motion is described in the Stokes-Einstein equation (Eq. 6.17):

Eq. 6.17
$$D = \frac{k_b T}{6\pi\eta r}$$

where D is the diffusion constant, k_b is Boltzmann's constant, T is the absolute temperature, η is viscosity and r is the radius of the spherical particle.

As the particles diffuse, the intensity of the scattered light appears to fluctuate, and over time the correlation (similarity) of intensity signal will decrease.

The instrument displays the correlation function of variation of scattered light intensity by time, and from this it extracts the decay rates for a number of size classes to produce a size distribution of particles.

For the analysis, hCA1 was dissolved in Standard Buffer and filtered with 0.22 µm porosity membrane, final concentration 0.9 mg/ml, then 750 µl volume was inserted in the appropriate quartz cuvette. Figure 6.34 shows the DLS results and the determined protein D_h after fitting the correlation data by distribution fit function. This multi-exponential decay function assumes that there are several classes of particles, in this

case three classes, which give different decay of correlated intensity signal. This was due to the presence of dust particles in the cuvette.

Finally D_h was obtained from fitted data by number weighted size method, using for 100-size classes. This method is based on the fact that large particles scatter much more light than small particles (light intensity $I \propto d^6$), that is why it is important to weight the intensity over diameter size. The D_h of hCA1 was 5.8 ± 0.7 nm.

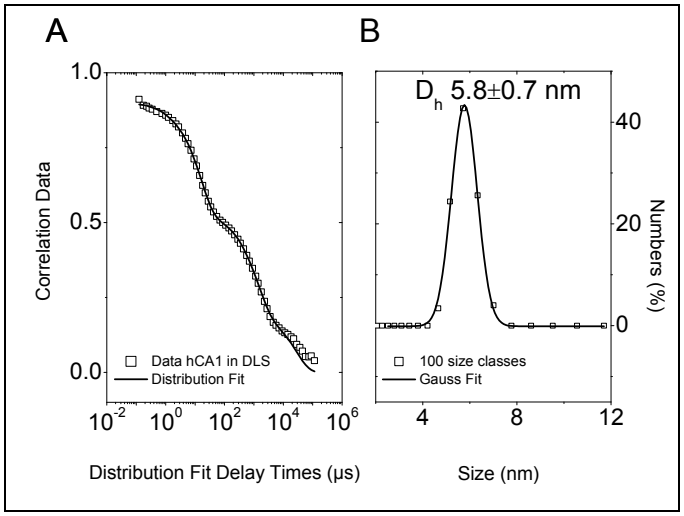

Figure 6.34 hCA1 D_h measured in DLS. A: correlogram of scattered light intensity over time in black squares, and distribution fit applied on raw data in red. B: number weighted size analysis of fitted intensity gave a D_h of 5.8 ± 0.7 nm.

6.4.4.2 Hydrodynamic diameter of hCA1 on switchSENSE

The switching dynamics data (TRM) of hCA1-DNA layer were fitted by the "Lollipop Model" (Langer et al, Paper in progress A) in order to evaluate the D_h

Briefly, the model considers ds-DNA as a charged tethered nanorod, whose orientation on the surface depends on the applied electric potential. On application of a potential change, the nanorod is forced to rotate into a new angular conformation, characterized by the rotational diffusion coefficient D_r of the DNA. If a globular protein is bound at the extremity of ds-DNA; the final D_r changes due to an increased friction of the system, which doesn't have any more a simple rod shape, but a "lollipop" shape. Finally, the fitted values of D_r are translated into a hydrodynamic diameter.

In more detail, the model uses continuum electrostatic Poisson-Boltzmann models and the Fokker-Plank equation (FPE) to calculate the steady state as well as the dynamic behaviour of the nanorods in DC and AC electric fields. The known energy transfer function between the fluorescence dye at the DNA distal-end and the gold surface is applied to convert the obtained solutions of the FPE into fluorescence intensity. Crucial for the solution is the magnitude of electrical screening, which can be described by the

Debye-length of the electrode covering electrolyte solution. It is calculated from the relative permittivity of water, the vacuum permittivity, the Boltzmann constant, the Avogadro constant and the elementary charge. Other experimental parameters are the absolute temperature, the buffer and salinity concentration and the salt and buffer valencies. For measurements in Standard Buffer at 25°C, the inverse Debye-length is equal to 0.8 nm^{-1}. The D_r for bare ds-DNA is calculated according to (Tirado et al, 1984). It is important to understand that D_r essentially depends on the solution viscosity and the length of used ds-DNA. For bare 48-mer ds-DNA the D_r is 0.49 μs^{-1}. The finite charging process of the electrode is modelled by a surface charging time τ, an initial effective positive potential Φ_0 and the applied potential amplitude ΔΦ.

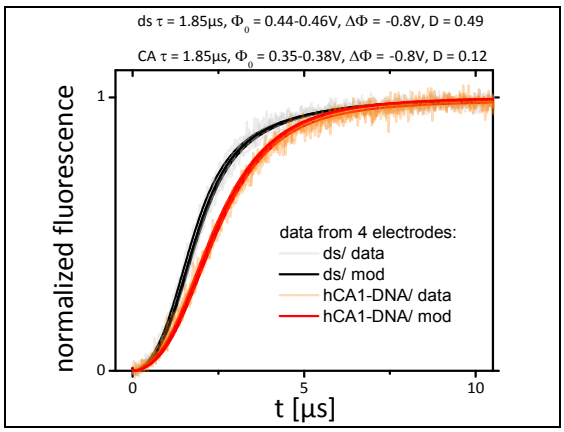

Figure 6.35 Fit of switching dynamics data with the Lollipop Model. Data of hCA1-DNA layers (in orange), obtained from four independent experiments, were fitted (in red), as well as data correspondent to the initial ds-DNA layer (in grey raw data, in black fitted data). The set parameters were: charging time constant τ (1.85 µs), initial applied positive potential Φ_0 (ranged between 0.44-0.46 V for initial ds-DNA, and 0.35-0.38 for hCA1-DNA), applied potential amplitude ΔΦ (-0.8 V), rotational diffusion coefficient D_r 0.49 for initial ds-DNA and 0.12 for hCA1-DNA. (ID: C73FGW45_area02_EL04; C86FGW50_area03_EL09; C87FGW50_area01_EL02; C87FGW50_area01_EL03).

Figure 6.35 presents the fit of Lollipop Model on switching dynamics data in rising motion from four independent experiments on Prototype2, considering the data of hCA1-DNA layers and of the corresponding initial ds-DNA layer. The set parameters were: τ 1.85 µs, Φ_0 ranged over four experiments between 0.44-0.46 V for initial ds-DNA and 0.35-0.38 for hCA1-DNA, ΔΦ -0.8 V, D_r 0.49 μs^{-1} for ds-DNA and 0.12 μs^{-1} for hCA1-DNA. One more parameter was considered for hCA1-DNA, the linker length between the protein and DNA of 2.5 nm. This was calculated following the table of length of covalent bonds in (Whitten, 2009). Finally the presence of hCA1 on ds-DNA gave a reduced D_r of 0.12 μs^{-1}, corresponding to D_h of 6.2(±0.3) nm.

The latest version of the Lollipop model considers the steric effects present on surface on a protein-DNA assembly at applied attractive potential, whereby the DNA molecule covalently attached to a large protein cannot lie down completely on the gold surface. Therefore a new calculated D_h of hCA1 of 5.8(±0.3) nm was obtained (Langer et al, Paper in progress B).

6.4.5 Acetazolamide influence on hCA1 functionalized layers

The analysis of small molecule detection was carried out on hCA1-DNA layers, loading Acetazolamide inhibitor (AAZ). The purpose was to detect the influence on hCA1-DNA switching in presence of bound AAZ, deriving from variations in folding or charges of hCA1/AAZ complex.

AAZ was previously dissolved in DMSO, and then the dilutions were prepared in Inhibition Buffer from 0.1 to 300 nM, keeping the DMSO concentration constant at 0.1% v/v. Generally activity and inhibition tests for CA-enzymes are performed in basic pH (Khalifah, 1971; Maren et al, 1960; Wilbur & Anderson, 1948), therefore the Inhibition Buffer had pH 8.1. The AAZ was loaded on hCA1 functionalized surface and bare DNA negative control at 1ml/min for 20 min at 25°C, afterward the measurements were taken at 0.1 ml/min.

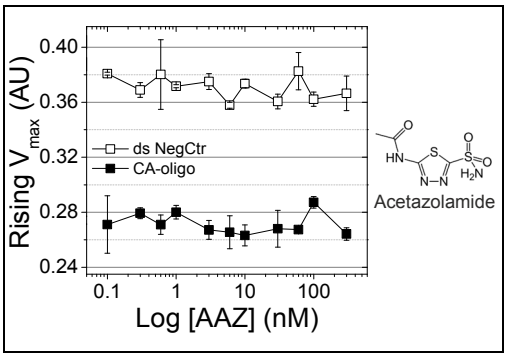

Figure 6.36 Results of binding detection of AAZ on hCA1 *switch*SENSE layer. Rising V_{max} of hCA1/DNA layer (black square) was plotted versus logarithmic concentration of AAZ; this was compared to the response of negative control layer (open square), treated in the same manner. Rising V_{max} was averaged over two electrode signals. No influence on switching was observed. Measurement data file: C69FGW45_Area02_03.

Figure 6.36 displays the comparison between obtained Rising V_{max} of hCA1/DNA layer and negative control layer, as function of logarithmic concentration of AAZ; the velocity was averaged over two electrode signals.

Finally, no significant change in switching behaviour was observed until 300 nM. In a second experiment AAZ 3 µM was injected, but again the signal remained indistinguishable, a feature that was confirmed by VR measurements.

6.5 Conclusion

The mono conjugate of hCA1 and DNA were successfully prepared optimizing Solulink™ chemistry on hCA1 protein and amino-terminated oligonucleotide. The preparation focused in mono conjugate preparation with no rest of unreacted oligonucleotide in the sample. This issue was solved purifying the reaction sample in electroelution upon a separation of mono conjugates in native gel.

The correct functionalization of *switch*SENSE surface with hCA1-DNA mono conjugates was detected in LFM, VR and TRM measurements.

In LFM the mono conjugate showed a slow hybridization rate, 10^4 $M^{-1}s^{-1}$ at 25°C in Standard Buffer loading 200 nM, in stop-flow. This rate was 10 times lower compared to the hybridization of c-ss-48-mer 200 nM, probably caused by a slower diffusion of oligonucleotides covalently bound to a larger globular protein.

The presence of hCA1 was displayed by a reduction of the standing fluorescence intensity. Moreover, hybridized hCA1-DNA presented a shift to more negative potential (-0.08 V). This shift resulted from an enrichment of negative charges around hCA1 protein and two hypotheses were considered: first the CO_2 hydration catalysed by hCA1, which could lead to a localized enhancement of bicarbonate anions; second, the acidic surface of hCA1.

The TRM measurements could discriminate hCA1-DNA multi conjugate from mono conjugate, due to the different dynamics in switching. The hybridized multi conjugates showed a velocity in rising motion of just 58 %, compare to ds-DNA layer, while mono conjugate had higher velocity, 75 %. The observed higher hydrodynamic friction of multi conjugate respect mono conjugate could be caused by the presence of not hybridized oligonucleotides, which being covalently attached to hCA1, could assume random conformations around hCA1.

The dynamic data of hCA1-DNA mono conjugate layers allowed an determination of the hydrodynamic diameter of hCA1. The Lollipop model in fact could fit a D_h of 6.2(±0.3) nm, which was in agreement with D_h measured in DLS of 5.8 ± 0.7 nm. However the latest version of the Lollipop model, which takes in account steric effects of protein-DNA conjugates on surface, calculated a new D_h for hCA1 of 5.8(±0.3) nm.

Acetazolamide inhibitor loaded on hCA1-DNA layer gave no significant change in switching dynamics till 3 µM injected amount. One explanation could be that the inhibitor entering in the binding site of hCA1 doesn't cause any visible conformational change, to be observed on *switch*SENSE.

Outlook: ss a new application, in the future protein-DNA conjugates made out of Convalin A could be tested on surface, in order to detect glycosylated protein and try to develop an analytic tool to measure the amount of glycosylated forms in a mixture. One limitation at the beginning could be the size of Convalin A, 104 kDa, and the fact that is a tetramer, but since there is a big pressure in this research field, analogs to this lectin could be search and checked on surface.

7. Antibody kinetics analysed in *switch*SENSE

7.1 Introduction

In the pharmaceutical industry the generation of new therapeutic monoclonal antibodies is being pushed beyond the boundaries for better diagnostics and higher efficacy of safer medicines. However, a deep characterization of large antibody libraries is required to select the best biomolecules in terms of kinetics, specificity, affinity, and selectivity shown to the target antigen. Hereby, the employment of surface-based biosensors allows to perform an extensive parallel detection in real-time on a single platform in a label-free manner.

Currently several technologies are employed for antibody/antigen analysis; these biosensors can be optical platforms, based either on surface plasmon resonance (SPR) (Liedberg et al, 1983), or on interferometry, namely biolayer interferometry (Yang et al, 2003). Furthermore, other platforms belong to surface acoustic wave sensor or quartz crystal microbalance sensors (Janshoff et al, 2000).

In this project the comparative study of antibody affinity was carried out selecting four monoclonal antibodies against hCA1. Their kinetics was characterized on *switch*SENSE upon surface functionalization with hCA1-DNA mono conjugates. The antibody kinetics was also evaluated in Biacore™ for a direct comparison. Furthermore, the consecutive injections of two different antibodies were tested to verify their binding to different hCA1 epitopes on *switch*SENSE. Eventually, the efficacy of switchable DNA layers was demonstrated to be employed for antibody characterization.

7.1.1 Surface-based sensor

Considering different surface-based sensor, the biolayer interferometry technology adopts an optical fibre with the immobilized protein, defined as biosensor tip. The quantification of molecular interactions is based on the interference pattern of white light, reflected from two surfaces, the layer with immobilized protein and an internal reference layer. Whereby, dipping the sensor tip in the sample solution, the variation of molecules bound to the biosensor tip causes a shift in the interference pattern that can be measured in real-time (Abdiche et al, 2008; Li et al, 2011).

Considering the quartz crystal microbalance (QCM) sensor, this is gravimetric technique that measures the change in resonant frequency of a piezoelectric crystal. The surface presents the immobilized protein and molecular interactions are monitored by changes in resonance frequency (Kierny et al, 2012; Yan et al, 2011).

7.1.2 SPR-based sensor

The surface plasmon resonance (SPR) phenomenon was discovered in the early 1900's (Wood, 1902). However, its application in biosensing is quite recent (Liedberg et al, 1983), and it has since then rapidly developed, due to the big research interest on label-free real-time analytical technology for biomolecular interactions studies, e.g for protein/protein (Benvegnu et al, 2009; Bergmann et al, 2004; Ma et al, 2011), or protein/DNA (Eisenberg et al, 2009; Henriksson-Peltola et al, 2007; Sakkhachornphop et al, 2009), or antigen/antibody interactions (Kron et al, 2008; Ramakrishnan et al, 2009; Reddy et al, 2012)

In SPR a gold metal film is placed at the interface of two media, a prism and, e.g., a buffer solution. The first medium, in this case a prism, is characterized by a higher refractive index, whereby, under conditions of total internal reflection, the polarized light propagating in the prism results in evanescent waves in the lower refractive index medium (buffer solution), which has a small penetration distance of about 300 nm(GE Healthcare, 2009). At a specific angle, the evanescent wave excites surface plasmons at the gold-solution interface, causing SPR phenomenon. These surface plasmons are quanta of plasma oscillation, a surface electromagnetic wave whose propagation is confined to the metal/dielectric interface.

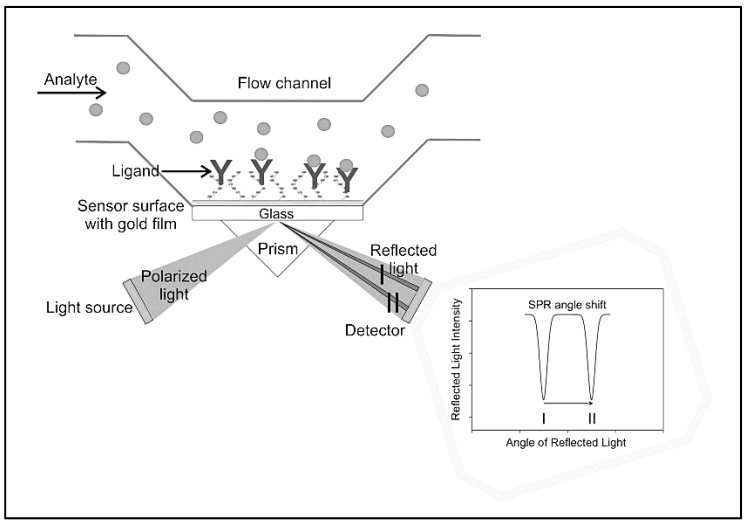

Figure 7.1 Surface Plasmon Resonance (SPR) based sensor. SPR angle is affected by the refractive index of solution at the metal interface and events like adsorption and desorption of molecules on the gold surface which vary this refractive index. The monitoring of the SPR angle change is used to detect and analyze association/dissociation events that occur on functionalized gold surface, with a biomolecule (ligand, here an antibody in green), after injection of a second biomolecule (analyte, here a globular protein in red).

At SPR occurrence, the intensity of the reflected light shows a minimum peak. This incident angle is called the SPR angle, at which the minimum reflectivity is observed.

Having the prism in a fixed position and the evanescent wave which penetrates the solution, SPR angle is affected by the refractive index of solution at the metal interface. Events like adsorption and desorption of molecules on the gold surface influence the refractive index. Therefore, the monitoring of the SPR angle change can be used to detect and analyse association/dissociation interactions that occur on the gold surface, for example those of protein-protein nature. In fact the metal surface can be functionalized with a biomolecule (ligand). The target molecule (analyte) can subsequently be injected allowing it to flow over the immobilized ligand (Figure 7.1).

7.2 Results

7.2.1 Employed monoclonal antibodies and experimental design

Initially five different monoclonal antibodies (mAbs) were selected to be used on surface analyses, simply defined as Ab1, Ab2, Ab3, Ab4 and Ab5 (Table 7.1). Ab2 displayed a strong unspecific interaction on the *switch*SENSE surface after 5 nM loading; therefore it was not used in data evaluation. The other four mAbs, Ab1, Ab3, Ab4 and Ab5 bound specifically to hCA1-DNA layers, until a concentration of 60 nM was reached (Figure 7.10). The declared initial concentration of mAb was double-checked by spectrophotometry, at 280 nm using a NanoDrop and a molar extinction coefficient of 21000 $M^{-1}mm^{-1}$ (Thermo Scientific, 2008).

Table 7.1 Selected monoclonal antibodies anti-hCA1 for surface protein/protein analyses.

Name	Isotype	Clone	Supplier	Observations
Ab1	mouse IgG2a	7G12	AbNova (#H00000759-M07)	
Ab2	mouse IgG1	G-6	Santa Cruz Biotechnology (#sc-271452)	Just unspecific interactions
Ab3	mouse IgG1	M2	AbDSerotec (#MCA2970Z)	
Ab4	mouse IgG2a	10E4	AbNova (#H00000759-M19)	
Ab5	mouse IgG2b	1F1	AbNova (#H00000759-M10)	

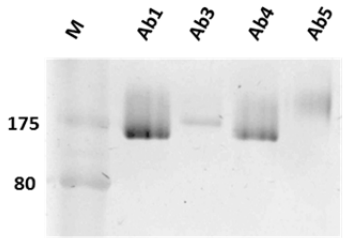

Figure 7.2 Monoclonal antibodies, Ab1, Ab3, Ab4 and Ab5 visualized in semi-native conditions SDS-PAGE, 12.5% polyacrylamide and Coomassie Blue staining. Of each mAb were loaded 0.9 µg. Color Plus Prestained Protein Marker (NEB) ladder was used.

As further control, the four mAbs were loaded on SDS-PAGE Tris-Gly buffer, 12.5% polyacrylamide, in semi-native conditions and stained with Coomassie Blue. In Figure 7.2, Ab1 and Ab4 showed a similar profile, while Ab3 runs a bit slower, and Ab5 is significantly smeared. Regarding the pI of murine immunoglobulins, generally IgG1 pI is around 7.0–8.5, for IgG2a 6.5–7.5, and for IgG2b 5.5–7.0 (Amersham Biosciences, 2002). Nevertheless Ab5 IgG2b had a smeared band indicating a more basic pI (pH of running buffer was 8.8). In the gel the high purity level of antibody preparations was confirmed.

The antibody kinetics of mAb-hCA1 interaction was characterized on Biacore™ SPR system and on switchSENSE. Figure 7.3 depicts schematically the different strategies tested on Biacore™ to directly compare the *switch*SENSE kinetic analysis.

On *switch*SENSE (Figure 7.3 B) hCA1 was immobilized on surface upon hCA1-DNA mono conjugate hybridization and the antibody binding was recorded based on Dynamic Response variation. The decided ligand-analyte orientation for the kinetic analysis was selected in this manner since the small size of hCA1 coupled to DNA enables the antibody detection, whereby the variation of switching dynamics upon antibody binding can be still revealed and differentiated.

Regarding Biacore™ (Figure 7.3 A), at first the same orientation used in *switch*SENSE was tried on CM5 chip, hCA1 as ligand and Ab3 analyte loading in multi-cycle manner, although this strategy proved to be problematic due to the regeneration step. The bound Ab3 removal from hCA1 immobilized on surface was problematic: solutions with a pH higher than 2.5 were ineffective, below pH 2.0 harmful, and neither high salinity nor addition of detergents were effective. Only 30 s injection at 10 µl/min of 10 mM NaOH was found to be suitable to bring the response to a level below the initial value. This indicated a loss of active binding sites after each regeneration step, due to unavoidable hCA1 denaturation on surface.

Subsequently, each single mAb was immobilized on CM5 chip and the analyte hCA1 was injected in multi-cycle program, this manner did not give any complication, the bound hCA1 to mAb could be easily removed by injecting 10 mM glycine-HCl pH 2.0 for 30 s at 10 µl/min. Furthermore, for a better comparison with the *switch*SENSE two-dimensional surface and to avoid the regeneration step, hCA1 was immobilized on the C1 chip and the interaction of each mAb was detected using a single-cycle method.

The applied protocols are described in Section 4.2.6.

Sensor chip CM5 is differentiated by C1 from the presence of a flexible dextran matrix on gold surface (GE Healthcare, 2009). Indeed CM5 is generally considered the standard sensor chip for Biacore experiments, having a thin surface layer 100 nm thick of a highly carboxymethylated dextran matrix. This dextran layer provides a hydrophilic environment for biomolecular interactions and increases the surface capacity for ligand immobilization many-fold in comparison with a flat 2D surface like sensor chip C1. The latter possesses a flat hydrophobic carboxylated surface comprised of a mercapto–alkane–carboxyl monolayer, which contains approximately 10% of the carboxyl groups present on CM5 chip (GE Healthcare, 2009). Furthermore, the lack of a dextran matrix implies that attached ligands are not free to move within the surface layer, and possible

avidity effects can be reduced. The orientation hCA1-ligand/Ab-analyte is characterized by a kinetics which is not described by the 1:1 Langmuir model: the antibody analyte binds hCA1 immobilized on surface, based on stoichiometry 1 Ab to 2 hCA1, whereby the presence of two binding sites on Ab molecule confers an avidity effect (Figure 7.3 C). In order to decrease the avidity on surface the ligand density must be minimized.

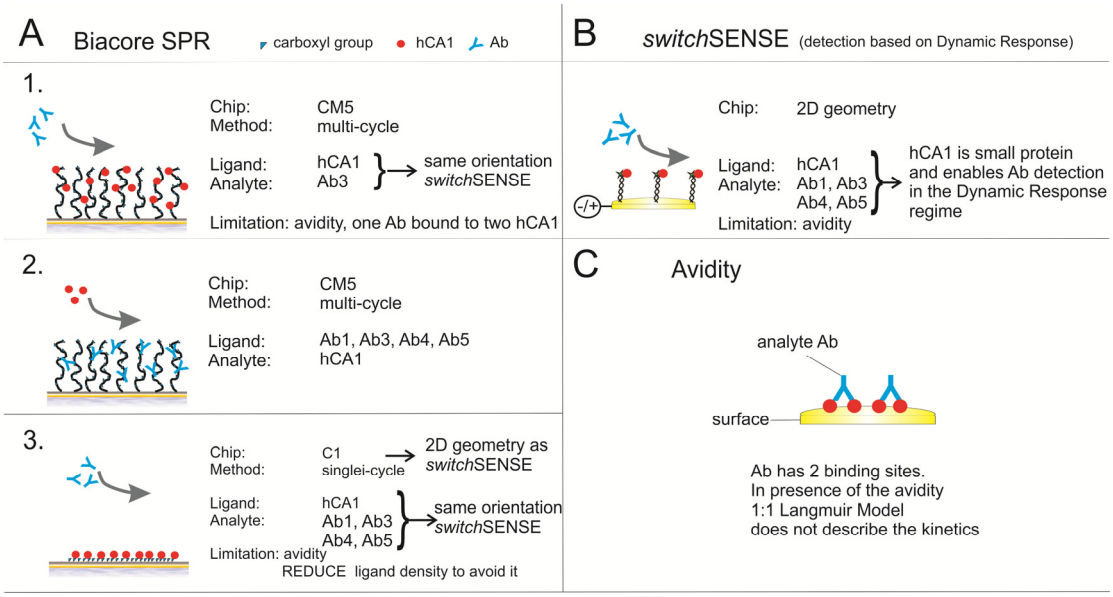

Figure 7.3 The antibody kinetics of mAb-hCA1 interaction was characterized on Biacore™ SPR system and on *switch*SENSE. A: different strategies were tested on Biacore™, whereby (1) ligand hCA1 was immobilized on CM5 chip (3D surface) and analyte Ab3 was injected in multi-cycle manner (this way was problematic due to the regeneration step which caused a reduction of binding sites on surface); (2) next, each single mAb was used as ligand on CM5 chips and analyte hCA1 was flowed over the surface in multi-cycle program; (3) furthermore, to be closer to *switch*SENSE 2D surface and to avoid the regeneration step, hCA1 was immobilized on C1 chip (2D surface) and each mAb was introduced in single cycle manner.
B: on *switch*SENSE hCA1 was immobilized on surface upon hCA1-DNA mono conjugate hybridization and the antibody binding was detected based on Dynamic Response variation; the small size of hCA1 coupled to DNA enables the antibody analysis, since the variation of switching dynamics upon antibody binding can be still detected and differentiated. C: the antibody binds hCA1 immobilized on surface based on stoichiometry 1 Ab to 2 hCA1; the presence of two binding sites on Ab molecule confers an avidity effect, therefore the 1:1 Langmuir model cannot describe the kinetics; to decrease the avidity on surface the ligand density must be minimized.

7.2.2 Kinetic analysis on the SPR system Biacore™ X100

7.2.2.1 Data analyses and results

The rate constants for association (k_{on}) and dissociation (k_{off}) events and the equilibrium constant for dissociation (K_D) were obtained using Langmuir binding model (1:1 binding model) for multi- and single-cycle method. The sensorgrams were evaluated using

Biacore X100 Evaluation Version 2.01 software. The curves were first corrected by subtracting the buffer signal, and the fit was globally performed appliing to multiple datasets the same fitting parameters, such as the kinetic constants and the analyte binding capacity of the surface, R_{max}, while refractive index contribution RI was set constant.

In all experiments, the measured curves were presented in grey and fitted curves in colours (Figure 7.4,

Figure 7.5, Figure 7.6). The fitted kinetic constants are listed in Table 7.2, with the kinetics written in bold font when not mass transfer limited. All tables of Biacore's evaluation were inserted in Appendix, Section 14.3.

To maximize the mass-transfer on surface, the highest flow rate of 30 µl/min was applied in association pahse. According to Eq. 5.1, the laminar velocity in Biacore corresponded to 0.30 m/s. The laminar velocity which occurs at the center of height was calculated considering the flow channel dimensions of Biacore™ X-100 (0.05×0.50 (height × widht) mm^2 and the employed flow rate $0.5*10^{-8}$ m^3s^{-1}.

To understand if the binding was measured in mass transfer limitation, the independent component of the mass transfer constant ***tc*** estimated in each fit was compared to the reference value ***tc*** calculated for hCA1 and mAb analytes, based on Biacore's guidelines (GE Healthcare, 2009). Finally the kinetics was considered valid if ***tc*** was higher than $5.32*10^{11}$ ($RU \cdot M^{-1}m^{-1}s^{-2/3}$) and $1.91*10^{12}$ ($RU \cdot M^{-1}m^{-1}s^{-2/3}$), for analyte hCA1 and mAb respectively (Table 7.2). The calculation of ***tc*** reference values and detailed description of mass transfer evaluation made in Biacore are presented in Appendix, Table 14.1.

Eventually three experiments resulted in mass transfer limited kinetics, not described by the employed model: hCA1 on functionalized Ab1-CM5 chip, hCA1 on functionalized Ab5-CM5 chip, and Ab5 on functionalized hCA1-C1 chip (Table 14.4, Table 14.7, Table 14.11). The Ab5-hCA1 affinity could not be characterized on Biacore, since the kinetics on both CM5 and C1 chips was mass transfer limited, indicating that the orientation did not affect the interaction neither the type of used surface. The charge and folding of this mAb was perhaps connected of this diverse behaviour on surface; in native gel this was the only antibody displaying a smeared band indicating a basic pI (Figure 7.2) but how this could be the cause to this problem it is not clear.

The fit quality was overall good as described by Chi-square value, which was higher than 5 just for hCA1 on Ab4- and Ab5-CM5 sensor chip experiments (Chi-square values 10 and 6 respectively, in Appendix Table 14.6, Table 14.7).

Table 7.2 Estimated rate constants for Ab1, Ab3, Ab4 and Ab5 in affinity binding with hCA1 in Biacore™. The used sensor chip is indicated, as well as if the antibodies Ab1, Ab3, Ab4 and Ab5 were ligand or analyte during the experiment. The SD values are in round brackets. The bold font marks the kinetics, which were not mass transfer limited.

Chip	*Antibody*	k_{on} *[10^5 $M^{-1}s^{-1}$]*	k_{off} *[10^{-3} s^{-1}]*	K_D *[nM]*
CM5	Ab1 ligand	0.62 (0.01)	4.32 (0.03)	69.6 (0.6)
	Ab3 ligand	**0.46 (0.01)**	**2.12 (0.01)**	**46.3 (0.2)**
	Ab4 ligand	**0.69 (0.01)**	**4.22 (0.01)**	**61.6 (0.3)**
	Ab5 ligand	0.64 (0.01)	4.33 (0.03)	67.8 (0.7)
	Ab3 analyte	**0.98 (0.02)**	**0.21 (0.07)**	**2.1 (0.7)**
C1	**Ab1 analyte**	**5.96 (0.06)**	**2.44 (0.02)**	**4.1 (0.1)**
	Ab3 analyte	**2.78 (0.02)**	**0.83 (0.01)**	**3.0 (0.1)**
	Ab4 analyte	**3.23 (0.03)**	**2.24 (0.02)**	**6.9 (0.1)**
	Ab5 analyte	3.0 (0.1)	3.04 (0.08)	10.1 (0.4)

For Ab3 association/dissociation on functionalized hCA1-CM5 chip, the measured sensorgrams were grouped in 1st and 2nd loaded serial dilution and fitted singularly setting first Rmax as global and then as local parameter. As it is evident in Figure 7.4, the best fit was obtained by setting Rmax as local parameter, since the regeneration step decreased the ligand immobilized level cycle by cycle and variating the expected binding capacity Rmax. Finally the average values of k_{on}, k_{off}.and K_D were calculated.

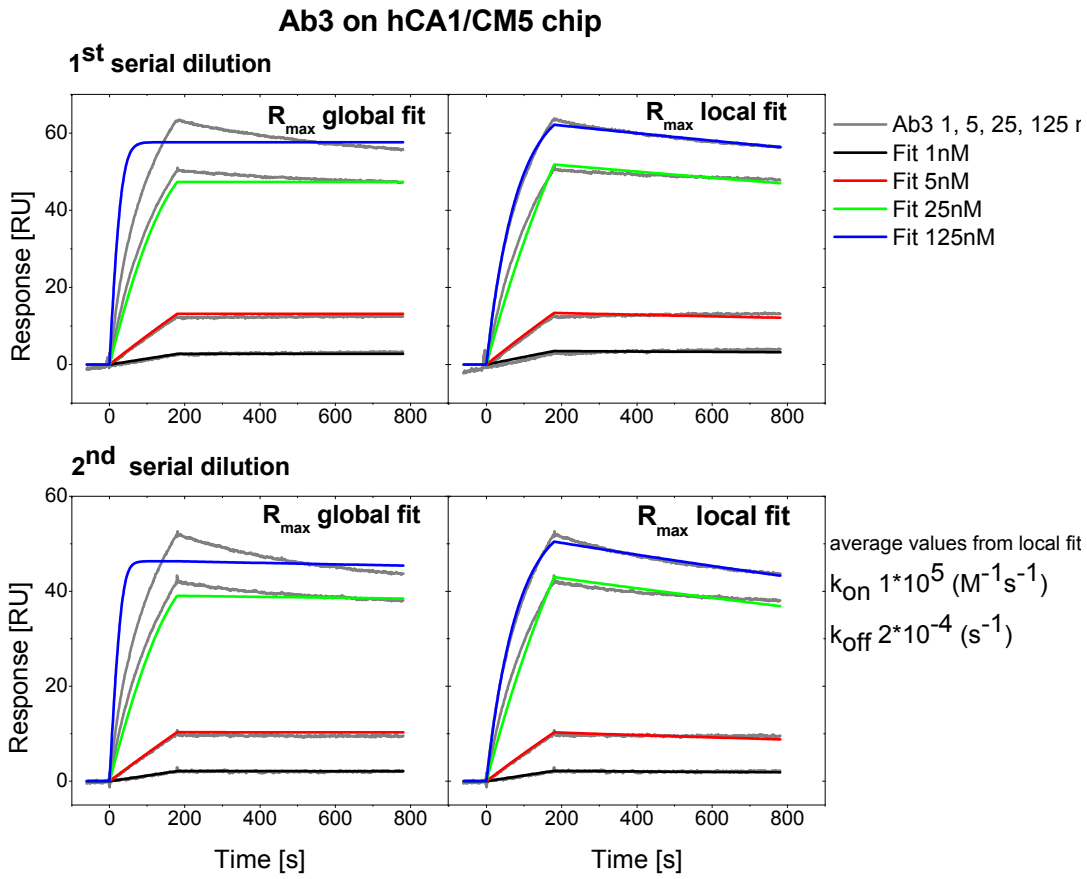

Figure 7.4 Sensorgrams of Ab3 association and dissociation on functionalized hCA1-CM5 surface in multi-cycle assay. Ab3 dilutions, from 1 to 125 nM prepared in running buffer HBS-P, were injected twice on hCA1-CM5 surface (immobilization level 300 RU) at 30 µl/min and 25 °C, and a buffer-only tube was run between every single series. The association was observed for 180 s, and dissociation for 600 s. The regeneration step was harmful (30 s contact 10 mM NaOH at 10 µl/min); therefore measured sensorgrams, in grey, were grouped in 1st and 2nd loaded serial dilution (upper and lower graphs, respectively) and fitted singularly with Rmax as global or local parameter (left and right graphs, respectively; fitted curves in colours). Just local Rmax gave good fits. Finally the average values of k_{on}, k_{off}.and K_D were calculated.

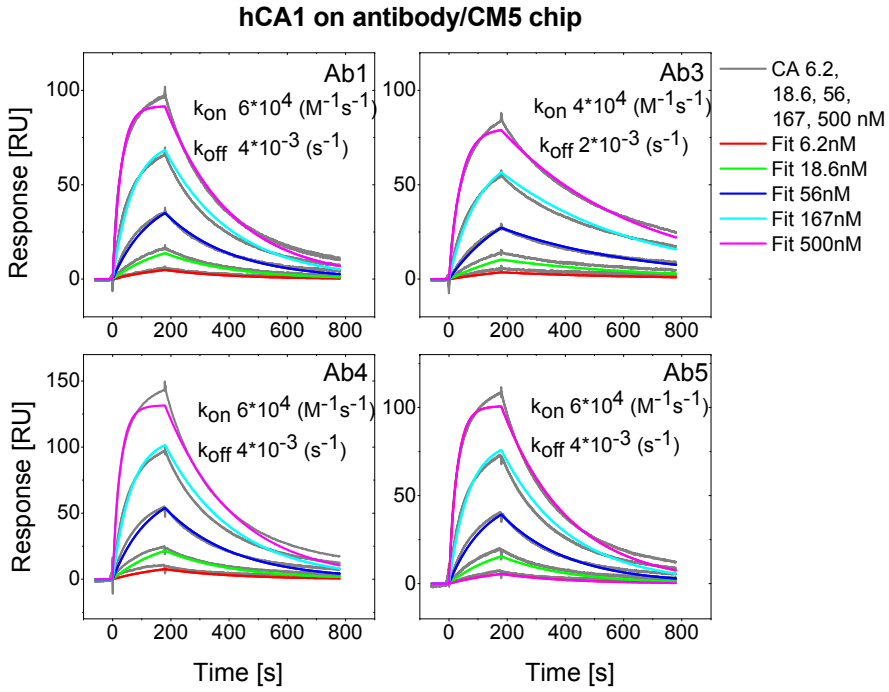

Figure 7.5 Sensorgrams of hCA1 association and dissociation on functionalized Ab1, Ab3, Ab4 and Ab5-CM5 surface in multi-cycle assay. hCA1 dilutions, from 6.2 to 500 nM prepared in running buffer HBS-P, were injected twice on Ab-CM5 surface (immobilization levels to range from 1100 to 1500 RU) at 30 µl/min and 25 °C, and a buffer-only tube was run between every single series. The association was observed for 180 s, and dissociation for 600 s, followed by a regeneration step (30 s contact 10 mM Gly-HCl pH 2.0 at 10 µl/min). The measured sensorgrams, in grey, were globally fitted (coloured curves) obtaining the corresponding k_{on} and k_{off}.

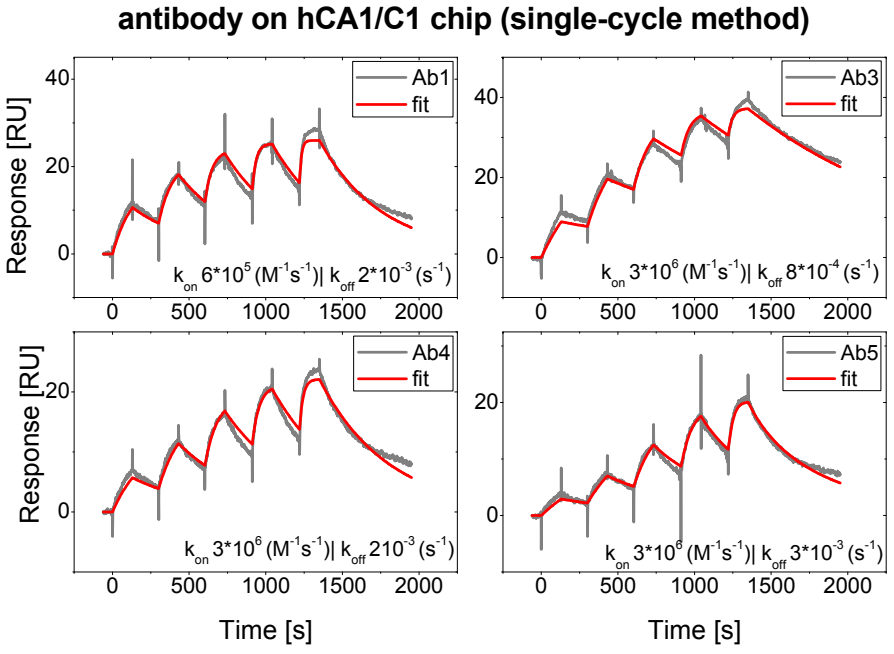

Figure 7.6 Sensorgrams of Ab1, Ab3, Ab4 and Ab5 association and dissociation on functionalized hCA1-C1 surface in single-cycle assay. Antibody dilutions (7.8, 15.6, 31.2, 62.4 and 125 nM) prepared

in running buffer HBS-P, were subsequently injected on hCA1-C1 surface (immobilization level 50 RU) at 30 µl/min and 25 °C, and a buffer-only tube was run before analyte dilution series. The association was observed for 130 s and dissociation for 170s. After the last analyte concentration, the observed dissociation lasted 600s, followed by a single regeneration step (30 s contact of 10 mM NaOH at 30 µl/min). The measured sensorgrams, in grey, were globally fitted (red curves) obtaining the corresponding k_{on} and k_{off}.

7.2.3 Kinetic analysis on *switch*SENSE

7.2.3.1 Experimental design

Generally monoclonal antibodies are considered very strong binders, with K_D's in the picomolar range. In order to reduce the mass transfer limitation on surface, the prototype SWA1 was employed. The microfluidic geometry of its chips is designed to allow kinetic measurements (Section 5.2.2).

The hCA1-DNA mono conjugate layers were prepared as described in Section 6.4.1. The solutions of mAbs were diluted in StdB-T, which contained Tween20 0.05% (v/v) and injected at 1 ml/min. For Ab3 a titration experiment was performed, injecting 7.5, 15, 30 and 60 nM, while for Ab1, Ab4 and Ab5 a single point injection was recorded, at 7.5 nM antibody concentration. The association was observed for 100 s, at 25 °C, followed by 3000 s of dissociation flowing StdB-T at 50 µl/min (Figure 7.7). The electrodes were not regenerated; after dehybridization with NaOH 10 mM solution, re-hybridized layers with c-ss-48-mer had a much slower dynamics compared to the initial corresponding ds-DNA layers. Hence different gold electrodes were used for each injection. The negative control measurements were taken on ds-DNA layers without hCA1, loading mAbs in the same manner.

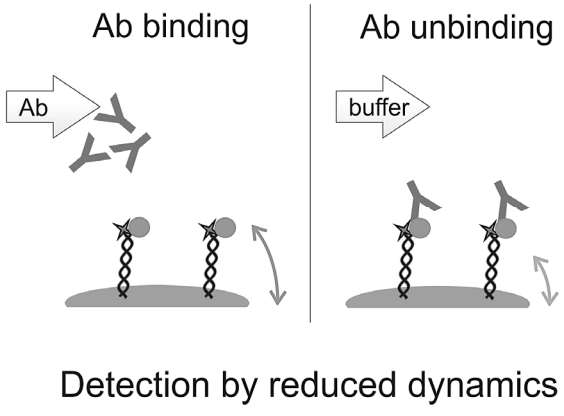

Figure 7.7 Detection of association and dissociation of mAb on *switch*SENSE hCA1-DNA mono conjugate layers. The mAb was injected observing the binding event in real-time by Dynamic Response, DynRes. By flowing buffer over the surface, the unbinding was recorded. Finally DynRes was analyzed to estimate the kinetics and affinity of different mAb loaded on hCA1-DNA layers.

The Dynamic Response, DynRes, was recorded on one electrode of the experimental flow channel. DynRes of rising motion (integrated area of 0-10 µs region) was obtained in KM mode (Section 5.3.1.6), choosing the applied switching potential of amplitude 0.8 V based on the inflection point (Ip) correction of VR curve. The switching amplitude was applied at 10 kHz and the fluorescence was recorded over time, with LED power of 5 V. Rising V_{max} was not used for the analysis because upon antibody binding the signal was too noisy compared to DynRes and therefore less sensitive.

Eventually, the titration experiments in steady-state were tried on Ab3, but with no success, therefore the affinity obtained in kinetics could not be compared to K_D from the steady-state experiment.

7.2.3.2 Data analysis and results

For the data evaluation of kinetic experiments, DynRes curves of binding and unbinding were normalized dividing by the initial value, before antibody injection. Smoothing data was done using Adjacent Averaging, setting 5 and 50 points of window, respectively for binding and unbinding curves. The fluorescence levels, F_{st} and F_{ly}, of association were normalized based on corresponding initial values.

All resulting curves were fitted in Origin 8.5, with Exponential Decay 1 ($y = y_0 + A \cdot e^{-x/\tau}$) to get the time constants for association τ_{on}, and dissociation τ_{off}, described by the Langmuir adsorption isotherm Eq. 6.11. τ_{on} was fitted from DynRes, F_{st} and F_{ly} data for a direct comparison, while for τ_{off} only DynRes curves were used. The kinetic constants, k_{on} and k_{off}, and the equilibrium constant K_D were lastly calculated by Eq. 6.5, Eq. 6.12 and Eq. 6.13.

Because of the large amount of evaluated data, all fits for DynRes curves and normalized fluorescence are inserted in Appendix Section 14.4. Moreover, as data support the initial ds-DNA fluorescence levels recorded in LFM are listed in Appendix Section 14.6.

7.2.3.2.1 Ab3 kinetics in titration analyses

The initial experiment concerned the injection of 15 nM of Ab3 at 1 and 5 ml/min. The resulting association time constants were comparable, 7(±1) s at 1 ml/min and 5(±1) s at 5 ml/min (Figure 7.8), therefore all experiments could be performed at 1 ml/min with no transfer limitation affection on kinetic data analysis.

According to Eq. 5.1, the laminar velocity in *switch*SENSE corresponded to 0.42 m/s. The laminar velocity which occurs at the center of height was calculated considering the flow channel dimensions of *switch*SENSE (0.06×1.00 (height × width) mm^2) and the employed flow rate $1.67*10^{-8}$ m^3s^{-1}.

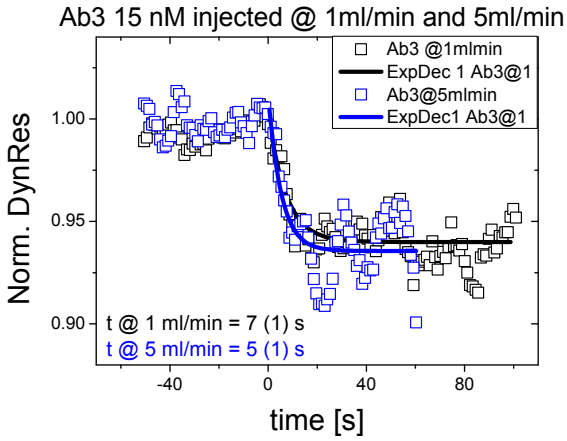

Figure 7.8 Dynamic Response curves of 15 nM Ab3 injected at flow rate 1 ml/min and 5 ml/min on hCA1-DNA layer. The association time constant for 1 ml/min injection (black square data, black line fit) was 7(±1) s, comparable to the one measured for 5 ml/min (blue square data, blue line fit) of 5(±1) s.

Figure 7.9 presents the normalized DynRes observed in association and dissociation, loading from 7.5 nM to 60 nM Ab3 on hCA1-DNA layers. Figure 7.10 illustrates the observed variation of normalized fluorescence levels, whereby a decrease in F_{st} and an increase in F_{ly} resulted in lower fluorescence amplitude upon antibody binding.

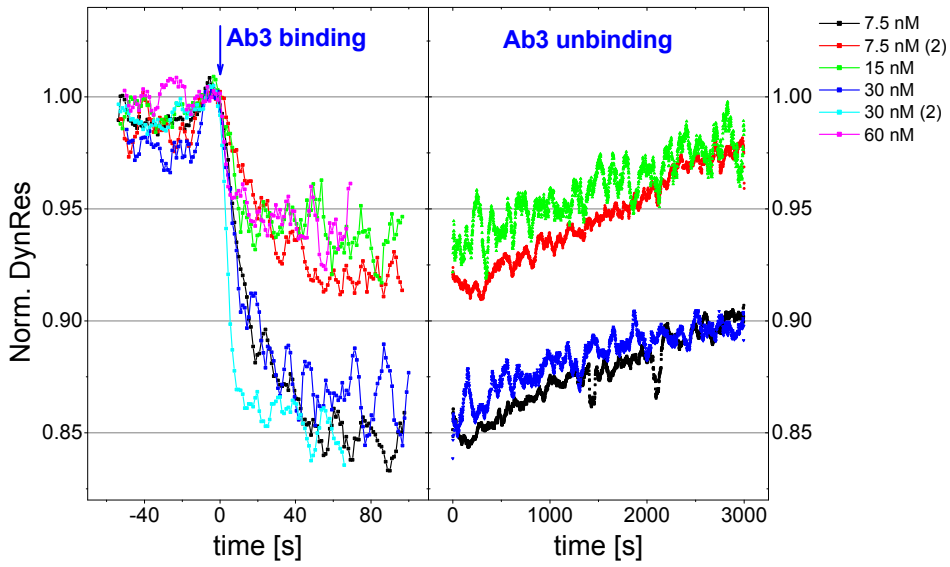

Figure 7.9 Normalized Dynamic Response of observed association and dissociation of Ab3 loaded on hCA1-DNA layers. The antibody was injected at different concentration (7.5, 15, 30, and 60 nM, respectively black, red, green, blue, cyan and magenta squares) at 1 ml/min, 25°C, in StdB-T. The dissociation was performed flowing at 50 µl/min StdB-T. The variation wasn't correlated to Ab3

concentration, since the initial level of ds-DNA after electrical desorption varied through the different electrodes.[3]

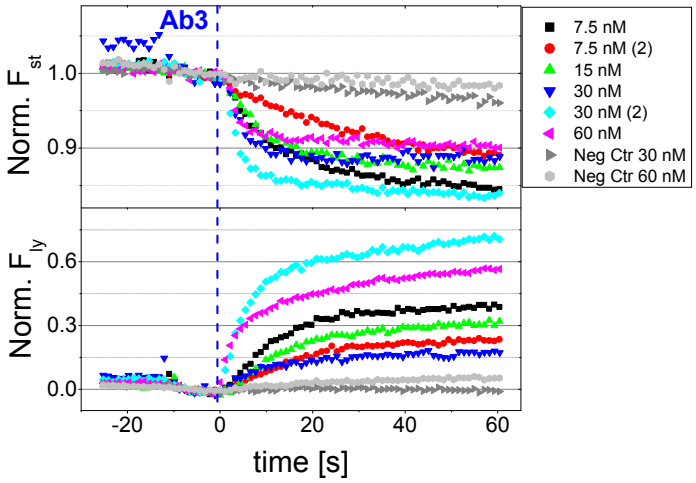

Figure 7.10 Normalized fluorescence levels, F_{st} and F_{ly}, of observed association of Ab3 loaded on hCA1-DNA layers. Ab3 was injected at different concentration (7.5, 15, 30, and 60 nM, respectively black, red, green, blue, light blue and pink symbols) at 1 ml/min, 25°C, in StdB-T. On ds-DNA layer were loaded 30 and 60 nM of Ab3 as negative control (dark and light grey). Both fluorescence levels changed, resulting in lower amplitude. The variation wasn't correlated to Ab3 concentration, since the initial level of ds-DNA varied through the different electrodes.

The first observation is that the variation of response was not correlated to Ab3 concentration, even replicates of 7.5 nM differed from each other. This effect was caused by inconsistent initial ds-DNA densities through all prepared electrodes, used in these measurements. Regarding old chips, employed in Prototype2, they displayed a robustness in SAM preparation and in electrical desorption, obtaining similar surface density (Table 6.5). However, the new chips presented a broader distribution of fluorescence levels after electrical desorption for the initial ds-DNA, with F_{ly} 16(±10) kcps and F_{st} 38(±18) kcps, recorded in LFM at LED power 0.2 V for 30 different electrodes. This observed irregularity with the new chips is currently under investigation. The binding of Ab3 on higher packed layers gave overall a smaller relative reduction of DynRes, due to steric hindrance. However, the absolute fluorescence

[3] Data files: 01_KM_Ab3_7.5nM_1mlmin-20120705-183229.dyn; 02_KM_Ab3_7.5nM_1mlmin-20120706-155952.dyn; 04_KM_Ab3_15nM_1mlmin-20120625-150912.dyn; 02_KM_Ab3_30nM_1mlmin-20120626-131749.dyn; 03_KM_Ab3_30nM_1mlmin-20120706-195248.dyn; 06_KM_Ab3_60nM_1mlmin-20120705-135816.dyn; 01_KM_Ab3_30nM-20120703-201543.dyn; 01_KM_Ab3_60nM-20120703-205050.dyn; 01_KM_unbindinfAb3_7.5nM-20120705-191023.dyn; 02_KM_unbindingAb3_7.5nM-20120706-162857.dyn; 03_KM_Ab3_unbinding-20120625-200926.dyn; 02_KM_Ab3_unbinding_50ulmin-20120626-135327.dyn; 03_KM_unbinding_Ab3_30nM-20120706-201854.dyn; 01_KM_Ab3_60nM_OFF-20120703-211452.dyn.

intensities were less correlated to the layer density; at similar high density sometimes the effect on F_{ly} and F_{st} was minor, sometimes major.

Even though the resulting hCA1-DNA layers had a distributed density of hCA1, the data remained valid for the kinetics of all four mAbs, since the rates of binding and unbinding are not affected by the number of probe present on surface. Eventually, the kinetics was influenced by avidity, as it is discussed later on in Section 7.2.5.4.

On bare ds-DNA the loading of Ab3 at 30 and 60 nM concentrations did not specific binding, the variation in fluorescence intensities in fact was very small (Figure 7.10).

The global evaluation of Ab3 dissociation resulted in a significantly deviated τ_{off} (between 2000 and 8000 s), whereby the complex dissociation was not described by Exponential Decay 1 function. Observing 3000 s, the complete dissociation was not measured, therefore it was taken a τ_{off} of 5000(±1000) s because, corresponding to a k_{off} equivalent to $2.0(\pm0.4)*10^{-4}$ s^{-1}.

Since a big variation was observed on both fluorescence levels, the association constant τ_{on} at each Ab3 concentration was evaluated fitting DynRes and absolute fluorescence F_{ly} and F_{st}, listed in Table 7.3.

Table 7.3 Association time constant τ_{on} obtained fitting absolute fluorescence F_{st} and F_{ly} signals, and DynRes, for each injected concentration of Ab3. Errors were indicated in round brackets.

	fitted Ab3 τ_{on} [s]			
	7.5 nM	**15 nM**	**30 nM**	**60 nM**
F_{st}	15.9 (0.5); 31 (1)	9.7 (0.4)	4.8 (0.3); 4.6 (0.3)	3.8 (0.3)
F_{ly}	13.8 (0.4); 19.2 (0.6)	14.4 (0.5)	11.3 (0.8); 8.2 (0.4)	10.7 (0.6)
DynRes	17.3 (0.7); 21 (1)	7 (1)	13 (1); 5.0 (0.4)	6 (1)

Figure 7.11 displays the linear regressions of k_1, the inverse of τ_{on}, as a function of Ab3 nanomolar concentration, for DynRes, F_{ly} and F_{st} data. The association rate k_{on} was evaluated based on Eq. 7.1:

Eq. 7.1 $$k_1 = 1/\tau_{on} = k_{on} \cdot c + k_{off}$$

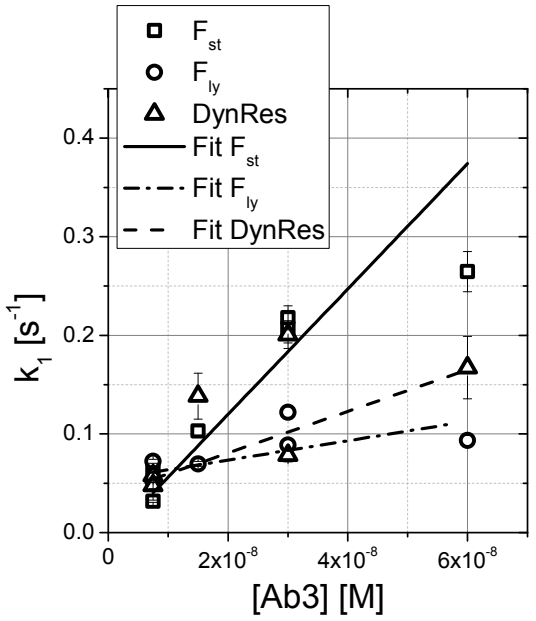

Equation	y = a + b*x	Weight	Instrumental
Fst	--	Residual Sum of Squares	239.58
--	--	Pearson's r	0.85
	--	Adj. R-Square	0.64
		Value	Standard Error
k1 [s-1]	Intercept	-0.007	0.02
	Slope	6.36E+06	2.01E+06

Equation	y = a + b*x	Weight	Instrumental
Fly	--	Residual Sum of Squares	138.46
--	--	Pearson's r	0.67
	--	Adj. R-Square	0.31
		Value	Standard Error
k1 [s-1]	Intercept	0.05	0.01
	Slope	9.81E+05	5.45E+05

Equation	y = a + b*x	Weight	Instrumental
DynRes	--	Residual Sum of Squares	76.44
--	--	Pearson's r	0.69
	--	Adj. R-Square	0.34
	--	Value	Standard Error
k1 [s-1]	Intercept	0.04	0.01
	Slope	2.11E+06	1.11E+06

Figure 7.11 Linear regressions of inverse of τ_{on}, k_1, vs [Ab3] of data from F_{st} (data in square, linear fit in black line), F_{ly} (data in circle, linear fit in dashed line), and DynRes (data in triangle, linear fit in dashed-dotted line).

Table 7.4 Kinetic constant k_{on} obtained by linear regression of $k_1 \propto$ [Ab3] from F_{st}, F_{ly} and DynRes. The k_{on} values had the same order of magnitude, 10^6 $M^{-1}s^{-1}$, and similar SD (which are indicated in the round brackets). The corresponding equilibrium constant K_D was calculated considering k_{off} $2*10^{-4}$ s^{-1}.

	Ab3	
	k_{on} [10^6 $M^{-1}s^{-1}$]	K_D [pM] considering k_{off} $2*10^{-4}$ s^{-1}
F_{st}	6 (2)	33 (13)
F_{ly}	1.0 (0.6)	200 (110)
DynRes	2 (1)	100 (54)

The best correlation based on Pearson's R and adjusted R^2 was obtained from F_{st} data. While considering the lowest RSS term, the linear regression on DynRes was the best. Overall the data originating from F_{ly} gave the worst fit. Nevertheless, the estimated constants k_{on} was in general 10^6 $M^{-1}s^{-1}$ (Table 7.4). The constants k_{off} from linear fit were not taken in account, but only the approximated value was considered, $2*10^{-4}$ s^{-1}. Finally the equilibrium constant for K_D was in the picomolar regime, roughly 110 pM (Table 7.4).

7.2.3.2.2 *Kinetics of Ab1, Ab4 and Ab5 from single-injection experiments*

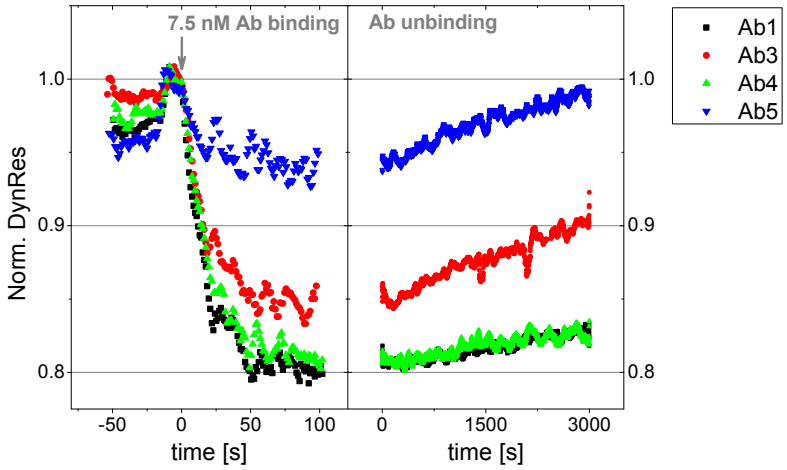

Figure 7.12 Normalized Dynamic Response of observed association and dissociation for Ab1, Ab3, Ab4 and Ab5, loading 7.5 nM on hCA1-DNA layers. The single-injections for 7.5 nM of Ab1 (black symbol), Ab4 (green symbol) and Ab5 (blue symbol) were done at 1 ml/min, 25°C, in Stdb-T (Tween20 0.05%). The dissociation was performed flowing StdB-T at 50 µl/min. Here the curves were compared to Ab3 7.5 nM 1st injection[4].

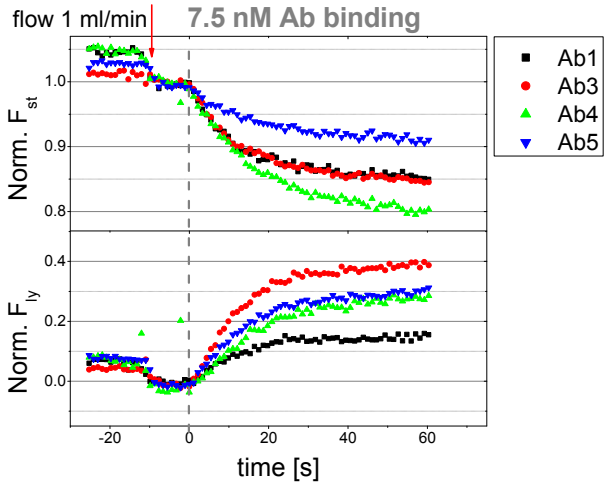

Figure 7.13 Normalized fluorescence levels, F_{st} and F_{ly}, of observed association Ab1, Ab3, Ab4 and Ab5 loaded on hCA1-DNA layers. The single-injections for 7.5 nM of Ab1 (black symbol), Ab4 (green symbol) and Ab5 (blue symbol) were done at 1 ml/min, 25°C, in Stdb-T (Tween20 0.05%). The curves were compared to Ab3 7.5 nM 1st injection. Both fluorescence levels changed, resulting in lower amplitude. The variation was not correlated to the amount of bound antibody, since the initial level of ds-DNA varied through the different electrodes.

[4] Further data files: 03_KM_Ab1_7.5nM_1mlmin-20120713-185540.dyn, 03_KM_Ab4_7.5nM_1mlmin-20120713-150225.dyn, 06_KM_Ab5_7.5nM_1mlmin-20120714-145721.dyn, 01_KM_Ab1_7.5-20120713-192319.dyn, 03_KM_Ab4_unbinding-20120713-152702.dyn, 06_KM_Ab5unbinding-20120714-152410.dyn.

Figure 7.12 presents the normalized DynRes observed in association and dissociation, loading one single concentration at 7.5 nM of Ab1, Ab4 and Ab5 on hCA1-DNA layers. These were compared to the first injection of Ab3 at 7.5 nM. Figure 7.13 illustrates the variation of normalized fluorescence levels, F_{st} and F_{ly} during antibody binding. Due to the inconstant initial ds-DNA densities the variation of observed response was not correlated to the amount of bound antibody on surface.

Table 7.5 lists the dissociation constants τ_{off} and k_{off}, of Ab1, Ab4 and Ab5 estimated based on DynRes. Table 7.6 summarizes the estimated constants τ_{on} and k_{on}, obtained as before from F_{ly}, F_{st} and DynRes evaluations, equally done for K_D summed up in Table 7.7.

Table 7.5 Dissociation time constants τ_{off} and kinetic constants k_{off}, of Ab1, Ab4 and Ab5 obtained fitting the DynRes curves. The values were compared to Ab3's constants, evaluated from the titration experiment. The SD values are indicated in round brackets.

	fitted τ_{off} [s]	k_{off} [10^{-4} s^{-1}]
Ab1	21700 (130)	0.46 (0.01)
Ab3	5000 (1500)	2.0 (0.4)
Ab4	24900 (260)	0.40 (0.01)
Ab5	3210 (120)	3.1 (0.1)

Table 7.6 Association time constants τ_{on} and kinetic constants k_{on} of Ab1, Ab4 and Ab5 obtained fitting absolute fluorescence F_{st} and F_{ly} signals, and DynRes. The values were compared to Ab3's constants, evaluated from the titration experiment. The SD values are indicated in round brackets.

	Ab1		Ab4		Ab5	
	τ_{on} [s]	k_{on} [10^6 $M^{-1}s^{-1}$]	τ_{on} [s]	k_{on} [10^6 $M^{-1}s^{-1}$]	τ_{on} [s]	k_{on} [10^6 $M^{-1}s^{-1}$]
F_{st}	13.5 (0.5)	9.9 (0.4)	20.2 (0.5)	6.6 (0.2)	18.5 (0.8)	7.2 (0.3)
F_{ly}	10.3 (0.5)	12.9 (0.7)	21.9 (0.8)	6.1 (0.2)	16.7 (0.5)	7.9 (0.2)
DynRes	16.5 (0.6)	8.1 (0.3)	18.2 (0.5)	7.3 (0.2)	16 (2)	8.0 (1.0)

Table 7.7 The equilibrium constants K_D of all four antibodies, calculated on k_{on} from absolute fluorescence F_{st} and F_{ly} signals, and DynRes. The SD values are indicated in round brackets.

	K_D [pM]			
	Ab1	**Ab3**	**Ab4**	**Ab5**
F_{st}	4.7 (0.2)	33 (13)	6.1 (0.2)	43 (3)
F_{ly}	3.6 (0.2)	200 (110)	6.6 (0.3)	39 (2)
DynRes	5.7 (0.2)	100 (54)	5.5 (0.2)	37 (5)

7.2.4 Tested cross-binding of monoclonal antibodies on *switch*SENSE

On *switch*SENSE the consecutive injections of two different antibodies were tested to verify their binding to different hCA1 epitopes, upon surface functionalization with hCA1-DNA mono conjugates (Figure 7.14).

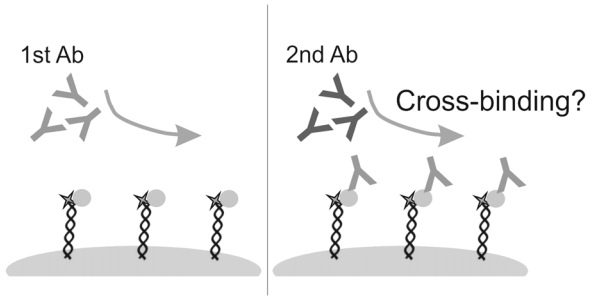

Figure 7.14 Experimental design for cross-binding detection on hCA1-DNA layers.

These experiments were performed on Prototype2. The antibodies were diluted in Standard Buffer at 15 nM final concentration and the injections were performed at 0.2 ml/min at 25 °C recording the association in real-time in KM mode for 20 min. After finished binding, VR and TR curves were measured for ds-hCA1-DNA layers and on bare ds-DNA layers.

For the evaluation, the Rising V_{max} resulting from the TRM curves was employed, because it was affected by low noise therefore the Standard Deviation was small. The Rising V_{max} after antibody injection was compared to the value of the initial layer. laminar velocity corresponded to 0.016 ms^{-1})

According to Eq. 5.1, the laminar velocity in Prototype2 flow cell corresponded to 0.016 m/s, which was calculated considering the flow channel dimensions of (0.8×4.0 (height × width) mm^2) and the employed flow rate $3.3*10^{-8}$ m^3s^{-1}. Therefore kinetic analysis was not performed.

Figure 7.15 displays the TRM data of cross-binding results. In all experiments, the curves of 1st and 2nd mAb injections overlapped each other, indicating that only the 1st mAb interacted significantly with hCA1 present on surface and the binding of the second loaded mAb was not observed.

The negative control layer did not show a significant unspecific binding for all injected antibodies: Figure 7.16 presents the data only for Ab1-Ab3 combination, whereas all the other results for negative control layers are presented in the Appendix (Section 14.5).

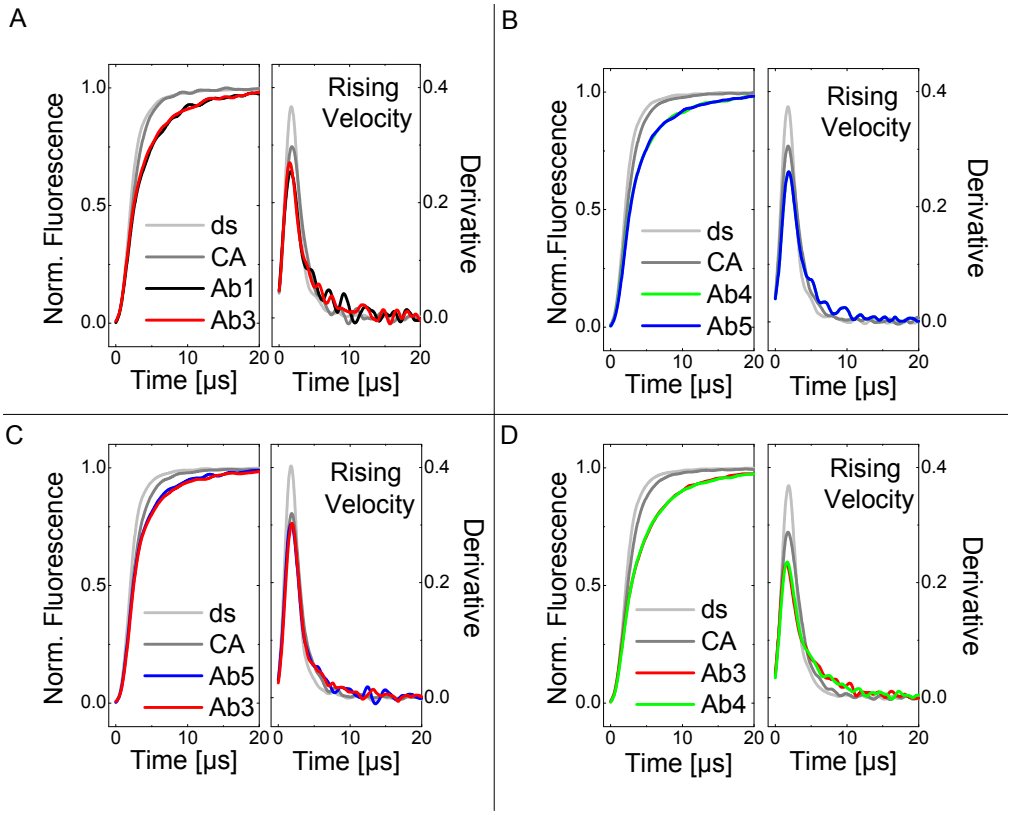

Figure 7.15 Time Resolved Measurements of cross-binding experiments of monoclonal antibodies on *switch*SENSE hCA1-DNA layers. Two different antibody solutions of 15 nM were injected in succession on hCA1-DNA and ds-DNA layers, (A) Ab1-Ab3, (B) Ab4-Ab5, (C) Ab5-Ab3, (D) Ab3-Ab4. The normalized fluorescence curves showed a significant binding by 1st injected mAb, and no further binding by 2nd loaded mAb, the curves in fact overlapped each other.[5]

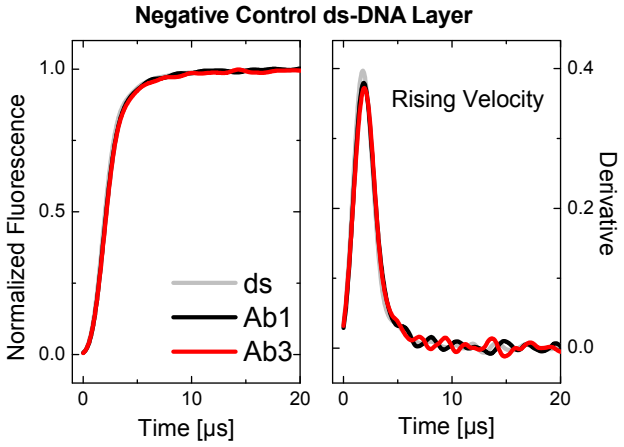

Figure 7.16 Time Resolved Measurements of cross-binding experiments of monoclonal antibodies on ds-DNA negative control. The consecutive loading of Ab1 and Ab3 (15 nM concentration) gave no unspecific binding on ds-DNA layers. Similar TRM data were obtained for Ab4-Ab5, Ab5-Ab3 and Ab3-Ab4 experiments (Appendix Section 14.5).

[5] data files: C86FGW50_area03_04_2012023; C89FGW50_area01_02_20120309; C90FGW50_20120311; C90FGW50_area01_02_20120310.

However a small affection on bare ds-DNA layer was visible in the evaluation of Rising V_{max} % (Figure 7.17).

Considering the first loaded antibody, Ab1 and Ab4 gave a Rising V_{max} 85% respect the initial value of hCA1-DNA layer (Figure 7.17 A-B), while the binding of Ab3 was more prominent (80%) (Figure 7.17 D). As for Ab5 the effect on surface was really weak, 95%, nevertheless Ab3 couldn't bind hCA1 after Ab5 (Figure 7.17 C). This indicates that Ab5 did bind hCA1, saturating the layer and preventing further binding by Ab3. Looking at negative control signals, ds-DNA layers showed to be in minor part affected by 1st mAb loading, and after the 2nd loading this effect became a bit more pronounced. This was observed in all four measurements, meaning that the unspecific signal did not depend on which antibody was loaded. Probably this is all due to a degeneration of surface, resulting from a constant injection of protein solution.

Two combinations, Ab1/Ab4 and Ab1/Ab5, were not checked on surface. Finally Ab3 didn't binding hCA1 after Ab1, Ab4 and Ab5, hence Ab1 was considered not able to bind hCA1 after Ab4 and Ab5.

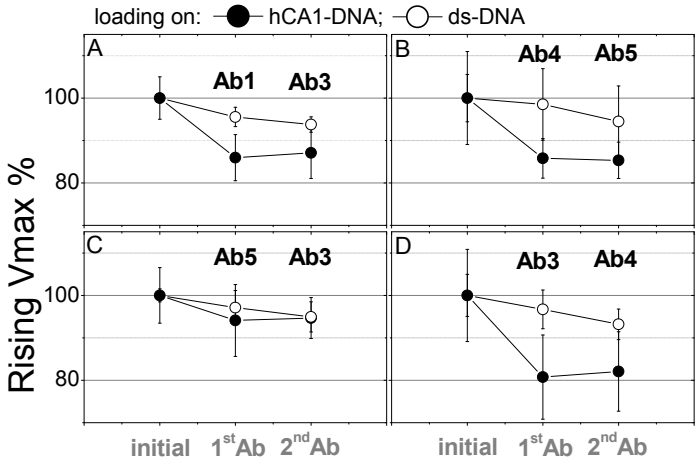

Figure 7.17 Rising maximum velocity % of cross-binding experiments of monoclonal antibodies on hCA1-DNA *switch*SENSE. Two consecutive injections of different mAbs were done on both hCA1-DNA and ds-DNA layers, (A) Ab1-Ab3, (B) Ab4-Ab5, (C) Ab5-Ab3, (D) Ab3-Ab4. The resulting rising maximum velocity, measured after the binding event occurred, was normalized by percentage (rising velocity %), considering the initial velocity of hCA1-DNA, as experimental layer (black circle), or of ds-DNA as negative control layer (open circle). Not all six combinations were measured; due to the results, Ab1 was considered not able to cross-bind Ab4 and Ab5.

7.2.5 Discussion

7.2.5.1 Immobilized ligand level on Biacore

The residual binding activity of the ligand immobilized on surface was roughly evaluated as percentage ratio of fitted Rmax (indicated in each corresponding evaluation table in Appendix, Section 14.3) and expected Rmax, taking in account the stoichiometric ratio of the interaction and the avidity effect on CM5 surface with immobilized hCA1 (one molecule of Ab3 per two molecules of immobilized hCA1, using Eq. 7.2).

Eq. 7.2
$$\boldsymbol{binding\ capacity\ (RU)} = \frac{\boldsymbol{MW_{analyte}}}{\boldsymbol{MW_{ligand}}} \cdot \boldsymbol{immobilized\ ligand\ (RU)}$$

It is expressed in Response Unit (RU), whereby 1 RU corresponds approximately to 1 pg of protein per mm^2 on CM5.

Considering hCA1 on CM5 chip, a much high immobilization level was required, ca. 300 RU, to achieve Rmax value for Ab3 binding of 60 RU. The immobilized ligand corresponded to ∽0.01 pmol/mm^2 (15-fold higher respect the theoretical value). This indicates a strongly reduced "activity" of hCA1 on surface, with a residual binding activity approximately of 8%.

The different orientations and folding state of immobilized hCA1 surely affected the total binding sites on surface, recognizable by Ab3. Furthermore, as described in Section 6.2.2.1.1, the initial sample of hCA1 displayed ∽7% of glycosylated forms; a feature that results in the glycosylation is to hide peptide epitopes recognised by mAb, thus further decreasing the number of binding sites.

As for mAb Ab1, Ab3, Ab4 and Ab5 on CM5 chip, once more high ligand immobilization levels were necessary, to range from 1100 to 1500 RU related to ∽0.01 pmol/mm^2 (approximately 5-fold higher respect calculated value). In this condition, the Rmax values achieved for hCA1 binding were between 80-140 RU. The obtained residual binding activity of mAbs was about 20-30%.

In order to observe the saturation level, a serial dilution of hCA1 high concentration regime was loaded on the Ab3-CM5 chip, from 0.1 to 12.5 μM, in a multi-cycle manner (Figure 7.18). At high loaded concentration the saturation level of hCA1 bound on Ab3 was not observed, most likely due to a multi-layer formation of hCA1 on the surface.

As mentioned before, adverse orientations and folding state of immobilized mAbs affect their binding activity. Even the initial probe activity of received mAb can be a probable cause, but that could not be verified, due to the high material costs. Similarly in (Drake et al, 2012), they observed a significant reduction in activity for a mAb immobilized on

CM5 surface. Their hypothesis was that due to the acidic pI of analyte (5.0-6.5 range), this could not bind to mAb buried in the dextran matrix, being electrostatically repelled by the negative dextran charge. As for hCA1, pI is around 6.5, this could be one more reason to explain the reduced activity of mAbs on surface. Regarding the reverse orientation, Ab3 on hCA1-CM5, the pI for this murine IgG1 should be around 7.0–8.5 (Amersham Biosciences, 2002), so no electrostatic affection should be involved in the observed reduced activity.

With regard to the C1 chip experiment, hCA1 immobilized level was adjusted to *switch*SENSE estimated surface density. Considering the upper limit of 10^{11} molecules/cm^2 for ds-DNA (Arinaga et al, 2007), and assuming a complete coverage by hybridized hCA1 mono-conjugate, the evaluated protein density is 2 fmol/mm^2 or 48 pg hCA1/mm^2, that translated in Biacore terms is equal to ∽48 RU immobilized ligand level. The achieved Rmax for Ab1, Ab3, Ab4 and Ab5 was in a range of between 22 and 38 RU. The obtained residual binding activity was 11% neglecting the avidity, as explained in the following section.

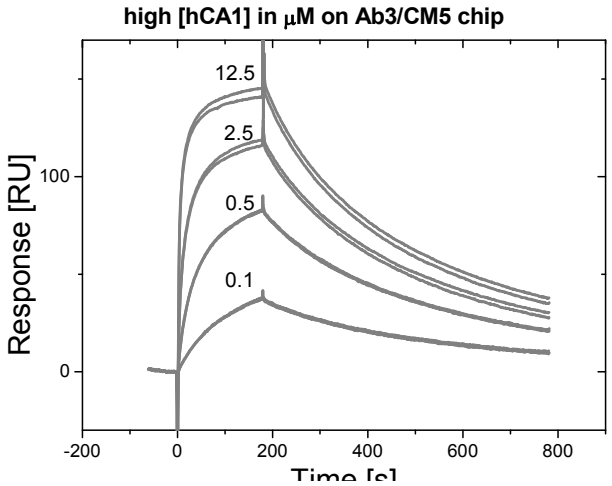

Figure 7.18 Sensorgrams of hCA1 association and dissociation on functionalized Ab3-CM5 surface in multi-cycle assay. hCA1 dilutions, 0.1, 0.5, 2.5, 12.5 µM prepared in running buffer HBS-P, were injected twice on Ab3-CM5 surface (immobilization level 1250 RU) at 30 µl/min and 25 °C, and a buffer-only tube was run between every single series. The association was observed for 180 s, and dissociation for 600 s, followed by a regeneration step (30 s contact 10 mM Gly-HCl pH 2.0 at 10 µl/min). The saturation level in binding wasn't achieved due to a multi-layer formation of hCA1 on CM5 chip.

7.2.5.2 Comparison of measured kinetic constants on Biacore

In Biacore, the different surface chip and immobilization orientation resulted in dissimilar kinetic parameters.

Discussing first the surface type affection, the dextran matrix present on CM5 chip affected physically the rate constants of Ab3 analyte on hCA1 ligand, like already described in literature (Drake et al, 2012; Fong et al, 2002; Xiaodi et al, 2007). This hydrogel matrix is highly carboxymethylated and generally preferred to simpler 2D self-assembled monolayers (SAM) due to the high surface capacity for ligand immobilization, which allows in some cases an enhancement of sensitivity. However, considering the Ab3 analyte interacting with the hCA1 ligand, on C1 chip the association rate was 3-fold higher than on CM5 chip, k_{on} 2.78(±0.02)*10^5 $M^{-1}s^{-1}$ and 0.98(±0.02)*10^5 $M^{-1}s^{-1}$, respectively. The dissociation rate on C1 chip was 4 times higher compared to the CM5 chip, k_{off} 0.83(±0.01)*10^{-3} s^{-1} and 0.21(±0.07)*10^{-3} s^{-1}, respectively. This indicates that observed binding and unbinding events were both faster on C1 chip (Figure 7.19 A). Similarly, Drake *et al.* observed 10 times higher k_{on} on C1 chip compared to CM5, maintaining the same orientation analyte-ligand (the k_{off} constants were similar) (Drake et al, 2012). They justified this behaviour by electrostatic repulsion of the acidic analyte on dextran matrix, not present on C1 chip. Also, Fong *et al.* using a self–made SAM noted higher k_{on} and k_{off} rates (15- and 2-times, respectively), in contrast with the CM5 surface (Fong et al, 2002). The authors attributed the observed differences to steric hindrance and to mass transport artefacts, as the analyte diffusion was prevented by dextran matrix. In this work, the second hypothesis can describe better what was observed, namely that 2D SAM reduced some of the steric effects presented by 3D dextran surface.

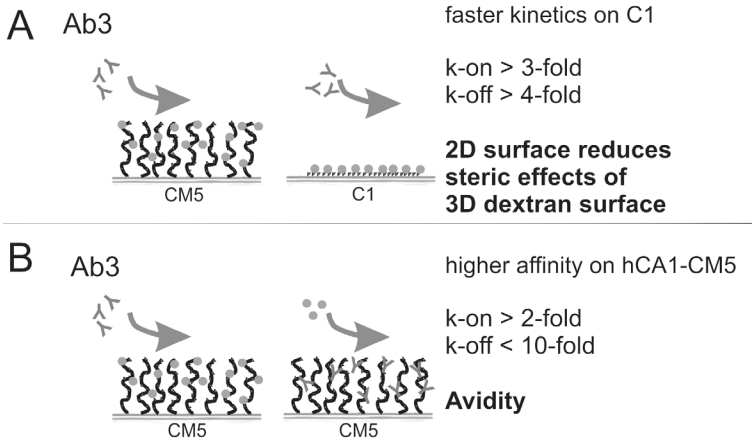

Figure 7.19 The measured kinetics of Ab3 on Biacore was dissimilar depending on the used surface chip and immobilization orientation. A: having hCA1 immobilized on surface, the association and dissociation were both faster on C1 chip than on CM5, due to the decreased steric effect on 2D surface geometry. B: Ab3 displayed higher affinity binding immobilized hCA1 on CM5, compared to the opposite orientation, due to the avidity effect.

Considering the orientation of ligand-analyte experiment, the avidity, or bivalent binding, should be taken in to account on CM5 chip with immobilized hCA1. An antibody

possesses two identical binding sites, and while one site has already bound one ligand, the second free site is in close contact with another ligand molecule. This will affect the K_D, stabilizing the complex. The formation of the second binding depends on the flexibility of both analyte and ligand on the dextran layer and the density of immobilized ligand.

The measured K_D 2.1(±0.7) nM of Ab3 analyte on hCA1-CM5 chip was affected by avidity effect: compared to the opposite orientation, the association rate was 2-fold higher (k_{on} $0.98(\pm0.02)*10^5 M^{-1}s^{-1}$ and $0.458(\pm0.001)*10^5 M^{-1}s^{-1}$, respectively) and the dissociation rate was 10 times slower (k_{off} $0.21(\pm0.07)*10^{-3}$ s^{-1} and $2.122(\pm0.004)*10^{-3}$ s^{-1}, respectively) (Figure 7.19 B).

Regarding C1 experiments having mAb as analyte and hCA1 as ligand, the bivalent binding by the Ab was excluded and the kinetics resembled one to one interaction between mAb and hCA1. The main reason was the significantly diluted density of immobilized ligand, $\backsim 10^{11}$ molecules/cm^2, resulting in one molecule of hCA1 on 1000 nm^2 (1000 nm^2 is a square of 31.6 nm side). A very high excess of antibody was loaded on surface, in the nanomolar concentrations, approximately 10^{15} molecules per litre. Consequentially, based on the dimensions of both proteins, the probability that the free binding site of antibody came into close proximity to a second hCA1 molecule was low and therefore neglected (Figure 7.20). The hydrodynamic diameter D_h of IgG at pH 7.6 is around 11 nm (Armstrong et al, 2004; Jossang et al, 1988), as for hCA1, D_h was measured in this work at neutral pH, equal to $\backsim$6 nm (Section 6.4.4).

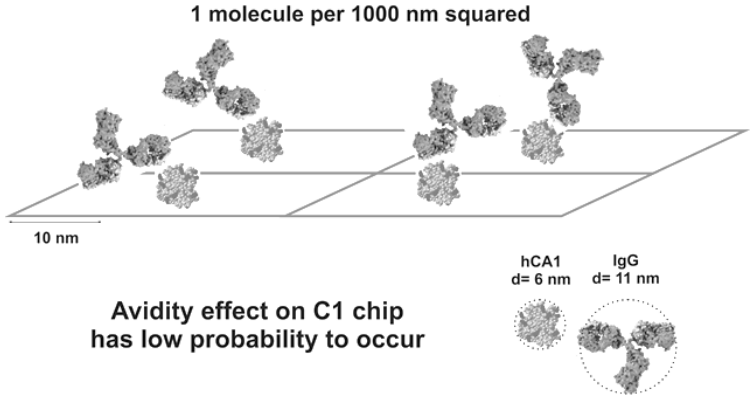

Figure 7.20 IgG analyte, binding hCA1, immobilized on C1 surface chip. The avidity displayed by IgG on the C1 chip was considered negligible, due to the much diluted density of immobilized ligand, 10^{11} molecules/cm^2 and equal to one hCA1 per 1000 nm^2, and also due to the dimensions of both proteins, hCA1 with D_h of 6 nm and IgG of 11 nm[6].

[6] IgG picture was taken from http://ghr.nlm.nih.gov/handbook/illustrations/igg

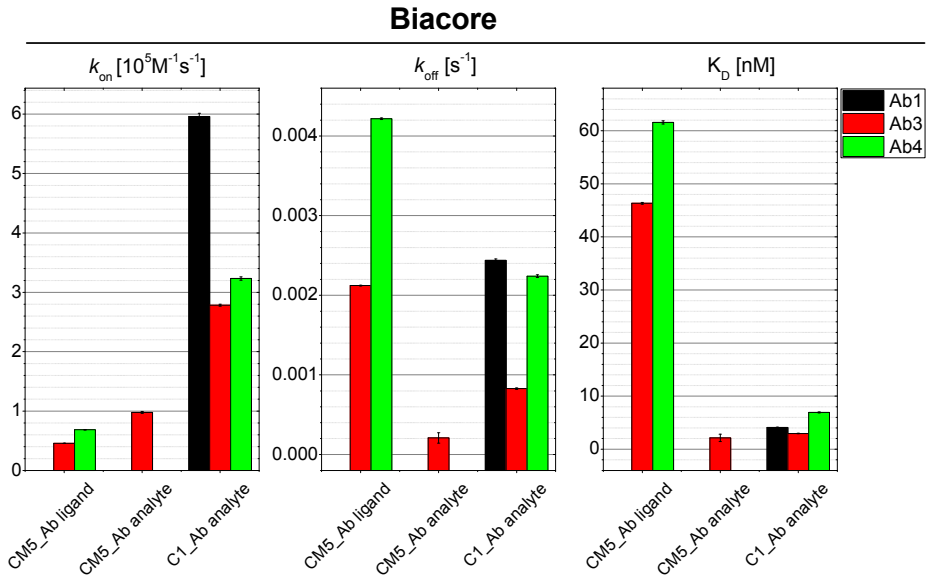

Figure 7.21 Estimated rate and equilibrium constants for Ab1, Ab3, Ab4 in affinity binding with hCA1 in Biacore. In a bar chart all k_{on}, k_{off} and K_D were compared (Ab1 in black, Ab3 in red, Ab4 in green), obtained using different orientation and surface type. The resulting kinetics of Ab5 was mass transfer limited on both CM5 and C1 chips.

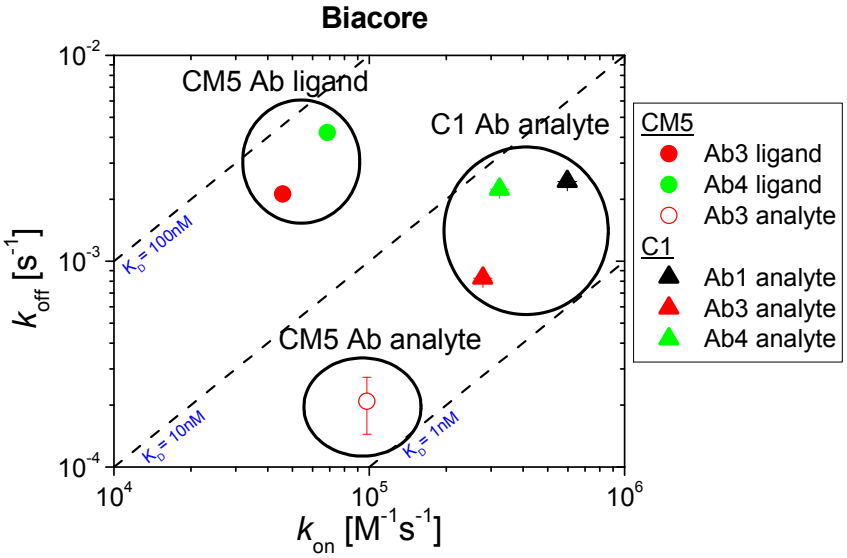

Figure 7.22 k_{off} vs. k_{on} plot of rate constants for the affinity of monoclonal antibodies and hCA1, measured on Biacore. The constants were evaluated for Ab1, Ab3 and Ab4 (black, red and green symbol, respectively). Ab3 was observed on CM5 chip as analye (open red circle) and as ligand (filled red circle) and on C1 chip ad analyte (red triangle), while Ab4 on CM5 as ligand (green circle) and on C1 as analyte (green triangle). The kinetics of Ab1 was not mass limited just on C1 chip, injected as analyte (black triangle). Excluding the avidity on highly diluted hCA1-C1 chip, the association rates of the antibody Ab3 and Ab4 to hCA1 were faster compare to CM5 surface. The dissociation rates were instead all similar, with k_{off} distributed around $2*10^{-3}$ s^{-1}. Finally Ab3 displayed the highest affinity.

Excluding the avidity on C1 chip, the bar chart (Figure 7.21) and the k_{off} vs. k_{on} plot (Figure 7.22) present the faster association rates of the analytes Ab3 and Ab4 with the hCA1 ligand on C1 chip, k_{on} 2.78(±0.02)*10^5 M^{-1}s^{-1} and 3.23(±0.03)*10^5 M^{-1}s^{-1}, respectively. On CM5 surface the measured k_{on} were 0.458(±0.001)*10^5 M^{-1}s^{-1} and 0.685(±0.005)*10^5 M^{-1}s^{-1} for Ab3 and Ab4, respectively. The dissociation rates were instead all similar, distributed around 2*10^{-3} s^{-1}, confirming no avidity effect on C1 chip.
Finally the measured affinity on C1 chips were in the nanomolar regime, with K_D value of 4.09(±0.05) nM for Ab1, 6.9(±0.1) nM for Ab4 and 2.97(±0.04) nM for Ab3, which displayed the highest affinity.

7.2.5.3 Comparison of measured kinetic constants on switchSENSE

Figure 7.23 presents the measured rate constants and affinity values for all four antibodies.

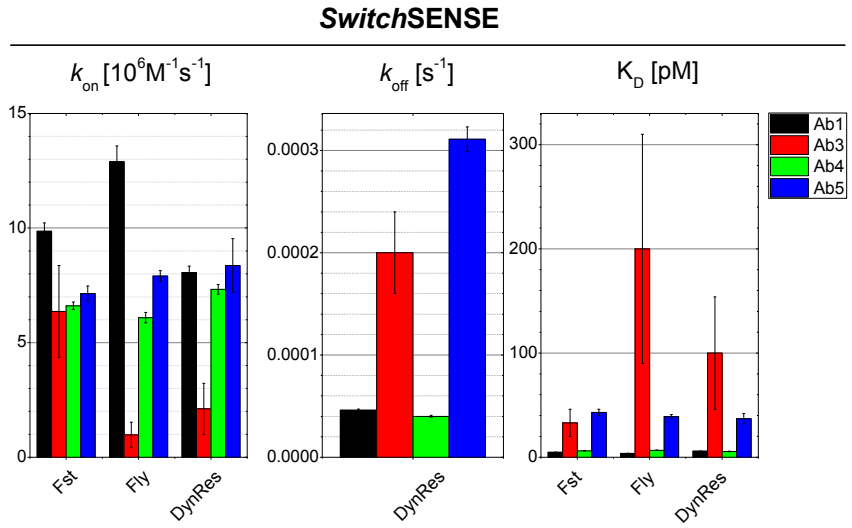

Figure 7.23 Estimated rate and equilibrium constants for Ab1, Ab3, Ab4 and Ab5 in affinity binding on hCA1-DNA layers. All k_{on}, k_{off} and K_D were compared (Ab1 in black, Ab3 in red, Ab4 in green, Ab5 in blue), obtained by k_{on} fitted from F_{st}, F_{ly}, and DynRes.

The dissociation of Ab1 was as slow as the dissociation of Ab4, k_{off} ∽0.4*10^{-4} s^{-1}. While compared to them, Ab3 and Ab5 dissociated 5 times faster, k_{off} ∽2*10^{-4} s^{-1}.
In association, the evaluation of k_{on} from F_{st}, F_{ly} and DynRes gave related results within one injected antibody, with average k_{on} of ∽10*10^6 M^{-1}s^{-1}, ∽7*10^6 M^{-1}s^{-1} and ∽8*10^6 M^{-1}s^{-1} for Ab1, Ab4 and Ab5, respectively (Table 7.6). Considering the titration experiment for Ab3 (Table 7.4), the linear regression gave more distributed k_{on} values from F_{st}, F_{ly} and DynRes but still comparable between each other, k_{on} ∽1*10^6 M^{-1}s^{-1}.

The unusual effect on absolute fluorescence levels observed during antibody binding needs to be expanded on the following Section 7.2.5.5. Whereas DynRes curves remains more suitable for data evaluation, being the integrated area independent from any quenching effect on Cy3 and clearly correlated with the dynamics of DNA strands at applied repulsive potential.

Based on DynRes evaluation, Ab1 and Ab4 presented the highest affinity, with analogues K_D of 5 pM, followed by Ab5 K_D 37(±5) pM and Ab3 K_D 100(±54) pM. Finally, the kinetics of Ab3 had higher deviation, since the titration experiment introduced more experimental variation.

In Section 7.2.5.4 the comparison between *switch*SENSE and Biacore results was discussed on the values obtained in DynRes evaluation.

7.2.5.4 Comparison of kinetics measured on switchSENSE and Biacore

Figure 7.24 presents the k_{on} and k_{off} evaluated in *switch*SENSE and Biacore in a k_{off} vs. k_{on} plot, and Table 7.8 summarizes all values. Remarkably, the surface geometry and the detection method affected the kinetic results. As it was previously discussed in Section 7.2.5.2, the 2D surface geometry reduced the steric effects presented by 3D dextran surface, allowing faster kinetics in both association and dissociation phases.

Furthermore, *switch*SENSE displayed higher detection sensitivity in antibody binding, compared to 2D surface of C1 chips.

On DNA layers the observed k_{off} was one order of magnitude lower and k_{on} one order of magnitude higher with respect to the kinetic rates measured on C1 surface. The influence on faster association and slower dissociation deriving from the negative charge of switchable DNA layers was excluded, since unspecific interaction was not observed loading the antibody solutions on bare ds-DNA.

On switchable DNA layers the much slower dissociation was due to the avidity, which it is discussed in more detail in the following section. Regarding the faster association, the laminar velocity of the analyte solution in the flow channel of *switch*SENSE was slightly higher (0.42 m/s and 0.30 m/s, in *switch*SENSE and in Biacore respectively), however this cannot explain a 10 time higher association, which is probably due to the high detection sensitivity of the switching dynamics. Consequent to these differences observed in k_{on} and k_{off}, the affinity values were distributed in the picomolar regime on switchable DNA layers and in the nanomolar regime on C1 chips.

Table 7.8 The constants k_{on}, k_{off} and K_D measured for the antibodies on *switch*SENSE and Biacore. Since the affinity values were drastically different, K_D for *switch*SENSE was expressed in picomolar, for Biacore in nanomolar. On *switch*SENSE DynRes data were evaluated for kinetic analyses. The

kinetics affected by mass transfer limitation were not indicated. The SD values are indicated in round brackets.

switch*SENSE (*DynRes)			
Antibody	k_{on} **[10^5 $M^{-1}s^{-1}$]**	k_{off} **[10^{-4} s^{-1}]**	K_D **[pM]**
Ab1	81 (3)	0.46 (0.01)	5.7 (0.2)
Ab3	20 (10)	2.0 (0.4)	100 (54)
Ab4	73 (2)	0.40 (0.01)	5.5 (0.2)
Ab5	80 (10)	3.1 (0.1)	37 (5)
Biacore (*C1 chip)*			
	k_{on} **[10^5 $M^{-1}s^{-1}$]**	k_{off} **[10^{-4} s^{-1}]**	K_D **[nM]**
Ab1	5.96 (0.06)	24.4 (0.2)	4.09 (0.05)
Ab3	2.78 (0.02)	8.3 (0.1)	2.97 (0.04)
Ab4	3.23 (0.03)	22.4 (0.2)	6.9 (0.1)
Ab5	Mass transfer limited	Mass transfer limited	Mass transfer limited
Biacore (*CM5 chip)*			
	k_{on} **[10^5 $M^{-1}s^{-1}$]**	k_{off} **[10^{-4} s^{-1}]**	K_D **[nM]**
Ab1 (ligand)	Mass transfer limited	Mass transfer limited	Mass transfer limited
Ab3 (ligand)	0.46 (0.01)	2.12 (0.01)	46.3 (0.2)
Ab4 (ligand)	0.69 (0.01)	4.22 (0.01)	61.6 (0.3)
Ab5 (ligand)	Mass transfer limited	Mass transfer limited	Mass transfer limited
Ab3 analyte	0.98 (0.02)	0.21 (0.07)	2.1 (0.7)

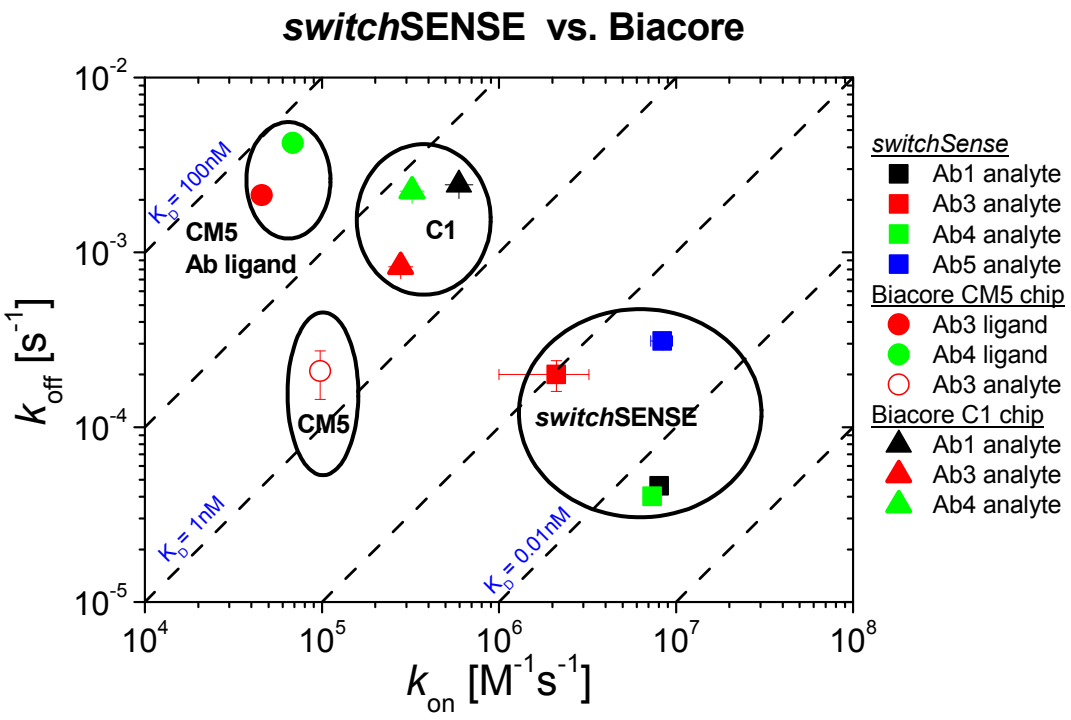

Figure 7.24 Comparison of k_{on} and k_{off} measured for the antibodies on *switch*SENSE and Biacore. The constants for Ab1, Ab3, Ab4 and Ab5 (black, red, green and blue symbols, respectively) were evaluated in kinetic analyses on *switch*SENSE (squares) by DynRes and on Biacore CM5 and C1 surfaces (circles and triangles, respectively). The plot displays the kinetics which were not mass limited in Biacore.

7.2.5.5 Inter-linking of antibody due to avidity on switchSENSE

The effects on absolute fluorescence levels are here discussed, since these variations were observed during antibody binding (Figure 7.10 and Figure 7.13) on SWA1 but not on Prototype2.

On Prototype2 the antibodies were analysed in cross-binding experiments, as describe in Section 7.2.4. Using the previous fluidic channel, kinetic analyses could not be performed due to mass transport limitation, nevertheless the binding of 1st injected mAb was also measured in KM mode recording the absolute fluorescence levels, and instead no dissociation curve was documented since it was not required from the experiment. Figure 7.25 shows the comparison of F_{st} and F_{ly} in KM measurements, loading 15 nM of Ab3 on SWA1 and on Prototype2. Interestingly, F_{st} decreased in both experiments, whereas F_{ly} increased in intensity just on SWA1 layer (Figure 7.25, left plot). Analogue observations were seen detected loading 15 nM of Ab1, Ab4 and Ab5 on Prototype2 (Appendix, Section 14.5).

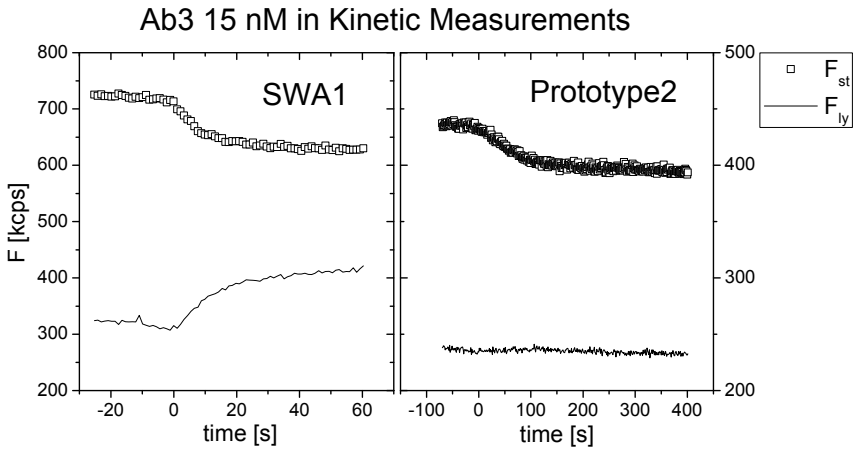

Figure 7.25 Absolute fluorescence levels in Kinetic Measurements for Ab3 15 nM concentration, loaded in SWA1 and in Prototype2. A solution of 15 nM Ab3 was loaded on hCA1-DNA layers in SWA1 (left graph) and Prototype2 (right graph). Here the resulting fluorescence levels, F_{st} and F_{ly} (black open square and black line, respectively), obtained in Kinetic Mode measurements, were compared. In both machines the same LED power was applied. Finally, F_{st} decreased in both experiments, whereas F_{ly} increased in intensity just on SWA1 layer. The initial ds-DNA density on SWA1 chips was higher than the density of Prototype2 chip. Consequently, Ab3 showed an avidity effect in binding hCA1 on surface.

Considering the ss-DNA on surface all hybridized to hCA1-DNA mono conjugates, what makes the different is the initial ds-DNA density between the two experiments.
The fluorescence levels of Prototype2 electrodes, averaged over four ds-DNA layers for KM recordings, were F_{ly} and F_{st} 13/25 kcps, ΔF_{rel} 51 % (already converted to LED 0.2 V). Considering all used electrodes for kinetic analyses in SWA1, the average values of fluorescence intensity were 19/49 kcps, ΔF_{rel} 61 %, so the density was significantly higher (data of fluorescence levels in Appendix, Section 14.6, for SWA1 and Prototype2). As a result, Ab3 showed probably an avidity effect inter-linking two hCA1-DNA strands on SWA1 layer.

The definition of "ultra-low density" layer assumes a 2D monolayer with a hexagonal-close packing (hcp) (Rant, 2005), having the average distance between two neighbouring strands exciding the minimum distance for interactions (no steric hindrance). As for ds-48-mer (16.3 nm length), no steric hindrance would occur below the critical density of 10^{11} molecules/cm^2 with a minimum distance of 32.6 nm.
In presence of covalently attached hCA1 (D_h ∽6 nm, linker length 2.5 nm, total length 24.8 nm), the minimum distance would increase to 49.6 nm. Moreover, IgG has the two

antigen binding sites, 10 nm far from each other; hence the avidity effect would not occur at minimum distance of 59.6, approximated to 60 nm.

Considering the calculation of Langer and Kaiser (Langer et al, Paper in progress A), at repulsive potential the highest probable orientation of ds-DNA has an angle α of ∽45°, while at attractive potential α is approximately 10°-12°. Because hCA1 covalently bound to ds-DNA gives steric hindrance on surface, the angle α at attractive potential was assumed equal to 14°.

Now, to calculate the new minimum distance, the problem was solved in trigonometry.

The right-angled triangle possesses an angle α=14° (converted in radian α=0.244) and its hypotenuse *h* is equal to the total length of ds-hCA1-DNA plus one IgG binding site (5 nm), *h*= 29.8 nm. The resulting base of triangle is 28.9 nm. Hence the minimum distance would be slightly reduced to 57.8 nm (ca. 58 nm) (Figure 7.26 A). Finally the critical density σ, having hcp-radius r of ≈300 Å would result in $3.5*10^{10}$ molecules/cm^2, according to Eq. 7.3 (Rant, 2005):

Eq. 7.3 $$\boldsymbol{r = \left(2\sqrt{3} \cdot \sigma\right)^{-1/2}}$$

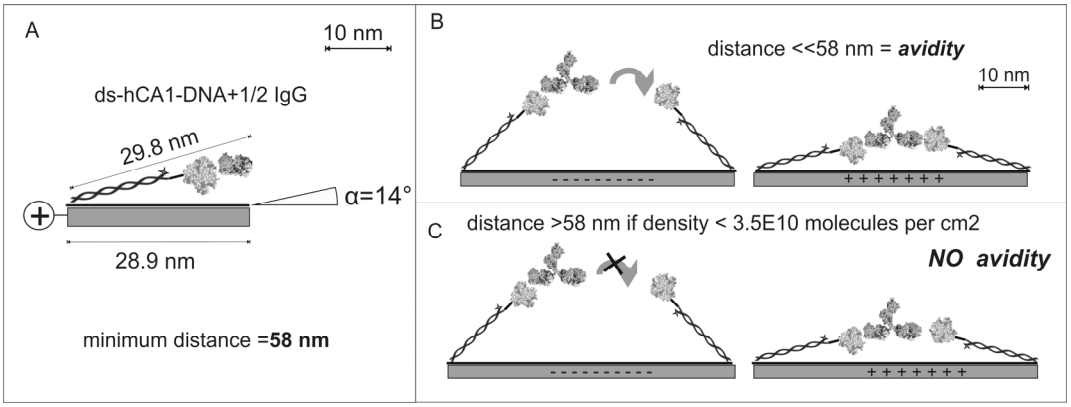

Figure 7.26 Avidity effect of antibody binding on *switch*SENSE based on calculated minimum distance. A: the critical density of 3.5E10 molecules per squared-cm of ds-hCA1-DNA was estimated, characterized by a minimum distance of 58 nm. B: above this density value, the IgG, which is already bound to one hCA1-DNA strand, can interact by its second binding site with a proximal hCA1 during the at tractive potential. C: below this density value, the IgG cannot reach a second hCA1-DNA strand, displaying no inter-linking.

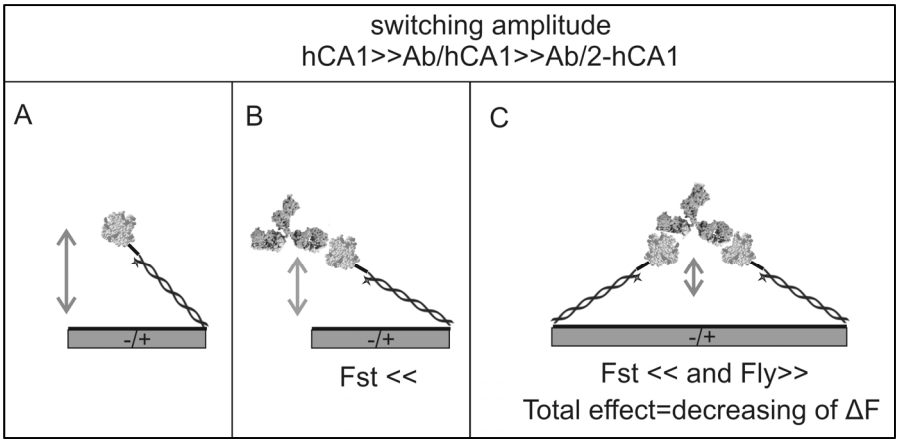

Figure 7.27 The affection of fluorescence levels by the constrained dynamics of Ab/2-hCA1-DNA complex. A: hCA1-DNA strands are characterized by certain switching amplitude. B: upon one antibody binding to one hCA1-DNA, the complex becomes bigger, the amplitude decreases resulting in a reduced F_{st} because the complex cannot stand up as it could previously do. C: if one antibody is bound to two hCA1-DNA strands, the complex becomes much tighter, the switching amplitude decreases affecting also the falling movement, whereby F_{ly} increases since the complex cannot lie down as it could initially do.

Transferring this ideas on what was observed in Figure 7.25, on SWA1 chips the layer density was considered above of calculated critical value, consequently the antibody already attached to one hCA1-DNA strand, could inter-link by its second binding site a proximal hCA1, during the attractive potential (Figure 7.26 B). Whereas on Prototype2 chips the layer density was below the critical value and the antibody could not reach a second hCA1-DNA strand; hereby the distance between ds-hCA1-DNA was increased (Figure 7.26 C)[7].

The switching dynamics of an antibody bound on 2 ds-hCA1-DNA strands is difficult to predict. Surely, this assembly is more constrained and tighter compared to the monomeric interaction IgG/hCA1. The observed effect in KM measurements (Figure 7.10, Figure 7.13 and Figure 7.25) on absolute fluorescence could be explained by diminished switching amplitude. Initially, hCA1-DNA strands are characterized by a certain switching amplitude (Figure 7.27 A). Once IgG/hCA1-DNA complex is formed, by steric hindrance and reduced entropy the switching amplitude decreases and F_{st} intensity goes down, because the complex cannot stand up as the hCA1-DNA could previously do (Figure 7.27 B). Eventually, if IgG is bound to two hCA1-DNA, the complex

[7] The fits of DynRes curves on Prototype2 gave k_{on} values 10 times lower compared to SWA1 and the bivalent binding was excluded. However, the kinetics was mass transfer limited (Appendix Section 14.5).

becomes even tighter, as a result the switching amplitude turns out to be smaller and F_{ly} increases, since the complex cannot lie down as the initial hCA1-DNA could do (Figure 7.27 C).

What remains an issue is to model and simulate a bivalent binding on *switch*SENSE to extract the two rates in both association and dissociation phases. The simulation should quantify the influence of bivalent binding on the fluorescence signals and in switching dynamics, as a function of the DNA probe density, the analyte concentration, and the binding site distance within the analyte molecule. Due to the complexity of this surface, the issue is currently under investigation.

7.2.5.6 No cross-binding of monoclonal antibodies on switchSENSE

Loading consecutively two different antibodies on hCA1-DNA layers, the second injected mAb did not bind in any of the different combinations.

Considering the all binding sites saturated by the first injected antibody, this could indicate that the selected monoclonal antibodies recognize the same epitope of hCA1. Another possibility might be that the presence of a bound mAb on hCA1 screens the epitope recognized by the second loaded mAb, preventing its binding. Due to the dimensions of IgG and hCA1 (Figure 7.20) there is no strong reason that the first bound antibody should avoid by steric hindrance the binding of the second loaded antibody. Usually, to detect cross-binding or competition between antibodies a competitive ELISA assay is performed (Gu et al, 2011; Marissen et al, 2005), whereby the antigen density is very high in the coated well and the steric hindrance effect is therefore much more substantial.

7.3 Conclusion

The comparative study of antibody affinity was presented. It was carried out selecting four monoclonal antibodies against hCA1. Their kinetics was characterized on *switch*SENSE upon surface functionalization with hCA1-DNA mono conjugates. The antibody kinetics was also evaluated in Biacore™ for a direct comparison. Furthermore, the consecutive injections of two different antibodies were tested to verify their binding to different hCA1 epitopes on *switch*SENSE.

Remarkably, the surface architecture and the detection method influenced the kinetic results. On Biacore™, the 2D surface geometry of C1 chip reduced the steric effects presented by 3D dextran surface of CM5 chip, allowing faster kinetics of antibody/hCA1 interactions in both association and dissociation phases.

Additionally, *switch*SENSE displayed higher sensitivity detecting antibody binding, compared to 2D surface of C1 chip. On DNA layers the observed k_{off} was one order of magnitude lower and k_{on} one order of magnitude higher with respect to the kinetic rates measured on C1 surface.

On switchable DNA layers the much slower dissociation was due to the avidity. Regarding the faster association, *Switch*SENSE displayed higher detection sensitivity, based on DNA switching dynamics, in comparison with SPR signal. Consequent to these differences observed in k_{on} and k_{off}, the affinity values were distributed in the picomolar regime on switchable DNA layers and in the nanomolar regime on C1 chips.

The inter-linking of the antibody on *switch*SENSE surface was observed on high density DNA layers, whereby an IgG could bind two hCA1-DNA strands, which were in close proximity.The critical density of molecules arranged in hcp 2D geometry was estimated to be $3.5*10^{10}$ molecules/cm^2.

The consecutive injections of different combinations of monoclonal antibodies did not display a second binding event, meaning no cross-binding on hCA1 was observed among these four antibodies. Due to the dimensions of IgG and hCA1, there is no solid reason that the first bound antibody should avoid by steric hindrance the binding of the second loaded antibody. Therefore, the selected monoclonal antibodies might recognize the same epitope of hCA1 or another possibility is that the presence of a bound mAb on hCA1 screens the epitope recognized by the second loaded mAb, preventing its binding.

8. Human p53 analysed in *switch*SENSE

8.1 Introduction: p53 tumour suppressor

The protein p53 is often described as "the guardian of the genome" due to its role in preserving the genome stability from mutations (Lane, 1992). For this good reason, p53 is one of the most extensively studied proteins.

The protein was discovered thirty years ago as a cellular partner of simian virus 40 large T-antigen, the oncoprotein of this tumour virus (Lane & Crawford, 1979). Then it became clear that p53 is not an oncogene but a tumour suppressor that is very frequently mutated in human cancer.

After transactivation to stress stimuli, such as DNA damage, UV light or presence of oncogenes, p53 acts as a transcription factor and binds to specific DNA consensus sequences of promoter regions to stimulate the transcription of the corresponding target genes. The products of these genes are then responsible for the induction of the cell cycle arrest (Giono & Manfredi, 2006; Gottifredi et al, 2000; North & Hainaut, 2000), DNA repair mechanisms (Okorokov, 2003; Sengupta & Harris, 2005; Soddu & Sacchi, 1997), or, if the repair is not successful, for the induction of apoptosis (Amaral et al, 2010; Marchenko et al, 2000; Meulmeester & Jochemsen, 2008; Nayak et al, 2009).

The critical role in cancer prevention is highlighted by the presence of inactive p53 in more than 50% of all human tumours (Petitjean et al, 2007; Soussi et al, 1994; Vogelstein et al, 2000). Most of those mutations interfere with the DNA-binding ability of the protein (Brachmann et al, 1998), resetting the response pathways under p53's control.

As schematically represented in Figure 8.1, p53 is the hub of a complex broad network and enables the integration of an assortment of signal cascades (Evan & Vousden, 2001; Jin & Levine, 2001). *In vivo*, p53 protein levels are normally low in unstressed cells, the suggested basal level of p53 is around 1-10 nM (Sakaguchi et al, 1997). This is due to the autoregulatory feedback loop with MDM2 (Barak et al, 1993; Picksley & Lane, 1993; Wu et al, 1993) that keeps the turnover of p53 rapid. Hereby, p53 stimulates the expression of MDM2, which in return inhibits p53 activity in at least three different ways: firstly, by binding to its N-terminal transactivation domain, it inhibits its transcriptional activity (Kussie et al, 1996; Momand et al, 1992); secondly, MDM2 promotes p53 degradation via ubiquitin/proteasome, acting as an ubiquitin ligase (Fang et al, 2000; Honda &

Yasuda, 2000); and thirdly, MDM2 bound to p53 favours the export of p53 from the nucleus because it contains a nuclear export signal (Roth et al, 1998).

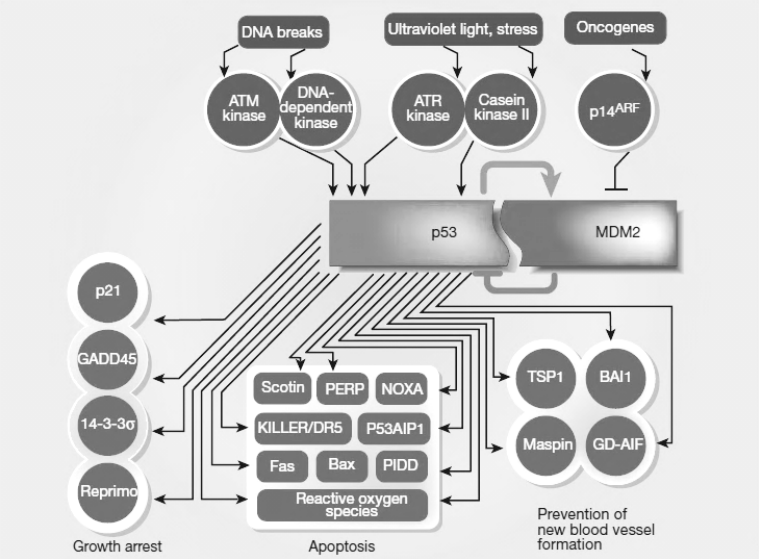

Figure 8.1 Simplified network of the p53 transcription factor. Upon stress stimuli such as DNA damage, UV light and oncogenes, the network of p53 is activated and p53 enables the transcription of its target genes. These genes are mainly involved in processes like cell cycle arrest and apoptosis. Reproduced from (Vogelstein et al, 2000).

Many other components of p53 network have been found, which are involved in a variety of further effects, including the induction of cellular differentiation (Molchadsky et al, 2010), and the production of extracellular matrix (Zhu et al, 2009) and cytoskeleton formation (Carney et al, 2012). The components of the network, its inputs and outputs, vary according to cell type.

The complexity of the p53 assembly is acknowledged, hence in the following section the structure of each domain and the related function, as well as the quaternary structure of p53 are introduced to allow a comprehensive understanding.

8.1.1 Structure and function of individual p53 domains

The *human p53* gene (Benchimol et al, 1985) codes for a protein of 393 amino acids, which is biologically active as a homotetramer. The monomer possesses two intrinsically disordered regions, the N-terminus and the extreme C-terminus, and two folded parts, the central core and the tetramerization domains.

Particularly, the N-terminus is the transactivation domain (NTD; residues 1-61), followed by a proline-rich SH3 target-region (residues 64–92). The prominent part of the protein is constituted by the core domain (CD), responsible for the specific DNA-binding (residues 94-292). The vast majority of p53 mutations related to human cancer is located in this domain (Petitjean et al, 2007). Adjacent to the core domain is the

tetramerization domain (TD; residues 325-356), which is followed by a regulatory domain, the extreme C-terminus (CTD; residues 363–393) (Figure 8.2) (Joerger & Fersht, 2008).

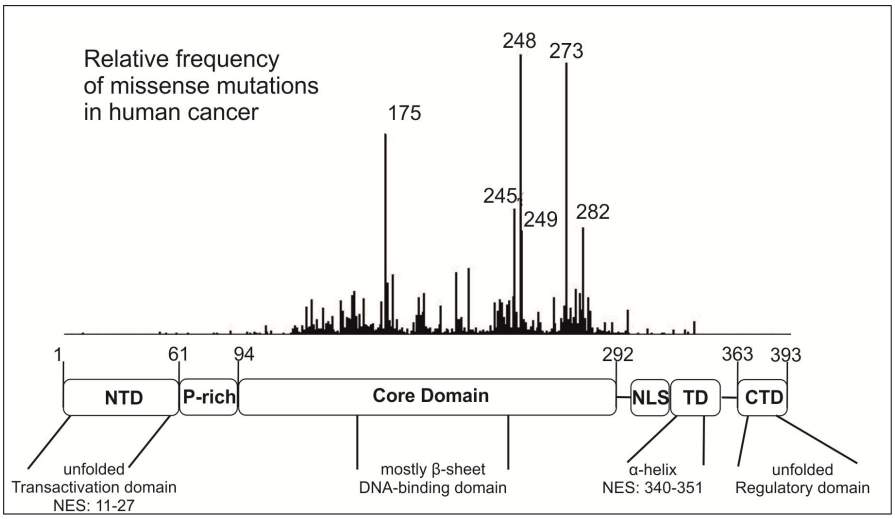

Figure 8.2 The structure of the full-length p53 is organized in: unfolded N-terminal domain (NTD), which is the transactivation domain and contains one nuclear export signal (NES); proline-rich region (P-rich); the folded central core domain (CD), which possesses the DNA-binding activity; the nuclear localization signal (NLS); the folded tetramerization domain (TD), overlapped with the second NES; the unfolded extreme C-terminus (CTD), defined as regulatory domain. The domains are associated to the relative distribution of missense mutations in human p53. Latest version R15 by International Agency for Research on Cancer TP53 Database, 2010 (Petitjean et al, 2007).

Furthermore, the protein possesses two nuclear export signals (NES), one at N-terminus (residues 11-27) and one at C-terminus (340-351) (Stommel et al, 1999; Zhang & Xiong, 2001), while the nuclear localisation signals (NLS) are mainly located at the C-terminus, NLSI (residues 305–322), which is highly conserved, and two weaker motifs, NLSII (366–372) and NLSIII (376–381) (Liang & Clarke, 1999; Shaulsky et al, 1990).

8.1.1.1 N-terminal domain (NTD)

The N-terminus is natively unfolded (Bell et al, 2002; Dawson et al, 2003) and it consists of two contiguous transcriptional activation subdomains, TAD1 (residues 1–40) and TAD2 (residues 40–61), and an adjacent proline-rich SH3 target-region (residues 64–92) (Chang et al, 1995; Walker & Levine, 1996).

The whole TAD is a binding site for many interacting proteins, such as components of the transcription machinery (Di Lello et al, 2006; Lu & Levine, 1995; Thut et al, 1995), the transcriptional coactivator histone acetyltransferase p300/CBP (CREB-binding protein)(Gu et al, 1997) and the negative regulator MDM2 (Kussie et al, 1996). The phosphorylation of serine and threonine residues by several different protein kinases

modulates the interactions with coactivators and regulators, e.g., upon phosphorylation of Thr-18 p53-MDM2 complex is weakened (Schon et al, 2002) while p300/CBP binding to p53 get stabilized (Dornan & Hupp, 2001).

The exact role of the proline-rich region is poorly understood. In human p53 this region contains five PXXP motifs (Walker & Levine, 1996). Such motifs are generally known to mediate numerous protein-protein interactions in signal transduction (Kay et al, 2000).

8.1.1.2 Core domain (CD): DNA-binding domain

The first structure of the p53 core domain in complex with DNA was resolved by Cho *et al.* in 1994 (Cho et al, 1994), and since that time many other crystal structures came out increasing the understanding of DNA site-specific recognition by p53 and its inactivation in tumours.

The 25 kDa domain has a basic scaffold consisting of an immunoglobulin-like β-sandwich (Figure 8.3 A-B). Then two structural motifs bind target DNA. The loop-sheet-helix motif binds to DNA major groove and includes loop L1, part of β-sandwich and the C-terminal α-helix H2. The two large loops (L2 and L3) and α-helix H1 bind to DNA minor groove, stabilized by the presence of zinc ion. The zinc ion is coordinated by a histidine and three cysteine residues (Cys-176 and His-179 in H1, Cys-238 and Cys-242 in L3). Zinc loss causes a significant decrease in folding stability (Duan & Nilsson, 2006).

Human CD is moderately stable and melts slightly above body temperature, 44°-45°C (Ang et al, 2006). The reason is the presence of buried polar residues which do not form hydrogen bonds, like Tyr-236 and Thr-253, contributing to p53's instability (Canadillas et al, 2006).

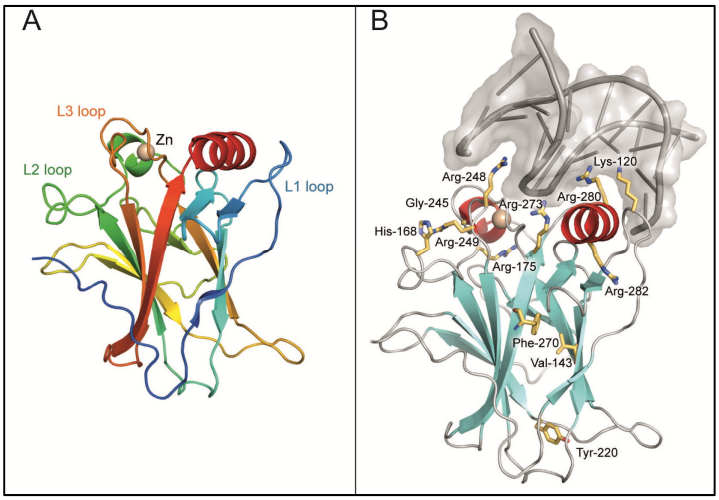

Figure 8.3 A: Structure of p53 core domain (CD) shown with colour gradient, from N terminus blue to C terminus red, PDB 2OCJ (Wang et al, 2007), with immunoglobulin-like β-sandwich motif, loops L1, L2 and L3, the essential zinc ion, and α-helix 1 in green and α-helix 2 in red. B: p53 CD bound to DNA

(PDB 2AHI) (Kitayner et al, 2006); the buried polar residues that cause CD instability and the key residues in CD-DNA interface are shown in orange. Reproduced from (Joerger & Fersht, 2008).

8.1.1.3 DNA site-specific recognition

The transcription factor p53 binds cooperatively as a tetramer to a specific double-stranded DNA sequence present in the promoter region of target genes, so called response element (RE) (Weinberg et al, 2004b). The canonical sequence is organized in two decameric half-site palindromes, with general formula 5'-RRRCA/T A/TGYYY-3' (whereby R and Y represent purine and pyrimidine bases, respectively), separated by 0–13 base pairs (El-Deiry, 1998; Eldeiry et al, 1992; Funk et al, 1992; Riley et al, 2008). The recognition by p53 of non-canonical REs and the possible roles in the human genome regulation are afterwards discussed in Section 8.5.4.

Figure 8.3 B shows the key residues in CD-DNA interface which directly contact one half-site, such as Lys-120, Ser-241, Arg-248, Arg-273, Ala-276, Cys-277, and Arg-280 (Cho et al, 1994; Kitayner et al, 2006).

The DNA minor groove is contacted via Arg-248, which makes either direct or water-mediated contacts with the backbone, depending on the DNA complex studied. Then Arg-273 interacts with the backbone at the centre of the half-site and forms a salt bridge with Asp-281, which in turn approaches DNA indirectly via a water-mediated contact.

In the major groove, Arg-280 establishes invariant contacts with the conserved guanine base at position seven of the half-site, while contacts made by Lys-120, Ala-276 and Cys-277 are sequence specific for RE recognition (Kitayner et al, 2006).

8.1.1.4 Tetramerization domain, TD

The tetramerization domain permits full-length p53 to reversibly form tetramers. This domain is located in the C-terminal region (residues 325‑356) (Sakaguchi et al, 1997). The tetrameric structure of the domain was solved by X-ray crystallography (Jeffrey et al, 1995) and in solution by NMR (Lee et al, 2000). The monomer TD consists of a β-strand, a tight turn and an α-helix (Figure 8.4). Two monomers form primary a dimer. Next the dimers are packed via an antiparallel intermolecular β-sheet and antiparallel helix interaction, forming the central stable hydrophobic core with residues Leu-330, Ile-332, and Phe-341 (Figure 8.4).

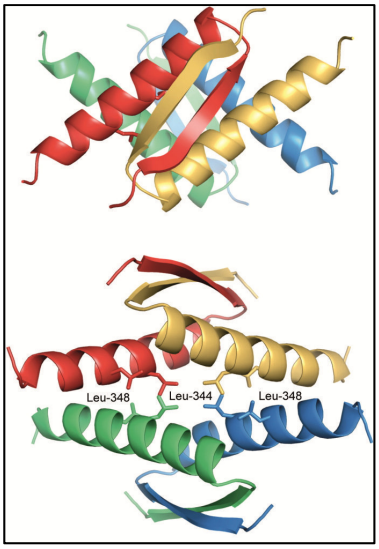

Figure 8.4 The p53 tetramerization domain assembled as a dimer of dimers, shown in two different orientations. Each monomer is differently coloured. The lower orientation displays the hydrophobic interface. The antiparallel intermolecular β-sheet and antiparallel helix packing stabilizes oligomeric state. PDB 1C26 (Jeffrey et al, 1995). Reproduced from (Joerger & Fersht, 2008).

The whole isolated conformation is characterized by a high association of tetramer-dimer transition with K_D values of 150(±10) nM and 60(±9) nM, measured at 37 °C and 20 °C respectively (Rajagopalan et al, 2011). Additionally, phosphorylation of serine-392 increases the stability of tetramer conformation (Sakaguchi et al, 1997).

This topology enables p53 folding pathway, which proceeds via a dimeric intermediate. Nicholls *et a*l. studied p53 biogenesis *in vitro*, observing the formation of dimers by co-translation on the polysome. Tetramers instead were formed in solution by the dimerization of dimers (Nicholls et al, 2002).

8.1.1.5 The extreme C-terminus (CTD): regulatory domain

The CTD is intrinsically disordered and subjected to extensive posttranslational modifications, including acetylation, ubiquitination, phosphorylation, sumoylation, methylation, and neddylation, that regulate p53 function and cellular protein levels (Gu & Zhu, 2012; Kruse & Gu, 2008; Lavin & Gueven, 2006).

The function of this domain and the role of each single modification are debated in literature. The controversial results reflect the complexity of the p53 pathway.

The CTD can either positively or negatively regulate p53's transactivation by the suggested allosteric activation (Gu & Roeder, 1997; Hupp et al, 1993), uncovering the p53 core domain. For example, the acetylation of CTD by CBP/p300 neutralizes multiple lysine residues (positions 370, 372, 373, 381, 382 and 386) enhancing sequence-specific DNA binding *in vitro* and *in vivo* (Gu & Roeder, 1997; Gu et al, 1997; Luo et al, 2004).

On the other hand, further studies show that on large molecules of DNA or chromatin the presence of unmodified CTD is necessary for an effective binding to consensus sequences and successively the gene transcription requires CBP/p300 (Barlev et al, 2001; Espinosa & Emerson, 2001; McKinney et al, 2004). Possibly, acetylation of the CTD involves multiple mechanisms, including changes in DNA-binding and coactivator recruitment.

When not modified, the CTD itself binds DNA nonspecifically *in vitro* due to its basicity (Weinberg et al, 2004a). This capability of CTD to bind DNA nonspecifically promotes the linear diffusion on DNA, and neither acetylation-mimicking mutations nor phosphorylation of residues within the CTD stimulates linear diffusion, hence this domain is a positive regulator of DNA binding (McKinney et al, 2004). The role of the sliding for p53 on DNA and the CTD nonspecific binding activity are further discussed and expanded in Section 8.5.1.

8.1.1.6 Human p53 quaternary structure

Due to the disordered regions, a complete crystal structure of tetrameric p53 could not be achieved. Recently, Tidow *et al.* solved the quaternary structure of human p53 and p53-DNA complex combining NMR, small-angle X-ray scattering (SAXS) and electron microscopy 3D maps (Tidow et al, 2007). Furthermore, they redefined the model according to the high-resolved structures of p53 core (PDB ID code: 1TUP, 2AC0 (Cho et al, 1994; Kitayner et al, 2006)) and tetramerization domains (PDB ID code: 1C26 (Jeffrey et al, 1995)). They estimated a quite big dimension of isolated tetrameric full-length p53 in SAXS, which has a radius of gyration of 68.2(±0.3) Å and maximum particle size of 240(±30) Å. Their model consists of an extended cross-shaped structure with loosely coupled core domains and tetramer domain at the centre, while the four NTD are mainly stretched out from this central part (Figure 8.5 A). This conformation would allow all varied regulations of p53 activity by interaction with protein mediators. Moreover, the open arrangement could act as a clamp, once p53 contacts a DNA filament, clinging to it from both sides and keeping distal the tetramer domain (Figure 8.5 B-C).

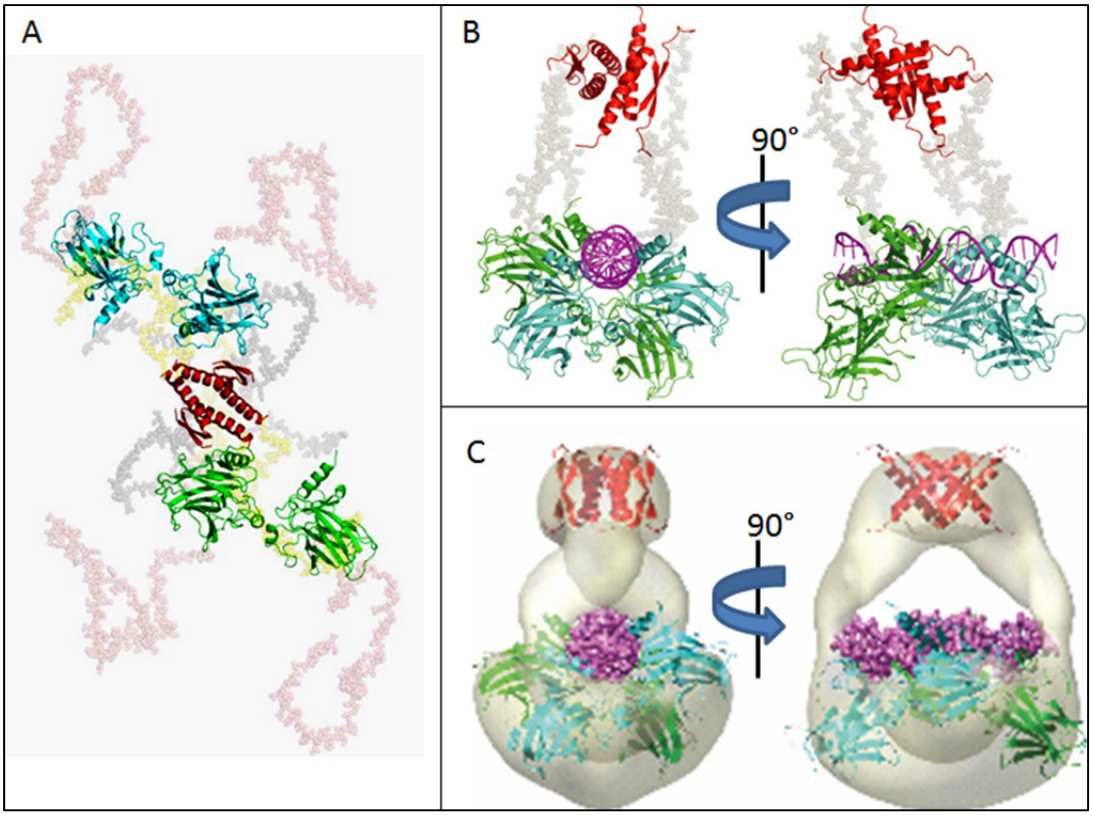

Figure 8.5 Quaternary structures of human full-length p53, free and bound to DNA. A: free p53 in solution with represented in cartoon the four core domains (coupled in green and blue colours) and tetramerization domain (red); the connecting linkers (grey), NTD (salmon) and CTD (yellow) were displayed in semi-transparent spacefill model. B: model of a p53–DNA complex displayed in two orthogonal views; ds-DNA in lilac and the CTD were not inserted. C: 3D-EM map of p53–DNA complex (semi-transparent grey) with fitted coordinates of core and tetramer domains in two orthogonal views. Reproduced from (Tidow et al, 2007).

This quaternary organization model was confirmed in NMR spectra (Bista et al, 2012), whereby the tetramerization of full-length p53 occurred via TD domain and TD domain remained tetramerized in DNA Complex. The alternative postulated model (Aramayo et al, 2011), implying existence of structured N/C termini nodes comprised of monomeric TD and NTD domains, had therefore no confirmation in NMR spectra.

8.2 Motivation

Until now p53 has been poorly studied with surface based sensors due to its difficult handling *in vitro*. Just a few examples are present in literature: wt-p53 pre-activated with monoclonal antibody DO-7 and analysed in SPR in presence of *WAF1*, *mdm2*, and *bax* REs (Maillart et al, 2004); cell lysate loaded on SPR for simultaneous DNA and monoclonal antibody interactions (Wang et al, 2009); DNA interaction of wt-p53 core domain in "metal-oxide semiconductor field-effect transistor" biosensor, shortly called MOSFET (Han et al, 2010).

Recently, the *switch*SENSE platform was successfully employed for the detection of a transcription factor, the *E. coli* integration host factor, based on its DNA binding activity (Spuhler et al, 2010). The conformational changes of the protein/DNA complex were releaved in the fluorescence reduction, which was caused by the increased vicinity of the Cy3 dye to the gold surface, due to DNA bending. Therefore the *switch*SENSE technology was engaged in this project to analyse the p53-DNA interactions.

For the investigation on switchable DNA layers, a physiologically relevant RE was chosen, namely the strong binding RE *p21* 5' site (in *p21* promoter at position −2281 to −2262 (Eldeiry et al, 1993), later simply named *p21*). The *p21* gene is tightly regulated by p53. The encoded protein, p21, is a cyclin-dependent kinase inhibitor and mediates the p53-dependent cell cycle G1 phase arrest in response to a variety of stress stimuli, binding to and inhibiting the activity of cyclin-CDK2 or -CDK4 complexes (LaBaer et al, 1997).

Furthermore, the left half of *p21* RE was selected (*half-p21*) to be related to the full *p21* site in Time Resolved Measurements (TRM), whereby the oligomerization state of bound p53, as a dimer or a tetramer, was analysed based on the DNA switching dynamics. A random sequence was also selected to detect the nonspecific binding to a DNA site, namely the "nonspecific activity" of p53.

In the experiment the human full-length wild-type p53 (wt-p53) was compared to the truncated construct at both N- and C-termini (ΔN93ΔC37) and the DNA-binding defective mutant (R280E). The truncated form ΔN93ΔC37 was chosen, to be related to wt-p53 on a random sequence binding, because in the literature the C-termini (residues 363–393) of p53 tetramer seem conferring the nonspecific binding activity to DNA (Ang et al, 2006; Melero et al, 2011; Weinberg et al, 2004a).

The binding and unbinding events of p53 were observed in real-time recording the fluorescence at -0.4 V in Low Frequency Measurements (LFM). The conformational changes of the "standing" DNA upon p53-DNA specific recognition were displayed in the

fluorescence reduction, resulting from the DNA bending which brings the Cy3 dye closer to the gold surface.

8.3 Experimental design

The detection of association and dissociation of the p53-DNA complex was measured on Prototype1, preparing ds-74-mer of *p21*, *half-p21* and random layers (Figure 8.6; Section 8.3.2). The "ultra-low" density layers were prepared as described in Section 5.3.1.1, reaching $<10^{11}$ molecules/cm^2, to enable the interaction of p53 to DNA without any steric hindrance. The proteins full-length wild-type p53, a truncated variant of p53 ΔN93ΔC37 and the DNA-binding defective mutant R280E were diluted in Binding Buffer (Hepes 40 mM pH 8.0, $MgCl_2$ 10 mM, KCl 50 mM, glycerol 5 %, TCEP-HCl 10 mM= total ionic strength 150 mM) and flowed over the surface at 40 µl/min, which corresponded to a laminar velocity of 0.0031 ms^{-1}. The temperature was set at 15 °C, because at 37 °C the full-length wt-p53 has a life-time of only 35 min (Friedler et al, 2003) and it aggregates in 20 min (Rajagopalan et al, 2011). Therefore the temperature was kept low to preserve on the surface the p53 active state for a long time (until 1.5 h in kinetic measurement at 10 nM).

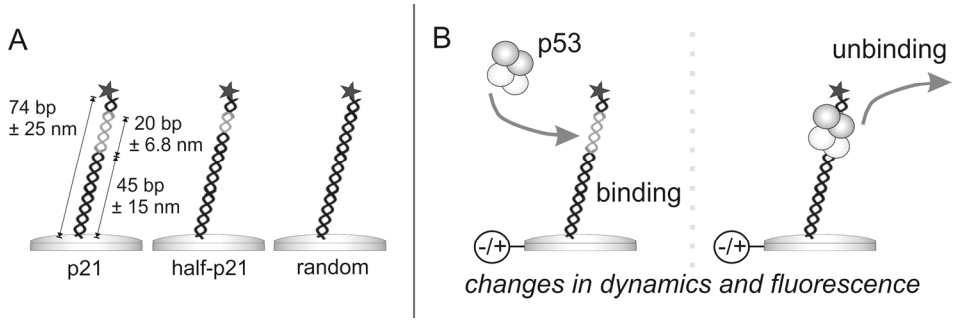

Figure 8.6 Real-time detection of association and dissociation of the p53-DNA complex on *switch*SENSE. A: The switchable DNA layers feautured a tethered ds-74-mer, incorporating in the distal part from gold electrode a 20 nt response element for either *p21*, *half-p21* or a random sequence. B: FL-wt-p53, ΔN93ΔC37 and R280E were loaded and analyzed in Low Frequency Measurements and Time Resolved Measurements to record the kinetic association and the switching dynamics. Afterwards, the buffer was flowed constantly to record protein dissociation kinetics.

The binding and unbinding events were observed in real-time, with applied switching bias of +0.4 to -0.4 V vs. Pt electrode. The dissociation was recorded by flowing Binding Buffer over the surface. The resulting "standing" fluorescence at -0.4 V, F_{st}, was evaluated in kinetic analysis. The curves were normalized to the initial ds-DNA level and fitted as described in Section 7.2.3.2.

Furthermore, a concentration dependent experiment for wt-p53 was performed in switching dynamics and in LFM mode to reveal the conformational changes occurring on DNA sequence upon p53-DNA specific recognition.
TRM were taken at complete protein-DNA binding and related to initial ds-DNA to observe how the p53-DNA complex slowed down the dynamics of DNA, due to increased hydrodynamic friction. The voltage amplitude was kept +0.4/-0.4 V and not corrected after VR, because the high ionic strength of the buffer limited the switching performances (ionic strength 150 mM, which is much more compared to 60 mM of Standard Buffer). Consequently, in VR bare ds-DNA could not lie down at attractive potential and the plateau in F_{ly} was not observed; in TRM the applied frequency was 3 kHz.
Beforehand, the conventional method, Electrophoretic Mobility Shift Assay (EMSA), was employed to optimize the buffer conditions on expressed p53 and to confirm the binding activity. Finally the results were discussed in context of findings presented in literature.

This investigation was conducted together with Makiko Maruyama, from Walter Schottky Institute TUM (Rant's group). Maruyama and I, we equally contributed to this project: particularly, she made the measurements on *switch*SENSE surface (data presented in Figures 8.11, 8.12, 8.13, 8.14, 8.15, 8.16, 8.17); I performed the biochemical part; together we analyzed the data.

8.3.1 The protein characterization

8.3.1.1 Human FL-wt-p53, ΔN93ΔC37 and R280E proteins

The human full-length wild-type p53 (wt-p53, UniProt #P04637) was expressed in *E. coli* cells and purified using chromatography, as described in Section 4.2.3. The other two proteins used in the investigation, the truncated construct at both N- and C-termini (ΔN93ΔC37) and the DNA-binding defective mutant (R280E), were generously supplied by Dr. Julia Rohrberg (Buchner's laboratory, Chemistry dept., TU München) (Figure 8.7).
Figure 8.8 presents the expression results of wt-p53, checked in SDS-PAGE and correctly identified in western blot (method in Section 4.2.4.5). The wild-type was compared to ΔN93ΔC37 and R280E in SDS-PAGE and native gel. All proteins showed high purity grade, and confirmed the respective sizes in denaturing conditions (Figure 8.8 B); in native gel the pH 8.0 of the buffer could solve the bands for wt-p53 and R280E dimer and tetramer, while ΔN93ΔC37 was smeared (Figure 8.8 C).

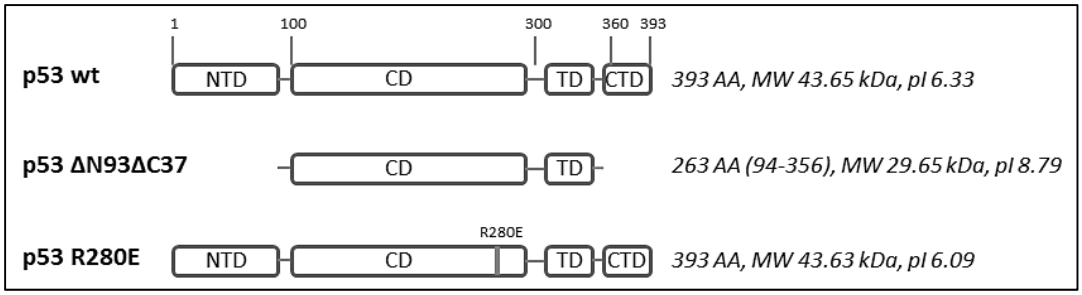

Figure 8.7 Proteins used in the investigation: the human full-length wild type p53 (wt-p53), the truncated form at N- and C-termini (ΔN93ΔC37) and the negative control mutant (R280E). The respective molecular weights and calculated pI[8] were indicated.

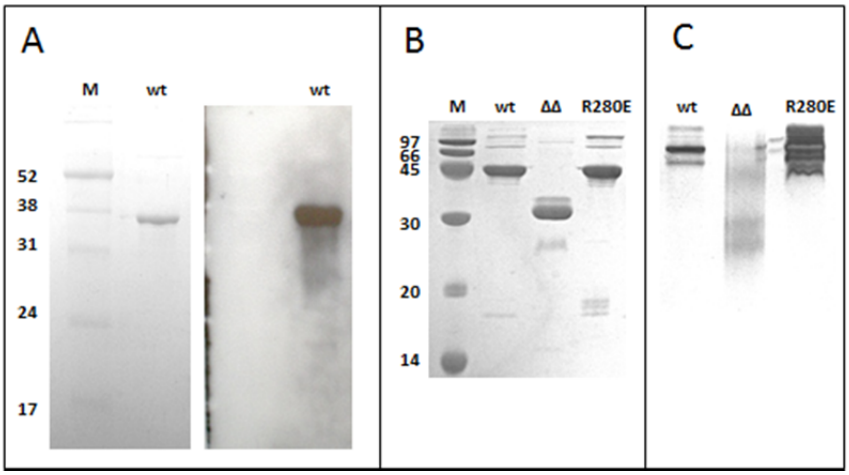

Figure 8.8 Proteins used in the investigation checked in electrophoresis. A: Expressed wt-p53 in SDS-PAGE 12.5 % acrylamide, left picture, and corresponding western blot, right picture. B: wt-p53, N93ΔC37 and R280E in SDS-PAGE 15 % acrylamide. C: wt-p53, ΔN93ΔC37 and R280E in native gel 8 % acrylamide.

In this investigation the employment of human full-length wild-type p53 with no purification tag must be emphasised. In literature most of publications presenting results of tagged full-length p53 engaged the thermostable variant, since the handling *in vitro* is less difficult. This form contains four mutations in the core domain (M133L, V203A, N239Y, N268D), which stabilize the folding. Hence the melting temperature of the whole protein increases from 45.1(±0.2) °C for the wild-type to 49.7(±0.7) °C for the mutant, without affecting the DNA binding kinetics (Ang et al, 2006; Nikolova et al, 1998).

This is the reason why the discussed references have indicated **FL-wt-p53** if the study used full-length wild-type p53, otherwise **the thermostable full-length** was implied and indicated as FL-p53.

[8] http://web.expasy.org/protparam/
Used # P04637 P53_HUMAN Cellular tumor antigen p53 as protein sequence template.

8.3.1.2 Isoelectric focusing (IEF) for wt-p53 and R280E mutant

The proteins wt-p53 and R280E, but not ΔN93ΔC37, were analysed in IEF to double check the calculated pI, because they resulted being more relevant in the analyses on surface measurements.

The proteins were separated in pH gradient employing IPG gel strips, and afterwards resolved by size in SDS-PAGE (method described in Section 4.2.4.2). The assay confirmed a slight acidic pI of both wt-p53 and R280E (Figure 8.9), whereby the bands were closed to pH 7 extremity of IPG strip. Nevertheless the pI between 6.3 and 6.1 could not be discriminated, due to the imprecise alignment and blocking of each strip on precast gels.

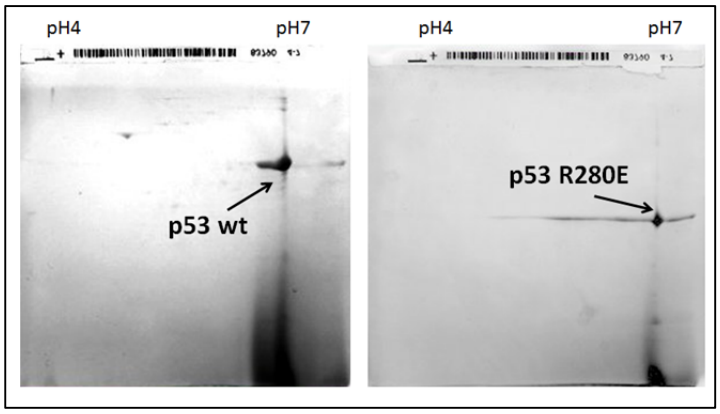

Figure 8.9 IEF of FL-wt-p53 and R280E mutant. The slight acidic pI of p53 and R280E was confirmed, loading separately the proteins on IPG gel strip. Afterwards SDS-PAGE was performed and results were visualized in Coomassie Blue Staining.

8.3.2 Oligonucleotide design

The modular sense-strand 74-mer was designed from 5' to 3' having:

- 45-nt of mixed sequence;
- the 20-nt RE;
- 9-nt of mixed sequence.

For the *half-p21*, the left half of the *p21* sequence was shifted to the 3' terminus of the sense-strand.

Table 8.1 shows the REs of *p21* and *half-p21* and the random sequence, which were taken from (Noureddine et al, 2009). A drawing of ds-DNA on surface is represented in Figure 8.6 A to better visualize the position of RE sites. All sense-strands were synthesized with 5' SH-$(CH_2)_6$ and 3' Cy3 for SAM formation and the complete oligonucleotide sequences are listed in Section 4.1. The sequences were analysed in

OligoAnalyzer 3.1[9] to verify the presence of stable secondary structures and relative melting temperatures, therefore the hybridization of the DNA probes followed a high temperature treatment at 95 °C for 15 minutes (Section 5.3.1.1).

Table 8.1 REs and oligonucleotides used in p53 binding experiments.

Name	RRRC(A/T)	(A/T)GYYY	RRRC(A/T)	(A/T)GYYY
p21	GAACA	TGTCC	CAACA	TGTTG
half-p21	*Mixed*	atgag	GAACA	TGTCC
Random	Gaaag	gtgga	tttag	gtgga

p21:

CTTTCTGGCCATCATAGCTCTGGCATAGAATAGTCGTGAGATGAG***GAACATGTCCCAACATGTTG***AGCTCTGAT

half-p21:

CTTTCTGGCCATCATAGCTCTGGCATAGAATAGTCGTGAGCACATTCGTAATGAG***GAACATGTCC***AACGCTGAT

Random:

CTTTCTGGCCATCATAGCTCTGGCATAGAATAGTCGTGAGCACAT***GAAAGGTGGATTTAGGTGGA***AACGCTGAT

8.4 Results

8.4.1 EMSA results

Before starting the investigation on surface, the DNA-binding activity of p53 was tested for ds-74-mer labelled with Cy3 in Electrophoretic Mobility Shift Assay, EMSA. This technique is typically used in laboratories to screen *in vitro* the DNA-binding activity of p53 at varied conditions, such as temperature, buffer, and presence of co-factor proteins (Dehner et al, 2005; Hansen et al, 1996; Lubin et al, 2010).

The method applied in Buchner's laboratory (Bell et al, 2002) was modified to optimize the buffer for *switch*SENSE surface. First the reaction was tested without the presence of monoclonal antibody PAb421 (clone Ab-1) (Resnick-Silverman et al, 1998). PAb421 increases the activity of p53 by allosteric regulation, binding the CTD (Hupp et al, 1993). DTT was replaced successfully by TCEP, which is not harmful to the DNA layer on gold surface. DTT instead competes with thiolated DNA, causing damages on DNA monolayer. Another modification was to reduce the amount of glycerol from 15% to 5% (v/v).

Figure 8.10 shows the EMSA results for the binding activities of wt-p53, ΔN93ΔC37 and R280E on *p21*, *half-p21* and random ds-DNA-Cy3. The reactions contained excess p53 (6:1= [tetramer p53]: DNA) and oligonucleotides as competitor (6:1=oligos:DNA), as described in Section 4.2.4.1. Each run was compared to the corresponding reaction with

[9] http://eu.idtdna.com/analyzer/Applications/OligoAnalyzer/

no protein addition (DNA). The upper half of the gel displayed the proteins wt-p53 and ΔN93ΔC37 binding specifically to *p21* and *half-p21* sequences and weakly to the random sequence, even in presence of competitor. On the other hand, R280E mutant could hardly bind to all three ds-74-mer. The complex of ΔN93ΔC37 with *p21* and *half-p21* gave a bit faster shift compared to wt-p53 interaction due to its smaller size.

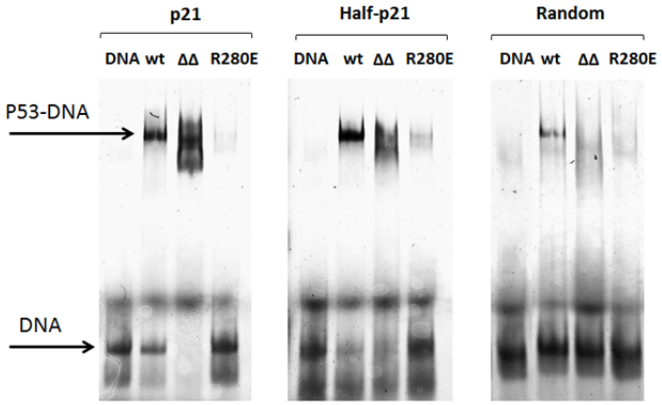

Figure 8.10 DNA-binding of p53 in EMSA. Binding activities of wt-p53, ΔN93ΔC37 and R280E mutant were verified, loading the sample reactions with *p21*, *half-p21* and random ds-DNA-Cy3 labelled. Each run was related to the corresponding reaction with no protein addition (DNA). The upper half of the gel showed p53-DNA complex, the lower part free DNA. The background band, at the bottom of the gel, close to DNA band, was Bromophenol Blue.

8.4.2 Detection of p53-DNA binding activity on *switch*SENSE

8.4.2.1 The binding kinetics

The resulting fluorescence at -0.4 V, F_{st} was evaluated for the kinetic analysis, being significantly affected by the DNA conformational changes upon protein binding. To allow the comparison of the measurements carried out on different electrodes, the curves were normalized to the fluorescence amplitude ΔF of initial ds-DNA level setting zero at time t= 0 s.

Figure 8.11 illustrates the association and dissociation of wt-p53 at 68 nM on *p21*, *half-p21* and random sequences. At this concentration, the binding saturation was observed at approximately 25 min, having F_{st} reached the plateau for all three layers. The protein dissociation from all ds-DNA layers was similarly slow. The unspecific binding of p53 to the random sequence at this concentration was pronounced.

At 10 nM concentration, wt-p53 interacted specifically with *p21* layer reaching the plateau at approximately 1.5 h, and resulting in a significant reduced nonspecific interaction with the random sequence (Figure 8.12). The dissociation was not recorded at this concentration.

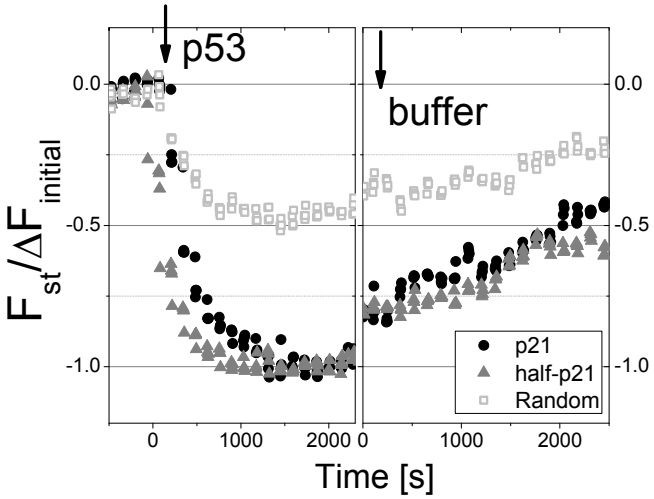

Figure 8.11 Real-time detection of binding and unbinding of wt-p53 on DNA recorded in Low Frequency Measurements. The wt-p53 concentration of 68 nM was injected at 15 °C on *p21*, *half-p21* and random layers (black circles, grey triangles and open-grey squares, respectively). The F_{st} signals were normalized to initial ΔF to allow a comparison through different layers. The binding event was monitored by a significant reduction in fluorescence F_{st}. The unbinding event was observed under continuous buffer flow.

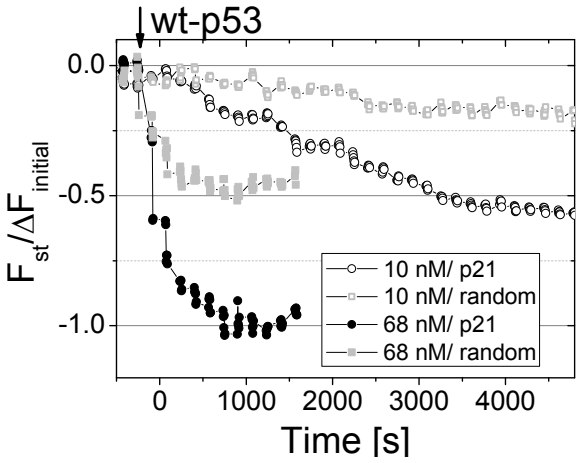

Figure 8.12 Association of wt-p53 to the DNA at 10 and 68 nM injections. The F_{st} signals, normalized to initial ΔF, were compared for 10 nM and 68 nM injections (open and filled symbols, respectively) on *p21* and random sequences (black and grey squares).

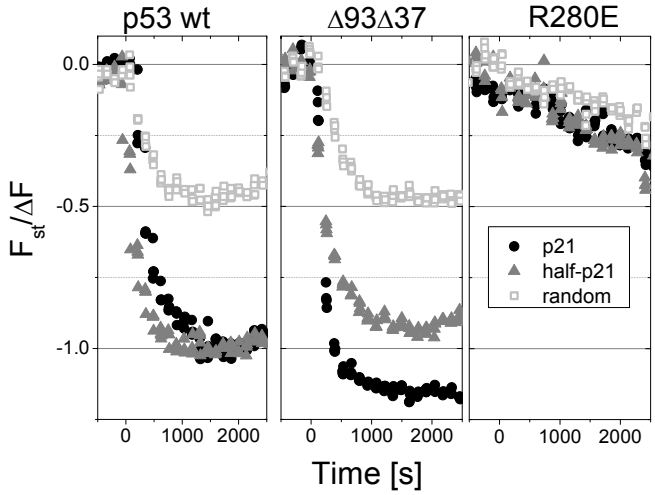

Figure 8.13 Comparison between wt-p53, truncated ΔN93ΔC37 and mutant R280E loaded at 68 nM on DNA layers. The proteins were injected on *p21*, *half-p21* and random sequences (black circles, grey triangles and open grey squares, respectively) and F_{st} signals, normalized to initial ΔF were compared. The protein ΔN93ΔC37 displayed an equivalent nonspecific binding to random sequence as detected for wt-p53, and bit more pronounced binding on *p21* layer. As for R280E, neither specific nor unspecific binding was observed on DNA layers.

Figure 8.13 shows the association of ΔN93ΔC37 and R280E compared to wt-p53, loading the same amount of monomeric protein on the three DNA layers. The protein ΔN93ΔC37 bound to random sequence with a comparable velocity, according to the standard error (τ_{on} 413.0(±19.5) s and 377(±11) s, for ΔN93ΔC37 and wt-p53, respectively). Remarkably, the mutant R280E loaded at 68 nM concentration barely could bind *p21* and *half-p21*, and no unspecific binding was observed on random sequence. The inactivity of R280E due to the incorrect folding state was excluded. The mutant was previously characterized by Retzlaff (Buchner's laboratory) in circular dichroism spectra and analytic chromatography with size exclusion column, and the melting temperature and tetramer oligomerization state were confirmed to be the same of FL-wt-p53. Furthermore he used the mutant in fluorescence anisotropy on *p21* RE also without detecting any binding activity (Retzlaff, 2009).

The wt-p53 kinetics was evaluated and Table 8.2 lists obtained rate constants and affinity values loading 10 nM and 68 nM of protein, on *p21*, *half-p21* and random sequences. The dissociation of p53, loaded at 68 nM, had a similar rate for all used sequences, $k_{off} \approx 2*10^{-4}$ s^{-1}. At 10 nM monomer concentration, wt-p53 bound specifically to *p21* and to *half-p21*, resulting in $k_{on} \backsim 0.9*10^{4}$ $M^{-1}s^{-1}$. The nonspecific binding was approximately 7 times weaker with $k_{on} \backsim 0.1*10^{4}$ $M^{-1}s^{-1}$.

At 68 nM monomer concentration, the binding affinities of wt-p53 to the sequences were all similar. The k_{on} was much quicker, 10-fold higher on *p21* and *half-p21*

sequences and 70-fold higher on random sequence, K_D values of 5.8(±0.4) nM, 3.9(±0.2) nM and 5.9(±0.6) nM for, respectively, *p21*, *half-p21* and random sequences.

This discrepancy of the measured association constants at different protein concentration was unexpected and suggests a nontriavial binding behaviour, like one to one complex, but a cooperative interaction between oligomeric p53 and DNA sequence.

Table 8.2 Kinetic constants and binding affinities of wt-p53 on p21, half-p21 and random sequences, for 10 nM and 68 nM monomer concentrations. The SD values are indicated in round brackets.

Wild-type p53 loaded at 10 nM monomer concentration

	τ_{on} [s]	k_{on} [10^4 $M^{-1}s^{-1}$]	k_{off} [10^{-4} s^{-1}]	K_D [nM]
p21	3156 (117)	0.79 (0.16)	Not measured	Not measured
half-p21	3250 (36)	0.93 (0.18)	Not measured	Not measured
Random	4514 (50)	0.12 (0.27)	Not measured	Not measured

Wild-type p53 loaded at 68 nM monomer concentration

	τ_{on} [s]	k_{on} [10^4 $M^{-1}s^{-1}$]	k_{off} [10^{-4} s^{-1}]	K_D (nM)
p21	329 (117)	4.13 (0.16)	2.37 (0.09)	5.8 (0.4)
half-p21	257 (9)	5.56 (0.20)	2.15 (0.18)	3.9 (0.2)
Random	377 (11)	3.61 (0.13)	2.10 (0.05)	5.9 (0.6)

These results were in agreement with the affinity data of p53-*p21* present in literature, considering the different experimental conditions and the employed thermostable protein. For instance, Weinberg *et* al. obtained in fluorescence anisotropy for p53CT (p53CT corresponds to residues 94–360, similarly as ΔN93ΔC37)a K_D of 4.6(±0.9) nM on *p21* RE, considering the dimer concentration of p53 (Weinberg et al, 2005). The measurement was done at 20 °C in total ionic strength 225 mM, because in a previous study they observed a strong nonspecific binding of p53CT to the DNA at ionic strength below 225 mM, giving "artefacts" in the analysis (Weinberg et al, 2004b). Recently, Rajagopalan *et al.* measured in fluorescence correlation spectroscopy (FCS) a K_D of 7 nM for FL-p53 on *p21* RE and corresponding k_{on} $1.2*10^4$ $M^{-1}s^{-1}$ and k_{off} $2.3*10^{-4}$ s^{-1} at 20 °C joining 10 nM of protein to 5 nM of DNA. The total ionic strength was 215 mM, which they defined physiological (Rajagopalan et al, 2011).

Generally the physiological range of ionic strength is considered in biochemistry to be distributed between 0.05M and 0.35M in eukaryotes and prokaryotes (Alberty, 2003; Fleming et al, 2009), meaning that 150 mM buffer ionic strength used in this

investigation was correct to evaluate p53-DNA recognition. Finally this nonspecific binding, characterized by high affinity, was not considered an artefact, but rather a feature of p53, as an active transcription factor, which deserves to be further discussed.

8.4.2.2 The concentration dependent analyses in LFM and TRM

A concentration dependent experiment of wt-p53 was performed in Low Frequency Measurements and Time Resolved Measurements.

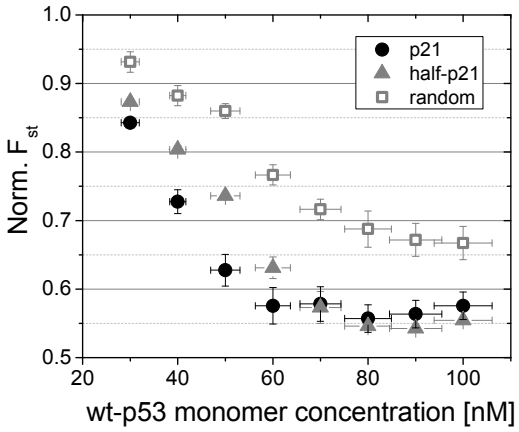

Figure 8.14 Normalized fluorescence level F_{st} as a function of concentration of wt-p53 binding to DNA. Increasing concentrations of wt-p53 (from 30 to 100 nM) were loaded on *p21*, *half-p21* and random layers (black circles, grey triangles and opened grey squares, respectively). At completed binding reaction, F_{st} was measured in Low Frequency Measurements, normalized to initial F_{st} and plotted vs. wt-p53 monomer concentration.

Figure 8.14 presents the standing fluorescence level F_{st} measured at completed binding reaction on surface, after loading in succession increasing concentrations of wt-p53, from 30 nM to 100 nM. On all three sequences, p53 binding caused diminished fluorescence intensity, dependent on the protein concentration. On *p21* layer, the drop of F_{st} was the most pronounced and at 60 nM p53 concentration the signal stopped decreasing, indicating ∽100 % coverage of binding sites on surface. On *half-p21* layer, F_{st} was as low as on *p21* layer after 70 nM p53 injection. The fluorescence of random sequence was also reduced, but it never reached *p21* and *half-p21* levels, showing signal saturation at 90 nM p53 injection.

In Time Resolved Measurements the rising dynamic curves were taken at completed binding of p53 on *p21*, half-*p21* and random layers upon each concentration injection (from 30 to 100 nM) and data were compared to initial ds-DNA and to, namely anti-biotin layers.

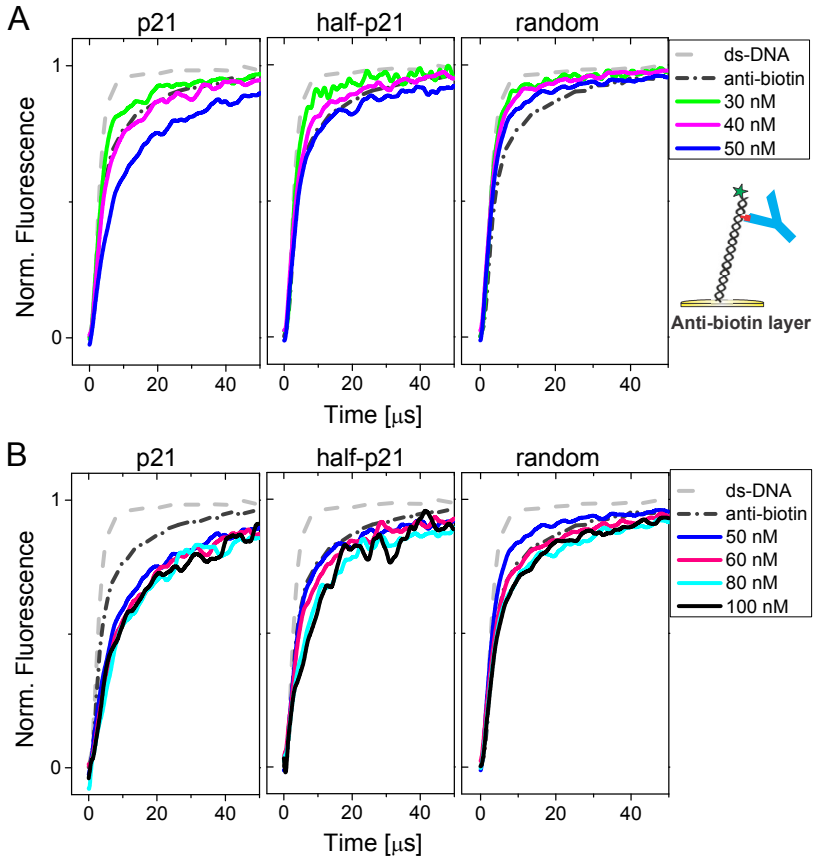

Figure 8.15 Time Resolved Measurement data analysis of wt-p53 concentration dependence. Increasing concentrations of wt-p53 were loaded on *p21*, *half-p21* and random sequences. A: TRM data for "low concentration" injections, 30, 40 and 50 nM (green, magenta, blue curves). B: TRM data for "high concentration" injections, 50, 60, 80 and 100 nM (blue, red, cyan and black curves). All TRM data were compared to the initial ds-DNA signal (grey dashed curve) and antibody anti-biotin on biotinylated ds-DNA layer (black short dash dot curve).

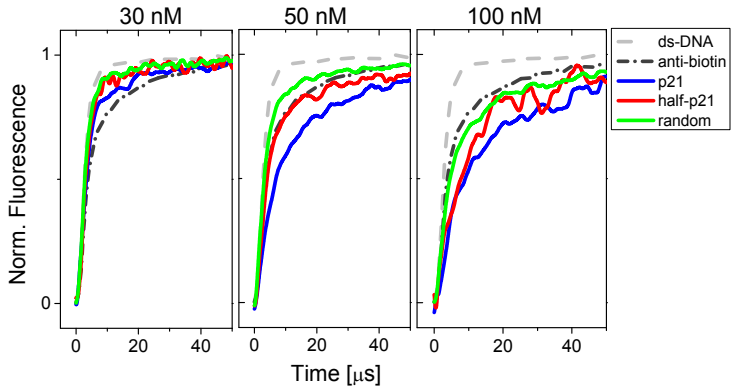

Figure 8.16 Time Resolved Measurement data for 30, 50 and 100 nM injections of wt-p53. The signals of *p21*, *half-p21* and random sequences (blue, red and green, respectively) were compared loading on surface 30, 50 and 100 nM of wt-p53. All TRM data were compared to the initial ds-DNA signal (grey dashed curve) and antibody anti-biotin on biotinylated ds-DNA layer (black short dash dot curve).

In order to get a rough idea about the dimension of p53 bound to DNA, a reference measurement was done saturating the biotinylated DNA layer with monoclonal antibody anti-biotin (anti-biotin layer). The biotin was coupled on the random 74-mer sequence at the level of RE fragment position (drawing in Figure 8.15 A). The hydrodynamic diameter of IgG is around 11 nm (Armstrong et al, 2004; Jossang et al, 1988), which should be smaller than the dimension of p53 tetramer. According to small-angle X-ray scattering (SAXS) analysis for a full-length tetrameric p53-DNA complex (Figure 8.5), Tidow *et al.* determined a quite big dimension, which has a diameter of ~14 nm (Tidow et al, 2007).

Figure 8.15 shows TRM results from the three DNA layers, separated in "low concentration" loading (30, 40 and 50 nM) and "high concentration" loading regime (60, 80 and 100 nM); the curve at 50 nM injection was plotted in both figures A and B as a guide to the eye.

Till 50 nM loading (Figure 8.15 A), p53 bound specifically *p21* and *half-p21* layers. The rising dynamics was substantially diminished on *p21* layer, on *half-p21* the motion was less affected compared to *p21* layer but still p53 bound to it. As for random sequence, the curves showed a very small presence of bound p53.

Looking at the high concentration regime (Figure 8.15 B), *p21* layer was saturated at 60 nM while *half-p21* layer at 80 nM. However above 60 nM injection, the nonspecific binding started being significantly high as already observed in kinetics and LFM measurements.

From the rising dynamics, the bound p53 on saturated *p21* and *half-p21* layers (60 and 80 nM, respectively) was larger than mAb anti-biotin.

By increasing concentration of the loaded protein, the switching dynamics of the complex p53/*half-p21* slowed down until reaching the similar dynamics of the complex p53/*p21* (100 nM p53; Figure 8.16). To understand this effect, all rising dynamic curves measured at each p53 concentration were evaluated by:

- the integrated area of the curve obtained after loading p53 (0-50 µs range, defined as Dynamic Response *DynRes*) was subtracted to the initial ds-DNA integrated area, calculating the reduced Dynamic Response *ΔDynRes* ($\Delta DynRes = DynRes_{initial} - DynRes_{p53}$);
- the relative variation responses *Relative DynRes* of p53 bound on *half-p21* layer compared to p53 on *p21* layer were calculated from the difference of respective *ΔDynRes* normalized to *ΔDynRes* of random sequence layer (*Relative* $DynRes = (\Delta DynRes_{p21} - \Delta DynRes_{half\text{-}p21}) / \Delta DynRes_{random}$).

Hence, *Relative DynRes* was equivalent to the observed deviation of dynamic response between *half-p21* and *p21*-layers. Plotted as a function of p53 monomer concentration (Figure 8.17) *Relative DynRes* made in evidence a gradual transition from a light state (fast dynamics) to a heavy state (slow dynamics) on *half-p21* layer. The observed trend was fitted with sigmoidal Boltzmann function, which 1st derivative resulted in a state transition occurring at 60(±9) nM (Appendix, Section 14.7).

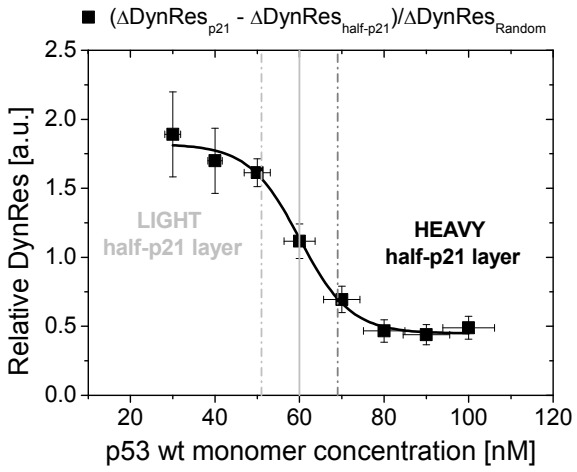

Figure 8.17 Relative Dynamic Response vs. wt-p53 monomer concentration on *p21* and *half-p21* layers. *Relative DynRes* (black squares) was equivalent to the observed deviation of dynamic response between *half-p21* and *p21*-layers. Finally on half-21 layer a gradual transition from a fast dynamics (light layer) to a slow dynamics (heavy layer) was detected. The trend was fitted with sigmoidal Boltzmann function (black line), resulting a state transition at 60(±9) nM (Appendix, Section 14.7).

8.4.2.3 Summary

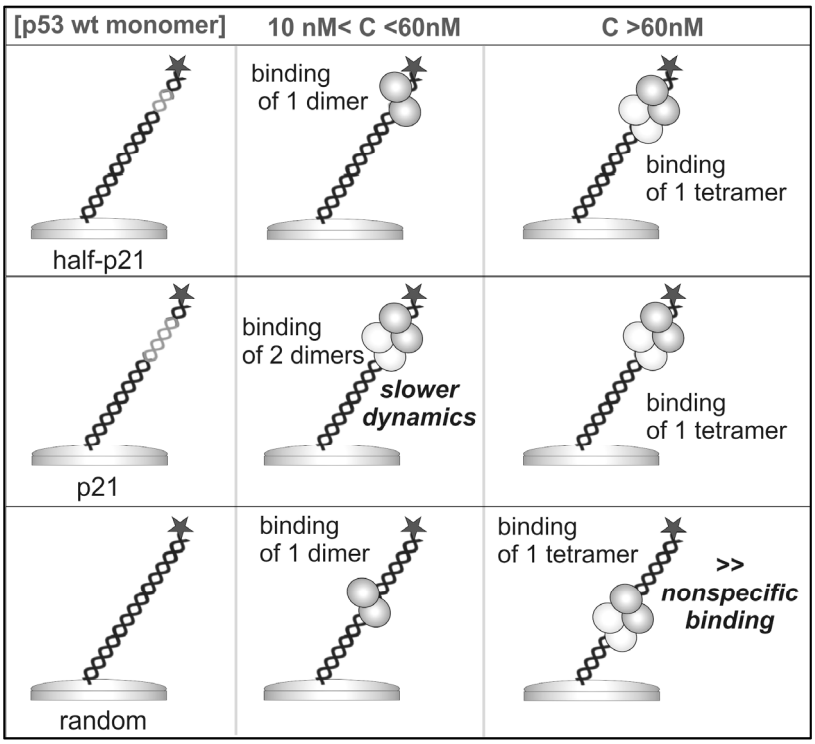

Figure 8.18 Oligomerization transition dimer-tetramer of wt-p53 observed on surface. Below 60 nM, the dimers present in solution bound specifically to the REs, one dimer on one half biding site, resulting in a slower dynamics on *p21* layer. Above 60 nM, the tetramers present in solution bound to all three sequences. The slower dynamics observed on *p21* and *half-p21* compared to random sequence was attributed to different folding states of the p53-RE complex, deriving from site-specific recognition.

Summing up all results for wild-type p53, the kinetics of protein monomer at loaded concentration of 10 nM gave related association rates binding specifically to *p21* and *half-p21* layers, with $k_{on} \backsim 0.9*10^4$ $M^{-1}s^{-1}$ (Table 8.2). Therefore the surface coverage by p53 of the binding sites on the two layers was assumed being the same.

However, in TRM concentration dependence, p53 bound to *half-p21* gave a faster dynamics than p53-*p21* layer (from 30 to 50 nM) (Figure 8.15 A). Moreover, at 68 nM protein concentration, the kinetics of p53 to random sequence was as quick as p53 to specific REs ($K_D \backsim 5$ nM) (Table 8.2), but in TRM the random layer was still faster than *p21* and *half-p21* after p53 binding (Figure 8.15 B).

In LFM, the concentration dependence experiment gave similar results (Figure 8.14): the drop of F_{st} was significantly pronounced on *p21* layer until 70 nM, at this concentration *half-p21* layer resulted in comparable low fluorescence intensity, while the random sequence never reached the same reduced intensity.

Considering the reaction saturation, this occurred at different protein concentrations: on *p21* layer at ∽60 nM, on *half-p21* layer at ∽70 nM and on random layer at ∽90 nM (Figure 8.14).
Finally concentration dependence analysis of dynamic response revealed on *half-p21* layer a transition state between fast and slow dynamics occurring at 60 (±9) nM protein concentration (Figure 8.17).
The explanation to all these effects was the oligomerization state of p53, present in solution as dimer at concentration below 60 nM and as a tetramer above 60 nM (Figure 8.18).

Considering the kinetics detected at 10 nM, dimers of p53 present on surface interacted with the three sequences. On *p21* and *half-p21* sequences the site-specific recognition occurred stabilizing the complex protein-DNA, by which a single dimer contacted a single half site of the RE, meaning one dimer on the *half-p21* and two dimers on the *p21* fragments.
At increased amounts of p53, between 30 and 50 nM, the situation remained the same on *half-p21* and random sequences. However, on *p21* the amount of two dimers per fragment increased rendering the DNA a catalyst of p53 tetramerization. Consequently the dynamic of DNA became significantly slower.
Above 60 nM, the quaternary structure of p53 changes from the dimer to the tetramer form, the biologically active state of the p53 transcription factor. As a tetramer, p53 contacted the DNA with high affinity (kinetics measured at 68 nM), saturating *half-p21* and *p21* layers (slow switching dynamics) and displaying a strong nonspecific binding activity (slow switching dynamics on random sequence). The slower dynamics observed on *p21* and *half-p21* at saturated layer was attributed to a different folding state of the p53-RE complex and distribuited localizations, deriving from sequence-specific recognition. On random sequence the tetramer was less stable in term of conformation, probably sliding and hopping on it, as it will be discussed in Section 8.5.1.

Regarding the LFM concentration dependent experiment, the fluorescence intensity of the DNA standing orientation was severely reduced upon p53 binding on all three layers. Nevertheless, this effect was mostly evident on *p21* layer, and it became analogous on *half-p21* sequence above 70 nM of p53. After excluding the quenching coming from the p53-DNA complex in solution analysis (Appendix, Section 14.7), the drop of intensity was imputed to an induced bending of DNA in presence of bound p53, which brought closer the Cy3 dye to the gold surface, causing a partial quenching of the fluorescence. At saturation, the binding site coverage of all three layers was assumed to

be proportionally analogous, because the measured kinetics at 68 nM p53 concentration was equal in the nanomolar range. Hence an inefficient bending or small perturbations on random sequence could explain the minor effect on fluorescence quenching, because p53 did not recognize a specific RE and continued the search of this site (Section 8.5.1). The bending angle could not be evaluated, though from the height of Cy3 dye the "apparent height" of bent ds-74-mer upon p53 binding was estimated. From Andreas Langer's calculations (Langer, 2010), the bare ds-74-mer was characterized by an angle of 39.2° and 16.9 nm standing height at repulsive potential of -0.4 V having in solution 150 mM total ionic strength. On *p21* and *half-p21* sequences, p53 bound the RE fragment at ∽15 nm (45 bp) away from the gold metal surface. At this distance the protein could not feel the repulsion of the electric field, though at pH 8.0 it was slightly negative charged. Therefore a variation of 39.2° angle of standing ds-DNA at -0.4 V deriving from the protein charge was neglected. Using the correlation of fluorescence intensity versus DNA strand height (Appendix, Section 14.7; Andreas Langer's calculations), the apparent height of Cy3 dye on saturated *p21* and *half-p21* layers was below 5.3 nm. Figure 8.19 represents schematically the bending influence on the apparent height of the p53-DNA complex on surface, from normalized fluorescence analysed in LFM. Below 60 nM, *p21* was contacted by two dimers which could bend efficiently DNA at the RE site, while a single dimer bound to half-*p21* site did not complete the specific recognition affecting less DNA folding. Starting from 70 nM, the tetramer recognized specifically *p21* and *half-p21* causing bending, while the random sequences were less distorted by the presence of the tetramer.

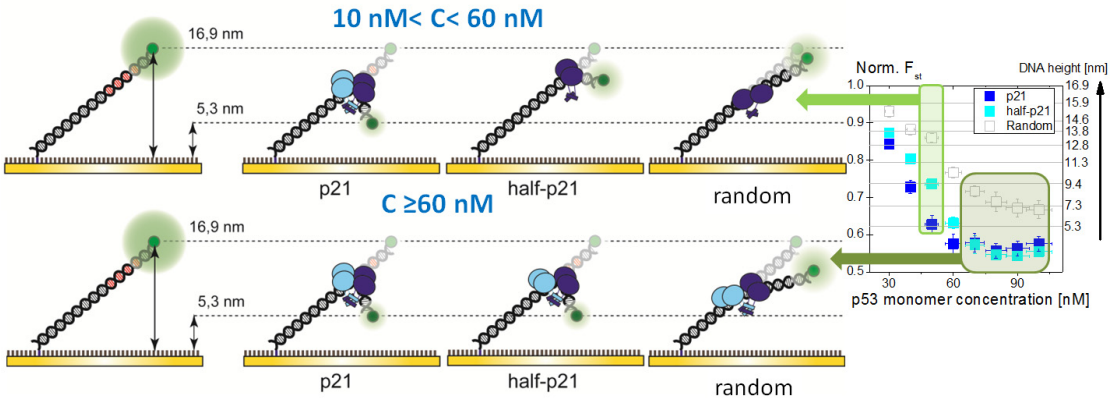

Figure 8.19 Schematic representation of the apparent height of the p53-DNA complex consequent to the DNA bending. The Low Frequency Measurement concentration dependence analysis (right plot) displayed a reduced fluorescence intensity of the standing DNA, correlated to wt-p53 concentration. This effect was attributed to the DNA bending, which led the Cy3 dye closer to the gold metal surface resulting in a partial quenching of the fluorescence. Below 60 nM (upper part), *p21* was contacted by

two dimers which could efficiently bend the DNA at the RE site reducing the apparent height from 16.9 nm to 5.3 nm. At this concentration a single dimer bound to the *half-p21* site affected less the DNA folding. Above 70 nM (lower part), the tetramer recognized specifically *p21* and *half-p21* causing bending and bringing both DNA sequences at the same height of 5.3 nm, while the random fragments were less distorted by the presence of the tetramer. The schematic picture was drawn by Makiko Maruyama.

8.5 Discussion

8.5.1 The nonspecific binding of p53 to DNA

The kinetic measurements showed a specific binding of wt-p53 to *p21* and *half-p21* sequences at 10 nM monomer protein, characterized by an association rate k_{on} of about $0.9*10^4$ $M^{-1}s^{-}1$. However, at 68 nM p53 bound all three sequences with an apparent $K_D \backsim 5$ nM, displaying pronounced nonspecific binding activity. On the other hand at this concentration, the ΔN93ΔC37 truncated form bound to the random sequence as fast as wt-p53, whereas the R280E mutant barely bound *p21* and *half-p21*, presenting no interactions with the random sequence on surface. These two effects, the nonspecific binding displayed by both wt-p53 and ΔN93ΔC37, and no DNA interactions in presence of R280E mutant, were equally observed in EMSA, whereby the presence of DNA competitor could not avoid the nonspecific binding.

Nonspecific association with DNA is crucial for the p53 transcription factor. The great structural complexity of p53, caused by the high proportion of disordered regions, allows an efficient search of DNA by sliding and hopping mechanisms. For instance, McKinney *et al.* showed how p53 can slide along the DNA, but only in presence of C-terminus (CTD 363–393) (McKinney et al, 2004). Furthermore, Tafvizi *et al.*'s findings support this model (Tafvizi et al, 2011): they visualized in real time by single-molecule imaging tools the one-dimensional diffusion along λ-DNA of FL-p53, truncated TC (tetramerization domain +CTD) and core domain. They concluded that TC slides much faster than FL-p53, with respective diffusion coefficients of $6.71(\pm0.58)*10^6$ bp^2s^{-1} and $1.40(\pm0.15)*10^6$ bp^2s^{-1} in 75 mM total salt concentration; instead the core domain, which is unable to slide, hops along DNA.

Finally, they suggested two distinct conformational states of the p53-DNA complex (Figure 8.20): during the search mode, p53 contacts the DNA just by its CTDs and this state is characterized by mostly nonspecific binding and fast sliding; at the sequence-specific recognition, p53 interacts also with core domains, decreasing the translocation speed.

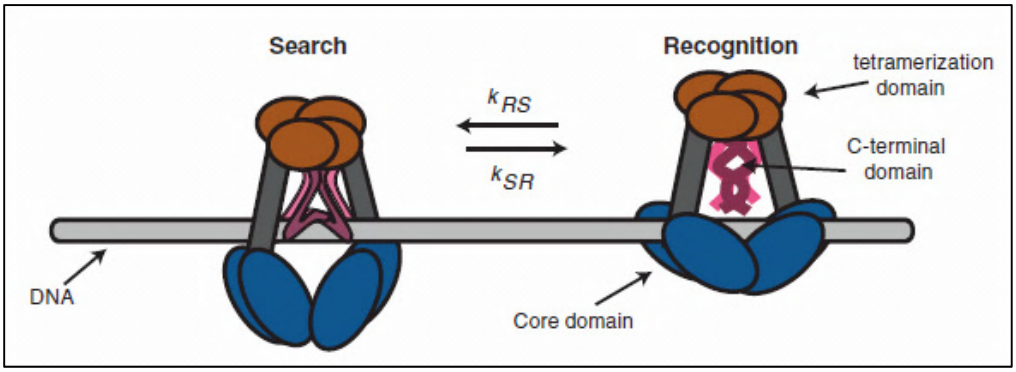

Figure 8.20 The drawing by Tafvizi *at al.* suggests two different binding modes of p53 when searching for its target site on DNA. In the search mode (left), the protein is bound to DNA with just its CTDs causing a fast sliding along DNA. In the recognition mode of a specific binding site (right), the protein contacts DNA also with core domains, decreasing the translocation speed. Resproduced from (Tafvizi et al, 2011).

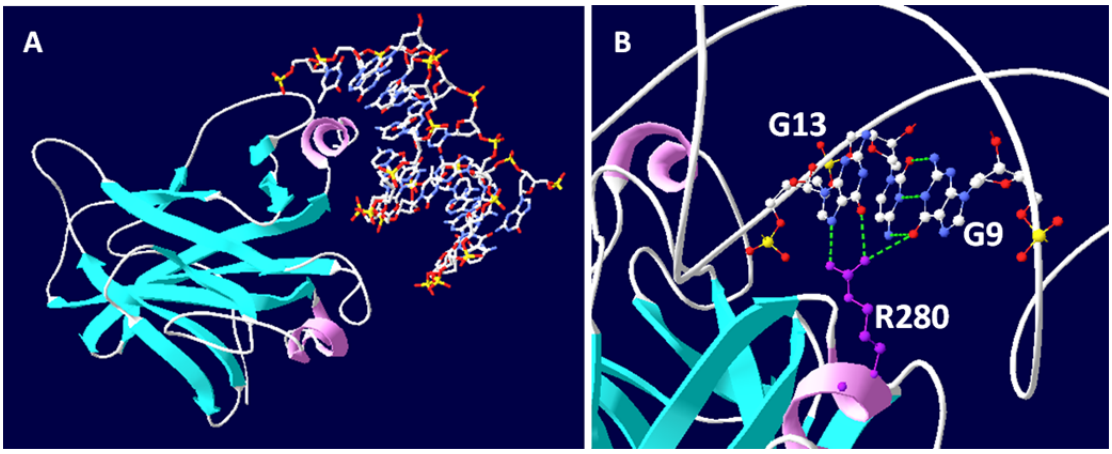

Figure 8.21 A: The α-helix-2 of p53 core domain (α-helix in magenta, β-sheet in cyan) interacting with the major groove of DNA. B: Enlargement on R280 residue and computed hydrogen bond. Arginine can form multiple H-bonds with guanine 13 and 9 from sense and anti-sense strands at the protein-DNA interface. PBD: 1TSR (Cho et al, 1994). The molecules B, E and F were imaged in DeepView.

In this work analogous binding rates to the random sequence were observed for FL-wt-p53 and p53 with deleted CTD; however, no DNA interaction from the R280E mutant was detected. These results suggested a role of p53 core domain in nonspecific binding. On the contrary, in literature the core domain is generally considered the responsible for the site-specific recognition, while the CTD of p53 confers the nonspecific binding activity to the DNA (Weinberg et al, 2004a). Melero *et al.* observed in fluorescence anisotropy FL-p53 binding to a 100 bp random sequence with an affinity of ~150 nM at 122–172 mM ionic strength; however when the CTD was missing, the affinity binding was reduced to ~ 2.2 μM (Melero et al, 2011). Also, Ang *et al*. observed a reduced nonspecific binging with deleted CTD, but in addition they detected a further lower

binding to random DNA sequence by mutating a single arginine in the core domain of FL-p53 (R273H) (K_D FL-p53= 360±60 nM; truncated p53= 680±20 nM; R273H= 1500±200 nM; at 225 mM ionic strength). Finally they did not discuss the R273H mutant, being focused on the role of CTD (Ang et al, 2006).
Eventually, the effect of single mutations on the nonspecific association was considered in the mathematical predictions by Khazanov and Levy (Khazanov & Levy, 2011). They modelled the wiring on DNA of FL-wt-p53 tetramer and single missense mutants (the most frequent mutations that occur at the p53–DNA interface, including R280E) and they analysed their sliding dynamics. They concluded a co-participation of the core and C-terminal domains in the nonspecific DNA binding, because single mutations in the core domain cause an important loss of electrostatic interactions at the protein-DNA interface, resulting in faster predicted diffusion. Figure 8.21 displays the protein α-helix-2 at the interface of the DNA-p53 core domain and the R280 residue which contacts the major groove forming multiple hydrogen bonds with guanine bases. If this residue is mutated, the interaction at the interface is disrupted, resulting in a net loss of DNA binding (Wright et al, 2002).

Concluding, the p53 tetramer associates to DNA by core and C-terminal domains. The protein could be likened to ***an eight wheel truck on the DNA-highway***: the CTDs are four low friction wheels which slide along DNA backbone; the core domains are instead high friction wheels that contact DNA bases in the major groove. If CTDs are missing, the big p53 slows down the translocation, but if the high friction wheels suddenly become low friction tires (e.g. R280E single mutation), then the big quaternary p53 slides out the highway.

8.5.2 The p53 dimer-tetramer transition detected on surface

The oligomerization state of p53 is an important factor, as the tetramer represents the active form in the cell for gene transcription. The protein exists as monomers, dimers and tetramers in equilibrium. Recently, two papers from the same research group were published, presenting discordant results about the dimer-tetramer equilibrium. In the first publication, Rajagopalan *et al.* observed a dissociation constant of 120 nM for FL-p53 in analytical ultracentrifugation (Rajagopalan et al, 2008). The temperature was not indicated, but they compared the data to anisotropy measurements, made at 20°C, so that should be also the temperature used in AUC. For the detection the protein was labelled by FLAsH dye, introducing a tetracysteine motif at the C-terminal (Griffin et al, 1998). In the second study, they investigated the oligomerization state of FL-p53

labelled with Atto-655 dye in fluorescence correlation spectroscopy (FCS), since this method has higher sensitivity respect to the traditional assays *in vitro* (Rajagopalan et al, 2011). They measured tetramer-dimer transitions at 20(±3) nM and 50(±7) nM, respectively at 20 °C and 37 °C, and estimated the dimer-monomer equilibrium at a concentration below 0.25 nM. In both investigations they employed the thermostable variant FL-p53; the used buffers were similar in ionic strength (215 nM) and reductive conditions, but in AUC analysis there was 10% glycerol, while in FCS glycerol was exchanged with 0.05% Tween 20.

Here in dynamic analysis, a transition from the dimeric to the tetrameric state was recorded at 60(±9) nM, slightly dissimilar from 20(±3) nM (Rajagopalan et al, 2011). The value was measured at 15°C, in presence of 5% glycerol and at lower ionic strength (150 mM); therefore the discrepancy was imputed to the diverse experimental conditions and to the different used proteins.

Eventually the measured kinetics at 10 nM protein concentration represented the binding activity of the protein as dimer, while at 68 nM the activity was referred to the protein tetramer. Hence, the association constants were expressed for p53 dimer at 5 nM injection, resulting for *p21* and *half-p21* sequences in $k_{on} \backsim 1.7*10^4$ $M^{-1}s^{-1}$, and for the random sequence in $k_{on} \backsim 0.2*10^4$ $M^{-1}s^{-1}$ (Table 8.3). At 17 nM tetramer concentration the k_{on} was 10-fold higher on *p21* and *half-p21* sequences and 70-fold higher on random sequence; the dissociation rate k_{off} was equal to $2*10^{-4}$ s^{-1} on all three layers, while the resulting dissociation constant K_D was approximately at 1 nM (Table 8.3).

Table 8.3 Association rate constants and affinity values recalculated for 5 nM dimer concentration and for 17 nM tetramer concentration. The SD values are indicated in the round brackets.

	p53 dimer at 5 nM (10 nM monomer)	**p53 tetramer at 17 nM (68 nM monomer)**		
	k_{on} **[10^4 $M^{-1}s^{-1}$]**	k_{off} **[10^{-4} s^{-1}]**	k_{on} **[10^4 $M^{-1}s^{-1}$]**	K_D **[nM]**
p21	1.59 (0.32)	2.40 (0.11)	16.5 (0.9)	1.45 (0.11)
half-p21	1.85 (0.10)	2.17 (0.07)	21.7 (1.1)	1.00 (0.06)
Random	0.23 (0.11)	2.11 (0.19)	14.4 (0.7)	1.46 (0.15)

In vivo the low concentration of p53 is kept by the autoregulatory feedback loop with the MDM2 (Picksley & Lane, 1993; Wu et al, 1993). Furthermore, the oligomeric state is tightly regulated by partner proteins which are themselves under specific controls, making the whole network of p53 a massively intricate system. For instance, the phosphorylation of p53's C-terminal domain by either the 14-3-3 protein family or the c-Abl tyrosine kinase facilitates and stabilizes the tetramerization state (Nie et al, 2000;

Rajagopalan et al, 2008). Another regulation is operated by the S100 protein family: these proteins, when overexpressed, bind to monomeric, dimeric or tetrameric forms of p53 in order to regulate its activity in the cytosol (Fernandez-Fernandez et al, 2005; van Dieck et al, 2009).

This fine p53 regulation is essential to keep the cellular homeostasis, since how it was observed in this work, p53 tetramer is itself active and ready to recognize response elements on DNA. To guarantee the efficacy of genetic responses and protein pathways, p53's network must be under a strict control.

8.5.3 The DNA bending upon p53 binding

In the result section, the drop of fluorescence intensity in the concentration dependent experiment was attributed to DNA bending, resulting from wt-p53 binding to *p21* and *half-p21* layers. A minor effect was observed also on random sequence, especially above 70 nM. Recently, Spuhler *et al.* detected conformational changes of ds-DNA upon the specific binding of *E. coli* integration host factor on *switch*SENSE (Spuhler et al, 2010). They demonstrated that the fluorescence reduction was caused by the increased vicinity of the Cy3 dye to the gold surface, due to DNA bending.

The DNA bending occurs in the great majority of protein–DNA complexes. The sequence-specific recognition is generally stabilized by DNA backbone distortions. In a localized point, the double stranded DNA gets melted by the protein, which takes contact with the bases by hydrogen bonds and π stacking interactions.

The DNA bending was observed in crystal structures of many transcription factors in numerous reports, from prokaryotes and eukaryotes: a few examples are the *E. coli* catabolite gene activator protein (CAP) (McKay et al, 1982), the *E. coli trp* repressor (Schevitz et al, 1985), the *E. coli met* repressor (Rafferty et al, 1989), the *EcoR* I restriction endonuclease (McClarin et al, 1986) and the cooperative binding of NFAT and Fos-Jun (Chen et al, 1998).

Regarding p53, in literature the DNA bending upon the site-specific recognition has been proven employing different methods. The first study was published by Balagurumoorthy *et al*.: by DNA circularization they demonstrated the ability of four p53 core domains to direct a considerable conformational change of 60° bending in RE DNA (Balagurumoorthy et al, 1995). Later, by using A-tract phasing experiments Nagaich *et al.* detected FL-wt-p53 bending the DNA by 51–57°, on RE sites having a ds-CATG sequence at the junction of two consensus pentamers in each half-site (Nagaich et al, 1997; Nagaich et al, 1999). Moreover, they could see a direct correlation between the DNA bending angle and the binding affinity of p53 to the REs. In transmission electron

microscopy, Cherny *et al.* observed that the bending induced by FL-wt-p53 varied from 40° to 48° upon decreasing of KCl concentration, from 50 mM to 1 mM (Cherny et al, 1999). Furthermore, from a resolved crystal structure, Ho *at al.* could see a dimer of mouse p53 core domain bound to the RE half site causing the bending by circa 20°. The structure revealed that one core domain interacted with one pentamer, symmetrically to the opposite faces of ds-DNA, forcing the distortion (Ho et al, 2006).

However, detailed structures of the bent DNA and the FL-p53/DNA complex are still unavailable. Hence, recently Pan and Nussinov simulated in molecular dynamics the DNA bending upon the binding of one or two dimers of p53 core domain to RE sequence. They confirmed that one dimer can bend the RE half site by 20°C, while two dimers, making dimer-dimer interaction, required conformational changes in the DNA, leading to the bending at the centre of the full site by 35° (Figure 8.22) (Pan & Nussinov, 2007).

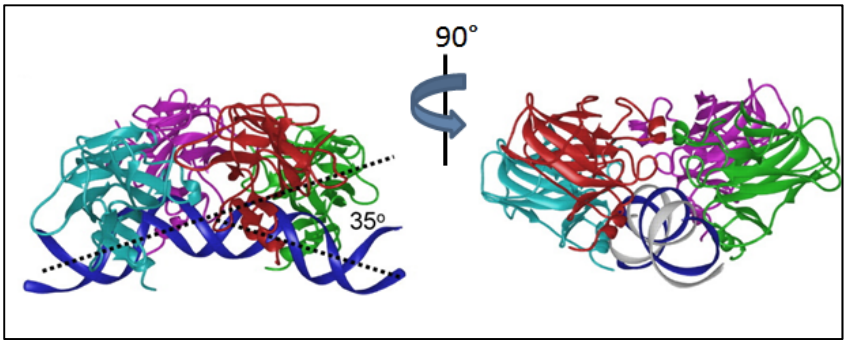

Figure 8.22 Simulation in molecular dynamics of DNA bending upon binding to four p53 core domains. In the two orthogonal views, the core domains were paired (cyan and magenta, red and green), while binding to the DNA. The left panel illustrates the DNA bending angle of 35°. Reproduced from (Pan & Nussinov, 2007).

Concluding, on *switch*SENSE surface the site-specific recognition of *p21* and *half-p21* was observed based on the DNA bending. The drastic drop of fluorescence observed on both sequences, above 70 nM p53 concentration, was attributed to p53 tetramer binding the RE sites and causing an efficient distortion at the ds-CATG junction point (bending angle of ∽35° (Pan & Nussinov, 2007)). At concentrations smaller than 60 nM, each of the two dimers of p53 contacted a single half site of *p21* RE and by localized tetramerization produced the conformational change on DNA. However, the *half-p21* site was recognized by one dimer, which gave a smaller bending (by ∽20°C (Ho et al, 2006)). Possibly p53 perturbed also the random sequence by an inefficient and small bending, continuing the scansion of DNA in search of one RE site.

8.5.4 The role of the half site response elements

From the kinetic analysis, p53 loaded at 10 nM monomer presented an equal binding association to *p21* and *half-p21*, $k_{on} \backsim 0.8*10^4$ $M^{-1}s^{-1}$ (Table 8.2), indicating that the p53 dimer recognized the half site on both REs in the same manner. The identical situation occurred at the tetrameric regime, where p53 bound all three sequences as a tetramer, but just on *p21* and *half-p21* the recognition resulted in a efficient DNA bending.

The fact that *in vitro*, in an isolated system, p53 showed similar behaviour to half or to the entire *p21* RE should not surprise. However, the sequence-specific recognition is not strictly correlated to the transactivation of p53 for gene transcription. In their study, Jordan *et al.* investigated the transactivation of wt-p53 in human cell culture in presence of one half of the *p21*-5' RE (left or right half site), which was inserted in the promoter of luciferase reporter vector. Comparing to the negative control, they observed a small transactivation (7-fold higher) only at high levels of induced p53 expression (CMV promoter for p53 gene vector), while wt-p53 on full *p21* RE was 35-fold greater (Jordan et al, 2008).

Recently many non-canonical REs, composed by half or three-quarter sites, have been identified in promoter regions of genes under p53's control (Jordan et al, 2008; Menendez et al, 2009). It has been suggested that p53 half-sites may play a role in conveying together different transcriptional networks as described for a SNP in the *FLT-1* promoter (Menendez et al, 2007). In their study, Menendez *et al.* detected a co-regulation of *FLT-1* mutated promoter by p53 and estrogen receptor. Finally, the response elements composed by a single half site could assist several roles in the genome, expanding the regulation mechanisms of genes belonging to p53's network.

8.6 Conclusion

On *switch*SENSE sensor the binding of human full-length wild-type p53 was detected on ds-DNA layers integrating *p21* and *half-p21* response elements.

For the first time p53 was investigated without any purification tags or stabilizing mutations, and the kinetic association and the oligomerization state of full-length p53 was determined on one single platform.

In DNA switching dynamics, the concentration dependent experiment releaved on *half-p21* layer a transition state between fast and slow dynamics occurring at 60(±9) nM p53 monomer concentration. The dimer-tetramer equilibrium was discriminated on *switch*SENSE surface sensor.

Additionally, the association constants were measured at both dimerization and tetramerization regimes. Below 60 nM, the specific binding of p53 to *p21* and *half-p21* sequences was characterized by an association rate k_{on} of $1.7*10^4$ $M^{-1}s^{-1}$ on both response elements, which was 8-fold greater than the nonspecific interaction to the random sequence.

Above 60 nM, p53 gave similar binding kinetics to specific and to nonspecific DNA sequences. The k_{on} was 10-fold higher on *p21* and *half-p21* sequences and 70-fold higher on random sequence; the dissociation rate k_{off} was equal to $2*10^{-4}$ s^{-1} on all three layers, while the resulting dissociation constant K_D was approximately at 1 nM.

At the same concentration regime, the truncated p53 variant, with deleted N- and C-termini (ΔN93ΔC37) presented similar association behaviour to all three sequences, while the R280E mutant resulted in a complete loss of DNA binding activity.

The nonspecific binding by wt-p53 and ΔN93ΔC37 and the inactivity of R280E were observed also in the conventional method EMSA, suggesting a role of the p53 core domain in nonspecific DNA interactions.

However, the specific recognition of the response elements by the p53 tetramer could be detected in switching dynamics and fluorescence intensity. The tetramer could stabilize the interaction at the RE site leading to DNA bending. This conformational change was visible in the slow dynamics and the quenching of fluorescence intensity at repulsive potential.

On the other hand, the identified tetramer attached to the random sequence was related to p53 sliding and hopping along the DNA, searching for the response element.

Concluding, p53 tetramer presented an equivalent activity in recognizing DNA on surface, indicating that in an isolated system the protein can efficiently scan the double

stranded molecules. Therefore in the cell p53 is tightly controlled to guarantee the efficacy of genetic responses and protein pathways when it is required.

9. Conclusion

In this work the *switch*SENSE platform was successfully employed in protein characterization. The chip design enabled a versatile functionalization of the surface with ligands to accomplish the detection and analyses of protein-protein and protein-DNA interactions in a real-time and label-free manner.

Hereby the ligand human Carbonic Anhydrase 1 was immobilized on electro-switchable DNA layers upon the preparation of protein-DNA mono conjugates. The presence of hCA1 was confirmed on surface by switching dynamic measurements. Consequently, a comparative study of antibody affinity could be performed on hCA1-DNA layers. Loading the antibodies at nanomolar concentration on surface, the association and dissociation phases were monitored based on switching dynamic response of the electrically modulated layers. The dynamics revealed the binding state of antibodies on hCA1, since the increase in hydrodynamic drag slowed the switching movement. The kinetics of four monoclonal antibodies was evaluated. The direct comparison with SPR Biacore™ presented discordant results, whereby the kinetics measured in *switch*SENSE displayed affinities at the picomolar range, against the nanomolar range measured in Biacore. Two factors were involved: i) the higher detection sensitivity of *switch*SENSE technology and ii) the avidity observed on switchable hCA1-DNA surface, which stabilized the antibody-hCA1 complex maximizing the strength of the interaction.

Additionally, *switch*SENSE was employed for the characterization of p53 DNA-binding activity. The binding of human full-length wild-type p53 was detected on ds-DNA layers integrating *p21* and *half-p21* response elements, employing steady-state fluorescence quenching as well as dynamic DNA-switching experiments. For the first time, human wild-type p53 could be characterized in the absence of any purification tags or stabilizing mutations. In DNA switching dynamic measurements, the oligomerization of p53-dimers to p53-tetramers could be directly observed with the surface-based sensor and a transition was identified at 60 nM of p53 monomer concentration. In the dimerization concentration regime, the kinetic analysis evidenced the *specific* binding of p53 to *p21* and *half-p21* sequences, with an association rate k_{on} of $1.7*10^4$ $M^{-1}s^{-1}$ which was independent of the length of the response elements. In the tetramerization concentrationregime, p53 exhibited similar binding kinetics to specific and to nonspecific DNA sequences, characterized by an association rate which is app. 10 times higher than for the dimeric form and an apparent equilibrium constant K_D of

approximately 1 nM. Moreover, p53-induced conformational changes of the DNA structure, that is a pronounced bending, was detected by fluorescence quenching.

The presented results demonstrate the relevance of electro-switchable DNA layers for the analysis of proteins, and show the merit of obtaining multiple parameters – k_{on}, k_{off}, K_D, size and oligomerization state, occurrence of structural changes – in a single assay.

10. References

Abdiche Y, Malashock D, Pinkerton A, Pons J (2008) Determining kinetics and affinities of protein interactions using a parallel real-time label-free biosensor, the Octet. *Analytical Biochemistry* **377**: 209-217.

Aggarwal M, McKenna R (2012) Update on carbonic anhydrase inhibitors: a patent review (2008 - 2011). *Expert opinion on therapeutic patents* **22**: 903-915.

Agrawal BBL, Goldstei.Ij (1968) PROTEIN-CARBOHYDRATE INTERACTION .7. PHYSICAL AND CHEMICAL STUDIES ON CONCANAVALIN A HEMAGGLUTININ OF JACK BEAN. *Archives of Biochemistry and Biophysics* **124**: 218-229.

Alberts B, Johnson A, Walter P, J. L, Raff M, Roberts K (2008) *Molecular Biology of the Cell*, 5th edn.: Garland Science, New York.

Alberty RA. (2003) Thermodynamics of Biochemical Reactions. *Wiley-Interscience.*

Amaral JD, Xavier JM, Steer CJ, Rodrigues CMP (2010) Targeting the p53 Pathway of Apoptosis. *Current Pharmaceutical Design* **16**: 2493-2503.

Amersham Biosciences (2002) *Antibody Purification: Handbook.*: *Edition AC.*

Ang HC, Joerger AC, Mayer S, Fersht AR (2006) Effects of common cancer mutations on stability and DNA binding of full-length p53 compared with isolated core domains. *Journal of Biological Chemistry* **281**: 21934-21941.

Arinaga K, Rant U, Knezevic J, Pringsheim E, Tornow M, Fujita S, Abstreiter G, Yokoyama N (2007) Controlling the surface density of DNA on gold by electrically induced desorption. *Biosensors & Bioelectronics* **23:** 326-331.

Aramayo R, Sherman MB, Brownless K, Lurz R, Okorokov AL, Orlova EV (2011) Quaternary structure of the specific p53-DNA complex reveals the mechanism of p53 mutant dominance. Nucleic Acids Research 39: 8960-8971.

Armstrong JK, Wenby RB, Meiselman HJ, Fisher TC (2004) The hydrodynamic radii of macromolecules and their effect on red blood cell aggregation. *Biophysical Journal* **87**: 4259-4270.

Bahar T, Tuncel A (2004) Concanavalin A carrying reactive beads for yeast invertase purification. *Reactive & Functional Polymers* **61**: 203-210.

Bailey RC, Kwong GA, Radu CG, Witte ON, Heath JR (2007) DNA-encoded antibody libraries: A unified platform for multiplexed cell sorting and detection of genes and proteins. *Journal of the American Chemical Society* **129**: 1959-1967.

Balagurumoorthy P, Sakamoto H, Lewis MS, Zambrano N, Clore GM, Gronenborn AM, Appella E, Harrington RE (1995) FOUR P53 DNA-BINDING DOMAIN PEPTIDES BIND NATURAL P53-RESPONSE ELEMENTS AND BEND THE DNA. *Proceedings of the National Academy of Sciences of the United States of America* **92**: 8591-8595.

Barak Y, Juven T, Haffner R, Oren M (1993) MDM2 EXPRESSION IS INDUCED BY WILD TYPE-P53 ACTIVITY. *Embo Journal* **12:** 461-468.

Barlev NA, Liu L, Chehab NH, Mansfield K, Harris KG, Halazonetis TD, Berger SL (2001) Acetylation of p53 activates transcription through recruitment of coactivators/histone acetyltransferases. *Molecular Cell* **8**: 1243-54.

Bell S, Klein C, Muller L, Hansen S, Buchner J (2002) p53 contains large unstructured regions in its native state. *Journal of Molecular Biology* **322**: 917-927.

Benchimol S, Lamb P, Crawford LV, Sheer D, Shows TB, Bruns GAP, Peacock J (1985) TRANSFORMATION ASSOCIATED P53 PROTEIN IS ENCODED BY A GENE ON HUMAN CHROMOSOME-17. *Somatic Cell and Molecular Genetics* **11:** 505-509.

Benvegnu S, Franciotta D, Sussman J, Bachi A, Zardini E, Torreri P, Govaerts C, Pizzo S, Legname G (2009) Prion Protein Paralog Doppel Protein Interacts with Alpha-2-Macroglobulin: A Plausible Mechanism for Doppel-Mediated Neurodegeneration. *Plos One* **4**: e5968.

Bereli N, Akgol S, Yavuz H, Denizli A (2005) Antibody purification by concanavalin a affinity chromatography. *Journal of Applied Polymer Science* **97**: 1202-1208.

Bergmann S, Rohde M, Hammerschmidt S (2004) Glyceraldehyde-3-phosphate dehydrogenase of Streptococcus pneumoniae is a surface-displayed plasminogen-binding protein. *Infection and Immunity* **72.**

Bista M, Freund SM, Fersht AR (2012) Domain-domain interactions in full-length p53 and a specific DNA complex probed by methyl NMR spectroscopy. Proceedings of the National Academy of Sciences of the United States of America 109: 15752–15756.

Bosley TM, Salih MA, Alorainy IA, Islam MZ, Oystreck DT, Suliman OSM, al Malki S, Suhaibani AH, Khiari H, Beckers S, van Wesenbeeck L, Perdu B, AlDrees A, Elmalik SA, Van Hul W, Abu-Amero KK (2011) The neurology of carbonic anhydrase type II deficiency syndrome. *Brain* **134**: 3502-3515.

Brachmann RK, Yu KX, Eby Y, Pavletich NP, Boeke JD (1998) Genetic selection of intragenic suppressor mutations that reverse the effect of common p53 cancer mutations. *Embo Journal* **17:** 1847-1859.

Brinkers S, Dietrich HRC, de Groote FH, Young IT, Rieger B (2009) The persistence length of double stranded DNA determined using dark field tethered particle motion. *Journal of Chemical Physics* **130**: 215105.

Brown PH, Schuck P (2006) Macromolecular size-and-shape distributions by sedimentation velocity analytical ultracentrifugation. *Biophysical Journal* **90**: 4651-4661.

Bustamante C, Bryant Z, Smith SB (2003) Ten years of tension: single-molecule DNA mechanics. *Nature* **421:** 423-427.

Canadillas JMP, Tidow H, Freund SMV, Rutherford TJ, Ang HC, Fersht AR (2006) Solution structure of p53 core domain: Structural basis for its instability. *Proceedings of the National Academy of Sciences of the United States of America* **103**: 2109-2114.

Carney BK, Silva VC, Cassimeris L (2012) The microtubule cytoskeleton is required for a G2 cell cycle delay in cancer cells lacking stathmin and p53. *Cytoskeleton* **69**: 278-289.

Chakravarty S, Kannan KK (1994) DRUG-PROTEIN INTERACTIONS - REFINED STRUCTURES OF 3 SULFONAMIDE DRUG COMPLEXES OF HUMAN CARBONIC-ANHYDRASE-I ENZYME. *Journal of Molecular Biology* **243**: 298-309.

Chang J, Kim DH, Lee SW, Choi KY, Sung YC (1995) TRANSACTIVATION ABILITY OF P53 TRANSCRIPTIONAL ACTIVATION DOMAIN IS DIRECTLY RELATED TO THE BINDING-AFFINITY TO TATA-BINDING PROTEIN. *Journal of Biological Chemistry* **270**: 25014-25019.

Chen L, Glover JNM, Hogan PG, Rao A, Harrison SC (1998) Structure of the DNA binding domains from NFAT, Fos and Jun bound specifically to DNA. *Nature* **392**: 42-48.

Cherny DI, Striker G, Subramaniam V, Jett SD, Palecek E, Jovin TM (1999) DNA bending due to specific p53 and p53 core domain-DNA interactions visualized by electron microscopy. *Journal of Molecular Biology* **294**: 1015-1026.

Chien HO, Sturtevant JM (1963) The kinetics of the hydration of carbon dioxide at 25 degree. *Jour Biol Chem* **238**: 3499-3501.

Cho YJ, Gorina S, Jeffrey PD, Pavletich NP (1994) CRYSTAL-STRUCTURE OF A P53 TUMOR-SUPPRESSOR DNA COMPLEX - UNDERSTANDING TUMORIGENIC MUTATIONS. *Science* **265**: 346-355.

Dawson R, Muller L, Dehner A, Klein C, Kessler H, Buchner J (2003) The N-terminal domain of p53 is natively unfolded. *Journal of Molecular Biology* **332**: 1131-1141.

De Simone G, Supuran CT (2010) Carbonic anhydrase IX: Biochemical and crystallographic characterization of a novel antitumor target. *Biochimica Et Biophysica Acta-Proteins and Proteomics* **1804**: 404-409.

Dehner A, Klein C, Hansen S, Muller L, Buchner J, Schwaiger M, Kessler H (2005) Cooperative binding of p53 to DNA: Regulation by protein-protein interactions through a double salt bridge. *Angewandte Chemie-International Edition* **44**: 5247-5251.

Di Lello P, Jenkins LMM, Jones TN, Nguyen BD, Hara T, Yamaguchi H, Dikeakos JD, Appella E, Legault P, Omichinski JG (2006) Structure of the Tfb1/p53 complex: Insights into the interaction between the p62/Tfb1 subunit of TFIIH and the activation domain of p53. *Molecular Cell* **22**: 731-740.

Dornan D, Hupp TR (2001) Inhibition of p53-dependent transcription by BOX-I phospho-peptide mimetics that bind to p300. *Embo Reports* **2**: 139-144.

Drake AW, Tang ML, Papalia GA, Landes G, Haak-Frendscho M, Klakamp SL (2012) Biacore surface matrix effects on the binding kinetics and affinity of an antigen/antibody complex. *Analytical biochemistry* **429**: 58-69.

Duan JX, Nilsson L (2006) Effect of Zn2+ on DNA recognition and stability of the p53 DNA-binding domain. *Biochemistry* **45**: 7483-7492.

Eisenberg S, Korza G, Carson J, Liachko I, Tye B-K (2009) Novel DNA Binding Properties of the Mcm10 Protein from Saccharomyces cerevisiae. *Journal of Biological Chemistry* **284**: 25412-25420.

El-Deiry WS (1998) Regulation of p53 downstream genes. *Seminars in Cancer Biology* **8:** 345-357.

Eldeiry WS, Kern SE, Pietenpol JA, Kinzler KW, Vogelstein B (1992) DEFINITION OF A CONSENSUS BINDING-SITE FOR P53. *Nature Genetics* **1:** 45-49.

Eldeiry WS, Tokino T, Velculescu VE, Levy DB, Parsons R, Trent JM, Lin D, Mercer WE, Kinzler KW, Vogelstein B (1993) WAF1, A POTENTIAL MEDIATOR OF P53 TUMOR SUPPRESSION. *Cell* **75**: 817-825.

Espinosa JM, Emerson BM (2001) Transcriptional regulation by p53 through intrinsic DNA/chromatin binding and site-directed cofactor recruitment. *Molecular Cell* **8**: 57-69.

Evan GI, Vousden KH (2001) Proliferation, cell cycle and apoptosis in cancer. *Nature* **411:** 342-348.

Faggiano S, Ronda L, Bruno S, Jankevics H, Mozzarelli A (2010) Polymerized and polyethylene glycol-conjugated hemoglobins: A globin-based calibration curve for dynamic light scattering analysis. *Analytical Biochemistry* **401**: 266-270.

Fang SY, Jensen JP, Ludwig RL, Vousden KH, Weissman AM (2000) Mdm2 is a RING finger-dependent ubiquitin protein ligase for itself and p53. *Journal of Biological Chemistry* **275**: 8945-8951.

Fernandez-Fernandez MR, Veprintsev DB, Fersht AR (2005) Proteins of the S100 family regulate the oligomerization of p53 tumor suppressor. *Proceedings of the National Academy of Sciences of the United States of America* **102**: 4735-4740.

Fleming RMT, Thiele I, Nasheuer HP (2009) Quantitative assignment of reaction directionality in constraint-based models of metabolism: Application to Escherichia coli. *Biophysical Chemistry* **145**: 47-56.

Fong CC, Wong MS, Fong WF, Yang MS (2002) Effect of hydrogel matrix on binding kinetics of protein-protein interactions on sensor surface. *Analytica Chimica Acta* **456:** 201-208.

Friedler A, Veprintsev DB, Hansson LO, Fersht AR (2003) Kinetic instability of p53 core domain mutants - Implications for rescue by small molecules. *Journal of Biological Chemistry* **278**: 24108-24112.

Funk WD, Pak DT, Karas RH, Wright WE, Shay JW (1992) A TRANSCRIPTIONALLY ACTIVE DNA-BINDING SITE FOR HUMAN P53 PROTEIN COMPLEXES. *Molecular and Cellular Biology* **12:** 2866-2871.

Furukawa K, Kobata A (1992) Protein glycosylation. *Current Opinion in Biotechnology* **3**: 4-10.

Gast K, Fiedler C (2012) Dynamic and static light scattering of intrinsically disordered proteins. *Methods in molecular biology (Clifton, NJ)* **896**: 137-161.

GE Healthcare (2009) *BIACORE™ X100 Handbook.*: *BR-1008-10 Edition AC.*

Gibbons BH, Edsall JT (1963) RATE OF HYDRATION OF CARBON DIOXIDE AND DEHYDRATION OF CARBONIC ACID AT 25 DEGREES. *Journal of Biological Chemistry* **238**: 3502-3507.

Giono LE, Manfredi JJ (2006) The p53 tumor suppressor participates in multiple cell cycle checkpoints. *Journal of Cellular Physiology* **209**: 13-20.

Gokarn YR, McLean M, Laue TM (2012) Effect of PEGylation on Protein Hydrodynamics. *Molecular Pharmaceutics* **9**: 762-773.

Gottifredi V, Shieh SY, Prives C (2000) Regulation of p53 after different forms of stress and at different cell cycle stages. *Cold Spring Harbor Symposia on Quantitative Biology* **65**: 483-488.

Griffin BA, Adams SR, Tsien RY (1998) Specific covalent labeling of recombinant protein molecules inside live cells. *Science* **281**: 269-272.

Gruber HJ, Hahn CD, Kada G, Riener CK, Harms GS, Ahrer W, Dax TG, Knaus HG (2000) Anomalous fluorescence enhancement of Cy3 and Cy3.5 versus anomalous fluorescence loss of Cy5 and Cy7 upon covalent linking to IgG and noncovalent binding to avidin. *Bioconjugate Chemistry* **11**: 696-704.

Gu B, Zhu W-G (2012) Surf the Post-translational Modification Network of p53 Regulation. *International Journal of Biological Sciences* **8**: 672-684.

Gu T-j, Wei W, Duan Y, Jiang C-l, Chen Y, Yu X-h, Wu J-x, Wu Y-g, Kong W (2011) Identification of Binding Epitope for Anti-Rabies Virus Glycoprotein Single-Chain Fv Fragment FV57. *Protein and Peptide Letters* **18**: 1099-1106.

Gu W, Roeder RG (1997) Activation of p53 sequence-specific DNA binding by acetylation of the p53 C-terminal domain. *Cell* **90**: 595-606.

Gu W, Shi XL, Roeder RG (1997) Synergistic activation of transcription by CBP and p53. *Nature* **387**: 819-823.

Haff L, Juhasz P, Martin S, Roskey M, Smirnov I, Stanick W, Vestal M, Waddell K (1998) Oligonucleotide analysis by MALDI-MS. *Analusis* **26:** 26-30.

Hampel P (2009) Dynamics of Surface-Tethered Protein-DNA Conjugates in AC Electric Fields. *Master's thesis, Walter Schottky Institute, TU München.*

Han SH, Kim SK, Park K, Yi SY, Park H-J, Lyu H-K, Kim M, Chung BH (2010) Detection of mutant p53 using field-effect transistor biosensor. *Analytica Chimica Acta* **665**: 79-83.

Hansen S, Hupp TR, Lane DP (1996) Allosteric regulation of the thermostability and DNA binding activity of human p53 by specific interacting proteins. *Journal of Biological Chemistry* **271**: 3917-3924.

Henriksson-Peltola P, Sehlen W, Haggard-Ljungquist E (2007) Determination of the DNA-binding kinetics of three related but heteroimmune bacteriophage repressors using EMSA and SPR analysis. *Nucleic Acids Research* **35**: 3181-3191.

Hermanson G (2008) *Bioconjugate techniques*, 2nd edn.: *Academic Press Elsevier.*

Ho WC, Fitzgerald MX, Marmorstein R (2006) Structure of the p53 core domain dimer bound to DNA. *Journal of Biological Chemistry* **281**: 691-699.

Honda R, Yasuda H (2000) Activity of MDM2, a ubiquitin Ligase, toward p53 or itself is dependent on the RING finger domain of the ligase. *Oncogene* **19**: 20494-20502.

Hupp TR, Meek DW, Midgley CA, Lane DP (1993) ACTIVATION OF THE CRYPTIC DNA-BINDING FUNCTION OF MUTANT FORMS OF P53. *Nucleic Acids Research* **21**: 3167-3174.

Janshoff A, Galla HJ, Steinem C (2000) Piezoelectric mass-sensing devices as biosensors - An alternative to optical biosensors? *Angewandte Chemie-International Edition* **39**: 4004-4032.

Jeffrey PD, Gorina S, Pavletich NP (1995) CRYSTAL-STRUCTURE OF THE TETRAMERIZATION DOMAIN OF THE P53 TUMOR-SUPPRESSOR AT 1.7 ANGSTROMS. *Science* **267:** 1498-1502.

Jin SK, Levine AJ (2001) The p53 functional circuit. *Journal of Cell Science* **114:** 4139-4140.

Joerger AC, Fersht AR (2008) Structural biology of the tumor suppressor p53. *Annual Review of Biochemistry* **77**: 557-582.

Jordan JJ, Menendez D, Inga A, Nourredine M, Bell D, Resnick MA (2008) Noncanonical DNA Motifs as Transactivation Targets by Wild Type and Mutant p53. *Plos Genetics* **4**: e1000104.

Jossang T, Feder J, Rosenqvist E (1988) PHOTON-CORRELATION SPECTROSCOPY OF HUMAN-IGG. *Journal of Protein Chemistry* **7**: 165-171.

Kaiser W, Rant U (2010) Conformations of End-Tethered DNA Molecules on Gold Surfaces: Influences of Applied Electric Potential, Electrolyte Screening, and Temperature. *Journal of the American Chemical Society* **132:** 7935-7945.

Kannan KK, Petef M, Waara I, Strandbe.B, Adler L, Bergsten PC, Nyman PO, Gothe PO, Falkbrin.So, Fridborg K, Liljas A, Lovgren S (1972) STRUCTURE OF HUMAN CARBONIC-ANHYDRASE B .1. CRYSTALLIZATION AND HEAVY ATOM MODIFICATIONS. *Journal of Molecular Biology* **63:** 601-604.

Kattah MG, Coller J, Cheung RK, Oshidary N, Utz PJ (2008) HIT: a versatile proteomicsplatform for multianalyte phenotyping of cytokines, intracellular proteins and surface molecules. *Nature Medicine* **14**: 1284-1289.

Kay BK, Williamson MP, Sudol P (2000) The importance of being proline: the interaction of proline-rich motifs in signaling proteins with their cognate domains. *Faseb Journal* **14**: 231-241.

Khalifah RG (1971) CARBON DIOXIDE HYDRATION ACTIVITY OF CARBONIC ANHYDRASE .1. STOP-FLOW KINETIC STUDIES ON NATIVE HUMAN ISOENZYME-B AND ISOENZYME-C. *Journal of Biological Chemistry* **246**: 172-176.

Khazanov N, Levy Y (2011) Sliding of p53 along DNA Can Be Modulated by Its Oligomeric State and by Cross-Talks between Its Constituent Domains. *Journal of Molecular Biology* **408**: 335-355.

Kierny MR, Cunningham TD, Kay BK (2012) Detection of biomarkers using recombinant antibodies coupled to nanostructured platforms. *Nano reviews* **3**.

Kitayner M, Rozenberg H, Kessler N, Rabinovich D, Shaulov L, Haran TE, Shakked Z (2006) Structural basis of DNA recognition by p53 tetrarners. *Molecular Cell* **22:** 741-753.

Knezevic J, Langer A, Hampel P, Kaiser W, Strasser R, Rant U (2012) Quantitation of affinity, avidity, and binding kinetics of protein analytes with a dynamically switchable biosurface. *Journal of the American Chemical Society* **134:** 15225-15228.

Kondo T, Murakami K, Ohtsuka Y, Tsuji M, Gasa S, Taniguchi N, Kawakami Y (1987) ESTIMATION AND CHARACTERIZATION OF GLYCOSYLATED CARBONIC ANHYDRASE-I IN ERYTHROCYTES FROM PATIENTS WITH DIABETES-MELLITUS. *Clinica Chimica Acta* **166**: 227-236.

Kozlov IA, Melnyk PC, Stromsborg KE, Chee MS, Barker DL, Zhao CF (2004) Efficient strategies for the conjugation of oligonucleotides to antibodies enabling highly sensitive protein detection. *Biopolymers* **73:** 621-630.

Kron MA, Cichanowicz S, Hendrick A, Liu A, Leykam J, Kuhn LA (2008) Using structural analysis to generate parasite-selective monoclonal antibodies. *Protein Science* **17**: 983-989.

Kruse J-P, Gu W (2008) SnapShot: p53 posttranslational modifications. *Cell* **133**: 930.

Kunji ERS, Harding M, Butler PJG, Akamine P (2008) Determination of the molecular mass and dimensions of membrane proteins by size exclusion chromatography. *Methods* **46**: 62-72.

Kussie PH, Gorina S, Marechal V, Elenbaas B, Moreau J, Levine AJ, Pavletich NP (1996) Structure of the MDM2 oncoprotein bound to the p53 tumor suppressor transactivation domain. *Science* **274**: 948-953.

Kuzuya A, Kimura M, Numajiri K, Koshi N, Ohnishi T, Okada F, Komiyama M (2009) Precisely Programmed and Robust 2D Streptavidin Nanoarrays by Using Periodical Nanometer-Scale Wells Embedded in DNA Origami Assembly. *Chembiochem* **10**: 1811-1815.

LaBaer J, Garrett MD, Stevenson LF, Slingerland JM, Sandhu C, Chou HS, Fattaey A, Harlow E (1997) New functional activities for the p21 family of CDK inhibitors. *Genes & Development* **11**: 847-862.

Lane DP (1992) CANCER - P53, GUARDIAN OF THE GENOME. *Nature* **358:** 15-16.

Lane DP, Crawford LV (1979) T-ANTIGEN IS BOUND TO A HOST PROTEIN IN SV40-TRANSFORMED CELLS. *Nature* **278**: 261-263.

Langer A (2010) SwitchDNA Surface Biosensors for the Detection and Sizing of His-Tagged Proteins. *Master's thesis, Walter Schottky Institute, TU München.*

Langer A, Hampel P, Kaiser K, Knezevic J, Welte T, Villa V, Maruyama M, Fischer F, Strasser R, Rant U (Manusript in preparation B) Protein sizing and conformation analysis with an electro-switchable DNA chip.

Langer A, Kaiser W, Rant U (Manusript in preparation A) Protein Analysis on a Chip: Molecular Dynamics of DNA-Protein Conjugates on Electrified Surfaces.

Lavin MF, Gueven N (2006) The complexity of p53 stabilization and activation. *Cell Death and Differentiation* **13**: 941-950.

Le Maire M, Arnou B, Olesen C, Georgin D, Ebel C, Moller JV (2008) Gel chromatography and analytical ultracentrifugation to determine the extent of detergent binding and aggregation, and Stokes radius of membrane proteins using sarcoplasmic reticulum Ca2+-ATPase as an example. *Nature Protocols* **3**: 1782-1795.

Lee H, Mok KH, Muhandiram R, Park KH, Suk JE, Kim DH, Chang J, Sung YC, Choi KY, Han KH (2000) Local structural elements in the mostly unstructured transcriptional activation domain of human p53. *Journal of Biological Chemistry* **275**: 29426-29432.

Lehtonen J, Shen BR, Vihinen M, Casini A, Scozzafava A, Supuran CT, Parkkila AK, Saarnio J, Kivela AJ, Waheed A, Sly WS, Parkkila S (2004) Characterization of CA XIII, a novel member of the carbonic anhydrase isozyme family. *Journal of Biological Chemistry* **279**: 2719-2727.

Li J, Schantz A, Schwegler M, Shankar G (2011) Detection of low-affinity anti-drug antibodies and improved drug tolerance in immunogenicity testing by Octet (R) biolayer interferometry. *Journal of Pharmaceutical and Biomedical Analysis* **54**: 286-294.

Liang SH, Clarke MF (1999) A bipartite nuclear localization signal is required for p53 nuclear import regulated by a carboxyl-terminal domain. *Journal of Biological Chemistry* **274**: 32699-32703.

Liedberg B, Nylander C, Lundstrom I (1983) SURFACE-PLASMON RESONANCE FOR GAS-DETECTION AND BIOSENSING. *Sensors and Actuators* **4:** 299-304.

Lin Y, Chen G, Ling M, Liang Z (2010) A method of purification, identification and characterization of beta-glucosidase from Trichoderma koningii AS3.2774. *Journal of Microbiological Methods* **83:** 74-81.

Lopez M, Salmon AJ, Supuran CT, Poulsen S-A (2010) Carbonic Anhydrase Inhibitors Developed Through 'Click Tailing'. *Current Pharmaceutical Design* **16**: 3277-3287.

Lu H, Levine AJ (1995) HUMAN TAF(II)31 PROTEIN IS A TRANSCRIPTIONAL COACTIVATOR OF THE P53 PROTEIN. *Proceedings of the National Academy of Sciences of the United States of America* **92**: 13852-13857.

Lu X-J, Olson WK (2008) 3DNA: a versatile, integrated software system for the analysis, rebuilding and visualization of three-dimensional nucleic-acid structures. *Nature Protocols* **3:** 1213-1227.

Lubin DJ, Butler JS, Loh SN (2010) Folding of Tetrameric p53: Oligomerization and Tumorigenic Mutations Induce Misfolding and Loss of Function. *Journal of Molecular Biology* **395**: 705-716.

Luo JY, Li MY, Tang Y, Laszkowska M, Roeder RG, Gu W (2004) Acetylation of p53 augments its site-specific DNA binding both in vitro and in vivo. *Proceedings of the National Academy of Sciences of the United States of America* **101**: 2259-2264.

Ma B-J, Alam M, Go EP, Lu X, Desaire H, Tomaras GD, Bowman C, Sutherland LL, Scearce RM, Santra S, Letvin NL, Kepler TB, Liao H-X, Haynes BF (2011) Envelope Deglycosylation Enhances Antigenicity of HIV-1 gp41 Epitopes for Both Broad Neutralizing Antibodies and Their Unmutated Ancestor Antibodies. *Plos Pathogens* **7**: e1002200.

Maillart E, Brengel-Pesce K, Capela D, Roget A, Livache T, Canva M, Levy Y, Soussi T (2004) Versatile analysis of multiple macromolecular interactions by SPR imaging: application to p53 and DNA interaction. *Oncogene* **23**: 5543-5550.

Malou N, Raoult D (2011) Immuno-PCR: a promising ultrasensitive diagnostic method to detect antigens and antibodies. *Trends in Microbiology* **19**: 295-302.

Marchenko ND, Zaika A, Moll UM (2000) Death signal-induced localization of p53 protein to mitochondria - A potential role in apoptotic signaling. *Journal of Biological Chemistry* **275:** 16202-16212.

Maren TH, Parcell AL, Malik MN (1960) A KINETIC ANALYSIS OF CARBONIC ANHYDRASE INHIBITION. *Journal of Pharmacology and Experimental Therapeutics* **130**: 389-400.

Marissen WE, Kramer RA, Rice A, Weldon WC, Niezgoda M, Faber M, Slootstra JW, Meloen RH, Clijsters-van der Horst M, Visser TJ, Jongeneelen M, Thijsse S, Throsby M, de Kruif J, Rupprecht CE, Dietzschold B, Goudsmit J, Bakker ABH (2005) Novel rabies virus-neutralizing epitope recognized by human monoclonal antibody: Fine mapping and escape mutant analysis. *Journal of Virology* **79**: 4672-4678.

Markham NR, Zuker M (2005) DINAMelt web server for nucleic acid melting prediction. *Nucleic Acids Research* **33**: W577-581.

Maruyama M (2008) Study of DNA Hybridization and Protein Binding Kinetics on Switchable DNA Surfaces. *Master's Thesis, Walter Schottky Institute, TU München*.

McClarin JA, Frederick CA, Wang BC, Greene P, Boyer HW, Grable J, Rosenberg JM (1986) STRUCTURE OF THE DNA-ECO RI ENDONUCLEASE RECOGNITION COMPLEX AT 3 A RESOLUTION. *Science* **234**: 1526-1541.

McKay DB, Weber IT, Steitz TA (1982) STRUCTURE OF CATABOLITE GENE ACTIVATOR PROTEIN AT 2.9-A RESOLUTION - INCORPORATION OF AMINO-ACID-SEQUENCE AND INTERACTIONS WITH CYCLIC-AMP. *Journal of Biological Chemistry* **257**: 9518-9524.

McKinney K, Mattia M, Gottifredi V, Prives C (2004) p53 linear diffusion along DNA requires its C terminus. *Molecular Cell* **16**: 413-424.

Meldrum NI, Roughton FJW (1933) Carbonic anhydrase. Its preparation and properties. *Jour Physiol* **80**: 113-142.

Melero R, Rajagopalan S, Lazaro M, Joerger AC, Brandt T, Veprintsev DB, Lasso G, Gil D, Scheres SHW, Maria Carazo J, Fersht AR, Valle M (2011) Electron microscopy studies on the quaternary structure of p53 reveal different binding modes for p53 tetramers in complex with DNA. *Proceedings of the National Academy of Sciences of the United States of America* **108:** 557-562.

Menendez D, Inga A, Resnick MA (2009) The expanding universe of p53 targets. *Nature Reviews Cancer* **9**: 724-737.

Menendez D, Inga A, Snipe J, Krysiak O, Schoenfelder G, Resnick MA (2007) A single-nucleotide polymorphism in a half-binding site creates p53 and estrogen receptor control of vascular endothelial growth factor receptor 1. *Molecular and Cellular Biology* **27**: 2590-2600.

Meulmeester E, Jochemsen AG (2008) p53: A guide to apoptosis. *Current Cancer Drug Targets* **8**: 87-97.

Molchadsky A, Rivlin N, Brosh R, Rotter V, Sarig R (2010) p53 is balancing development, differentiation and de-differentiation to assure cancer prevention. *Carcinogenesis* **31**: 1501-1508.

Mollenbeck M, Postberg J, Paeschke K, Rossbach M, Jonsson F, Lipps HJ (2003) The telomerase-associated protein p43 is involved in anchoring telomerase in the nucleus. *Journal of Cell Science* **116:** 1757-1761.

Momand J, Zambetti GP, Olson DC, George D, Levine AJ (1992) THE MDM-2 ONCOGENE PRODUCT FORMS A COMPLEX WITH THE P53 PROTEIN AND INHIBITS P53-MEDIATED TRANSACTIVATION. *Cell* **69**: 1237-1245.

Nagaich AK, Appella E, Harrington RE (1997) DNA bending is essential for the site-specific recognition of DNA response elements by the DNA binding domain of the tumor suppressor protein p53. *Journal of Biological Chemistry* **272**: 14842-14849.

Nagaich AK, Zhurkin VB, Durell SR, Jernigan RL, Appella E, Harrington RE (1999) p53-induced DNA bending and twisting: p53 tetramer binds on the outer side of a DNA loop and increases DNA twisting. *Proceedings of the National Academy of Sciences of the United States of America* **96:** 1875-1880.

Nayak SK, Panesar PS, Kumar H (2009) p53-Induced Apoptosis and Inhibitors of p53. *Current Medicinal Chemistry* **16**: 2627-2640.

Nicholls CD, McLure KG, Shields MA, Lee PWK (2002) Biogenesis of p53 involves cotranslational dimerization of monomers and posttranslational dimerization of dimers - Implications on the dominant negative effect. *Journal of Biological Chemistry* **277:** 12937-12945.

Nie Y, Li HH, Bula CM, Liu XA (2000) Stimulation of p53 DNA binding by c-Abl requires the p53 c terminus and tetramerization. *Molecular and Cellular Biology* **20**: 741-748.

Niemeyer CM, Wacker R, Adler M (2003) Combination of DNA-directed immobilization and immuno-PCR: very sensitive antigen detection by means of self-assembled DNA-protein conjugates. *Nucleic Acids Research* **31**: e90.

Nikolova PV, Henckel J, Lane DP, Fersht AR (1998) Semirational design of active tumor suppressor p53 DNA binding domain with enhanced stability. *Proceedings of the National Academy of Sciences of the United States of America* **95:** 14675-14680.

North S, Hainaut P (2000) p53 and cell-cycle control: a finger in every pie. *Pathologie Biologie* **48**: 255-270.

Noureddine MA, Menendez D, Campbell MR, Bandele OJ, Horvath MM, Wang X, Pittman GS, Chorley BN, Resnick MA, Bell DA (2009) Probing the Functional Impact of Sequence Variation on p53-DNA Interactions Using a Novel Microsphere Assay for Protein-DNA Binding with Human Cell Extracts. *Plos Genetics* **5**: e1000462.

Nuzzo RG, Dubois LH, Allara DL (1990) FUNDAMENTAL-STUDIES OF MICROSCOPIC WETTING ON ORGANIC-SURFACES .1. FORMATION AND STRUCTURAL CHARACTERIZATION OF A SELF-CONSISTENT SERIES OF POLYFUNCTIONAL ORGANIC MONOLAYERS. *Journal of the American Chemical Society* **112:** 558-569.

Okorokov AL (2003) p53 in a crosstalk between DNA repair and cell cycle checkpoints. *Cell cycle (Georgetown, Tex)* **2**: 233-235.

Pan Y, Nussinov R (2007) Structural basis for p53 binding-induced DNA bending. *Journal of Biological Chemistry* **282**: 691-699.

Pascault JR, Zhou HS (2008) Enhancement of DNA hybridization kinetics in microarrays by convective transport. *Chemical Engineering Communications* **195:** 167-186.

Petitjean A, Mathe E, Kato S, Ishioka C, Tavtigian SV, Hainaut P, Olivier M (2007) Impact of mutant p53 functional properties on TP53 mutation patterns and tumor phenotype: Lessons from recent developments in the IARC TP53 database. *Human Mutation* **28:** 622-629.

Picksley SM, Lane DP (1993) THE P53-MDM2 AUTOREGULATORY FEEDBACK LOOP - A PARADIGM FOR THE REGULATION OF GROWTH-CONTROL BY P53. *Bioessays* **15**: 689-690.

Rafferty JB, Somers WS, Stgirons I, Phillips SEV (1989) 3-DIMENSIONAL CRYSTAL-STRUCTURES OF ESCHERICHIA-COLI MET REPRESSOR WITH AND WITHOUT COREPRESSOR. *Nature* **341**: 705-710.

Rajagopalan S, Huang F, Fersht AR (2011) Single-Molecule characterization of oligomerization kinetics and equilibria of the tumor suppressor p53. *Nucleic Acids Research* **39:** 2294-2303.

Rajagopalan S, Jaulent AM, Wells M, Veprintsev DB, Fersht AR (2008) 14-3-3 activation of DNA binding of p53 by enhancing its association into tetramers. *Nucleic Acids Research* **36:** 5983-5991.

Ramakrishnan M, Kandimalla KK, Wengenack TM, Howell KG, Poduslo JF (2009) Surface Plasmon Resonance Binding Kinetics of Alzheimer's Disease Amyloid beta Peptide-Capturing and Plaque-Binding Monoclonal Antibodies. *Biochemistry* **48**: 10405-10415.

Rant U (2005) Electrical Manipulation of DNA-layers on Gold Surfaces. *PhD's Thesis, Walter Schottky Institute, TU München.*

Rant U, Arinaga K, Fujita S, Yokoyama N, Abstreiter G, Tornow M (2006a) Electrical manipulation of oligonucleotides grafted to charged surfaces. *Organic & Biomolecular Chemistry* **4:** 3448-3455.

Rant U, Arinaga K, Scherer S, Pringsheim E, Fujita S, Yokoyama N, Tornow M, Abstreiter G (2007) Switchable DNA interfaces for the highly sensitive detection of label-free DNA targets. *Proceedings of the National Academy of Sciences of the United States of America* **104:** 17364-17369.

Rant U, Arinaga K, Tornow M, Kim YW, Netz RR, Fujita S, Yokoyama N, Abstreiter G (2006b) Dissimilar kinetic behavior of electrically manipulated single- and double-stranded DNA tethered to a gold surface. *Biophysical Journal* **90:** 3666-3671.

Rant U, Pringsheim E, Kaiser W, Arinaga K, Knezevic J, Tornow M, Fujita S, Yokoyama N, Abstreiter G (2009) Detection and Size Analysis of Proteins with Switchable DNA Layers. *Nano Letters* **9**: 1290-1295.

Reddy SB, Anders RF, Beeson JG, Farnert A, Kironde F, Berenzon SK, Wahlgren M, Linse S, Persson KEM (2012) High Affinity Antibodies to Plasmodium falciparum Merozoite Antigens Are Associated with Protection from Malaria. *Plos One* **7**: e32242.

Resnick-Silverman L, St Clair S, Maurer M, Zhao K, Manfredi JJ (1998) Identification of a novel class of genomic DNA-binding sites suggests a mechanism for selectivity in target gene activation by the tumor suppressor protein p53. *Genes & Development* **12**: 2102-2107.

Riley T, Sontag E, Chen P, Levine A (2008) Transcriptional control of human p53-regulated genes. *Nature Reviews Molecular Cell Biology* **9**: 402-412.

Roth J, Dobbelstein M, Freedman DA, Shenk T, Levine AJ (1998) Nucleo-cytoplasmic shuttling of the hdm2 oncoprotein regulates the levels of the p53 protein via a pathway used by the human immunodeficiency virus rev protein. *Embo Journal* **17**: 554-564.

Said HM, Supuran CT, Hageman C, Staab A, Polat B, Katzer A, Scozzafava A, Anacker J, Flentje M, Vordermark D (2010) Modulation of Carbonic Anhydrase 9 (CA9) in Human Brain Cancer. *Current Pharmaceutical Design* **16**: 3288-3299.

Sakaguchi K, Sakamoto H, Lewis MS, Anderson CW, Erickson JW, Appella E, Xie D (1997) Phosphorylation of serine 392 stabilizes the tetramer formation of tumor suppressor protein p53. *Biochemistry* **36**: 10117-10124.

Sakkhachornphop S, Jiranusornkul S, Kodchakorn K, Nangola S, Sirisanthana T, Tayapiwatana C (2009) Designed zinc finger protein interacting with the HIV-1 integrase recognition sequence at 2-LTR-circle junctions. *Protein Science* **18**: 2219-2230.

Schaumann C, Oesch F, Unger KK, Wieser RJ (1993) ANALYTICAL TECHNIQUE FOR STUDYING THE STRUCTURE OF GLYCOPROTEIN N-GLYCANS. *Journal of Chromatography* **646**: 227-234.

Schevitz RW, Otwinowski Z, Joachimiak A, Lawson CL, Sigler PB (1985) THE 3-DIMENSIONAL STRUCTURE OF TRP REPRESSOR. *Nature* **317**: 782-786.

Schliebe N, Strotmann R, Busse K, Mitschke D, Biebermann H, Schomburg L, Koehrle J, Baer J, Roempler H, Wess J, Schoeneberg T, Sangkuhl K (2008) V2 vasopressin receptor deficiency causes changes in expression and function of renal and hypothalamic components involved in electrolyte and water homeostasis. *American Journal of Physiology-Renal Physiology* **295**: 1177-1190.

Schon O, Friedler A, Bycroft M, Freund SMV, Fersht AR (2002) Molecular mechanism of the interaction between MDM2 and p53. *Journal of Molecular Biology* **323**: 491-501.

Selvaraju S, El Rassi Z (2012) Tandem lectin affinity chromatography monolithic columns with surface immobilised concanavalin A, wheat germ agglutinin and Ricinus communis agglutinin-I for capturing sub-glycoproteomics from breast cancer and disease-free human sera. *Journal of Separation Science* **35**: 1785-1795.

Sengupta S, Harris CC (2005) p53: Traffic cop at the crossroads of DNA repair and recombination. *Nature Reviews Molecular Cell Biology* **6**: 44-55.

Shaulsky G, Goldfinger N, Benzeev A, Rotter V (1990) NUCLEAR ACCUMULATION OF P53 PROTEIN IS MEDIATED BY SEVERAL NUCLEAR-LOCALIZATION SIGNALS AND PLAYS A ROLE IN TUMORIGENESIS. *Molecular and Cellular Biology* **10**: 6565-6577.

Smith SB, Cui YJ, Bustamante C (1996) Overstretching B-DNA: The elastic response of individual double-stranded and single-stranded DNA molecules. *Science* **271:** 795-799.

Smith SB, Finzi L, Bustamante C (1992) DIRECT MECHANICAL MEASUREMENTS OF THE ELASTICITY OF SINGLE DNA-MOLECULES BY USING MAGNETIC BEADS. *Science* **258:** 1122-1126.

Soddu S, Sacchi A (1997) P53 role in DNA repair and tumorigenesis. *Journal of Experimental & Clinical Cancer Research* **16**: 237-242.

Solulink (S-9002-1) *S-HyNic Bioconjugation Technical Manual. Solulink* Cat. # 9002-2.

Soussi T, Legros Y, Lubin R, Ory K, Schlichtholz B (1994) MULTIFACTORIAL ANALYSIS OF P53 ALTERATION IN HUMAN CANCER - A REVIEW. *International Journal of Cancer* **57:** 1-9.

Spuhler PS, Knezevic J, Yalcin A, Bao Q, Pringsheim E, Droege P, Rant U, Uenlue MS (2010) Platform for in situ real-time measurement of protein-induced conformational changes of DNA. *Proceedings of the National Academy of Sciences of the United States of America* **107**: 1397-1401.

Squires TM, Messinger RJ, Manalis SR (2008) Making it stick: convection, reaction and diffusion in surface-based biosensors. *Nature Biotechnology* **26**: 417-426.

Steel AB, Herne TM, Tarlov MJ (1998) Electrochemical quantitation of DNA immobilized on gold. *Analytical Chemistry* **70:** 4670-4677.

Steinber.Iz (1971) LONG-RANGE NONRADIATIVE TRANSFER OF ELECTRONIC EXCITATION ENERGY IN PROTEINS AND POLYPEPTIDES. *Annual Review of Biochemistry* **40**: 83-114.

Stommel JM, Marchenko ND, Jimenez GS, Moll UM, Hope TJ, Wahl GM (1999) A leucine-rich nuclear export signal in the p53 tetramerization domain: regulation of subcellular localization and p53 activity by NES masking. *Embo Journal* **18**: 1660-1672.

Tafvizi A, Huang F, Fersht AR, Mirny LA, van Oijen AM (2011) A single-molecule characterization of p53 search on DNA. *Proceedings of the National Academy of Sciences of the United States of America* **108**: 563-568.

Thut CJ, Chen JL, Klemm R, Tjian R (1995) P53 TRANSCRIPTIONAL ACTIVATION MEDIATED BY COACTIVATORS TAF(II)40 AND TAF(II)60. *Science* **267**: 100-104.

Tidow H, Melero R, Mylonas E, Freund SMV, Grossmann JG, Carazo JM, Svergun DI, Valle M, Fersht AR (2007) Quaternary structures of tumor suppressor p53 and a specific p53-DNA complex. *Proceedings of the National Academy of Sciences of the United States of America* **104**: 12324-12329.

Tirado MM, Martinez CL, Delatorre JG (1984) COMPARISON OF THEORIES FOR THE TRANSLATIONAL AND ROTATIONAL DIFFUSION-COEFFICIENTS OF ROD-LIKE MACROMOLECULES - APPLICATION TO SHORT DNA FRAGMENTS. *Journal of Chemical Physics* **81**: 2047-2052.

van Dieck J, Fernandez-Fernandez MR, Veprintsev DB, Fersht AR (2009) Modulation of the Oligomerization State of p53 by Differential Binding of Proteins of the S100 Family to p53 Monomers and Tetramers. *Journal of Biological Chemistry* **284**: 13804-13811.

Vitale RM, Pedone C, Amodeo P, Antel J, Wurl M, Scozzafava A, Supuran CT, De Simone G (2007) Molecular modeling study for the binding of zonisamide and topiramate to the human mitochondrial carbonic anhydrase isoform VA. *Bioorganic & Medicinal Chemistry* **15**: 4152-4158.

Vogelstein B, Lane D, Levine AJ (2000) Surfing the p53 network. *Nature* **408:** 307-310.

Walker KK, Levine AJ (1996) Identification of a novel p53 functional domain that is necessary for efficient growth suppression. *Proceedings of the National Academy of Sciences of the United States of America* **93**: 15335-15340.

Wang J, Rivas G, Jiang MA, Zhang XJ (1999) Electrochemically induced release of DNA from gold ultramicroelectrodes. *Langmuir* **15:** 6541-6545.

Wang Y, Rosengarth A, Luecke H (2007) Structure of the human p53 core domain in the absence of DNA. *Acta Crystallographica Section D-Biological Crystallography* **63**: 276-281.

Wang Y, Zhu X, Wu M, Xia N, Wang J, Zhou F (2009) Simultaneous and Label-Free Determination of Wild-Type and Mutant p53 at a Single Surface Plasmon Resonance Chip Preimmobilized with Consensus DNA and Monoclonal Antibody. *Analytical Chemistry* **81**: 8441-8446.

Watson JD, Crick FHC (1953) MOLECULAR STRUCTURE OF NUCLEIC ACIDS - A STRUCTURE FOR DEOXYRIBOSE NUCLEIC ACID. *Nature* **171:** 737-738.

Weinberg RL, Freund SMV, Veprintsev DB, Bycroft M, Fersht AR (2004a) Regulation of DNA binding of p53 by its C-terminal domain. *Journal of Molecular Biology* **342**: 801-811.

Weinberg RL, Veprintsev DB, Bycroft M, Fersht AR (2005) Comparative binding of p53 to its promoter and DNA recognition elements. *Journal of Molecular Biology* **348:** 589-596.

Weinberg RL, Veprintsev DB, Fersht AR (2004b) Cooperative binding of tetrameric p53 to DNA. *Journal of Molecular Biology* **341:** 1145-1159.

Wilbur KM, Anderson NG (1948) ELECTROMETRIC AND COLORIMETRIC DETERMINATION OF CARBONIC ANHYDRASE. *Journal of Biological Chemistry* **176**: 147-154.

Wright JD, Noskov SY, Lim C (2002) Factors governing loss and rescue of DNA binding upon single and double mutations in the p53 core domain. *Nucleic Acids Research* **30**: 1563-1574.

Wu XW, Bayle JH, Olson D, Levine AJ (1993) THE P53 MDM-2 AUTOREGULATORY FEEDBACK LOOP. *Genes & Development* **7**: 1126-1132.

Xia JZ, Aerts T, Donceel K, Clauwaert J (1994) LIGHT-SCATTERING BY BOVINE ALPHA-CRYSTALLIN PROTEINS IN SOLUTION - HYDRODYNAMIC STRUCTURE AND INTERPARTICLE INTERACTION. *Biophysical Journal* **66**: 861-872.

Xiaodi S, Nan Y, Vinalia T, Knoll W (2007) Evaluation of two- and three-dimensional streptavidin binding platforms for surface plasmon resonance spectroscopy studies of DNA hybridization and protein-DNA binding. *Biosensors & Bioelectronics* **22**: 2700-2706.

Yan H, Shen Z, Mernaugh R, Zeng X (2011) Single Chain Fragment Variable Recombinant Antibody as a Template for Fc Sensors. *Analytical Chemistry* **83**: 625-630.

Yang DF, Wilde CP, Morin M (1997) Studies of the electrochemical removal and efficient re-formation of a monolayer of hexadecanethiol self-assembled at an Au(111) single crystal in aqueous solutions. *Langmuir* **13**: 243-249.

Yang Y, Tan Y, Liu B, Sun Y, Chen D, Tan H (2003) Study of optical fiber biosensor based on white-light interferometry. *Journal of Xi'an Jiaotong University* **37.**

Zarzosa-Alvarez AL, Sandoval-Cabrera A, Torres-Huerta AL, Bermudez-Cruz RM (2010) Electroeluting DNA fragments. *Journal of visualized experiments : JoVE*: 2136.

Zhang HT, Cheng X, Richter M, Greene MI (2006) A sensitive and high-throughput assay to detect low-abundance proteins in serum. *Nature Medicine* **12**: 473-477.

Zhang YP, Xiong Y (2001) A p53 amino-terminal nuclear export signal inhibited by DNA damage-induced phosphorylation. *Science* **292**: 1910-1915.

Zhong CJ, Porter MD (1997) Fine structure in the voltammetric desorption curves of alkanethiolate monolayers chemisorbed at gold. *Journal of Electroanalytical Chemistry* **425**: 147-153.

Zhu H, Evans B, O'Neill P, Ren X, Xu Z, Hait WN, Yang J-M (2009) A role for p53 in the regulation of extracellular matrix metalloproteinase inducer in human cancer cells. *Cancer Biology & Therapy* **8**: 1722-1728.

11. Publications

Andreas Langer, Paul A. Hampel, Wolfgang Kaiser, Jelena Knezevic, Thomas Welte, Valentina Villa, Makiko Maruyama, Frank Fischer, Ralf Strasser & Ulrich Rant,
"Protein sizing and conformation analysis with an electro-switchable DNA chip".
Manuscript in preparation.

Makiko Maruyama, Valentina Villa, Paul A. Hampel, Andreas Langer, Julia Rohrberg, Johannes Buchner, Ulrich Rant,
"Full-length wild-type p53 characterization on an electro-switchable DNA surface".
Manuscript in preparation.

Valentina Villa, Paul A. Hampel, Andreas Langer, Ralf Strasser, Ulrich Rant,
"Antibody kinetics with an electro-switchable biosurface".
Manuscript in preparation.

12. Acknowledgements

First of all I would like to thank Prof. Dr. Johannes Buchner, for his support and the opportunity to carry out my PhD in his department. Likewise I want to acknowledge Dr. Ulrich Rant, for giving me the chance to join his group and to work on this inspiring topic, while providing valuable advice when needed.

Furthermore, I owe special thanks to the whole Dynamic Biosensors' team: Simone (Twiggy), Frank (Dj Otzi), Ralf (der Mann), Valentin (Barman Papa) and Dirk (der große Mann). And thanks to Jens Niemax.

I am glad for the great time spent in the lab together with the entire BIEROGROUP and for all helpful discussions and advices I have received from them. Particularly, a big Domo Arigato to Maki-chan (Makicina) also for the delicious shared studies carried out in her kitchen; eine größe Danke zu Paul (Paolino), der lachende Singer, und zu Wolfi (Wolfango), immer lustig und spontan, zu Andi (Billy Elliots Fahrradshuhe), zu Jelena (the high heel girl), zu Thomas (der Junge mit dem roten Panda), zu Markus (der Kaffeebohne Mann), zu Alex (der Klettern Mann), zu Matthias (der entspannte Mann).

Additionally, I am also grateful to Dr. Martin Haslbeck, for his support and to Dr. Julia Rohrberg, for her supervision with p53 expression and for her sincere friendship.

Besides, thanks to my best fellows here in München, or better to say my best friend Mädchen: Nerea (the sweetest writer), Clara (the quiche Lorraine's master), Vera (the grown up woman) and Serena (the craziest).

Infine, grazie a mamma e a babbo, per l'amore e il SURSUM CORDA ripetuto mille volte, e grazie ai miei fratelloni Ciccio Luca e Ste, perché nella loro incomprensione c'é tutta la loro comprensione.

13. Declaration

I, Valentina Villa, hereby declare that I independently prepared the present thesis, using only the references and resources stated. This work has not been submitted to any examination board yet. Parts of this work have been or will be published in scientific journals.

Hiermit erkläre ich, Valentina Villa, dass ich die vorliegende Arbeit selbständig verfasst und keine anderen als die angegebenen Quellen und Hilfsmittel verwendet habe. Die Arbeit wurde noch keiner Prüfungskommission vorgelegt. Teile dieser Arbeit wurden bzw. werden in wissenschaftlichen Journalen veröffentlicht.

Valentina Villa

München, 11.10.2012

14. Appendix

14.1 C-48-mer folding

Thermodynamic properties of c-48-mer single stranded DNA calculated using DINAmelt Web Server, setting the conjugation reaction parameters, such as temperature 25°C, [NaCl] 150 mM and [ss-48-mer] 16 µM. The "Two-state Folding" model depicted one stable secondary structure (Figure A), and the "Two-state melting" model displayed a homodimeric folding (Figure B).

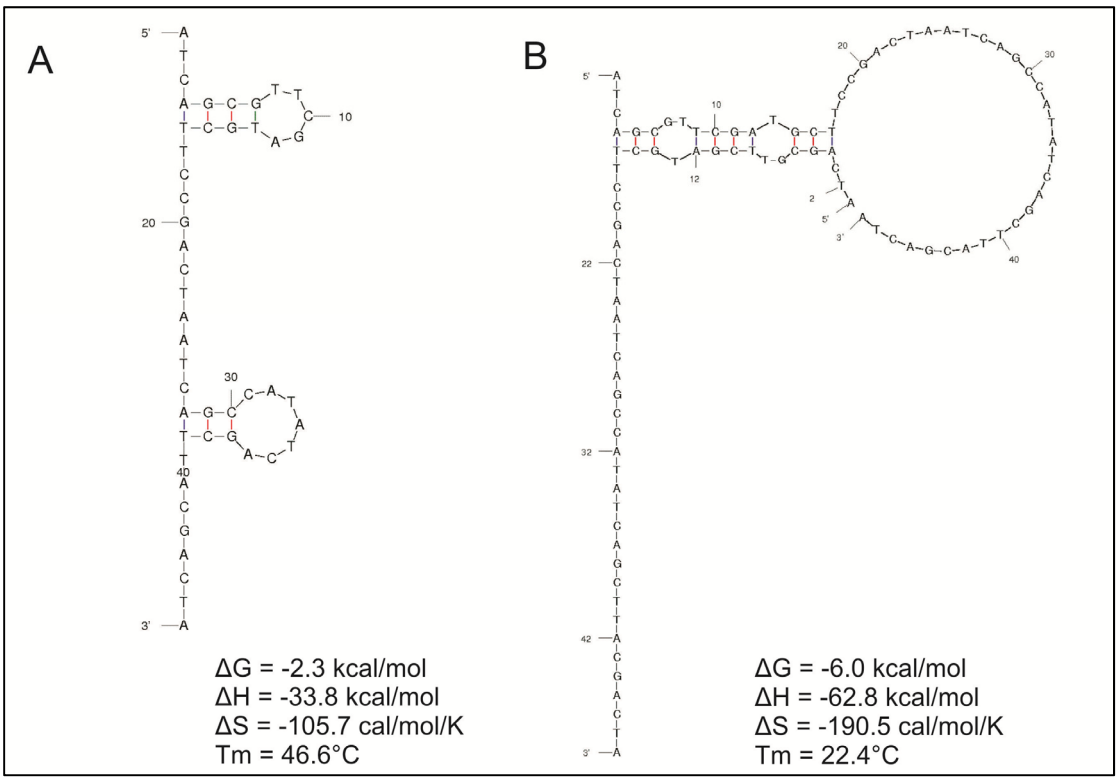

14.2 Hybridization kinetics

For all measurements, the switching amplitude ΔF (grey open square) was normalized, setting 0 % surface coverage at t = 0 min and 100 % at saturated level. The data were fitted by Exponential Decay 1 in Origin 8.5 (red line) to estimate the time constant $\boldsymbol{\tau}$.

hCA1-DNA mono conjugate hybridization kinetics:

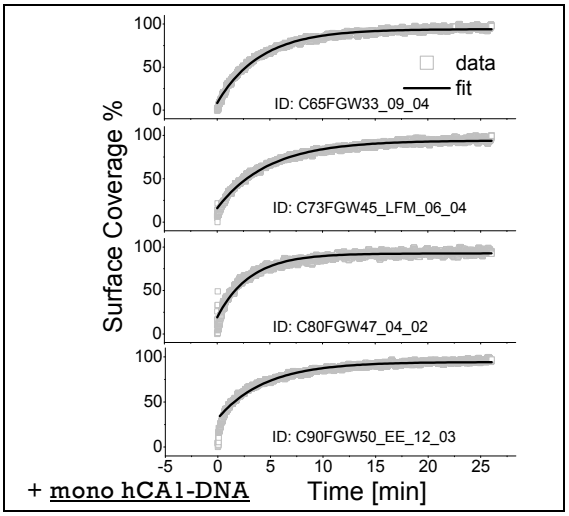

hCA1-DNA multi conjugate hybridization kinetics:

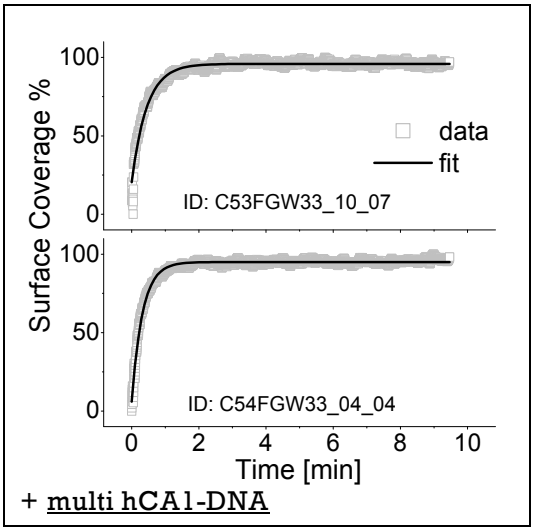

c-ss-48-mer hybridization kinetics:

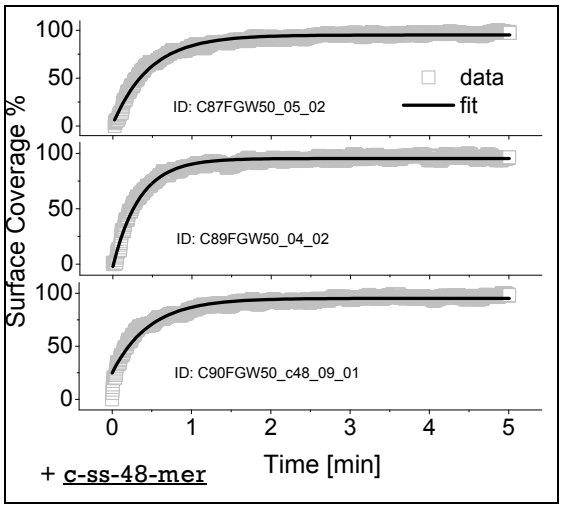

14.3 Antibody kinetic analysis in Biacore

The sensorgrams were evaluated using Biacore X100 Evaluation Version 2.01 software, both single- and multi-cycle runs with the same tool and fitting models. The rate constants for association (k_a) and dissociation (k_d) and affinity constant (K_D, $K_D=k_d/k_a$) were fitted by Langmuir binding model (1:1 binding model). In Chapter 7, for the comparison between *switch*SENSE and Biacore data, k_a and k_d were defined as k_{on} and k_{off}, respectively. The curves were first corrected subtracting the buffer signal, and the fit was usually done setting kinetic constants as global parameter, as well as for the analyte binding capacity of the surface, R_{max}, while refractive index contribution RI was set constant.

For hCA1 immobilized on CM5, the best regeneration condition was still a bit harsh, decreasing cycle by cycle the immobilized ligand level, that is why the curves were separated into 1st and 2nd serial dilutions, fitting each one with R_{max} as local parameter and finally the average values for k_a and k_d were calculated.

Table 14.1 Calculations for the mass-trasfer regime in Biacore™ X-100 for hCA1 and IgG, employed as ligands.

	hCA1	**mAb**	**Biacore Equations**
MW [kDa]	29	150	
$\boldsymbol{D}$ [m^2s^{-1}]♦	$7.69*10^{-11}$	$4.45*10^{-11}$	
$\boldsymbol{k_m}$ [m s^{-1}]	$3.14*10^5$	$2.18*10^{-5}$	$k_m = 0.98 \cdot (D/h)^{2/3} \cdot \left(\frac{f}{0.3 \cdot w \cdot l}\right)^{1/3}$
$\boldsymbol{k_t}$ [RU·$M^{-1}s^{-1}$]	$9.10*10^8$	$3.27*10^9$	$k_t = k_m \cdot MW \cdot 10^9$
$\boldsymbol{tc}$ [RU·$M^{-1}m^{-1}s^{-2/3}$]	$\mathbf{5.32*10^{11}}$	$\mathbf{1.91*10^{12}}$	$tc = kt/\left(f^{1/3}\right)$
Biacore's parameters			
$\boldsymbol{f}$ [m^3s^{-1}]	$5.00*10^{-9}$		
$\boldsymbol{h}$ [m]	$5.00*10^{-5}$		
$\boldsymbol{w \cdot l}$ [m^2]	$1.20*10^{-6}$		

♦values calculated in Biacore's website, considering the globular shape, water viscosity 1 centipoise at 20 °C, converted to T 25°C.
http://www.biacore.com/lifesciences/Application_Support/online_support/Diffusion_Coefficient_Calculator/index.html

Table 14.1 presents the calculation of mass-transfer regime for hCA1 and IgG, employed as ligands. In the Biacore flow cell, the rate of mass transfer of analyte (hCA1 or mAb) to the surface is characterized by the mass transfer coefficient $\boldsymbol{k_m}$, correlated, as indicated in the equation, to diffusion coefficient $\boldsymbol{D}$ of the analyte, the volume flow rate $\boldsymbol{f}$, the flow

cell dimensions height, width, length *h*, *w*, *l* respectively. The kinetic fit gives back the mass transfer constant $\boldsymbol{k_t}$, calculated adjusting $\boldsymbol{k_m}$ by the analyte molecular weight MW and by the conversion of surface concentration to RU. Furthermore the flow rate-independent component of the mass transfer constant *tc* is given.

Here follow the obtained report tables for each measurement evaluation. The tables contain:

- the rate constants with respective standard error (SE) terms;
- $\boldsymbol{tc}$ (RU·M^{-1}m^{-1}s$^{-2/3}$), $\boldsymbol{kt}$ (RU·M^{-1}s^{-1});
- U-value, which indicates the uniqueness of the calculated values for rate constants and Rmax, it is determined by testing the dependence of the fit on correlated variations in pairs of parameters (U-values below 15 indicate that absolute values for two or more of the parameters aren't significantly correlated and can be determined);
- Chi-square, lower values indicate higher overall quality of the fit between fitted and experimental values.

Table 14.2 _ 1st serial dilution of Ab3 on hCA1/CM5 chip (local R_{max}).

Curve 1st serial dilution	ka (1/Ms)	kd (1/s)	KD (M)	Rmax (RU)	Conc (M)	Tc	Flow (ul/min)	Chi² (RU²)	U-value
	9.86E+04	1.63E-04	1.66E-09			6.38E+14		1.11	4
Cycle: 2 1 nM	SE(ka)	SE(kd)		202.3	1.00E-09	kt (RU/Ms)	30		
Cycle: 3 5 nM	8.40E+02	2.90E-06		159.8	5.00E-09	1.98E+15	30		
Cycle: 4 25 nM				146.6	2.50E-08		30		
Cycle: 5 125 nM				70.39	1.25E-07		30		

Table 14.3 _ 2nd serial dilution of Ab3 on hCA1/CM5 chip (local R_{max}).

Curve 2nd serial dilution	ka (1/Ms)	kd (1/s)	KD (M)	Rmax (RU)	Conc (M)	Tc	Flow (ul/min)	Chi² (RU²)	U-value
	9.69E+04	2.55E-04	2.63E-09			5.95E+14		0.6	2
Cycle: 2 1 nM	SE(ka)	SE(kd)		129.9	1.00E-09	kt (RU/Ms)	30		
Cycle: 3 5 nM	7.60E+02	2.70E-06		126.1	5.00E-09	1.85E+15	30		
Cycle: 4 25 nM				124.2	2.50E-08		30		
Cycle: 5 125 nM				57.75	1.25E-07		30		

Table 14.4 _ hCA1 on Ab1/CM5 chip.

Curve	ka (1/Ms)	kd (1/s)	KD (M)	Rmax (RU)	Conc (M)	tc	Flow (ul/min)	Chi² (RU²)	U-value
	6.21E+04	0.004321	6.96E-08	104.4		2.46E+08		3.19	1
Cycle: 2 6,2 nM	SE(ka)	SE(kd)			6.20E-09	kt (RU/Ms)	30		
Cycle: 3 18,6 nM	3.90E+02	2.90E-05			1.86E-08	7.63E+08	30		
Cycle: 4 56 nM					5.60E-08		30		
Cycle: 5 167 nM					1.67E-07		30		
Cycle: 6 500 nM					5.00E-07		30		

Table 14.5 _ hCA1 on Ab3/CM5 chip.

Curve	ka (1/Ms)	kd (1/s)	KD (M)	Rmax (RU)	Conc (M)	tc	Flow (ul/min)	Chi² (RU²)	U-value
	4.58E+04	0.002122	4.63E-08	87.25		5.69E+18		3.14	1
Cycle: 2 6,2 nM	SE(ka)	SE(kd)			6.20E-09	kt (RU/Ms)	30		
Cycle: 3 18,6 nM	1.30E+02	4.40E-06			1.86E-08	1.77E+19	30		
Cycle: 4 56 nM					5.60E-08		30		
Cycle: 5 167 nM					1.67E-07		30		
Cycle: 6 500 nM					5.00E-07		30		

Table 14.6 _ hCA1 on Ab4/CM5 chip.

Curve	ka (1/Ms)	kd (1/s)	KD (M)	Rmax (RU)	Conc (M)	tc	Flow (ul/min)	Chi² (RU²)	U-value
	6.85E+04	0.004217	6.16E-08	147.8		3.62E+15		10.1	1
Cycle: 2 6,2 nM	SE(ka)	SE(kd)			6.20E-09	kt (RU/Ms)	30		
Cycle: 3 18,6 nM	2.90E+02	9.80E-06			1.86E-08	1.13E+16	30		
Cycle: 4 56 nM					5.60E-08		30		
Cycle: 5 167 nM					1.67E-07		30		
Cycle: 6 500 nM					5.00E-07		30		

Table 14.7 _ hCA1 on Ab5/CM5 chip.

Curve	ka (1/Ms)	kd (1/s)	KD (M)	Rmax (RU)	Conc (M)	tc	Flow (ul/min)	Chi² (RU²)	U-value
	6.38E+04	0.004331	6.78E-08	114.4		6.48E+08		5.79	2
Cycle: 2 6,2 nM	SE(ka)	SE(kd)			6.20E-09	kt (RU/Ms)	30		
Cycle: 3 18,6 nM	5.10E+02	3.00E-05			1.86E-08	2.02E+09	30		
Cycle: 4 56 nM					5.60E-08		30		
Cycle: 5 167 nM					1.67E-07		30		
Cycle: 6 500 nM					5.00E-07		30		

Table 14.8 _ Ab1 on hCA1/C1 chip.

Curve	ka (1/Ms)	kd (1/s)	KD (M)	Rmax (RU)	Conc (M)	Tc	Flow (ul/min)	Chi² (RU²)	U-value
	5.96E+05	0.002439	4.09E-09	26.83		4.44E+20		1.75	2
Single Cycle	SE(ka)	SE(kd)			7.81E-09	kt (RU/Ms)	30		
	5.50E+03	1.80E-05			1.56E-08	1.38E+21	30		
					3.13E-08		30		
					6.25E-08		30		
					1.25E-07		30		

Table 14.9 _ Ab3 on hCA1/C1 chip.

Curve	ka (1/Ms)	kd (1/s)	KD (M)	Rmax (RU)	Conc (M)	Tc	Flow (ul/min)	Chi² (RU²)	U-value
	2.78E+05	8.27E-04	2.97E-09	38.1		1.44E+21		1.95	2
Single Cycle	SE(ka)	SE(kd)			7.81E-09	kt (RU/Ms)	30		
	1.60E+03	8.90E-06			1.56E-08	4.49E+21	30		
					3.13E-08		30		
					6.25E-08		30		
					1.25E-07		30		

Table 14.10 _ Ab4 on hCA1/C1 chip.

Curve	ka (1/Ms)	kd (1/s)	KD (M)	Rmax (RU)	Conc (M)	Tc	Flow (ul/min)	Chi² (RU²)	U-value
	3.23E+05	0.00224	6.93E-09	23.34		4.34E+15		1.19	2
Single Cycle	SE(ka)	SE(kd)			7.81E-09	kt (RU/Ms)	30		
	2.90E+03	1.80E-05			1.56E-08	1.35E+16	30		
					3.13E-08		30		
					6.25E-08		30		
					1.25E-07		30		

Table 14.11 _ Ab5 on hCA1/C1 chip.

Curve	ka (1/Ms)	kd (1/s)	KD (M)	Rmax (RU)	Conc (M)	Tc	Flow (ul/min)	Chi² (RU²)	U-value
	3.02E+05	0.003044	1.01E-08	21.75		2.16E+06		0.769	3
Single Cycle	SE(ka)	SE(kd)			7.81E-09	kt (RU/Ms)	30		
	9.70E+03	7.60E-05			1.56E-08	6.71E+06	30		
					3.13E-08		30		
					6.25E-08		30		
					1.25E-07		30		

14.4 Antibody kinetic analysis in *switch*SENSE

The Dynamic Response curves of binding and unbinding were normalized dividing by the initial value (averaged value -10-0 s interval) before antibody injection, then they were smoothed using Adjacent Averaging setting 5 and 50 points of window, respectively for binding and unbinding curves. The fluorescence levels, F_{st} and F_{ly}, were normalized based on corresponding initial values, and they needed no smoothing. All resulting curves were fitted in Origin 8.5, with Exponential Decay 1 ($y = y_0 + A \cdot e^{-x/t}$) to get the time constant for association, τ_{on}, and dissociation, t_{off}, described by the Langmuir adsorption isotherm Eq. 6.11. The kinetic constants, k_{on} and k_{off}, and the equilibrium constant K_D were calculated using Eq. 6.5, Eq. 6.12, and Eq. 6.13.

FIT OF DYNRES FOR AB3

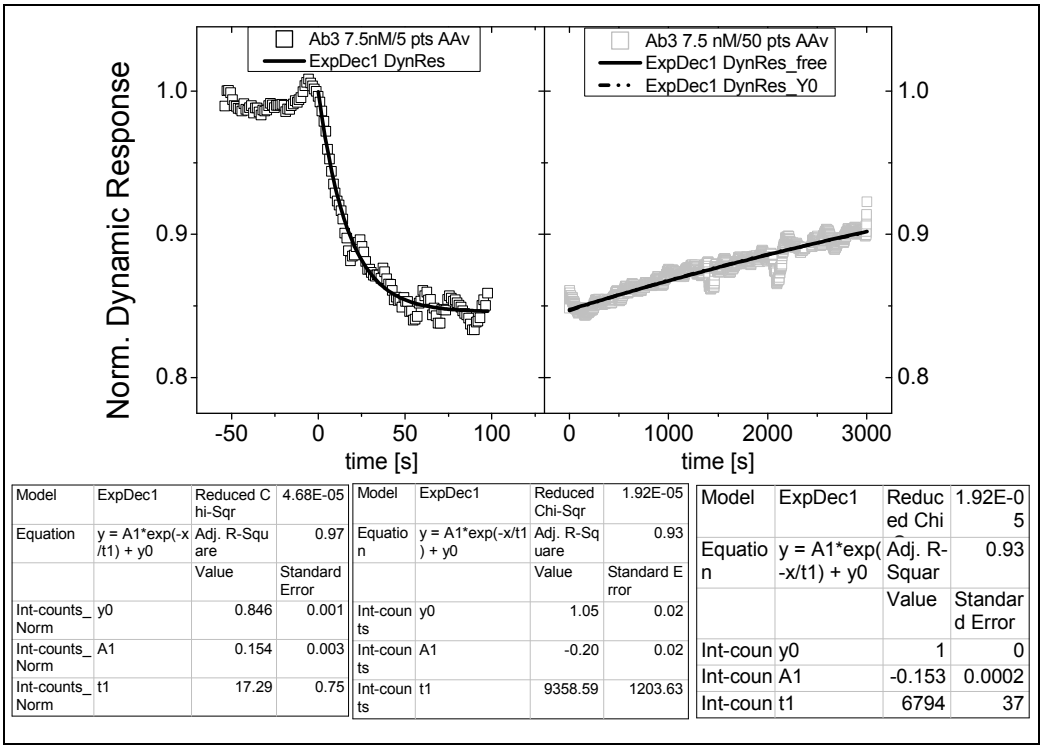

Model	ExpDec1	Reduced Chi-Sqr	4.68E-05
Equation	y = A1*exp(-x/t1) + y0	Adj. R-Square	0.97
		Value	Standard Error
Int-counts_Norm	y0	0.846	0.001
Int-counts_Norm	A1	0.154	0.003
Int-counts_Norm	t1	17.29	0.75

Model	ExpDec1	Reduced Chi-Sqr	1.92E-05
Equation	y = A1*exp(-x/t1) + y0	Adj. R-Square	0.93
		Value	Standard Error
Int-counts	y0	1.05	0.02
Int-counts	A1	-0.20	0.02
Int-counts	t1	9358.59	1203.63

Model	ExpDec1	Reduced Chi	1.92E-05
Equation	y = A1*exp(-x/t1) + y0	Adj. R-Square	0.93
		Value	Standard Error
Int-coun	y0	1	0
Int-coun	A1	-0.153	0.0002
Int-coun	t1	6794	37

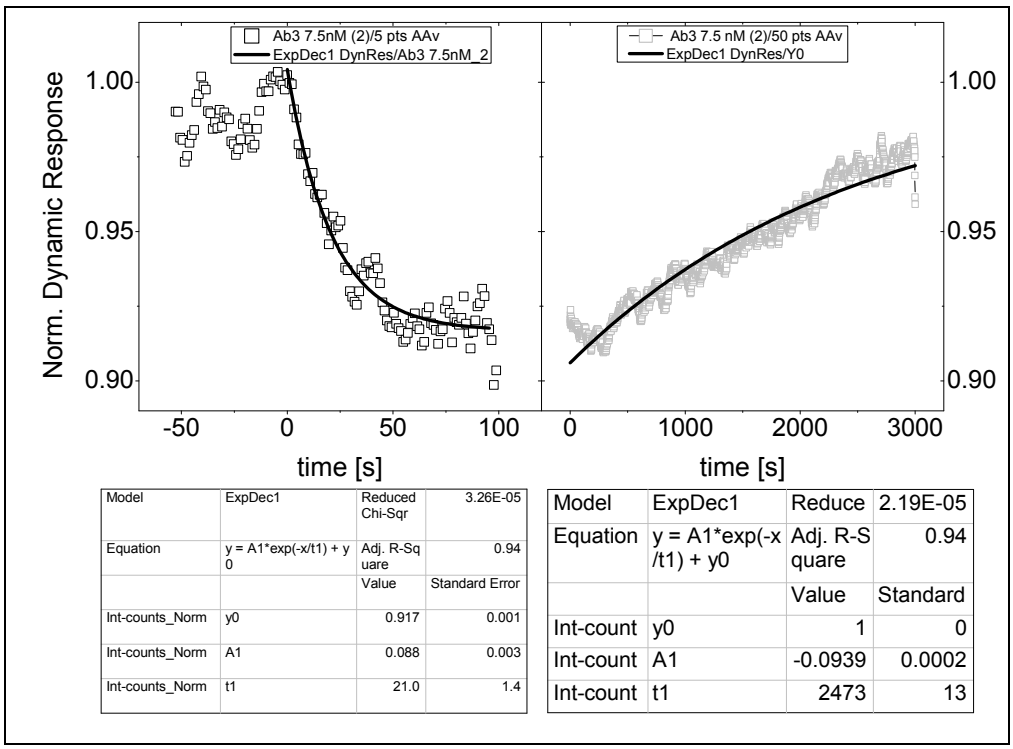

Model	ExpDec1	Reduced Chi-Sqr	3.26E-05
Equation	y = A1*exp(-x/t1) + y0	Adj. R-Square	0.94
		Value	Standard Error
Int-counts_Norm	y0	0.917	0.001
Int-counts_Norm	A1	0.088	0.003
Int-counts_Norm	t1	21.0	1.4

Model	ExpDec1	Reduce	2.19E-05
Equation	y = A1*exp(-x/t1) + y0	Adj. R-Square	0.94
		Value	Standard
Int-count	y0	1	0
Int-count	A1	-0.0939	0.0002
Int-count	t1	2473	13

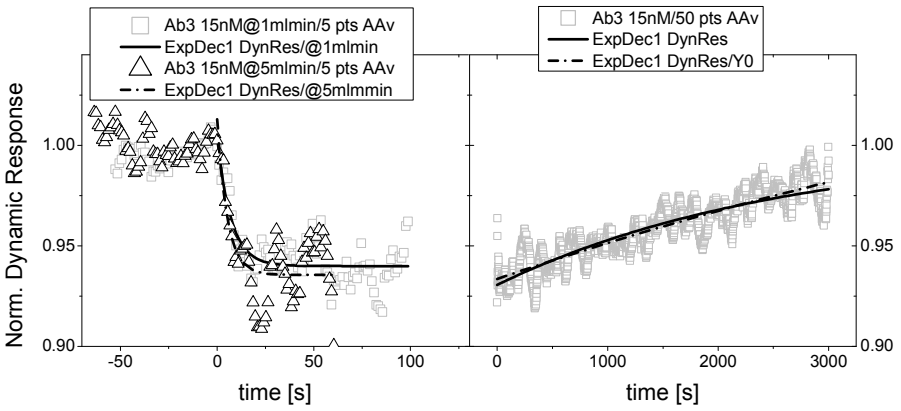

Model	ExpDec1	Reduced Chi	9.11E-0
Equation	y = A1*exp(-x/t1) + y0	Adj. R-Square	0.62
		Value	Standard Error
Int-counts	y0	0.940	0.001
Int-counts	A1	0.064	0.006
Int-counts	t1	7.2	1.2

Model	ExpDec1	Reduced Chi-Sqr	2.15E-04
Equation	y = A1*exp(-x/t1) + y0	Adj. R-Square	0.55
		Value	Standard Error
Int-counts	y0	0.936	0.002
Int-counts	A1	0.08	0.01
Int-counts	t1	5.3	1.3

Model	ExpDec1	Reduced Chi	5.04E-05
Equation	y = A1*exp(-x/t1) + y0	Adj. R-Squa	0.79
		Value	Standard Error
Int-cou	y0	1	0
Int-cou	A1	-0.069	0.0004
Int-counts	t1	2590	27

Model	ExpDec1	Reduced Chi	4.82E-05
Equation	y = A1*exp(-x/t1) + y0	Adj. R-Squar	0.80
		Value	Standard Error
Int-cou	y0	1.10	0.03
Int-cou	A1	-0.17	0.03
Int-counts	t1	8981	1992

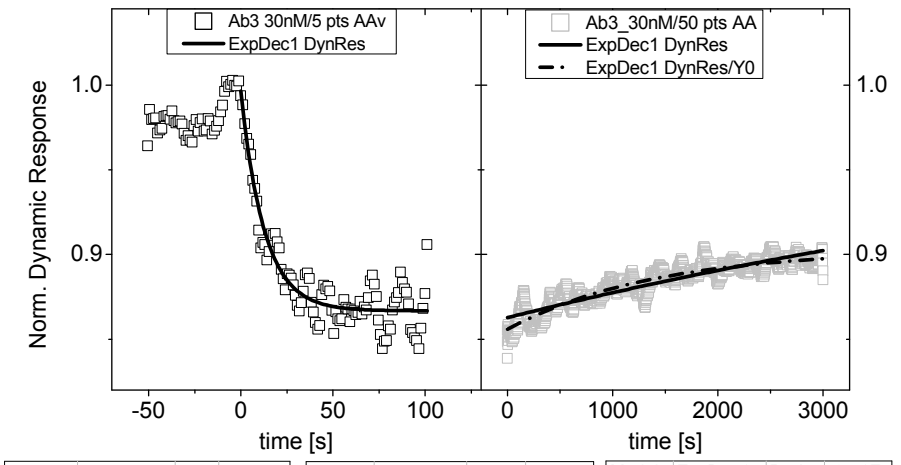

Model	ExpDec1	Redu	1.25E-04
Equation	y = A1*exp(-x/t1) + y0	Adj. R-Sq	0.87
		Value	Standard
Int-counts_Norm	y0	0.87	0.00
Int-counts_Norm	A1	0.12971	0.00604
Int-counts_Norm	t1	12.7525	1.0683

Model	ExpDec1	Redu	2.03E-
Equation	y = A1*exp(-x/t1) + y0	Adj. R-Squa	0.87
		Value	Standa
Int-cou	y0	0.902	0.0006
Int-cou	A1	-0.04	0.0005
Int-cou	t1	1381	41

Model	ExpDec1	Reduced Chi	2.71E-05
Equation	y = A1*exp(-x/t1) + y0	Adj. R-Squa	0.83
		Value	Standard Error
Int-cou	y0	1	0
Int-cou	A1	-0.13	0.0002
Int-cou	t1	8811	77

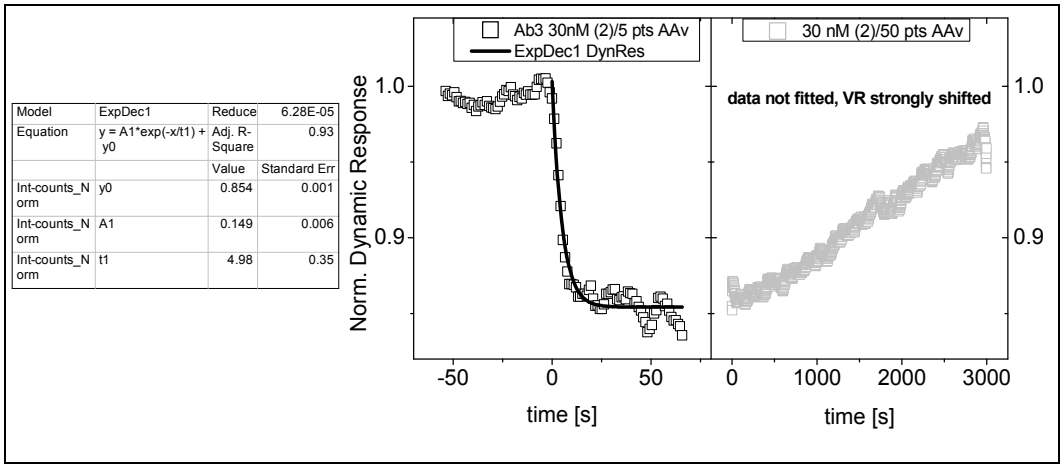

Model	ExpDec1	Reduce	6.28E-05
Equation	y = A1*exp(-x/t1) + y0	Adj. R-Square	0.93
		Value	Standard Err
Int-counts_Norm	y0	0.854	0.001
Int-counts_Norm	A1	0.149	0.006
Int-counts_Norm	t1	4.98	0.35

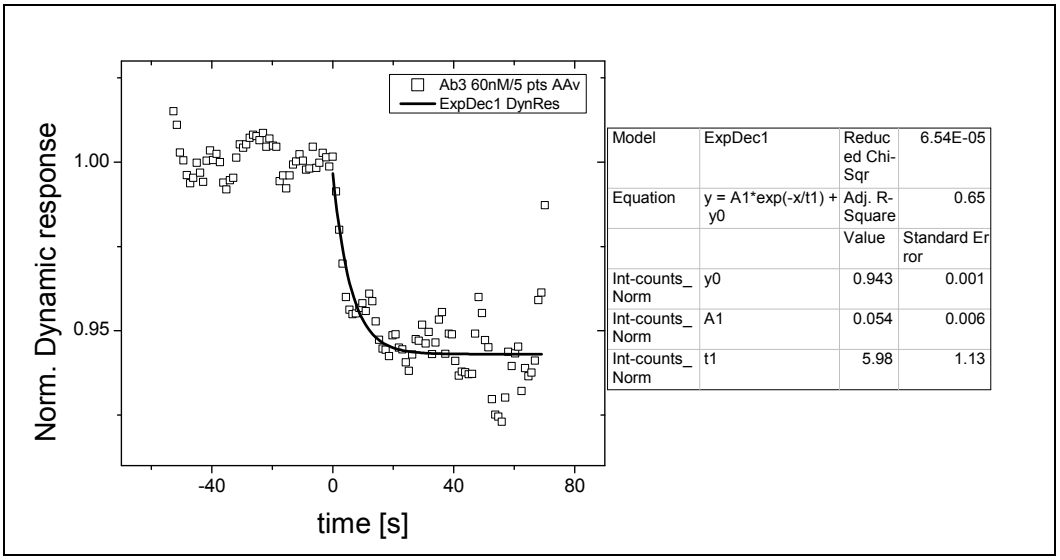

Model	ExpDec1	Reduced Chi-Sqr	6.54E-05
Equation	y = A1*exp(-x/t1) + y0	Adj. R-Square	0.65
		Value	Standard Error
Int-counts_Norm	y0	0.943	0.001
Int-counts_Norm	A1	0.054	0.006
Int-counts_Norm	t1	5.98	1.13

FIT OF ABSOLUTE FLUORESCENCE FOR AB3

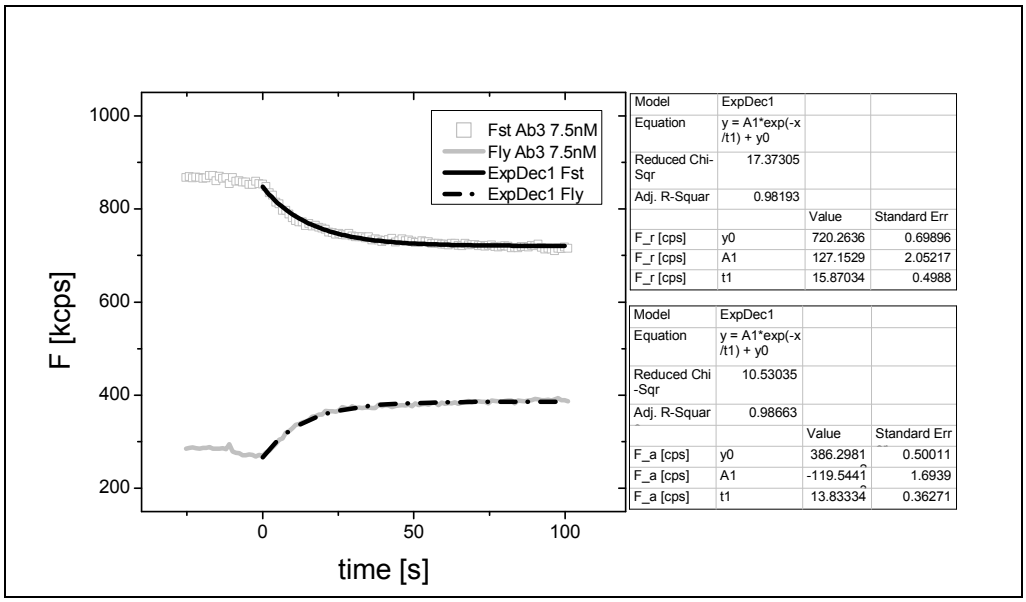

Model	ExpDec1		
Equation	y = A1*exp(-x/t1) + y0		
Reduced Chi-Sqr	17.37305		
Adj. R-Squar	0.98193		
		Value	Standard Err
F_r [cps]	y0	720.2636	0.69896
F_r [cps]	A1	127.1529	2.05217
F_r [cps]	t1	15.87034	0.4988

Model	ExpDec1		
Equation	y = A1*exp(-x/t1) + y0		
Reduced Chi-Sqr	10.53035		
Adj. R-Squar	0.98663		
		Value	Standard Err
F_a [cps]	y0	386.2981	0.50011
F_a [cps]	A1	-119.5441	1.6939
F_a [cps]	t1	13.83334	0.36271

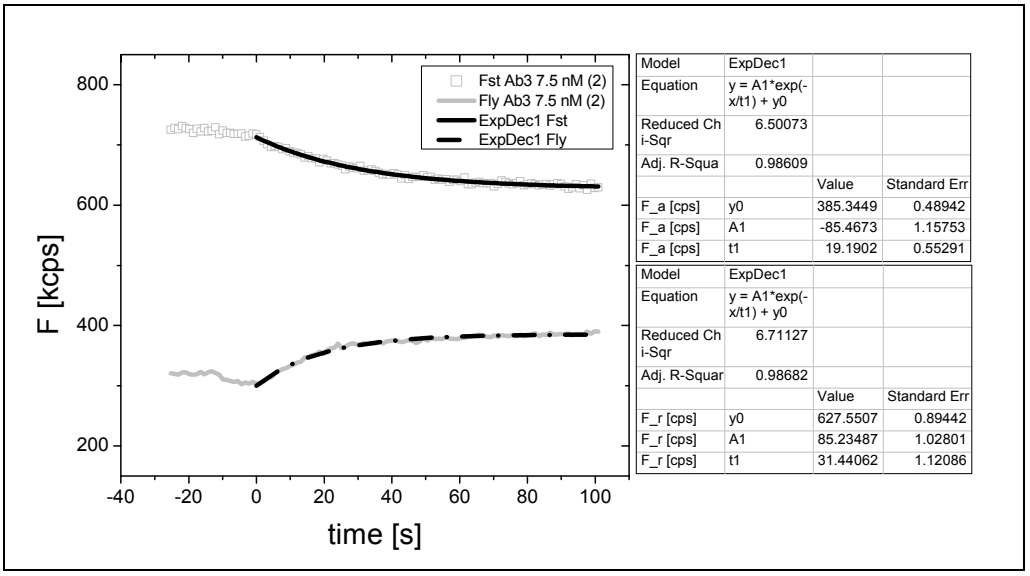

Model	ExpDec1		
Equation	y = A1*exp(-x/t1) + y0		
Reduced Chi-Sqr	6.50073		
Adj. R-Squa	0.98609		
		Value	Standard Err
F_a [cps]	y0	385.3449	0.48942
F_a [cps]	A1	-85.4673	1.15753
F_a [cps]	t1	19.1902	0.55291

Model	ExpDec1		
Equation	y = A1*exp(-x/t1) + y0		
Reduced Chi-Sqr	6.71127		
Adj. R-Squar	0.98682		
		Value	Standard Err
F_r [cps]	y0	627.5507	0.89442
F_r [cps]	A1	85.23487	1.02801
F_r [cps]	t1	31.44062	1.12086

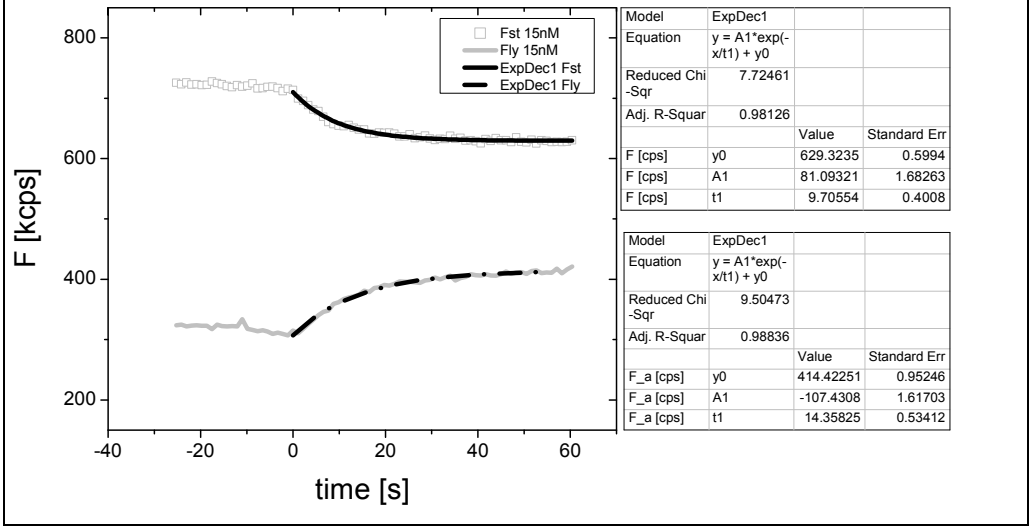

Model	ExpDec1		
Equation	y = A1*exp(-x/t1) + y0		
Reduced Chi-Sqr	7.72461		
Adj. R-Squar	0.98126		
		Value	Standard Err
F [cps]	y0	629.3235	0.5994
F [cps]	A1	81.09321	1.68263
F [cps]	t1	9.70554	0.4008

Model	ExpDec1		
Equation	y = A1*exp(-x/t1) + y0		
Reduced Chi-Sqr	9.50473		
Adj. R-Squar	0.98836		
		Value	Standard Err
F_a [cps]	y0	414.42251	0.95246
F_a [cps]	A1	-107.4308	1.61703
F_a [cps]	t1	14.35825	0.53412

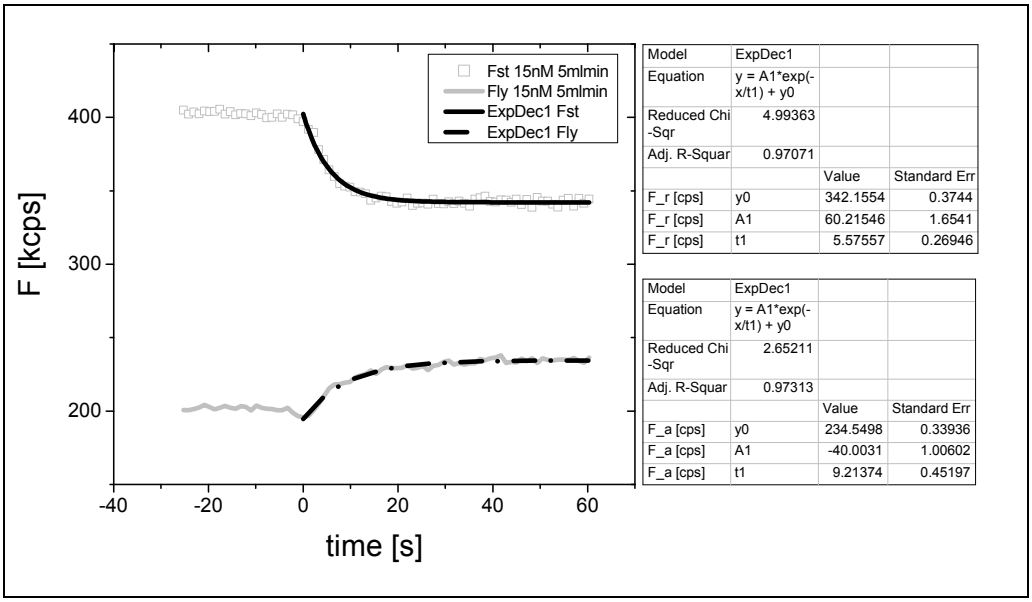

Model	ExpDec1		
Equation	y = A1*exp(-x/t1) + y0		
Reduced Chi-Sqr	4.99363		
Adj. R-Squar	0.97071		
		Value	Standard Err
F_r [cps]	y0	342.1554	0.3744
F_r [cps]	A1	60.21546	1.6541
F_r [cps]	t1	5.57557	0.26946

Model	ExpDec1		
Equation	y = A1*exp(-x/t1) + y0		
Reduced Chi-Sqr	2.65211		
Adj. R-Squar	0.97313		
		Value	Standard Err
F_a [cps]	y0	234.5498	0.33936
F_a [cps]	A1	-40.0031	1.00602
F_a [cps]	t1	9.21374	0.45197

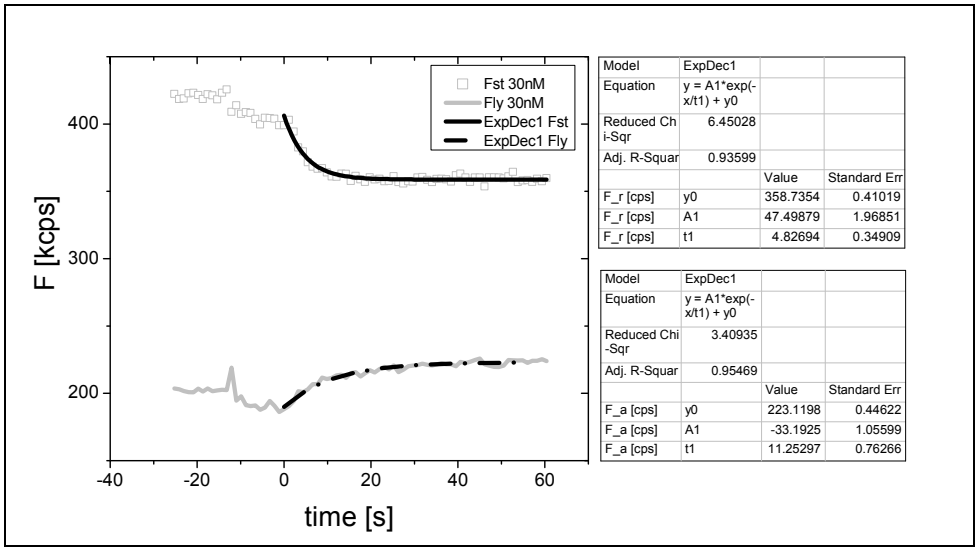

Model	ExpDec1		
Equation	y = A1*exp(-x/t1) + y0		
Reduced Chi-Sqr	6.45028		
Adj. R-Squar	0.93599		
		Value	Standard Err
F_r [cps]	y0	358.7354	0.41019
F_r [cps]	A1	47.49879	1.96851
F_r [cps]	t1	4.82694	0.34909

Model	ExpDec1		
Equation	y = A1*exp(-x/t1) + y0		
Reduced Chi-Sqr	3.40935		
Adj. R-Squar	0.95469		
		Value	Standard Err
F_a [cps]	y0	223.1198	0.44622
F_a [cps]	A1	-33.1925	1.05599
F_a [cps]	t1	11.25297	0.76266

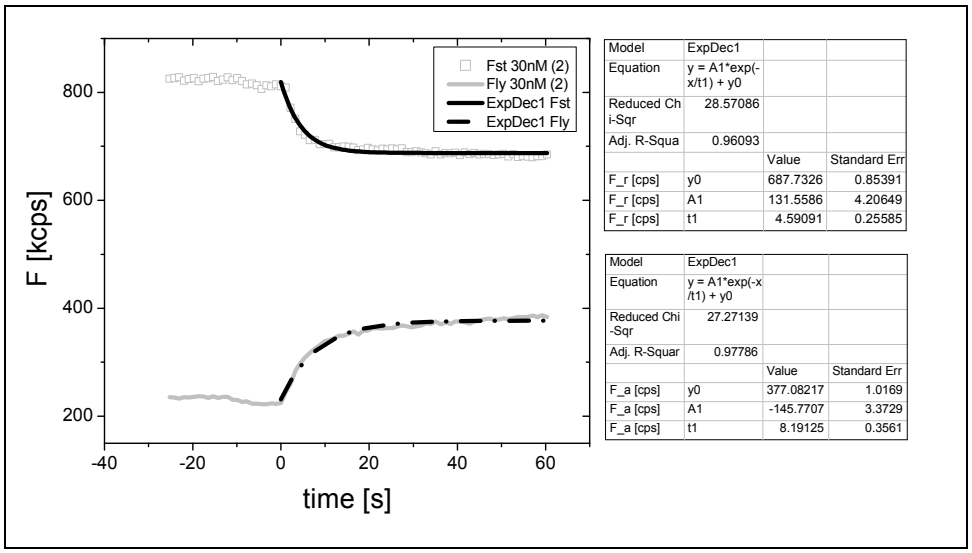

Model	ExpDec1		
Equation	y = A1*exp(-x/t1) + y0		
Reduced Chi-Sqr	28.57086		
Adj. R-Squa	0.96093		
		Value	Standard Err
F_r [cps]	y0	687.7326	0.85391
F_r [cps]	A1	131.5586	4.20649
F_r [cps]	t1	4.59091	0.25585

Model	ExpDec1		
Equation	y = A1*exp(-x/t1) + y0		
Reduced Chi-Sqr	27.27139		
Adj. R-Squar	0.97786		
		Value	Standard Err
F_a [cps]	y0	377.08217	1.0169
F_a [cps]	A1	-145.7707	3.3729
F_a [cps]	t1	8.19125	0.3561

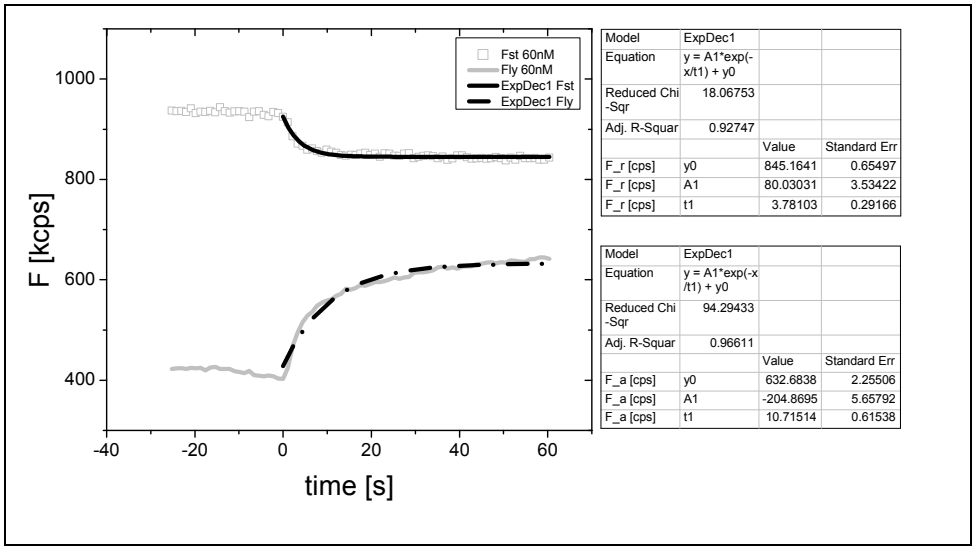

Model	ExpDec1		
Equation	y = A1*exp(-x/t1) + y0		
Reduced Chi-Sqr	18.06753		
Adj. R-Squar	0.92747		
		Value	Standard Err
F_r [cps]	y0	845.1641	0.65497
F_r [cps]	A1	80.03031	3.53422
F_r [cps]	t1	3.78103	0.29166

Model	ExpDec1		
Equation	y = A1*exp(-x/t1) + y0		
Reduced Chi-Sqr	94.29433		
Adj. R-Squar	0.96611		
		Value	Standard Err
F_a [cps]	y0	632.6838	2.25506
F_a [cps]	A1	-204.8695	5.65792
F_a [cps]	t1	10.71514	0.61538

FIT OF DYNRES AND ABSOLUTE FLUORESCENCE FOR AB1, AB4 AND AB5

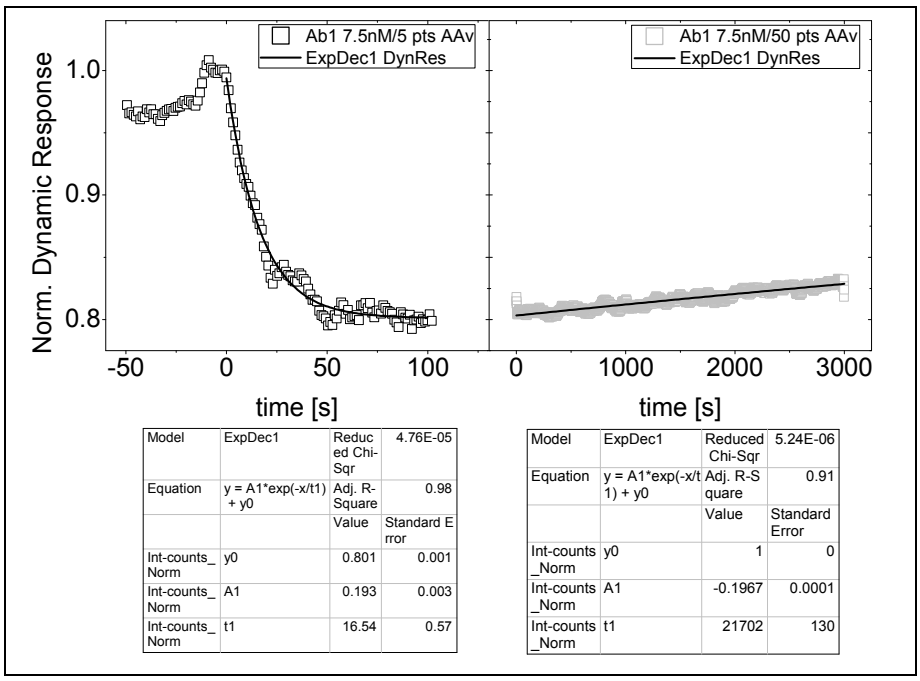

Model	ExpDec1	Reduced Chi-Sqr	4.76E-05
Equation	y = A1*exp(-x/t1) + y0	Adj. R-Square	0.98
		Value	Standard Error
Int-counts_Norm	y0	0.801	0.001
Int-counts_Norm	A1	0.193	0.003
Int-counts_Norm	t1	16.54	0.57

Model	ExpDec1	Reduced Chi-Sqr	5.24E-06
Equation	y = A1*exp(-x/t1) + y0	Adj. R-Square	0.91
		Value	Standard Error
Int-counts_Norm	y0	1	0
Int-counts_Norm	A1	-0.1967	0.0001
Int-counts_Norm	t1	21702	130

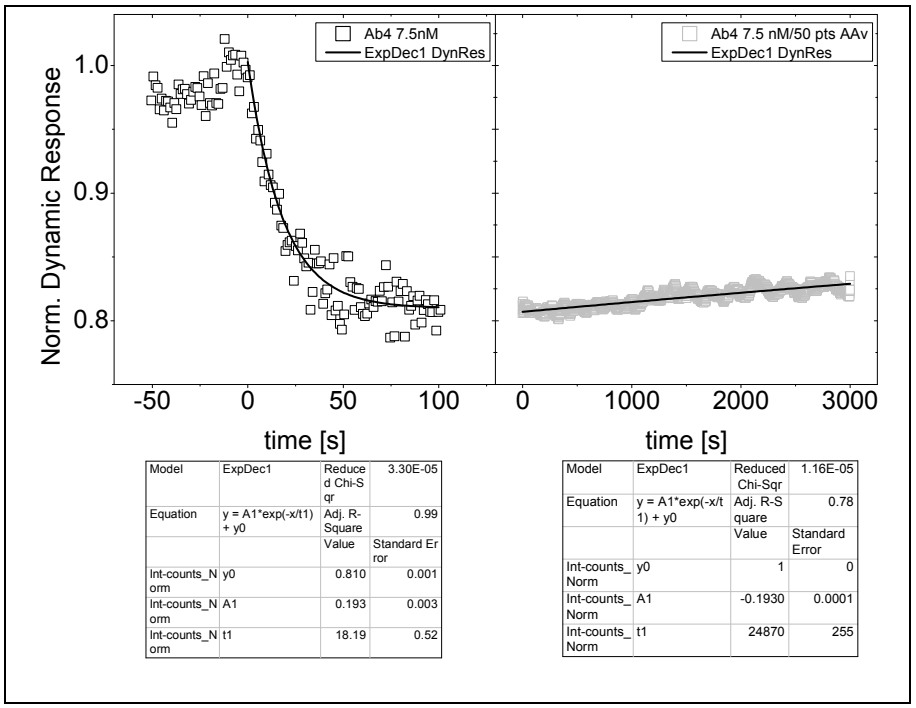

Model	ExpDec1	Reduced Chi-Sqr	3.30E-05
Equation	y = A1*exp(-x/t1) + y0	Adj. R-Square	0.99
		Value	Standard Error
Int-counts_Norm	y0	0.810	0.001
Int-counts_Norm	A1	0.193	0.003
Int-counts_Norm	t1	18.19	0.52

Model	ExpDec1	Reduced Chi-Sqr	1.16E-05
Equation	y = A1*exp(-x/t1) + y0	Adj. R-Square	0.78
		Value	Standard Error
Int-counts_Norm	y0	1	0
Int-counts_Norm	A1	-0.1930	0.0001
Int-counts_Norm	t1	24870	255

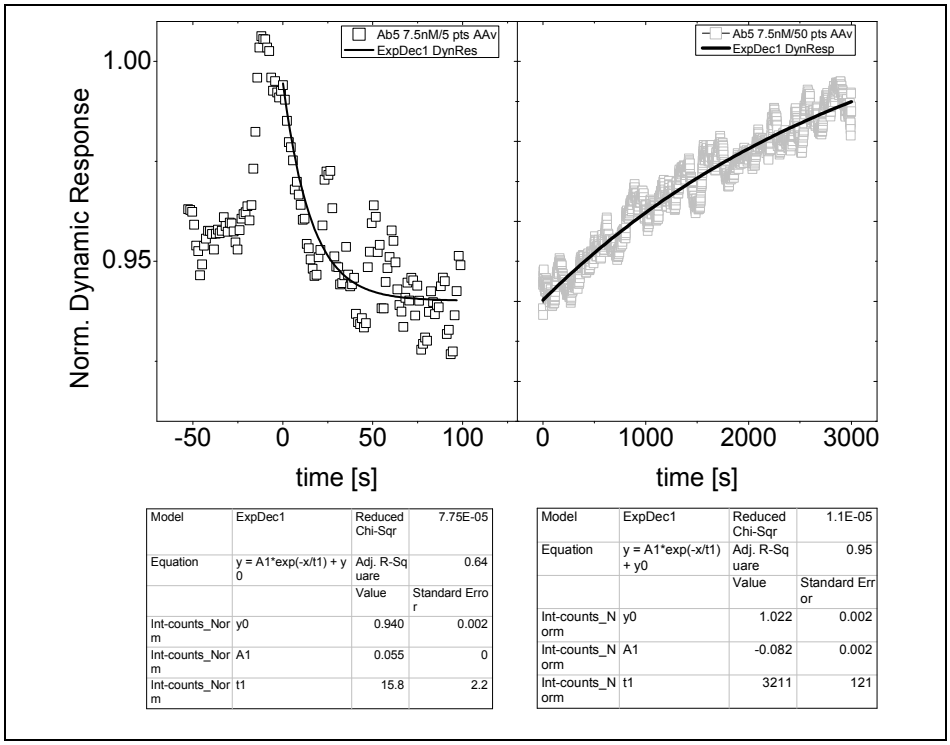

Model	ExpDec1	Reduced Chi-Sqr	7.75E-05
Equation	y = A1*exp(-x/t1) + y0	Adj. R-Square	0.64
		Value	Standard Error
Int-counts_Norm	y0	0.940	0.002
Int-counts_Norm	A1	0.055	0
Int-counts_Norm	t1	15.8	2.2

Model	ExpDec1	Reduced Chi-Sqr	1.1E-05
Equation	y = A1*exp(-x/t1) + y0	Adj. R-Square	0.95
		Value	Standard Error
Int-counts_Norm	y0	1.022	0.002
Int-counts_Norm	A1	-0.082	0.002
Int-counts_Norm	t1	3211	121

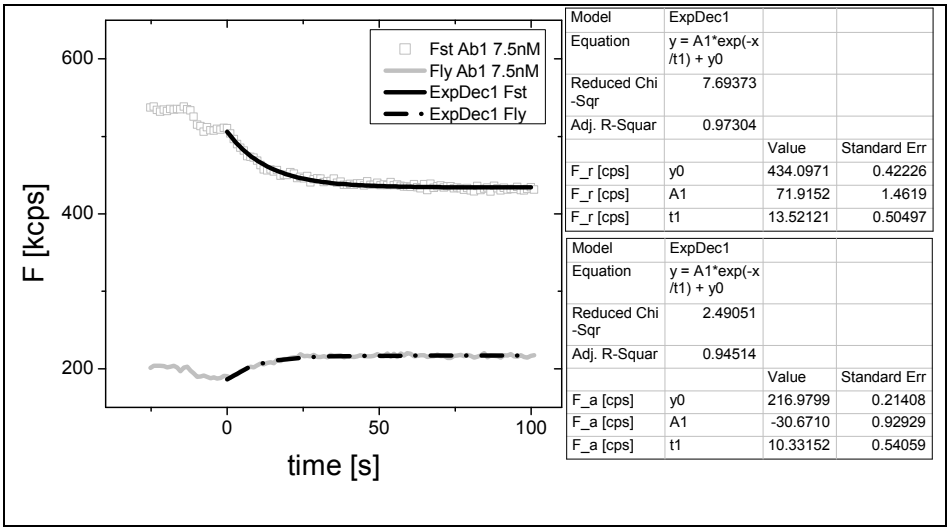

Model	ExpDec1		
Equation	y = A1*exp(-x/t1) + y0		
Reduced Chi-Sqr	7.69373		
Adj. R-Squar	0.97304		
		Value	Standard Err
F_r [cps]	y0	434.0971	0.42226
F_r [cps]	A1	71.9152	1.4619
F_r [cps]	t1	13.52121	0.50497

Model	ExpDec1		
Equation	y = A1*exp(-x/t1) + y0		
Reduced Chi-Sqr	2.49051		
Adj. R-Squar	0.94514		
		Value	Standard Err
F_a [cps]	y0	216.9799	0.21408
F_a [cps]	A1	-30.6710	0.92929
F_a [cps]	t1	10.33152	0.54059

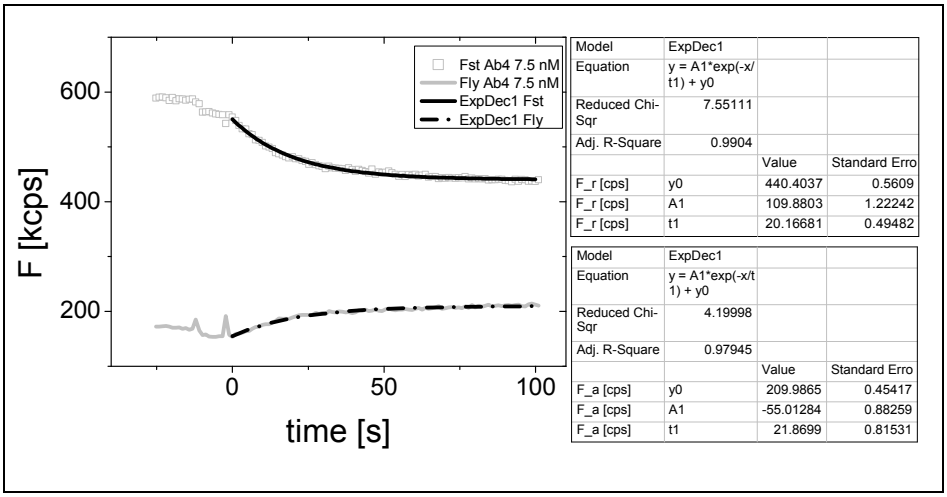

Model	ExpDec1		
Equation	y = A1*exp(-x/t1) + y0		
Reduced Chi-Sqr	7.55111		
Adj. R-Square	0.9904		
		Value	Standard Error
F_r [cps]	y0	440.4037	0.5609
F_r [cps]	A1	109.8803	1.22242
F_r [cps]	t1	20.16681	0.49482

Model	ExpDec1		
Equation	y = A1*exp(-x/t1) + y0		
Reduced Chi-Sqr	4.19998		
Adj. R-Square	0.97945		
		Value	Standard Error
F_a [cps]	y0	209.9865	0.45417
F_a [cps]	A1	-55.01284	0.88259
F_a [cps]	t1	21.8699	0.81531

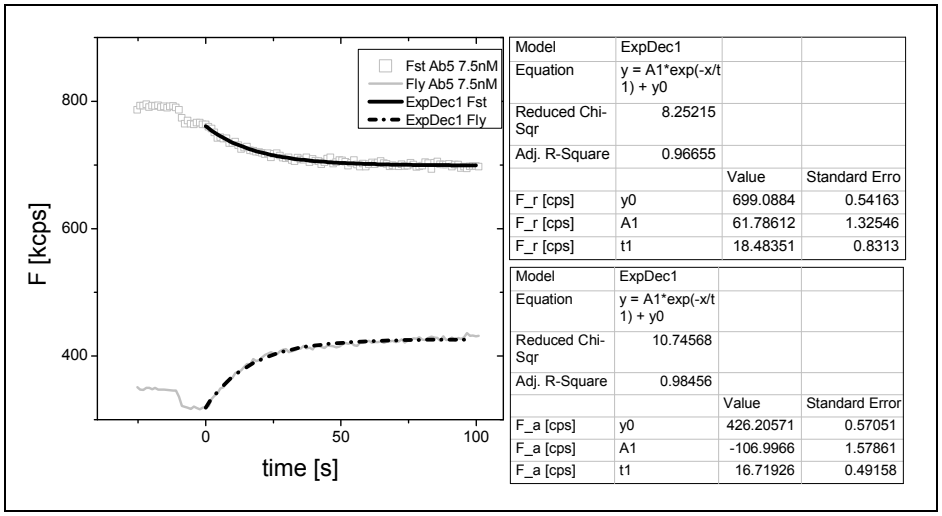

Model	ExpDec1		
Equation	y = A1*exp(-x/t 1) + y0		
Reduced Chi-Sqr	8.25215		
Adj. R-Square	0.96655		
		Value	Standard Erro
F_r [cps]	y0	699.0884	0.54163
F_r [cps]	A1	61.78612	1.32546
F_r [cps]	t1	18.48351	0.8313

Model	ExpDec1		
Equation	y = A1*exp(-x/t 1) + y0		
Reduced Chi-Sqr	10.74568		
Adj. R-Square	0.98456		
		Value	Standard Error
F_a [cps]	y0	426.20571	0.57051
F_a [cps]	A1	-106.9966	1.57861
F_a [cps]	t1	16.71926	0.49158

14.5 Cross-binding experiments of antibodies on prototype2

KM DATA IN PROTOTYPE2

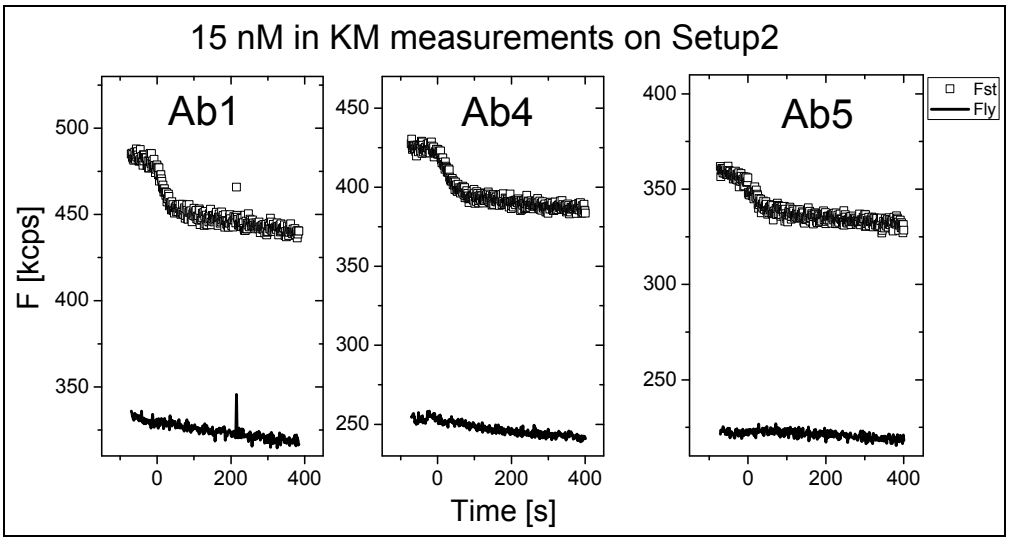

Injections of 15 nM Ab1, Ab4 and Ab5 on Prototype2 at 0.2 ml/min in KM measurements.

TRM DATA IN PROTOTYPE2

TRM data of 15 nM injections of 15 nM of Ab1, Ab4 and Ab5 on negative control layers, measured in cross-binding experiments.

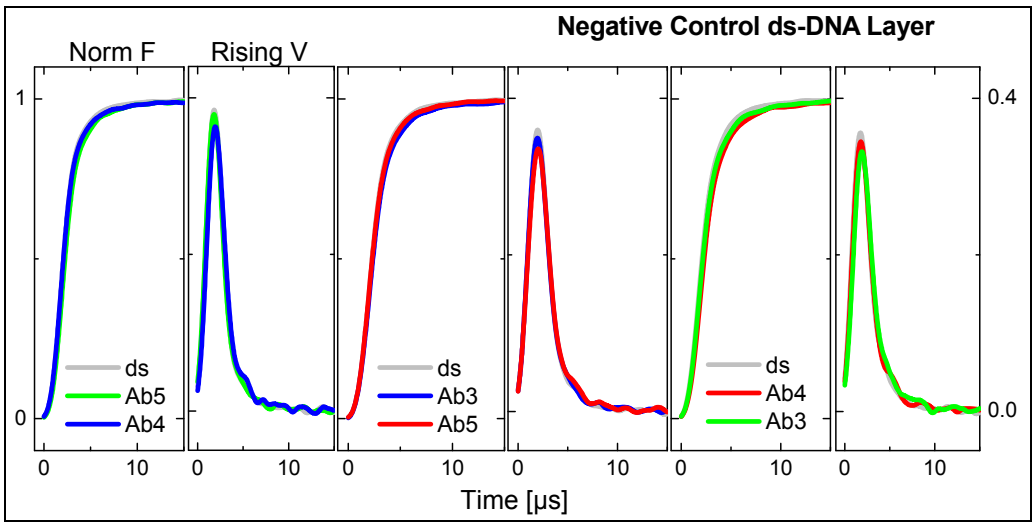

DYNRES IN PROTOTYPE2

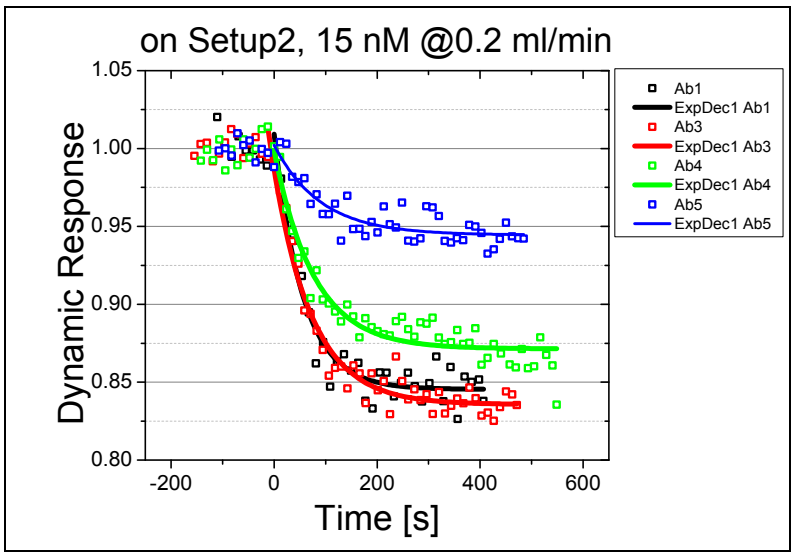

Measurement	τ_{on}[S]	k_{on} [$M^{-1}S^{-1}$]
Ab1 (15 nM)	56 (6)	1.E+06
Ab3 (15 nM)	77 (5)	9.E+05
Ab4 (15 nM)	72 (7)	7.E+05
Ab5 (15 nM)	90 (19)	9.E+05

DynRes of 15 nM injections of Ab1, Ab4 and Ab5 on hCA1-DNA layers at 0.2 ml/min

The obtained association rates were probably mass transfer limited, but multivalent binding should be excluded.

14.6 LFM data of initial ds-DNA layers on SWA1 and on Prototype2

SWA1

The absolute fluorescence, F_{ly} and F_{st}, and ΔF_{rel} of initial ds-DNA layers after electrical desorption were taken in LFM (LED power 0.2 V), in SWA1. The listed values corresponded to the layers used in antibody kinetic measurements; one single electrode was recorded in each experiment, loading the corresponding mAb as indicated.

Measurement	F_{ly} [kcps]	F_{st} [kcps]	ΔF_{rel} %
Ab3 (7.5 nM 1st)	18	55	67
Ab3 (7.5 nM 2nd)	18	40	55
Ab3 (15 nM)	16	50	68
Ab3 (30 nM 1st)	10	25	60
Ab3 (30 nM 2nd)	17	60	72
Ab3 (60 nM)	22	58	62
Ab3 (30 nM) Neg Ctr	23	60	62
Ab3 (60 nM) Neg Ctr	23	60	62
Ab1 (7.5 nM)	11	26	58
Ab4 (7.5 nM)	10	30	67
Ab5 (7.5 nM)	18	44	59

PROTOTYPE2

The absolute fluorescence, F_{ly} and F_{st}, and ΔF_{rel} of initial ds-DNA layers were taken in LFM (LED power 1 V), in Prototype2. The layers were used for antibody cross-binding experiments, loading the corresponding first mAb as indicated, and recording the DynRes. A rough calculation of fluorescence levels in LED power 0.2 V was done dividing by factor of 5, for fluorescence comparison with SWA1 measurements.

Measurement	F_{ly} [kcps]	F_{st} [kcps]	F_{ly} [kcps] 0.2 V	F_{st} [kcps] 0.2 V	ΔF_{rel} %
Ab1 (15 nM)	65	120	13	24	45
Ab3 (15 nM)	62	145	12	29	57
Ab4 (15 nM)	66	135	13	27	51
Ab5 (15 nM)	60	115	12	23	48

14.7 p53 project

A. Dimer-tetramer p53 transition in TRM data analyses

The transition of dimer-tetramer of p53 was evaluated analysing 1st derivative of sigmoidal fit (Figure 8.18) with Gaussian function fit, according to Eq. 14.1:

Eq. 14.1 $$y = y_0 + \frac{A}{w\sqrt{\frac{\pi}{2}}}\, e^{-2\frac{(x-x_c)^2}{w^2}}$$

The transition of dimer-tetramer for p53 wt FL, observed on surface on half-p21 layer was estimated to be at 60(±9) nM.

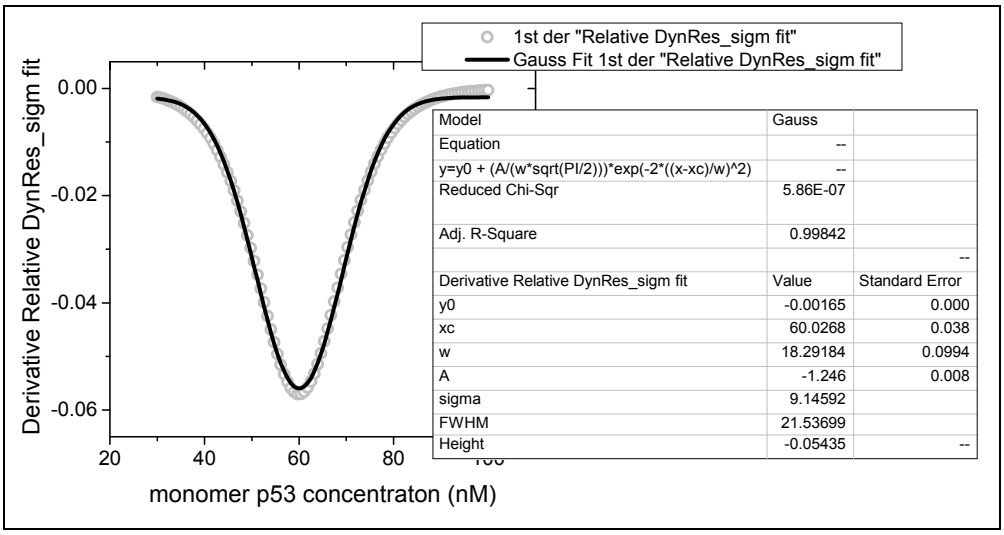

Model	Gauss	
Equation	--	
y=y0 + (A/(w*sqrt(PI/2)))*exp(-2*((x-xc)/w)^2)	--	
Reduced Chi-Sqr	5.86E-07	
Adj. R-Square	0.99842	
		--
Derivative Relative DynRes_sigm fit	Value	Standard Error
y0	-0.00165	0.000
xc	60.0268	0.038
w	18.29184	0.0994
A	-1.246	0.008
sigma	9.14592	
FWHM	21.53699	
Height	-0.05435	--

B. Quenching effect of p53-DNA complex in solution phase

Makiko Maruyama checked in solution the fluorescence reduction of p21 ds-74-mer-Cy3 in presence of bound p53 wt, at reaction concentration of 16.9 nM DNA and 68 nM p53. No reduction of the intensity was detected.

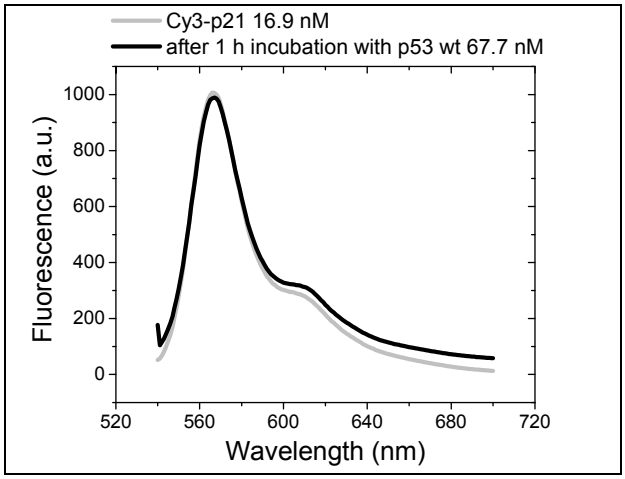

C. NORMALIZED FLUORESCENCE VS. DNA HEIGHT

Considering 140 mM total ionic strength, Andreas Langer estimated the correlation between normalized fluorescence intensity and height from surface of ds-74-mer (left plot), being the height dependent on applied potentials. The model (open blue circle) fitted very well the experimental data of VR curve (black square). The correlation between fluorescence intensity and height was used as a ruler in LFM concentration dependent data (Section 8.4.2.3, Figure 8.19) to estimate the height position of p21, half-p21 and random ds-74-mer from surface after p53 binding.